Natural Gas for Advanced Dual-Fuel Combustion Strategies

By

Nicholas Ryan Walker

A dissertation submitted in partial fulfillment of
the requirements for the degree of

Doctor of Philosophy

(Mechanical Engineering)

at the

UNIVERSITY OF WISCONSIN–MADISON

2016

Date of final oral examination: 6/1/2016

The dissertation is approved by the following members of the Final Oral Committee:

Rolf D. Reitz, Professor Emeritus, Mechanical Engineering
Jaal B. Ghandhi, Professor, Mechanical Engineering
David A. Rothamer, Associate Professor, Mechanical Engineering
Sage L. Kokjohn, Assistant Professor, Mechanical Engineering
George W. Huber, Professor, Chemical & Biological Engineering

For Nature

ABSTRACT

Natural gas fuels represent the next evolution of low-carbon energy feedstocks powering human activity worldwide. The internal combustion engine, the energy conversion device widely used by society for more than one century, is capable of utilizing advanced combustion strategies in pursuit of ultra-high efficiency and ultra-low emissions. Yet many emerging advanced combustion strategies depend upon traditional petroleum-based fuels for their operation. In this research the use of natural gas, namely methane, is applied to both conventional and advanced dual-fuel combustion strategies.

In the first part of this work (Chapters 4 and 5) both computational and experimental studies are undertaken to examine the viability of utilizing methane as the premixed low reactivity fuel in reactivity controlled compression ignition, a leading advanced dual-fuel combustion strategy. As a result, methane is shown to be capable of significantly extending the load limits for dual-fuel reactivity controlled compression ignition in both light- and heavy-duty engines.

In the second part of this work (Chapters 6 and 7) heavy-duty single-cylinder engine experiments are performed to research the performance of both conventional dual-fuel (diesel pilot ignition) and advanced dual-fuel (reactivity controlled compression ignition) combustion strategies using methane as the premixed low reactivity fuel. Both strategies are strongly influenced by equivalence ratio; diesel pilot ignition offers best performance at higher equivalence ratios and higher premixed methane ratios, whereas reactivity controlled compression ignition offers superior performance at lower equivalence ratios and lower premixed methane ratios.

In the third part of this work (Chapter 8) experiments are performed in order to determine the dominant mode of heat release for both dual-fuel combustion strategies. By studying the dual-fuel homogeneous charge compression ignition and single-fuel spark ignition, strategies representative of autoignition and flame propagation, respectively, detailed heat release analyses can be performed in order to determine the dominant mode of heat release. The results indicate, for lean conditions, that diesel pilot ignition is controlled by flame propagation and reactivity controlled compression ignition is controlled by autoignition. The results encourage the use of diesel pilot ignition for low-boost stoichiometric engine applications and the use of reactivity controlled compression ignition for high-boost lean-burn engine applications.

ACKNOWLEDGMENTS

To Professor Emeritus Rolf Reitz, I give my gratitude for his generous support and instruction. To my dissertation committee members, Professors Jaal Ghandhi, David Rothamer, Sage Kokjohn, and George Huber, I give my thanks for the oversight and criticism of my work. I extend my gratitude to the members of the Engine Research Center's Direct Injection Engine Research Consortium for supporting my studies and research.

To all ERCers: we've had endless pleasurable - and some painful - experiences together, here's to them all. Those on the highlight reel include Matt Labaza, Adam Dempsey, Derek Nieman, Dustin Witkowski, Martin Wissink, John Roberts, Chris Gross, Cory Adams, Flavio Chuahy, Matt Blessinger, Nick Neal, Dan DelVescovo, Josh Stein, and Sandeep Viswanathan, plus all the motorcycle goons including Ralph Braun and the Italians. Special thanks to Dave Montgomery, Val Gallegos, Dan Olsen, Seema Shah-Fairbank, Mike Andrie, and Jody Hoesly.

To my entire family I dedicate this work; without your support these words would not exist. And to Cate Briesemeister, *The Beast*, much appreciation for all the glorious days up North, the rip trips, and the love & happiness.

CONTENTS

Abstract **i**

Contents **iv**

List of Tables **ix**

List of Figures **xi**

Nomenclature **xviii**

1 Introduction **1**

1.1 Motivation 3

1.2 Objective 6

2 Literature Review **7**

2.1 The Internal Combustion Engine 7

2.2 Conventional Combustion Strategies 8

2.2.1 Spark Ignition 8

2.2.2 Compression Ignition 9

2.2.3 Dual-Fuel: Diesel Pilot Ignition 10

2.3 Advanced Combustion Strategies 10

2.3.1 Dual-Fuel: Reactivity Controlled Compression Ignition 13

2.4 Natural Gas as a Fuel in Internal Combustion Engines 14

2.4.1 Spark Ignition Systems 15

2.4.2 Compression Ignition Systems 16

2.4.3 Natural Gas Composition 18

3 Experimental Setup **21**

3.1 Experimental Engine Laboratory 21

3.2 Fuel System 23

3.3 Instrumentation and Control 29

3.4 Operation 33

3.5 Data Analysis 34

3.5.1 Uncertainty Propagation 34

3.5.2 Steady-State Calculations 36

3.5.2.1 Fuel Mixture Properties 36

3.5.2.2 Emissions 36

3.5.2.3 Intake Air and Trapped Mass 38

3.5.2.4 Efficiency Metrics 39

3.5.3 Individual Cycle Calculations 41

3.5.3.1 Volume and Area 41

3.5.3.2 Pressure 42

3.5.3.3 Indicated Work 42

3.5.3.4 Noise Metrics 43

3.5.3.5 Heat Release 44

3.5.3.6 Statistics and Ensembles 45

4 Computational Investigation of Reactivity Controlled Compression Ignition Combustion Using Methane in a Light-Duty Engine 47

4.1 Multi-Dimensional Engine CFD 47

4.2 Light-Duty Single-Cylinder Engine 49

4.3 Engine Simulation Conditions 50

4.4 Results and Discussion 51

4.4.1 Effect of Fuel Reactivity on Operating Range 51

4.4.2 Comparison of Operation at Fixed EGR Rate 54

4.5 Conclusions 56

5 Natural Gas for High Load Dual-Fuel Reactivity Controlled Compression Ignition in Heavy-Duty Engines 57

5.1 Experimental Setup 57
5.2 Operating Conditions 59
5.3 Results and Discussion 61
  5.3.1 Heat Release Analysis 62
  5.3.2 Fuel Effects on Engine Performance 67
  5.3.3 Analysis of Engine Load Capability 70
5.4 Conclusions 72

6 Comparison of Diesel Pilot Ignition (DPI) and Reactivity Controlled Compression Ignition (RCCI) in a Heavy-Duty Engine 74

6.1 Experimental Setup 74
6.2 Results and Discussion 76
  6.2.1 Combustion Regime Change from DPI to RCCI with Injection Timing 76
  6.2.2 Effect of Equivalence Ratio on DPI and RCCI Combustion 81
  6.2.3 DPI and RCCI Response to Fueling Rate Increase 89
6.3 Conclusions 94

7 Effect of Premixed Methane Ratio on DPI and RCCI Combustion in a Heavy-Duty Engine 96

7.1 Experimental Setup 96
7.2 Results and Discussion 98
  7.2.1 Effect of Equivalence Ratio and Premix Methane Ratio on Dual-Fuel Performance and Emissions 99
  7.2.2 Analyis of Global Emission and Efficiency Tradeoffs 104
7.3 Conclusions 109

8 Determination of Heat Release Mechanism in a Lean-Burn Dual-Fuel Heavy-Duty Engine 110

8.1 Experimental Setup 110

8.2 Results and Discussion 114

8.2.1 Performance and Emissions Characteristics of DF-HCCI, RCCI, DPI and SI Combustion Regimes in a Heavy-Duty Engine 114

8.2.2 Comparison of SI, DPI, RCCI, and DF-HCCI in a Heavy-Duty Engine at $\phi = 0.5$ 123

8.2.3 Effect of Engine Speed on the Rate of Heat Release in a Lean-Burn Dual-Fuel Heavy-Duty Engine 127

8.3 Conclusions 136

9 Summary & Future Work 140

9.1 CFD Investigation of Reactivity Controlled Compression Ignition Using Methane 140

9.1.1 Effect of Fuel Reactivity on Operating Range 140

9.1.2 Comparison of Operation at Fixed EGR Rate 140

9.2 Natural Gas for High Load Reactivity Controlled Compression Ignition . . . 140

9.2.1 Heat Release Analysis 141

9.2.2 Fuel Effects on Engine Performance 141

9.2.3 Analysis of Engine Load Capability 141

9.3 Comparison of Diesel Pilot Ignition and Reactivity Controlled Compression Ignition 142

9.3.1 Combustion Regime Change from DPI to RCCI with Injection Timing 142

9.3.2 Effect of Equivalence Ratio on DPI and RCCI Combustion 142

9.3.3 DPI and RCCI Response to Fueling Rate Increase 143

9.4 Effect of Premixed Methane Ratio on DPI and RCCI Combustion 143

- 9.4.1 Effect of Equivalence Ratio and Premix Methane Ratio on Performance and Emissions . . . 143
- 9.4.2 Analysis of Global Emission and Efficiency Tradeoffs . . . 144
- 9.5 Determination of Heat Release Mechanism for Diesel Pilot Ignition and Reactivity Controlled Compression Ignition . . . 144
  - 9.5.1 Performance and Emissions Characteristics of DF-HCCI, RCCI, DPI and SI Combustion Regimes . . . 144
  - 9.5.2 Comparison of SI, DPI, RCCI, and DF-HCCI in a Heavy-Duty Engine at $\phi = 0.5$ . . . 145
  - 9.5.3 Effect of Engine Speed on the Rate of Heat Release . . . 145
- 9.6 Future Work . . . 146
  - 9.6.1 CFD Optimization of High Power Density Natural Gas Dual-Fuel Engine . . . 146
  - 9.6.2 Kinetic Analysis of Dual-Fuel Combustion using Natural Gas . . . 146
  - 9.6.3 Multi-Mode Control Strategy for Natural Gas Dual-Fuel Engine . . . 146
  - 9.6.4 Study of Combustion Noise Effects in Natural Gas Dual-Fuel Combustion . . . 147
  - 9.6.5 Detailed Study of Heat Release Mechanisms in Natural Gas Dual-Fuel Combustion . . . 147
  - 9.6.6 Investigation of Natural Gas Fuel for Advanced Dual-Fuel Combustion 148

Bibliography **149**

LIST OF TABLES

2.1 Representative chemical composition of natural gas [88] 18

3.1 3401 Caterpillar SCOTE heavy-duty engine specifications. 21
3.2 Common rail injector specifications. 23
3.3 Specifications for the liquid and gaseous port fuel injectors. 23
3.4 Liquid fuel cart system hardware. 28
3.5 Low-speed instruments. 29
3.6 High-speed instruments. 29
3.7 Emissions instruments. 30
3.8 Low-speed data acquisition hardware 31
3.9 High-speed data acquisition hardware 31
3.10 Real-time control hardware 31

4.1 Light-duty engine specifications. 50
4.2 Engine operating conditions for the CFD study. 51
4.3 Performance and emissions results for the 35% EGR cases. 55

5.1 3401 Caterpillar SCOTE heavy-duty engine specifications. 57
5.2 Common rail injector specifications. 57
5.3 Engine operating conditions. 60
5.4 Maximum load at PPRR = 10 bar/deg using the equation [PPRR = α_1*(LOAD)^2 + α_2*(LOAD) + α_3] 72

6.1 3401 Caterpillar SCOTE heavy-duty engine specifications. 74
6.2 Common rail injector specifications. 75
6.3 Section 6.2.1 engine operating conditions. 76
6.4 Section 6.2.2 engine operating conditions. 82

6.5 Section 6.2.3 engine operating conditions. 90

7.1 3401 Caterpillar SCOTE heavy-duty engine specifications. 96
7.2 Common rail injector specifications. 96
7.3 Chapter 7 engine operating conditions. 98

8.1 3401 Caterpillar SCOTE heavy-duty engine specifications. 112
8.2 Common rail injector specifications. 112
8.3 SI hardware setup for the Chapter 8 SI experiments. 112
8.4 Fueling strategies for the multi-mode combustion experiments. 114
8.5 Section 8.2.1 engine operating conditions. 114
8.6 Section 8.2.3 engine operating conditions. 128
8.7 Section 8.2.3 ignition timings for the SI, DPI, and RCCI regimes. 128

LIST OF FIGURES

1.1 Carbon intensity of C1-C8 alkane hydrocarbons as a function of carbon number on an equal energy basis. 4

1.2 EROI for various primary energy resources. Black diamonds denote conventional oil gas; dark blue squares denote nuclear; green triangles denote traditional renewables; red circles denote solar energy; yellow triangles denote renewable energy crops; light blue diamonds denote modern hydraulic fracturing for natural gas. Where available, EROI ranges are shown. Data from References [5, 73]. 5

2.1 Pressure-volume path for the ideal Otto cycle. 8

2.2 Pressure-volume path for the ideal Diesel cycle. 9

2.3 Comparison of various conventional and advanced combustion strategies with respect to fuel stratification. Adapted from [110]. 11

2.4 Methane number measurement for simulated fuels, from [70]. 19

2.5 Ignition delay as a function of temperature for PRF0, PRF100, and CH_4, at ϕ = 0.3 and P = 40 bar. 20

3.1 Diagram of the SCOTE Laboratory. 22

3.2 Profiles of stock CDC piston (white outlined, CR = 16.1) and modified RCCI piston (gray, CR = 14.9). 22

3.3 Liquid fuel cart system diagram. 24

3.4 Picture of the two liquid fuel carts, with the common rail Cart 1 on the left and the port fuel Cart 2 on the right. 25

3.5 Diagram of the intake runner with the liquid and gaseous port fuel injection modifications. 26

3.6 Diagram of the gaseous port fuel injection system. 27

3.7 Process for converting raw voltage to measurement value with confidence intervals. 35
3.8 Process for estimating γ as a function of θ. 45
3.9 Fitting array data to normal distributions to create ensemble statistics. 46

4.1 Illustration of multi-dimensional engine CFD modeling of gasoline/diesel RCCI combustion using KIVA [21]. 48
4.2 KIVA computational sector mesh of the GM 1.9L engine geometry with the stock CDC piston. 49
4.3 Operating map for DI/PFI fuel combination of PRF0/PRF75 with the NO_x (green), PPRR (red), and η_{comb} (blue) limits imposed. 52
4.4 Operating map for DI/PFI fuel combination of PRF0/PRF100 with the NO_x (green), PPRR (red), and η_{comb} (blue) limits imposed. 53
4.5 Operating map for DI/PFI fuel combination of PRF0/CH_4 with the NO_x (green), PPRR (red), and η_{comb} (blue) limits imposed. 53
4.6 Pressure and heat release rates for 35% EGR conditions. 54
4.7 Overview of acceptable operating ranges for PRF0/PRF75, PRF0/PRF100, and PRF0/CH_4 fuel combinations. 56

5.1 SCOTE Laboratory configuration for the Chapter 5 experiments. 58
5.2 The modified RCCI piston (gray, CR = 14.9) profile used in the Chapter 5 experiments. 58
5.3 DI SOI timings as a function of engine load. Earlier injection timings are required for gasoline/diesel operation relative to methane/diesel operation. 60
5.4 Intake pressures for the experimental conditions presented in Chapter 5. 61
5.5 Apparent heat release rates for gasoline/diesel RCCI operation with CA50 = 0° aTDC combustion phasing. 62

5.6 Apparent heat release rates for gasoline/diesel RCCI operation with CA50 = 4° aTDC combustion phasing. 64

5.7 Apparent heat release rates for methane/diesel RCCI operation with CA50 = 0° aTDC combustion phasing. 65

5.8 Apparent heat release rates for methane/diesel RCCI operation with CA50 = 4° aTDC combustion phasing. 66

5.9 COV of IMEP. Methane/diesel operation has lower COV of IMEP relative to gasoline/diesel operation. 68

5.10 COV of PPRR. Methane/diesel operation has lower COV of PPRR relative to gasoline/diesel operation. 69

5.11 Peak cylinder pressure as a function of engine load. Both methane/diesel operation and delayed CA50 have lower peak cylinder pressure relative to gasoline/diesel operation and advanced CA50. 70

5.12 Peak pressure rise rate as a function of engine load. both methane/diesel operation and delayed CA50 have lower peak pressure rise rate relative to gasoline/diesel operation and advanced CA50. 71

6.1 SCOTE Laboratory configuration for the Chapter 6 experiments. 75

6.2 The modified RCCI piston (gray, CR = 14.9) profile used in the Chapter 6 experiments. 75

6.3 Pressure performance measurements for the SOI sweep. The vertical lines in each marker represent the range of one standard deviation. 77

6.4 Emission and efficiency performance measurements for the SOI sweep. The vertical lines in each marker represent the range of the 95% confidence interval. 79

6.5 Cylinder pressure (solid lines) and heat release rate (dashed lines) for the SOI sweep. Lines represent the ensemble average value, while shaded regions represent one standard deviation. 80

6.6 Pressure performance measurements for the equivalence ratio sweep. The vertical lines in each marker represent the range of one standard deviation. . . . 83

6.7 Emission and efficiency performance measurements for the equivalence ratio sweep. The vertical lines in each marker represent the range of the 95% confidence interval. 84

6.8 Cylinder pressure (solid lines) and heat release rate (dashed lines) for the equivalence ratio sweep. Lines represent the ensemble average value, while shaded regions represent one standard deviation. 85

6.9 Measured cyclic dispersion of peak apparrent heat release rate for DPI combustion. Red diamonds denote ϕ=0.72, black squares denote ϕ=0.64, and blue circles denote ϕ=0.50. 86

6.10 Measured cyclic dispersion of peak apparrent heat release rate for RCCI combustion. Red diamonds denote ϕ=0.71, black squares denote ϕ=0.64, and blue circles denote ϕ=0.50. 87

6.11 Measured cyclic dispersion of indicated mean effective pressure for DPI combustion. Red diamonds denote ϕ=0.72, black squares denote ϕ=0.64, and blue circles denote ϕ=0.50. 88

6.12 Measured cyclic dispersion of indicated mean effective pressure for RCCI combustion. Red diamonds denote ϕ=0.71, black squares denote ϕ=0.64, and blue circles denote ϕ=0.50. 89

6.13 Pressure performance measurements for the fueling rate sweep. The vertical lines in each marker represent the range of one standard deviation. 91

6.14 Emission and efficiency performance measurements for the fueling rate sweep. The vertical lines in each marker represent the range of the 95% confidence interval. 92

6.15 Energy balances for the fueling rate sweep. 93

7.1 SCOTE Laboratory configuration for the Chapter 7 experiments. 97

7.2 The stock CDC re-entrant piston (white, CR = 16.1) profile used in the Chapter 7 experiments. 97

7.3 Maximum NO_x (2,000 ppm) and HC (9,000 ppm) exhaust concentration limits for the DPI (solid lines) and RCCI (dashed lines) cases. 99

7.4 Pressure performance metrics for the DPI cases. Blue squares, yellow triangles, and purple circles denote 86%, 90%, and 95% premixed methane, respectively. The vertical lines in each marker represent the range of one standard deviation. 100

7.5 Emissions metrics for the DPI cases. Blue squares, yellow triangles, and purple circles denote 86%, 90%, and 95% premixed methane, respectively. The vertical lines in each marker represent the range of the 95% confidence interval. 101

7.6 Pressure performance metrics for the RCCI cases. Blue squares, yellow triangles, and purple circles denote 86%, 90%, and 95% premixed methane, respectively. The vertical lines in each marker represent the range of one standard deviation. 102

7.7 Emissions metrics for the RCCI cases. Blue squares, yellow triangles, and purple circles denote 86%, 90%, and 95% premixed methane, respectively. The vertical lines in each marker represent the range of the 95% confidence interval. 103

7.8 HC-NO_x relationship. Filled symbols are RCCI, open symbols are DPI; Square/blue symbols are 86% premixed CH4, triangle/gold symbols are 90% CH4, and diamond/purple symbols are 95% CH4. 105

7.9 CO-NO_x relationship. Filled symbols are RCCI, open symbols are DPI; Square/blue symbols are 86% premixed CH4, triangle/gold symbols are 90% CH4, and diamond/purple symbols are 95% CH4. 106

7.10 Noise-NO_x relationship. Filled symbols are RCCI, open symbols are DPI; Square/blue symbols are 86% premixed CH4, triangle/gold symbols are 90% CH4, and diamond/purple symbols are 95% CH4. 107

7.11 Efficiency-NO_x relationship. Filled symbols are RCCI, open symbols are DPI; Square/blue symbols are 86% premixed CH4, triangle/gold symbols are 90% CH4, and diamond/purple symbols are 95% CH4. 108

8.1 SCOTE Laboratory configuration for the Chapter 8 experiments. 111

8.2 The stock CDC re-entrant piston (white, CR = 16.1) profile used in the Chapter 8 experiments. 111

8.3 Modified NGK ER9EH spark plug in Caterpillar SCOTE engine head. 113

8.4 Ignition timings for the SI, DPI, and RCCI combustion regimes. 115

8.5 Methane energy fraction as a function of equivalence ratio for DF-HCCI, SI, DPI, and RCCI combustion regimes. 115

8.6 Pressure performance metrics for the DF-HCCI (green diamonds), SI (red circles), DPI (pink squares), and RCCI (blue triangles) cases. The vertical lines in each marker represent the range of one standard deviation. 116

8.7 Efficiency and emissions metrics for the DF-HCCI (green diamonds), SI (red circles), DPI (pink squares), and RCCI (blue triangles) cases. The vertical lines in each marker represent the range of the 95% confidence interval. 118

8.8 Breakdown of NO_x and THC emissions concentrations for the DF-HCCI (green diamonds), SI (red circles), DPI (pink squares), and RCCI (blue triangles) cases. The vertical lines in each marker represent the range of one standard deviation. 120

8.9 Ethylene (C_2H_4), formaldehyde (CH_2O), and n-pentene (nC_5H_{10}) emissions concentrations for the DF-HCCI (green diamonds), SI (red circles), DPI (pink squares), and RCCI (blue triangles) cases. The vertical lines in each marker represent the range of one standard deviation. 122

8.10 Cylinder pressure (solid lines) and heat release rate (dashed lines) for the equivalence ratio sweep. SI is denoted by red data, DPI is denoted by pink data, RCCI is denoted by blue data, and DF-HCCI is denoted by green data. 124

8.11 Energy balances for the DF-HCCI, SI, DPI, and RCCI combustion regimes at ϕ = 0.5. 126

8.12 Crank angle-based heat release rates for SI combustion. 900 RPM data are denoted by solid lines; 1300 RPM data are denoted by dashed lines. Spark timing and duration is illustrated. 129

8.13 Time-based heat release rates for SI combustion. 900 RPM data are denoted by solid lines; 1300 RPM data are denoted by dashed lines. Spark timing and duration is illustrated. 130

8.14 Crank angle-based heat release rates for DPI combustion. 900 RPM data are denoted by solid lines; 1300 RPM data are denoted by dashed lines; 1700 RPM data are denoted by dotted lines. Injection timing and duration is illustrated. . 131

8.15 Time-based heat release rates for DPI combustion. 900 RPM data are denoted by solid lines; 1300 RPM data are denoted by dashed lines; 1700 RPM data are denoted by dotted lines. Injection timing and duration is illustrated. 132

8.16 Crank angle-based heat release rates for RCCI combustion. 900 RPM data are denoted by solid lines; 1300 RPM data are denoted by dashed lines; 1700 RPM data are denoted by dotted lines. Injection timing and duration is illustrated. . 133

8.17 Time-based heat release rates for RCCI combustion. 900 RPM data are denoted by solid lines; 1300 RPM data are denoted by dashed lines; 1700 RPM data are denoted by dotted lines. Injection timing and duration is illustrated. 134

8.18 Peak apparent heat release rate as a function of engine speed. SI data are denoted by red circles; DPI data are denoted by pink squares; RCCI data are denoted by blue triangles. 135

8.19 Time-based location of peak apparent heat release rate as a function of engine speed. SI data are denoted by red circles; DPI data are denoted by pink squares; RCCI data are denoted by blue triangles. 135

NOMENCLATURE

Abbreviations

aTDC - After top dead center

bTDC - Before top dead center

BMEP - Brake mean effective pressure

CA50 - Crank angle at 50% heat release

CAD - Crank angle degrees

CDC - Conventional diesel combustion

CFD - Computational fluid dynamics

CI - Compression ignition

CN - Cetane number

CNG - Compressed natural gas

DDFS - Direct dual fuel stratification

DF-HCCI - Dual-fuel homogeneous charge compression ignition

DMP - Diesel micro pilot

DNS - Direct numerical simulation

DPI - Diesel pilot ignition

EGR - Exhaust gas recirculation

EROI - Energy returned on energy invested

EVC - Exhaust valve closing

EVO - Exhaust valve opening

GCI - Gasoline compression ignition

HCCI - Homogeneous charge compression ignition

HPDI - High pressure direct injection

HTHR - High temperature heat release

IMEP - Indicated mean effective pressure

ISFC - Indicated specific fuel consumption

IVC - Intake valve closing

IVO - Intake valve opening

LNG - Liquified natural gas

LPG - Liquified petroleum gas

LTC - Low temperature combustion

LTHR - Low temperature heat release

MN - Methane number

ON - Octane number

PPC - Partially premixed combustion

PPM - parts per million

PPRR - Peak pressure rise rate

PRF - Primary reference fuel

RCCI - Reactivity controlled compression ignition

RI - Ringing intensity

SCOTE - Single cylinder oil test engine

SI - Spark ignition

SPL - Sound pressure level

TDC - Top dead center

Elements and Molecules

DTBP - Di-tert-butyl peroxide

CH_20 - Formaldehyde

CH_4 - Methane

$C_{14}H_{30}$ - Tetradecane

C_2H_2 - Acetylene

C_2H_4 - Ethylene

CO - Carbon monoxide

EHN - 2-Ethylhexyl nitrate

HC - Hydrocarbon

iC_8H_{18} - iso-Octane

nC_5H_{10} - n-Pentene

nC_7H_{16} - n-Heptane

NO_x - Oxides of nitrogen

Symbols

° - Degree

ϕ - Equivalence ratio

Units

μm - Micrometer

A - Ampere

C - Celcius

J - Joule

K - Kelvin

L - Liter

min - Minute

mm - Millimeter

rev - Revolution

s - Second

1 INTRODUCTION

The internal combustion engine is at once both an elegantly-simple mechanical device (i.e., the slider-crank mechanism) and an chaotically-complex set of systems (i.e., fuel injection, air handling, valve actuation, etc.), working in harmony to convert chemical energy stored in the intramolecular bonds of the fuel into useful mechanical work, electrical power, or heat for the demands of human life. Phil Meyers stated it best:.

> ”... it features all of the elements of engineering: materials, fluids, thermodynamics, lubrication, chemistry, electronics, etc. The only thing missing is nuclear reaction.”

Stemming from the ubiquitous use of the internal combustion engine, stringent emissions and efficiency regulations have driven the research and development of advanced internal combustion engines capable of meeting regulatory targets. Currently, criteria pollutants such as oxides of nitrogen, carbon monoxide, sulfur dioxide, soot and particulate matter, and unburned hydrocarbons are the key emissions components targeted for reductions in order to improve air quality. In addition, increasing atmospheric concentrations of carbon dioxide are generating new greenhouse gas regulations for internal combustion engines, in view of which manufacturers are driven increase the thermal efficiency of their engines.

Historically, the base energy feedstock for the internal combustion engine has been petroleum, a sub-surface liquid mixture of hydrocarbons, from which both diesel and gasoline fuels are distilled. Traditionally, spark-ignition engine systems utilized gasoline (providing sufficient flame speeds while resisting autoignition) and compression-ignition engine systems used diesel (autoignites easily). Even today, the diesel combustion process differs little from Sir Harry R. Ricardo’s apt description:

”Before concluding, I am going to take a rather unconventional course, in a technical lecture, of asking you to accompany me, in imagination, inside the cylinder of a Diesel engine. Let us imagine ourselves seated comfortably on the top of the piston, at or about the end of the compression stroke. We are in complete darkness, the atmosphere is a trifle oppressive, for the shade temperature is well over 500 °C - almost a dull red heat - and the density of the air is such that the contents of an average sitting room would weigh about a ton: also, it is very draughty, in fact, the draught is such that in reality we should be blown off our perch and hurled about like autumn leaves in a gale. Suddenly, above our heads a valve is opened and a rainstorm of fuel begins to descend. I have called it a rainstorm, but the velocity of droplets approaches much more nearly that of rifle bullets than of raindrops. For a while nothing startling happens, the rain continues to fall, the darkness remains intense. Then suddenly, away to our right perhaps, a brilliant gleam of light appears moving swiftly and purposefully; in an instant this is followed by a myriad others all around us, some large and some small, until on all sides of us the space is filled with a merry blaze of moving lights; from time to time the smaller lights wink and go out, while the larger ones develop fiery tails like comets; occasionally these strike the walls, but being surrounded with an envelope of burning vapour they merely bounce off like drops of water spilt on a red hot plate. Right overhead all is darkness still, the rainstorm continues, and the heat is becoming intense; and now we shall notice that a change is taking place. Many of the smaller lights around us have gone out, but new ones are beginning to appear, more overhead, and to form themselves into definite streams shooting rapidly downwards or outwards from the direction of the injector nozzles. Looking round again we see that the lights around are growing yellower; they no longer move in definite directions, but appear to be drifting

> listlessly hither and thither; here and there they are crowding together in dense nebulae, and these are burning now with a sickly smoky flame, half suffocated for want of oxygen. Now we are attracted by a dazzle overhead, and, looking up, we see that what at first was cold rain falling through utter darkness, has given place to a cascade of fire, as from a rocket. For a little while this continues, then ceases abruptly as the fuel valve closes. Above and all around us are still some lingering fireballs, now trailing long tails of sparks and smoke and wandering aimlessly in search of the last dregs of oxygen which will consume them finally and set their souls at rest. If so, well and good; if not, some unromantic engineer outside will merely grumble that the exhaust is dirty and will set the fuel valve to close a trifle earlier. So ends the scene, or rather my conception of the scene, and I will ask you to realize that what has taken my nearly five minutes to describe may all be enacted in one five hundredth of a second or even less."

Truly incredible. However, traditional fuels and conventional combustion strategies allow little room for error with respect to meeting emissions and efficiency regulations in-cylinder. As a result, alternative fuels and advanced combustion strategies now provide pathways to ultra-low emissions and ultra-high efficiencies.

1.1 Motivation

To demonstrate the carbon-emission reduction capability of alkane hydrocarbons, Figure 1.1 illustrates the potential for a 21% reduction in carbon content for a C1 alkane (methane) relative to a C8 alkane (octane), on an energy basis.

While low-carbon (C1-C4) compounds are generally a byproduct of petroleum extraction, global natural gas reserves, including methane hydrates, are poised to be the naturally-occurring resource for low-carbon fuels in quantities sufficient for global demand. It is also worth noting that methane is a byproduct of many biogenic processes, providing

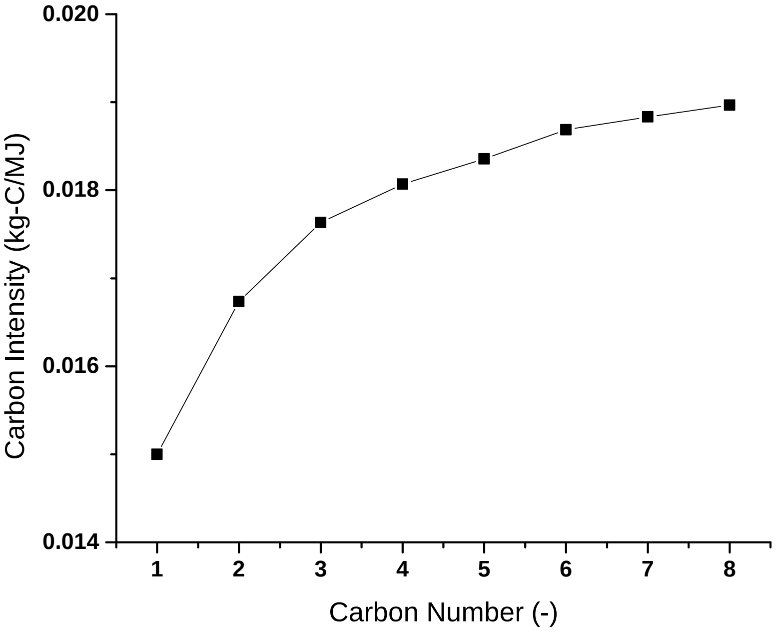

Figure 1.1: Carbon intensity of C1-C8 alkane hydrocarbons as a function of carbon number on an equal energy basis.

a significant opportunity for low-carbon biorenewable fuels derived from organic waste for use in internal combustion engines.

Another aspect to consider with respect to global energy feedstocks is the harvesting efficiency. One metric for measuring the efficiency of an energy harvesting process is the energy returned on energy invested (EROI). The EROI provides a relative signal towards the overall efficiency of the extraction process. It has been demonstrated that an EROI in the range of 7 to 8 is considered to be a sound break-even EROI threshold for an energy harvesting process. Figure 1.2 shows the EROI for a range of primary energy sources, with the data extracted from References [5, 73]. It is observed that modern technological advances (light blue diamond in Figure 1.2) have placed natural gas as an abundant and efficient primary energy resource, with a significantly lower carbon impact, for generations to come.

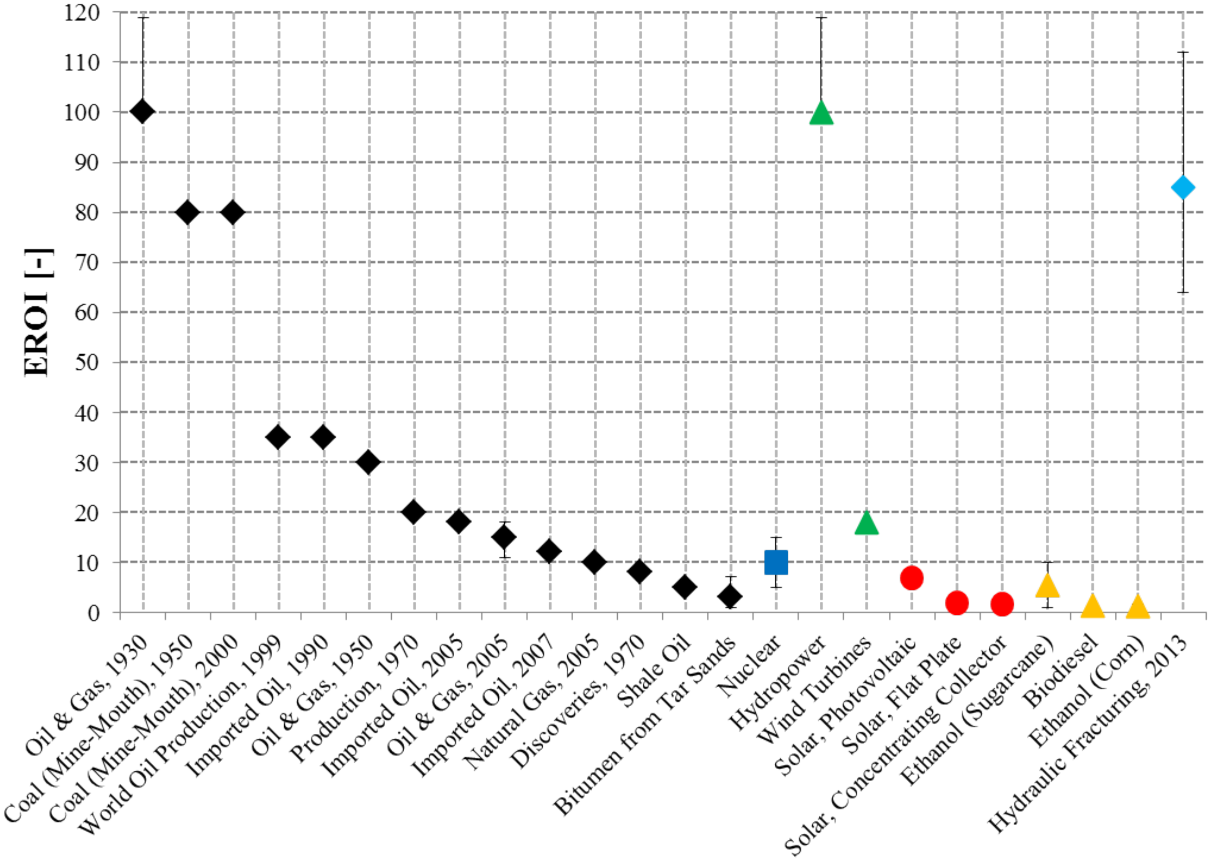

Figure 1.2: EROI for various primary energy resources. Black diamonds denote conventional oil gas; dark blue squares denote nuclear; green triangles denote traditional renewables; red circles denote solar energy; yellow triangles denote renewable energy crops; light blue diamonds denote modern hydraulic fracturing for natural gas. Where available, EROI ranges are shown. Data from References [5, 73].

In combination with advanced combustion strategies that are capable of improving the thermal efficiency of the combustion process, the benefits of utilizing low-carbon fuels for significant emissions reductions are only magnified.

1.2 Objective

There are five main objectives of this research:

1. Employ computational fluid dynamics modeling to study the operating space of a light-duty dual-fuel engine with both gasoline and methane as the premixed fuels.
2. Perform engine experiments to compare the load capability of a heavy-duty dual-fuel engine using both gasoline and methane as the premixed fuels.
3. Compare the more conventional and commercialized diesel pilot ignition approach with reactivity controlled compression ignition using methane in a heavy-duty engine.
4. Investigate the effect of in-cylinder mixture preparation on diesel pilot ignition and reactivity controlled compression ignition in a methane-fueled heavy-duty engine.
5. Determine the dominant mechanism of heat release for diesel pilot ignition and reactivity controlled compression ignition in a methane-fueled heavy-duty engine.

2 LITERATURE REVIEW

2.1 The Internal Combustion Engine

The internal combustion engine[1] was conceived in order to provide a safe and reliable device capable of converting the chemical energy stored in the intramolecular bonds of hydrocarbon compounds into useful mechanical, thermal, and eventually, electrical power. Early 19th century engineers focused on the fusion of simple mechanical devices coupled with the most efficient thermodynamic cycles in order to produce shaft power resulting from the combustion of hydrocarbon fuels in their machines. Numerous engine inventors plied their myriad of ideas and demonstrations; however, relatively few were successful in the commercial development of their inventions.

The first engine based on the two-stroke cycle was developed by J. J. E. Lenoir in 1858, with an efficiency of about 5%. The Lenoir engine proved to be reliable in operation and was successfully marketed. However, the four-stroke cycle, originally patented by A. B. de Rochas in 1862, was proven to offer superior performance as the engine co-developed by N. A. Otto and E. Langen in 1867 aptly demonstrated by achieving an efficiency of 11%. The Otto-Langen engine evolved into what is now known as the Otto-cycle engine, the base engine architecture for spark-ignition combustion. It was not until 1881 that D. Clerk produced the first practical two-stroke engine operating on the spark-ignition principle.

In 1872, G. Brayton developed a pilot flame constant pressure engine, from which the Brayton cycle used in turbine engines evolved. Taking a different track from the others, R. Diesel [27] by 1897 had perfected his engine design, which relied upon the compression ignition of a direct injection of liquid fuel into the combustion chamber. This novel design allowed for the use of higher compression ratios, with which Diesel's engine achieved an efficiency of 27%, far superior than the competing designs of the time.

---

[1] This introduction to the internal combustion engine and conventional combustion strategies has been derived from the works of Heywood [44], Ferguson & Kirkpatrick [33], Pulkrabek [84], and Basshuysen & Schäfer [6].

2.2 Conventional Combustion Strategies

The explosive demand for the internal combustion engine, coupled with a wide range of available engine designs, led to a consensus of sorts on base engine architectures: the Otto-cycle became popular on low-reactivity light liquid fuels (e.g., gasoline), providing the basis for spark ignition (SI) engines; the Diesel-cycle allowed for the use of high-reactivity heavy liquid fuels (e.g., diesel), providing the basis for compression ignition (CI) engines.

2.2.1 Spark Ignition

The spark ignition engine has historically operated upon the principle of igniting a fully-premixed air-fuel charge by means of electrical discharge across a small gap in the combustion chamber, producing a flame kernel from which the combustion reaction grows by means of a flame front. The electrical discharge, generally via a spark plug, produces a high-temperature plasma in the vicinity of 60,000 K peak (6000 K average).

The Otto cycle, the base thermodynamic cycle for spark ignition combustion, utilizes heat addition, Q_H, into the combustion chamber at a constant volume, as depicted in Figure 2.1.

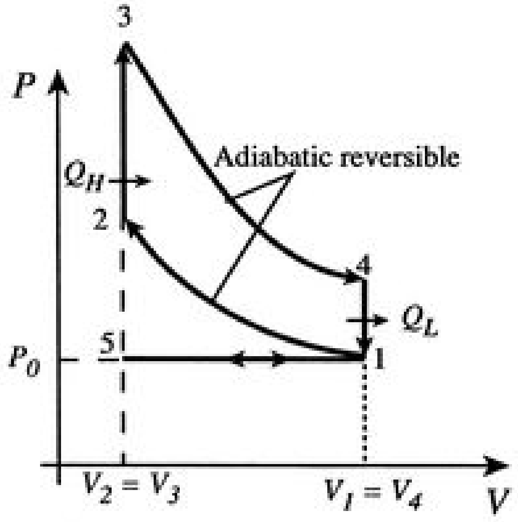

Figure 2.1: Pressure-volume path for the ideal Otto cycle.

The ignition timing is directly controlled by the timing of the spark event in the combustion chamber; the rate of combustion (i.e., flame speed) is augmented by modifying the strength of the swirl or squish flows and by varying the levels of in-cylinder turbulence. In general, stronger flow fields and higher turbulence levels increase flame speed.

Spark ignition engine systems have been designed to run on a range of fuels which display high resistance to autoignition such as gasoline, alcohols (e.g., ethanol), natural gas, synthesis gas (a mixture of hydrogen and carbon monoxide), and other liquified gases such as liquified natural gas (LNG) and liquified petroleum gas (LPG).

2.2.2 Compression Ignition

The compression ignition combustion process depends on the direct injection of the fuel, which undergoes autoignition to initiate the combustion process. Combustion occurs simultaneously at many locations of the fuel spray, which moves through a series of processes: The fuel spray begins to atomize, producing very small liquid droplets; then, the small droplets begin to evaporate into a vapor, which then mixes further with the air; eventually, the air-fuel mixture autoignites, commencing the combustion process.

The Diesel cycle, the base thermodynamic cycle for compression ignition combustion, utilizes heat addition, Q_H, into the combustion chamber at a constant pressure, as depicted in Figure 2.2.

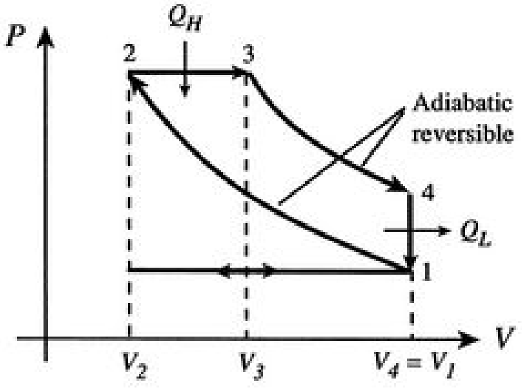

Figure 2.2: Pressure-volume path for the ideal Diesel cycle.

Compression ignition engine systems have been designed to run on a range of fuels which display high propensity to autoignition such as petroleum, heavy fuel oils, gas oil (e.g., diesel), vegetable oils, and methyl esters.

2.2.3 Dual-Fuel: Diesel Pilot Ignition

Interestingly, a merger between SI and CI engines appeared ready for appearance when Cooper-Bessamer put heavy development into a gas-diesel dual-fuel engine in 1927 [11]. This effort fell short of it's goals, and it wasn't until 1940 when the National Gas & Oil Engine Company Limited of England produced the first successful dual-fuel engine [31]. The basis for this dual-fuel combustion strategy relied upon the ignition of the premixed fuel (e.g., natural gas) by a direct-injected pilot fuel (e.g., diesel oil). The autoignition of the pilot fuel provided the ignition site(s) for the premixed fuel, and acted as a ”liquid spark plug” allowing sufficient ignition energy from which to propagate a flame, representing a merger of the ignition mechanisms of conventional SI and CI engine systems. While capable of using gasoline as the premixed fuel [30], diesel pilot ignition (DPI) is currently the industry-standard dual-fuel combustion strategy optimized for engines utilizing gaseous fuels [51, 103, 115].

2.3 Advanced Combustion Strategies

Advanced combustion strategies have arisen as pathways for achieving high efficiency and clean combustion in concert with modern engine systems. To improve the thermodynamic cycle efficiency, techniques for idealizing the heat release during combustion towards constant-volume energy conversion are applied. In addition, low temperature combustion (LTC) strategies for reducing the peak combustion temperatures reduce heat losses through the combustion chamber walls. Furthermore, emissions of nitric oxides are also reduced by lowering the peak combustion temperatures. By improving mixture formation and spray performance, reductions in peak equivalence ratios during combustion leads to reduced soot and particulate matter formation. Numerous strategies have been developed with the aim of achieving clean and efficient combustion, as summarized in Figure 2.3 [110].

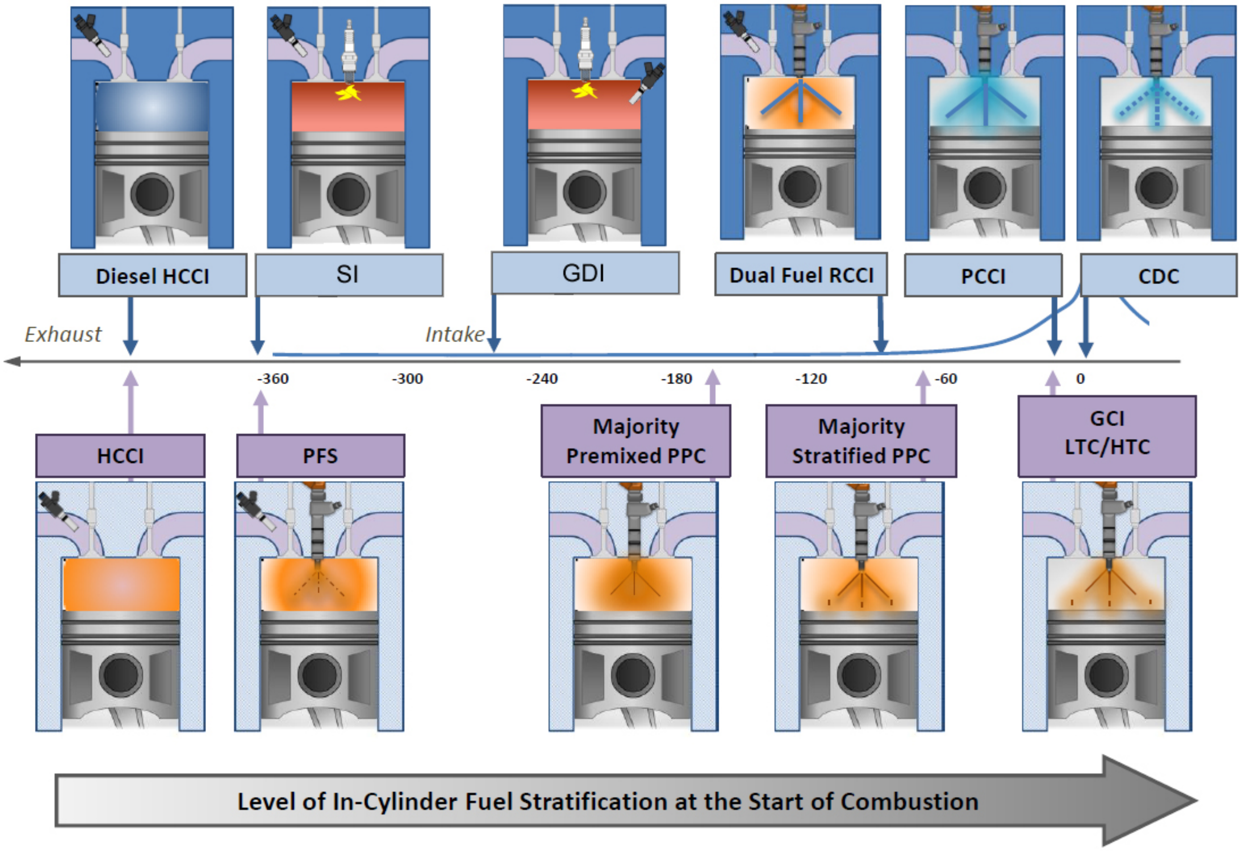

Figure 2.3: Comparison of various conventional and advanced combustion strategies with respect to fuel stratification. Adapted from [110].

Homogeneous charge compression ignition (HCCI) is an advanced low temperature combustion strategy utilizing the autoignition of a fully-premixed air-fuel charge. As a result of the fully-premixed homogenous air-fuel charge, nearly simultaneous heat release is achieved, resulting in short combustion durations. By realizing short combustion durations, an constant-volume approximation of the Otto cycle is approached, improving the thermal efficiency, coupled with reduced pollutant emissions. First demonstrated on a two-stroke SI engine, it was demonstrated that high levels of hot residual exhaust gas recirculation (EGR) provided the capability of autoigniting the fully-premixed air-fuel mixture without the use of spark ignition, and was initially termed ”Active Thermo-Atmosphere Combustion” [80]. Shortly after, HCCI underwent extensive research and development on a four-stroke engine [74], and in the 1990’s was successfully proved in a high-performance endurance racing application [50, 119]. More recent extensive fundamental research has demonstrated the high-load capability of HCCI [18, 19].

Partially premixed combustion (PPC) expands the HCCI operating range by both premixing and direct-injecting the fuel, providing in-cylinder fuel stratification. Using diesel fuel, the UNIBUS [43], PREDIC [106], and Modulated Kinetics [55] combustion strategies were developed [77]. However, using premixed diesel fuel severely limits the engine to low-load operation with acceptable performance. By switching from a high-reactivity fuel to a low-reactivity fuel, engine performance under PPC operation is improved [53]. Further PPC research and development by the engine community is highlighted by References [37, 71, 72]. By eliminating fully-premixed fuel injection and relying solely on the direct injection of the low-reactivity fuel, the gasoline compression ignition (GCI) combustion strategy is achieved, with promising results [87]. GCI has proven to be amenable to light duty high speed engines by reducing combustion noise with broad control over the fuel stratification prior to ignition [92–94].

Overall, advanced premixed compression ignition combustion strategies such as HCCI, PPC, and GCI provide pathways to high efficiency and clean combustion. However, in reality real world operating ranges are restricted due to limited control over the ignition timing and the rate of heat release [25]. By being limited to a single fuel, the combustion strategies can be tailored for either low-, mid- or high-load operation, but are inefficient at providing acceptable engine operation across the range of loads. Furthermore, high levels of premixed fuel combust in a rapid fashion under compression ignition, leading to high pressure rise rates and combustion noise, which adversely affects engine durability. Rapid combustion events can also lead to reduced thermal efficiencies due to increased heat transfer at the combustion chamber walls resulting from scrubbed boundary layers generated by strong ringing events. By simply moving to a dual-fuel stratified charge combustion strategy, concerns over the limited combustion control over the ignition timing and the rate of heat release can be assuaged [8, 49].

2.3.1 Dual-Fuel: Reactivity Controlled Compression Ignition

In order to address the limited control over ignition timing and rate of heat release for advanced single-fuel combustion strategies, the advanced dual-fuel reactivity controlled compression ignition (RCCI) combustion strategy was developed by Kokjohn and Reitz [62, 90][2]. Derived from the work of Inagaki [49] and Bessonette [8], RCCI utilizes two fuels with varying reactivity (e.g., gasoline and diesel) to control the in-cylinder fuel stratification, which allows for the optimization of combustion phasing, duration, and magnitude.

In standard practice, the low-reactivity fuel is fully premixed with the intake charge, and the high-reactivity fuel is direct-injected prior to ignition. However, the direct-injected fuel does not completely mix and remains stratified prior to the start of combustion. The combustion is initiated at the high-reactivity fuel-air mixture location(s), and the subsequent reaction progresses through the fuel reactivity range from high- to low-reactivity, thereby allowing a controllable sequential ignition event. As a result, by modifying the global fuel reactivity in combination with one or more direct injections, complete control over the combustion phasing and rate of heat release is accomplished [42, 56, 59, 60, 63, 101, 112]. This has allowed RCCI engine operation at combustion efficiencies in excess of 97% across a load range from 4 bar BMEP to 20 bar BMEP [102]. Additionally, gross indicated thermal efficiencies approaching 60% have been demonstrated experimentally [99]. RCCI engine operation has been expanded by the direct dual fuel stratification (DDFS) combustion strategy, which utilizes two direct injectors, each dedicated to either the low-reactivity fuel

---

[2] The reader is encouraged to study References [82, 90] for a thorough, up-to-date review of reactivity controlled compression ignition (RCCI) combustion.

or high-reactivity fuel, and centrally mounted in the combustion chamber so as to achieve clean and efficient RCCI combustion in a heavy-duty engine [117, 118].

By nature, RCCI is inherently a fuel-flexible advanced combustion strategy. RCCI combustion relies heavily on the fuel reactivity stratification gradient to generate clean and efficient combustion; as such, a broad range of fuels may be used. Due to their wide availability, gasoline and diesel have been used in much of the previous RCCI work as the low-reactivity and high-reactivity fuels, respectively [14, 16, 20, 42, 60, 100, 101, 111, 112]. In place of pump fuels, the primary reference fuels (PRF) of iso-octane and n-heptane have also been studied as the low-reactivity and high-reactivity fuels, respectively [26, 49, 56–58, 61]. Additionally, alcohol blends have been studied as low-reactivity fuels [15, 21, 23, 24, 26, 98, 100] and biodiesel has also been researched as a high-reactivity fuel for RCCI combustion [38, 41]. However, mobile engine applications may preclude the ability to carry large quantities of two separate fuels, and as a result, cetane improvers, such as di-tert-butyl peroxide (DTBP) and 2-ethylhexyl nitrate (EHN) have been studied as low-quantity additives to condition the low-reactivity fuel to perform as a high-reactivity fuel in order to approximate single-fuel RCCI operation [21, 38, 97, 98, 100]. It is also worth noting that early studies on dual-fuel engines operating on gaseous fuels demonstrated the characteristics of the RCCI combustion regime in some limiting cases [78, 107, 108].

2.4 Natural Gas as a Fuel in Internal Combustion Engines

While liquid fuels such as gasoline and diesel oil are commonly associated with the internal combustion engine in modern society, many of the early engine designs were aimed at utilizing gaseous fuels derived from coal deposits, known as coal gas, a mixture of methane, hydrogen, carbon monoxide, and a range of other gases. In fact, Diesel's original engine patent described the use of combustible gas as a fuel in his engine design [27].

2.4.1 Spark Ignition Systems

Historically, the spark ignition internal combustion engine has been the primary platform for the use of natural gas as a ”high octane” alternative fuel. Because natural gas is injected or inducted into the intake air stream, a reduction in volumetric efficiency can result, causing reduced power output from the engine. However, the high octane rating of natural gas allows for the use of higher compression ratios, resulting in an increase in cycle thermal efficiency. Compared to a liquid spray (e.g., gasoline), the gaseous jet generally provides a higher quality air-fuel mixture prior to ignition.

In the past spark ignition natural gas engines have predominantly been stationary engines for pumping purposes or power generation. More recently, gas storage technology has improved such that natural gas SI engines are readily available on the market for transportation purposes. For example, ”bi-fuel”[3] vehicles for the light-duty passenger vehicle market are available from a range of manufacturers, such as the Fiat Punto EVO 1.4L Natural Power and the Dodge Ram 2500 HD CNG (both of which offer a 1000 kilometer range on CNG). However, these bi-fuel platforms operate on a single fuel at a time (either gasoline or CNG), and do not offer the ability to use the two fuels simultaneously in a ”dual-fuel” mode.

Stoichiometric operation is commonly used in SI gas engines; however improvements in engine efficiency can be realized by operating under fuel lean conditions (equivalence ratio < 1.0). These efficiency gains come in two major forms: first, reduced use of intake throttling leads to lower pumping losses and, second, thermodynamic cycle efficiencies benefit from the resulting higher specific heat ratio [13]. Furthermore, under lean conditions, excess O2 in the exhaust makes the use of oxidation catalysts to remove CO and HC species from the exhaust stream effective in order to meet stringent CO and HC emissions limits.

---

[3] ”Bi-fuel” refers to the capacity to carry two fuels yet operate on either fuel independently in a single-fuel combustion mode; ”Dual-fuel” refers to the capacity to carry two fuels and utilize both of the fuels simultaneously in a dual-fuel combustion mode.

2.4.2 Compression Ignition Systems

Due to the fact that natural gas has a high tolerance to autoignition (i.e., low cetane number or high octane number), an ignition source is generally required to efficiently utilize natural gas in a compression ignition engine [66]. As a result, natural gas compression ignition engines are often operated in a "dual-fuel" mode by utilizing a relatively small amount ($<$ 30% of total fuel energy) of diesel fuel as a pilot ignition to ignite the premixed natural gas-air mixture. Using this strategy natural gas can be burned in a compression ignition engine system designed for conventional diesel combustion, often with the co-benefit of reducing NO_x and soot emissions. (It should be noted that HCCI operation is achievable using natural gas [47, 48, 52], however in application the HCCI engine is limited to low power density [46].)

Furthermore, by moving to the compression ignition engine, natural gas can be utilized in an even more efficient manner. CI engines do not use intake air throttling, and as a result the volumetric efficiency is improved (reduced pumping losses) over throttled SI engines. Increased burn rates are also achieved under CI operation, leading to more efficient constant-volume combustion. Overall, thermal efficiencies for natural gas CI engines are comparable to diesel CI operation, offering fuel-to-electricity efficiencies of approximately 49% [45]. Operating stability is maintained, with cycle-to-cycle variations that approximate CDC operation. Importantly, the power output across the engine operating map is maintained with ease under dual-fuel operation. As mentioned above, both NO_x and soot emissions are reduced under dual-fuel operation; however there is a tradeoff, as the premixed natural gas allows for fuel to reside in the combustion chamber crevices and remain unburned or partially oxidized, resulting in elevated HC and CO emissions.

Generally, natural gas usage in CI engines is utilized in the heavy-duty market. Market-available natural gas CI engines are offered by Volvo (FH12 Globetrotter), Wärtsilä (32GD - 50DF), Caterpillar (M 46 DF), and Cummins (QSK50 / ISL G), for example. The dual-fuel combustion strategies employed are most commonly called "diesel micro-pilot" (DMP) [69] or "high pressure direct injection" (HPDI) [35].

Recent work on the use of natural gas for RCCI engine operation has been undertaken on both a modeling and experimental basis. Numerical simulations used a genetic algorithm strategy coupled to multi-dimensional engine CFD to optimize RCCI engine operation across a broad range of speed/load conditions in a heavy-duty engine using natural gas [76]. It was shown that clean and efficient RCCI operation could be obtained over a range from 4 bar IMEP to 22 bar IMEP. Significant reductions of EGR requirements were achievable with natural gas/diesel RCCI operation compared to gasoline/diesel operation. Further computational work explored the use of natural gas/diesel RCCI operation and, when compared to a conventional diesel rated power point, was able to significantly reduce NO_x/soot emissions while meeting acceptable engine durability limits [120]. From an experimental standpoint, a heavy-duty diesel engine calibration map was optimized for natural gas/diesel RCCI operation [17]. The optimized calibration with approximately 50% natural gas substitution provided 15% NO_x reduction and 43% PM reduction averaged across the map. Furthermore, net indicated thermal efficiencies of 50% were realized. Further work estimated that approximately 80-85% percent of UHC in the exhaust stream under natural gas/diesel RCCI operation is methane, indicating the need for an oxidation catalyst to meet emissions limits. In addition, they showed that variations in the methane number (MN70 - MN100) had a small effect on operation [28]. Subsequent development has demonstrated natural gas/diesel RCCI operation over the full operating map of a heavy-duty engine, with and without EGR, where the use of EGR approximately halved NO_x emissions, significantly reducing the exhaust fluid requirements for exhaust aftertreatment [39, 40]. From this it is clear that natural gas, when coupled with advanced combustion strategies, is a promising fuel for internal combustion engines.

2.4.3 Natural Gas Composition

Natural gas composition is very important in determining the combustion characteristics under engine conditions, as discussed in References [75, 79].

Table 2.1 shows a typical composition and range of component species for natural gas:

Table 2.1: Representative chemical composition of natural gas [88]

Composition	Typical Analysis (mole %)	Range (mole %)
Methane	95.0	87.0 - 97.0
Ethane	3.2	1.5 - 7.0
Propane	1.2	0.1 - 1.5
i-Butane	0.2	0.01 - 0.3
n-Butane	0.03	0.01 - 0.3
i-Pentane	0.03	0.01 - 0.3
n-Pentane	0.01	trace - 0.04
Hexanes	0.01	trace - 0.04
Nitrogen	0.01	trace - 0.06
Carbon Dioxide	0.5	0.1 - 1.0
Oxygen	0.02	0.01 - 0.1
Hydrogen	trace	trace - 0.02

It was earlier mentioned that natural gas is characteristically resistant to autoignition in a CI engine. The relative octane number (ON) for natural gas is outside the high range of the octane rating scale (n-heptane is the reference for ON0 and iso-octane is the reference for ON100) and the relative cetane number (CN) is outside the low range of the cetane rating scale (α-methylnaphthalene is the reference for CN0 and cetane is reference for CN100). The industry has developed the methane number (MN) in order to classify natural gas fuels with high resistance to autoignition. Work by Malenshek and Olsen [70] has quantified the MN rating for a wide range of natural gas fuels from different sources, and showed that composition has a significant impact on the ignition behavior, as seen in Figure 2.4.

The ignition delay is an ideal universal baseline for comparing the ignition characteristics for a wide range of fuels. Figure 2.5 shows computational ignition delay calculations at

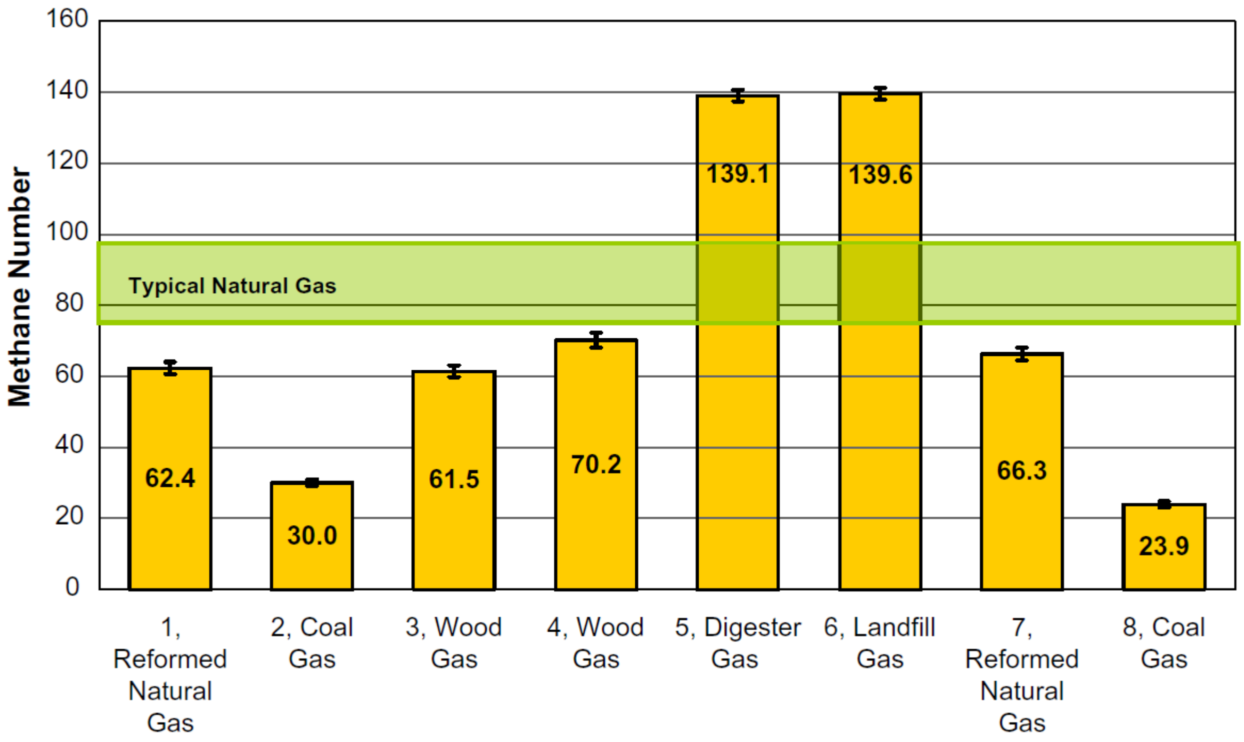

Figure 2.4: Methane number measurement for simulated fuels, from [70].

$\phi = 0.3$ and $P = 40$ bar using the reduced PRF mechanism of Ra and Reitz [86], which consists of 41 species and 130 reactions. PRF0, PRF100, and CH_4 fuels are shown, which are representative of high-cetane diesel fuel, high-octane gasoline, and pure methane, respectively. It is seen that at typical top dead center (TDC) temperatures (900 - 1,000 K) PRF100 can achieve an order of magnitude increase in ignition delay time over PRF0, and that CH_4 provides more than an order of magnitude increase in ignition delay time over PRF100.

Many stationary gas engines are fed from pipeline natural gas, which fluctuates due to source variations of the gas supplied to the pipeline, which may come from a range of feedstocks such as biogas, well head gas, synthesis gas, LNG, frack gas, to list a few. Gas engines are designed around a specified range of MN in order to guarantee acceptable engine operation. Too low a quality of gas may lead to reduced power output (due to low energy content of the gas) or engine failure due to knocking (due to higher hydrocarbons

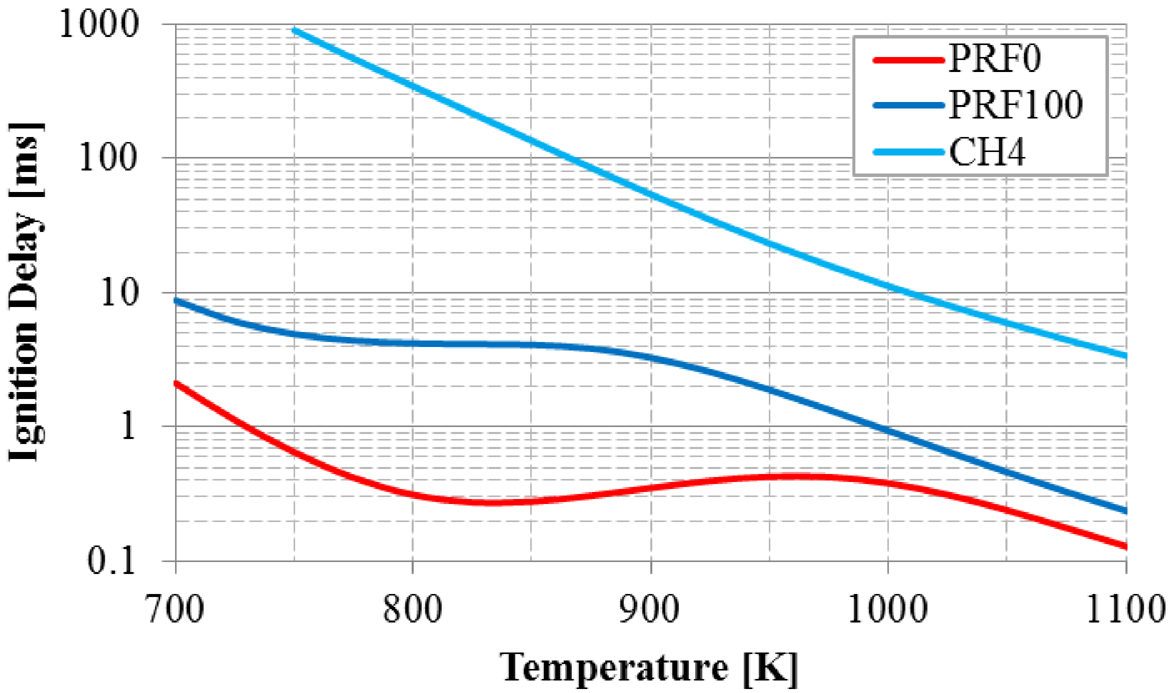

Figure 2.5: Ignition delay as a function of temperature for PRF0, PRF100, and CH_4, at ϕ = 0.3 and P = 40 bar.

with increased knock propensity). As a result, in order to ensure safe and reliable engine operation, it has been proposed that the methane number be 80 or above (> 65 for Japan), with limited gas impurities and low-frequency gas supply fluctuations [79].

3 EXPERIMENTAL SETUP

This chapter[4] presents the technical background and experimental procedures applied in the Caterpillar SCOTE Engine Laboratory at the University of Wisconsin-Madison.

3.1 Experimental Engine Laboratory

All experiments (with the exception of data for some of the CFD simulations presented in Chapter 4) were performed on a Caterpillar 3401E Single Cylinder Oil Test Engine (SCOTE), which is a single-cylinder variant of the Caterpillar 3406E six-cylinder diesel engine. The SCOTE is rated for 62 kW at 1800 RPM, and the engine specifications are given in Table 8.1. The stock cooling system and water pump were used, but the oil was driven by an external electric oil pump and all of the original fuel systems have been replaced, as described in Section 3.2. A diagram of the experimental setup is provided in Figure 3.1. Air was supplied to the engine by an external compressor, and was heated with two immersion style heaters. Pressure-controlled intake and exhaust surge tanks were used to simulate a turbocharger and to provide steady-state measurement points for temperature, pressure, and emissions.

Table 3.1: 3401 Caterpillar SCOTE heavy-duty engine specifications.

Displacement	2.44 L
Bore x Stroke	137.2 mm x 165.1 mm
Connecting Rod Length	261.6 mm
Number of Valves	4
Intake Valve Opening/Closing	335/-143° aTDC
Exhaust Valve Opening/Closing	130/-355° aTDC
Swirl Ratio	0.7
Piston Type	Articulated
Piston Profile	Re-entrant / Bathtub
Compression Ratio	16.1:1 / 14.9:1

---

[4] The technical and procedural material presented on the Caterpillar SCOTE Engine Laboratory at the University of Wisconsin-Madison is adapted from the work of Wissink [117].

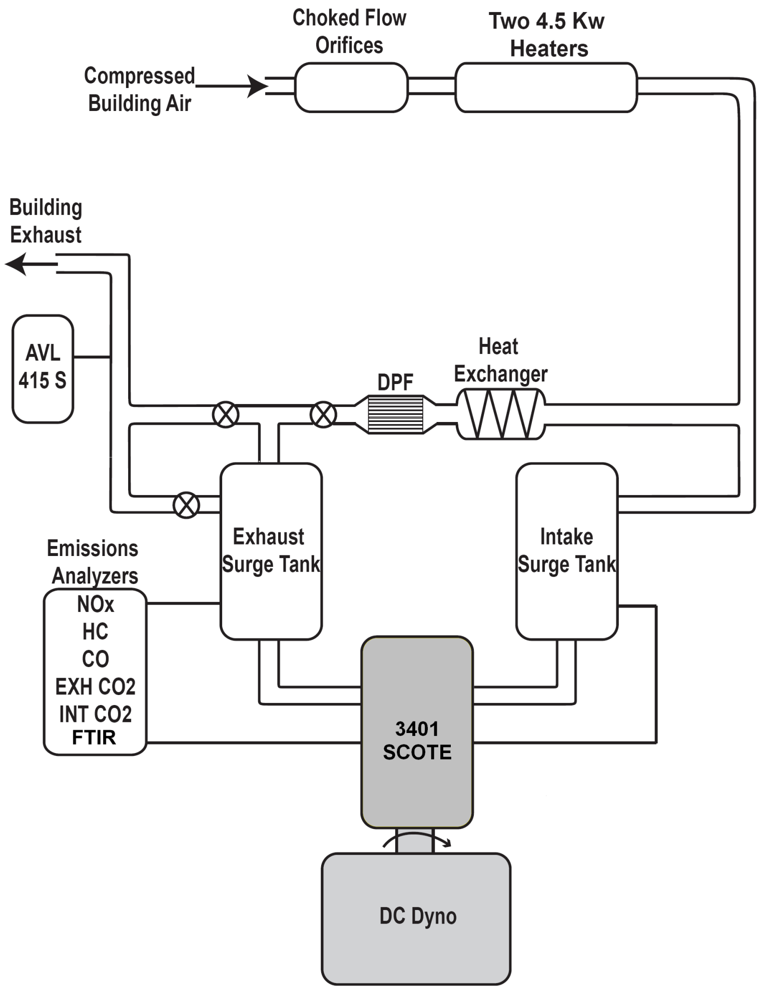

Figure 3.1: Diagram of the SCOTE Laboratory.

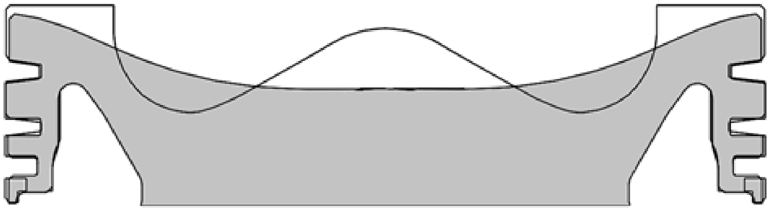

Figure 3.2: Profiles of stock CDC piston (white outlined, CR = 16.1) and modified RCCI piston (gray, CR = 14.9).

3.2 Fuel System

In order to perform dual-fuel engine experiments on both liquid and gaseous fuels, a multi-fuel injection system was developed for the laboratory. Three unique systems are included: a common-rail injection system, shown as Cart 1 in Figure 3.4, for the high-reactivity direct-injected fuels (F76, DF2, or n-heptane); a liquid port fuel injection system, shown as Cart 2 in Figure 3.4, for the low-reactivity liquid fuels (gasoline or iso-octane); and a gaseous port fuel injection system, shown in Figure 3.6 for the low-reactivity gaseous fuel (methane). Each of the liquid fuel carts are outlined in Figure 3.3, and the components are provided in Table 3.4. The details of the common rail injector, liquid port injector, and gaseous port injector are provided in Table 5.2. The intake runner, which has been modified to accomodate both liquid and gaseous port fuel injectors, is displayed in Figure 3.5.

Table 3.2: Common rail injector specifications.

Body Style	Bosch CRI2 Series
Body Part #	0986435088
Stock Nozzle Part #	DLLA148P1347
Number of Holes	7
Included Angle	148°
Hole Diameter	0.141 mm
Geometric Area	0.1093 mm^2
Nominal Hydraulic Flow	440 cm^3 per 30 s @ 10 MPa

Table 3.3: Specifications for the liquid and gaseous port fuel injectors.

	Liquid Injector	**Gaseous Injector**
Manufacturer	RC Engineering	AFS Fuel Systems
Part #	PL4-750	GS Type E
Inlet Style	Bosch	Cartridge
Current Profile (Peak/Hold)	4A / 2A	8A / 2A

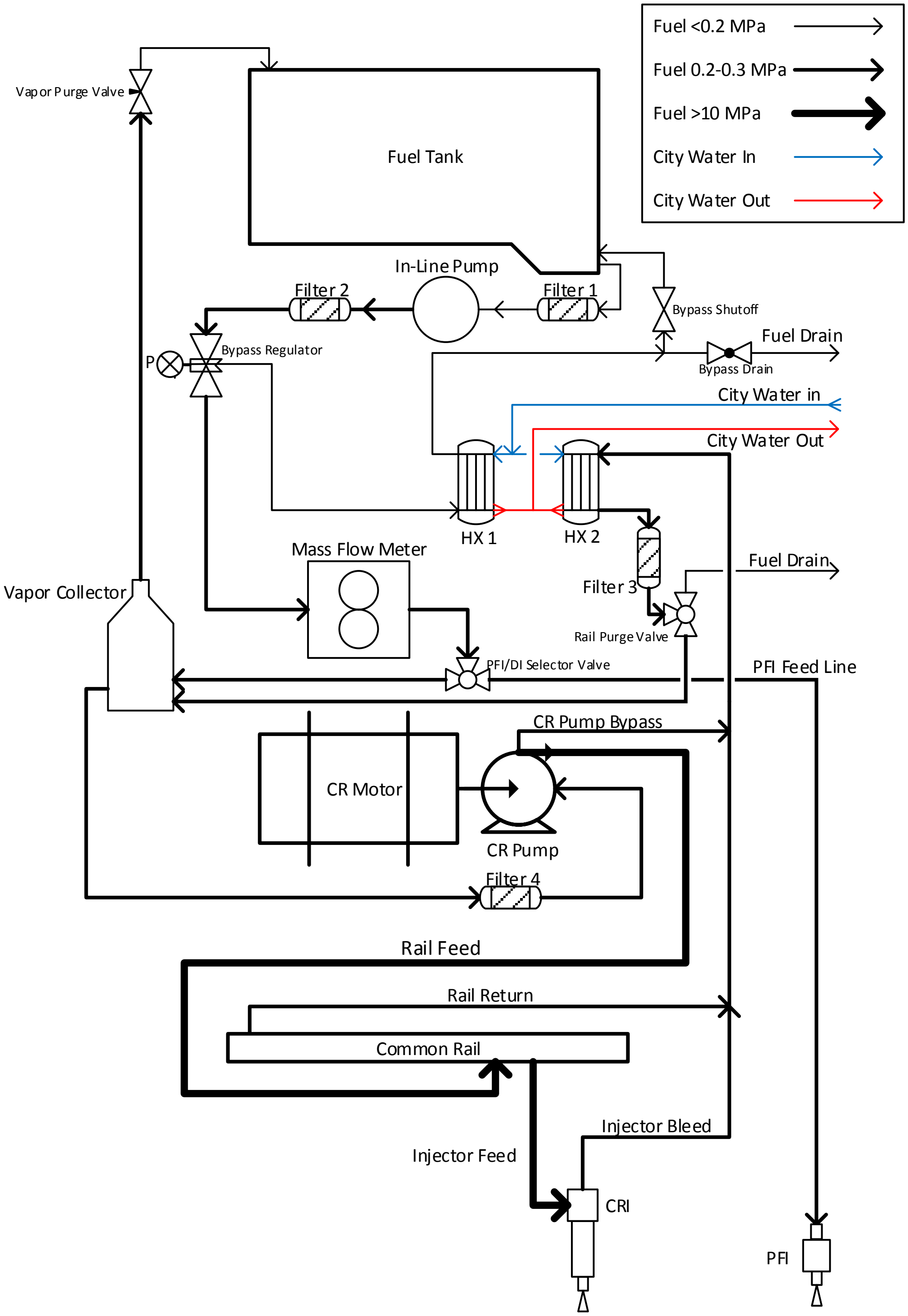

Figure 3.3: Liquid fuel cart system diagram.

Figure 3.4: Picture of the two liquid fuel carts, with the common rail Cart 1 on the left and the port fuel Cart 2 on the right.

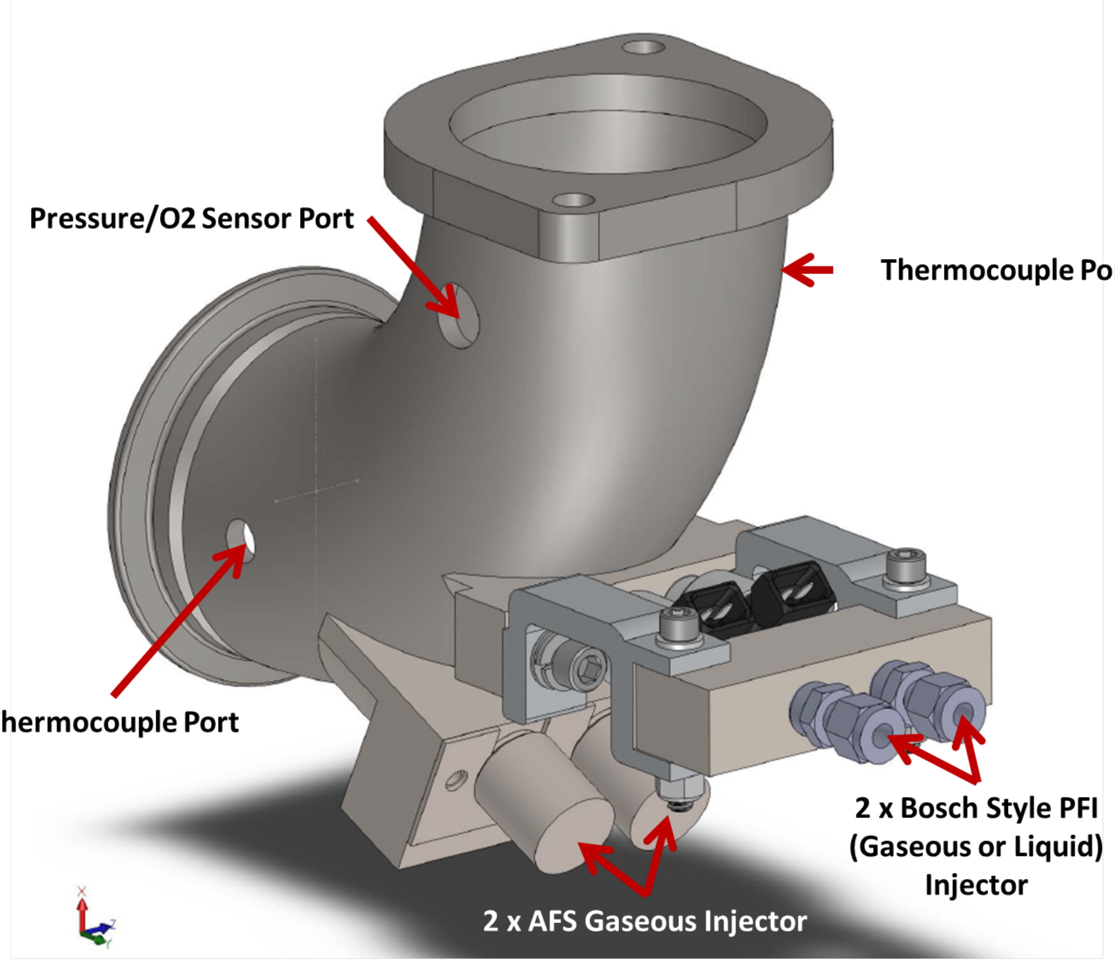

Figure 3.5: Diagram of the intake runner with the liquid and gaseous port fuel injection modifications.

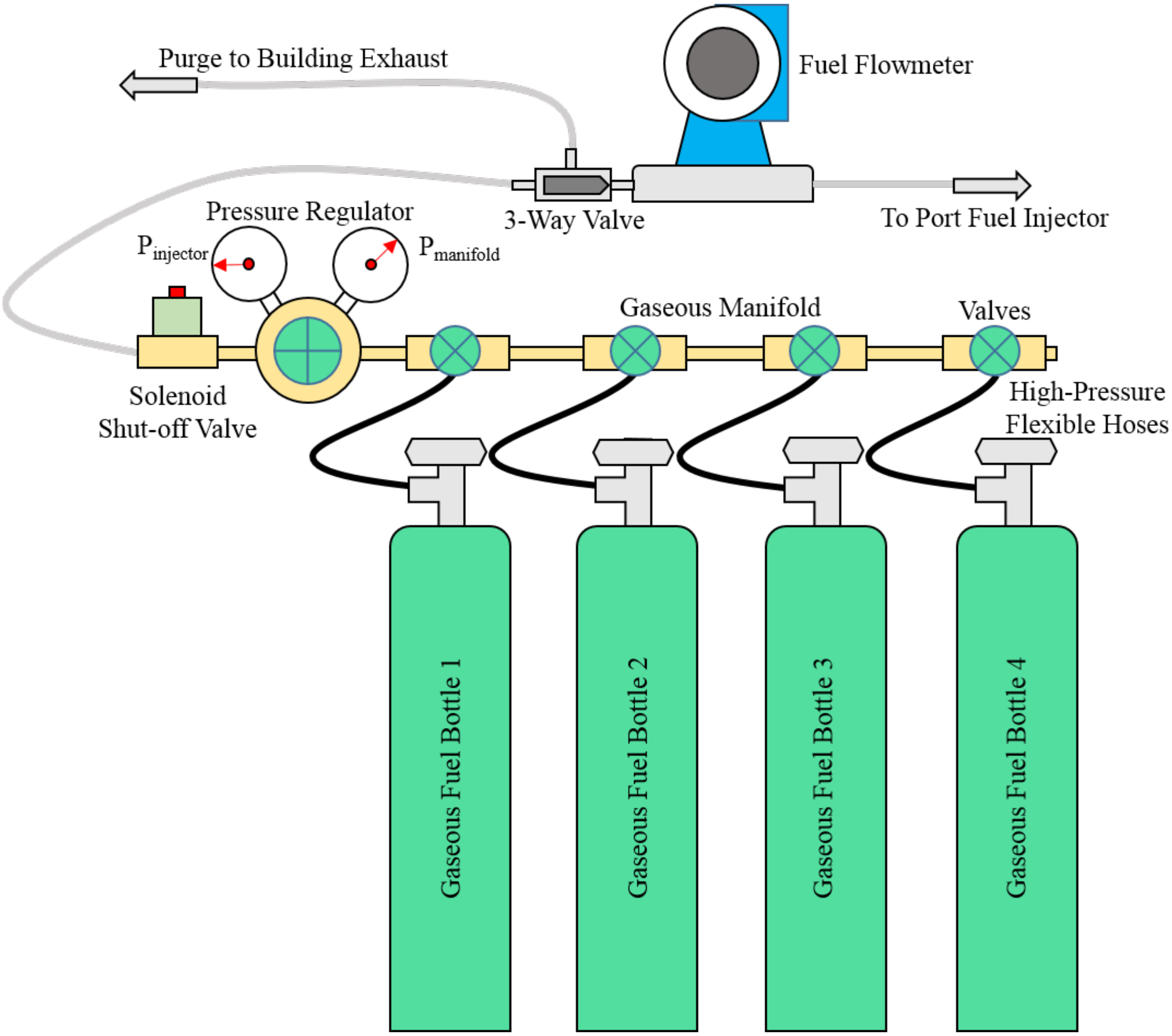

Figure 3.6: Diagram of the gaseous port fuel injection system.

Table 3.4: Liquid fuel cart system hardware.

Fuel System Name	Cart 1	Cart 2
Common Rail Pump	Bosch 0 445 020 030 CR/CP3S3/R110/30-789S	Bosch 0 986 437 332 CR/CP3HS3/R110/30-789S
Pump Motor	Emerson AD77 5 hp AC motor	Dayton 6VPE8 3 hp AC motor
Motor Controller	Baldor AC VFD 1D11205-EB	AC Tech SF230
Flexible High Pressure Fuel Line (Pump to Rail)	Parker Polyflex 4005ST 432307-001, 0.177"	Spir Star 5/4 M14x1.5
Common Rail	Bosch 0 445 214 038	Bosch 03L 130 089
Lift Pump	Summit Racing SUM-G3137	Holley 12-890
Heat Exchanger 1	Brazetek BT3x8-10	Brazetek BT3x8-10
Heat Exchanger 2	Brazetek BT3x8-10	Brazetek BT3x8-10
Filter 1	Aeromotive 12304 Canister & 12604 Element (100 μm)	Aeromotive 12304 Canister & 12604 Element (100 μm)
Filter 2	Aeromotive 12335 Canister & 12635 Element (40 μm)	Aeromotive 12335 Canister & 12635 Element (40 μm)
Filter 3	Aeromotive 12335 Canister & 12635 Element (40 μm)	Aeromotive 12335 Canister & 12635 Element (40 μm)
Filter 4	K&N 81-1000 Canister & Performance Fuel Systems PF-9010 Element (10 μm)	K&N 81-1000 Canister & Performance Fuel Systems PF-9010 Element (10 μm)
Fuel Flow Meter	Endress+Hauser Promass 80A	Endress+Hauser Promass 80A

3.3 Instrumentation and Control

The engine laboratory was fitted with a variety of pressure, temperature, flow rate, and emissions instruments. The acquisition and control of the various instruments and devices was separated into three categories: low-speed (~1 Hz), high-speed (~100 kHz), and real-time (~40 MHz). The low-speed category was for sensors, which were not time-critical, such as surge tank pressure transducers, thermocouples, mass flow rates, and emissions. These are listed in Tables 3.5 and 3.7. The high-speed category was for crank-angle-resolved measurements, such as in-cylinder pressure and the injector current profiles. The high-speed instruments are listed in Table 3.6. The real-time category was for control of critical sub-crank-angle-resolved devices, such as the fuel injectors and rail pressure controllers.

Table 3.5: Low-speed instruments.

Measurement	**Model**	**Range**
Upstream orifice pressure	Omega PX209-100A5V	0 to 100 psia
Intake tank pressure	Omega PX319-050AI	0 to 50 psia
Exhaust tank pressure	Omega PX215-200AI	0 to 200 psia
Thermocouples	Omega type-K	-200 to 1250C
Fuel flow rate	Endress+Hauser Promass 80A DN01	0 to 20 kg/h

Table 3.6: High-speed instruments.

Measurement	**Model**	**Range / Resolution**
In-cylinder pressure	Kistler 6125C21U20	0 to 30 MPa
Charge amplifier	Kistler 5010	±10 to 999000 pC
Injector current probes	Tektronix A622	0 to 100 A
Optical encoder	BEI xH25D-SS-3600-ABZC-28V/V-SM18	3600 pulses/rev

The emissions instruments are listed in Table 3.7. Gaseous emissions were measured with a 5-gas Horiba tailpipe “bag” bench converted to perform constant sampling, or were measured with a ThermoFischer FTIR Spectroscopy bench. HC emissions were measured on a wet basis by using a heated sampling system. All other gaseous emissions were measured on a dry basis by flowing through a condenser before entering the instruments,

Table 3.7: Emissions instruments.

Species / Instrument	Manufacturer	Model	Measurement Method
Exhaust NO/NO_2	Horiba	CLA-220	heated chemiluminescence detector
Exhaust CO	Horiba	AIA-220	non-dispersive infrared light absorption
Exhaust HC	Horiba	FIA-236	heated flame ionization detector
Exhaust CO_2	Horiba	AIA-220	non-dispersive infrared light absorption
Intake CO_2	Horiba	AIA-220	non-dispersive infrared light absorption
Particulate Matter	AVL	415s Smoke Meter	filter paper reflectivity
Wideband λ Sensor	Bosch	LSU 4.9	Nernst concentration cell
Wideband λ Module	ETAS	LA4	Calibration curve to convert signal from LSU sensor
FTI-R	ThermoNicolet	Nexus 670	absorbtion spectroscopy

except for the FTIR measurements, which were measured on a wet basis. PM measurements of filter smoke number (FSN) and mass density (mg/m^3) were performed with an AVL 415S smoke meter. For each steady-state operating condition, 5 samples of 2 L volume were taken with paper saving mode off. The mass density reported by the smoke meter, which is based on the AVL correlation for CDC, was used to calculate PM in g/kW-hr. Investigations of the PM generated by RCCI have shown that unlike CDC, it often has a very high fraction of organic carbon (>95%) and a significantly different size distribution, which is bimodal under certain conditions [20, 64]. Thus, we do not expect that the mass density reported by the smoke meter will be accurate when using RCCI or similar combustion strategies, and the results presented from this instrument are for reference only. However, RCCI is know to produce very low smoke levels.

With the ability to measure mass flow rates and the carbon emissions, there were two methods of calculating AFR. A third method was to use a wideband λ sensor, which measures oxygen concentration with a Nernst cell. Unfortunately, the accuracy of wideband λ sensors is significantly diminished with high HC levels and lean operation [12, 89], which are both characteristic of LTC strategies. Therefore, the sensor listed was used only as a diagnostic tool, and while the readings were recorded, they were excluded from the analysis.

Table 3.8: Low-speed data acquisition hardware

Part #	Description	Function
NI SCXI-1000	4-slot AC powered SCXI Chassis	Houses SCXI modules
NI SCXI-1300	General purpose voltage module	Receives all low-speed voltage inputs
NI SCXI-1303	Thermocouple module	Receives all thermocouple inputs

Table 3.9: High-speed data acquisition hardware

Part #	Description	Function
NI PCI-6143	Simultaneous Sampling Multifunction DAQ	Samples high-speed digital and analog inputs
NI SHC68-68-EPM	68-pin X Series and M Series Cable	Connects PCI-6143 to BNC-2090A
NI BNC-2090A	Shielded Rack-Mount BNC Connector Block	Receives high-speed analog inputs and digital timing from encoder

Table 3.10: Real-time control hardware

Part #	Description	Function
NI cRIO-9074	Integrated 400 MHz Real-Time Controller and 2M Gate FPGA	Houses all cRIO I/O modules and contains FPGA used for real-time control
NI 9411	Differential Digital Input	Receives digital timing from encoder
NI 9215	Simultaneous Analog Input	Receives analog input from common rail pressure transducers
NI 9758	Port Fuel Injector Driver	Drives current to PFI, inlet metering valves on common rail pumps, and high-pressure valves on common rails
NI 9751	Direct Injector Driver Module	Drives current to CRI
NI 9754	ESTTL Spark Driver Module	Drives IGBT Smart Coil

Data acquisition and real-time control were performed on a PC with the National Instruments LabVIEW 2011 environment. The software, originally developed by Sung [105] and heavily modified and extended for the present work, consists of three independent virtual instruments (VIs), one for each of the speed categories. The National Instruments acquisition and control hardware mirrored this separation of tasks. The low-speed VI acquired data via USB interface to an SCXI platform, as described in Table 3.8. This VI was responsible for calculating and displaying trends of temperature, pressure, fuel and air flow rate, emissions indices, equivalence ratios, EGR, etc. Low-speed data was acquired at 2 Hz, and 2 minutes of raw and calculated data were written to disk when a point was saved. The high-speed VI acquired data via PCI interface to a multifunction DAQ, as described in Table 3.9. This system acquired analog signals from the in-cylinder pressure transducer amplifier and the injector current probes, with timing provided by the optical encoder mounted on the crankshaft resulting in a resolution of 0.1 CAD. The high-speed VI calculated and displayed various pressure-derived metrics such as HRR, PPRR, and CA50, and was configured to save 250 cycles of raw and calculated data to disk. The real-time control VI was based on engine control software and hardware developed by Drivven, which since been merged with NI Powertrain Controls. The VI communicated via ethernet with the cRIO real-time control system described in Table 3.10. While the module sent and received updates from the PC, it contained an FPGA operating at 40 MHz that independently controlled fuel injection as well as the inlet metering valves on the common rail pumps and the high-pressure valves on the common rails.

There were other systems not directly controlled by the PC. Engine speed and load were maintained by a Westinghouse 68 kW DC dynamometer, which was operated via a DyneSystems Dyn-Loc IV digital dynamometer controller. Air flow rate was metered by controlling the upstream pressure on a bank of choked-flow orifices, which allowed for a wide range of flow rates to be measured with high accuracy. The flow rate measurement was derived from the upstream orifice pressure, which was recorded on the low-speed system, but control of that pressure was performed via a standalone proportional-integral-derivative (PID) controller mounted in a control cabinet. This control cabinet contained several other independent PID controllers responsible for maintaining exhaust pressure and the oil, coolant, intake, and EGR temperatures. The control cabinet also contained various diagnostic indicators as well as emergency stop circuits integrated with the dynamometer controller and fuel systems.

3.4 Operation

The engine was operated with a range of high-reactivity fuels (F76, DF2, n-heptane) and low-reactivity fuels (gasoline, iso-octane, methane). Because some of the fuels have very low lubricity and was being pressurized and injected with a common rail system designed for diesel and dependent on the fuel for lubrication, the fuels were doped at 100 ppm by volume with lubricity improver Infineum R655. Shell Rotella T15W-40 Oil with Advance Soot Control and CAT EC-1 Extended Life Coolant were used for lubrication and cooling.

In the interest of safety, a conservative peak cylinder pressure of 15 MPa and PPRR of 1.5 MPa per crank angle degree (CAD) were imposed as upper limits for the duration of the experiments. The location of TDC was fixed at the beginning of each experiment by setting peak motored cylinder pressure to 0.4 CAD before top dead center (BTDC). This loss angle was based on hardware determinations performed by Caterpillar for this engine platform, and agrees well with hot and cold motored traces taken on this particular engine setup. Data was acquired at approximately steady-state conditions, as determined by monitoring the pressure and temperature of the surge tanks as well as the power output and emissions levels over a span of several minutes. Where possible, data collection was randomized to reduce the impact of any progressively increasing errors on the observed trends.

3.5 Data Analysis

All data analysis, post-processing, and visualization were performed with a set of purpose-built MATLAB scripts. The data analysis was segmented in a similar fashion to the acquisition, with high-speed data (in-cylinder pressure) handled on a per-cycle basis, and the low-speed data handled in terms of a steady state condition.

3.5.1 Uncertainty Propagation

The raw voltages and LabVIEW-calculated values were read in from low- and high-speed tab-delimited text files. Each of the raw voltage variables in the low-speed file was a 1-dimensional vector (ν_i), which was passed through a calibration curve for the instrument of interest to find the measurement value (x_i), as shown in Figure 3.7. These values were then fit to a normal distribution to find the mean ($\bar{x}$), standard deviation (σ_x or $\sqrt{s_x}$), and the "precision" 95% confidence interval ($\epsilon_{x,p}$). The value for $\bar{x}$ was then fed back to the calibration curve to find the corresponding "accuracy" 95% confidence interval ($\epsilon_{x,a}$), which was added in quadrature with $\epsilon_{x,p}$ to find the total error, as:

$$\epsilon_x = \sqrt{\epsilon_{x,p}^2 + \epsilon_{x,a}^2} \tag{3.1}$$

This process resulted in scalar values of $\bar{x}$ and ϵ_x for each variable. For calculations based on these these values, $f = f(x, y, z, \ldots)$, the uncertainty represented by ϵ_x was propagated by substituting ϵ_x for s_x in the variance formula [67], as:

$$\epsilon_f = \sqrt{\left(\frac{\partial f}{\partial x}\right)^2 \epsilon_x^2 + \left(\frac{\partial f}{\partial y}\right)^2 \epsilon_y^2 + \left(\frac{\partial f}{\partial z}\right)^2 \epsilon_z^2 + \cdots} \tag{3.2}$$

The partial derivatives needed for uncertainty propagation were calculated using the MATLAB Symbolic Math Toolbox™. Each equation was entered symbolically, partial derivatives were calculated for each independent variable at the variable value, the symbolic

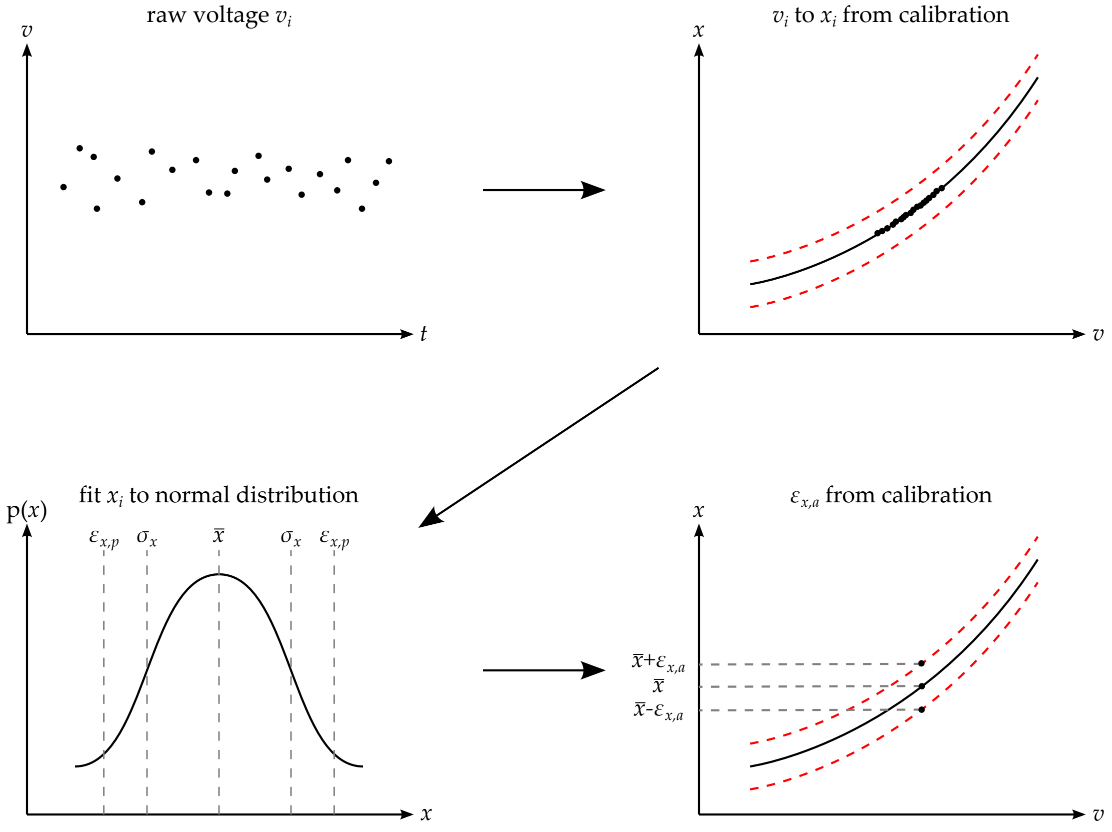

Figure 3.7: Process for converting raw voltage to measurement value with confidence intervals.

equation was evaluated, and the uncertainty propagation was performed. This process was carried out for each successive calculation, such that all calculated parameters had an associated 95% confidence interval.

Raw data from the high-speed files was loaded in a similar fashion, with measurement values being determined via calibration curves. However, the high-speed data consisted of 2-dimensional arrays of size $N_{\text{cycles}} \times N_{\text{elements}}$ representing cyclic variables ranging from -720 to +720ATDC. For the present study, all data were acquired for $N_{\text{cycles}} = 250$, with $N_{\text{elements}} = 2\frac{\text{pulses}}{\text{rev}} = 7200$. Instead of first calculating an ensemble average and then calculating combustion parameters based thereon, each cycle was processed independently such that a distribution was created for each of the scalar values associated with each cycle (e.g., PPRR, CA50). Each of the resulting distributions could then be fit to a normal or other distribution to generate statistical information regarding cyclic stability.

3.5.2 Steady-State Calculations

The low-speed data were used to perform the steady-state calculations, i.e., the variables which were represented only by a scalar value with an associated error term.

3.5.2.1 Fuel Mixture Properties

For performing emissions analysis, it is convenient to express the fuel composition on a per-moles-carbon (C1) basis. Ignoring impurities in the fuel other than water, the desired form of the fuel composition is:

$$\mathrm{CH}_y\mathrm{O}_z + n_{\mathrm{H_2O},fuel}\mathrm{H_2O} \tag{3.3}$$

Here y and z are the molar H/C and O/C ratios, respectively, and $n_{\mathrm{H_2O},fuel}$ is the molar water to carbon ratio in the fuel. For multiple fuels being measured on a mass basis, these combined fuel properties can be calculated by converting to molar flow rates.

3.5.2.2 Emissions

EGR was calculated based on the ratio of CO_2 concentration in the intake and exhaust surge tanks, with ambient CO_2 taken to be $[CO_2]_{amb}$ = 400 ppm.

$$\mathrm{EGR} = \frac{[\mathrm{CO_2}]_{in} - [\mathrm{CO_2}]_{amb}}{[\mathrm{CO_2}]_{exh} - [\mathrm{CO_2}]_{amb}} \tag{3.4}$$

For an oxygenated fuel $\mathrm{CH}_y\mathrm{O}_z$, a stoichiometric balance yields the following air-to-fuel ratio (AFR):

$$\alpha = \frac{2 + \frac{y}{2} - z}{2} \tag{3.5}$$

$$AFR_{stoich} = 4.76\alpha\frac{MW_{air}}{MW_{fuel}} \tag{3.6}$$

By performing a carbon balance with the emissions measurements, the number of moles of air per mole mole of fuel can be found on a C1 basis, expressed here as $n_{air,carbon}$. This allows for calculation of AFR and Φ based on carbon balance in addition to direct fuel and air mass flow measurements:

$$AFR_C = 4.76n_{air,carbon}\frac{MW_{air}}{MW_{fuel}} \tag{3.7}$$

$$AFR_m = \frac{\dot{m}_{air}}{\dot{m}_{fuel}} \tag{3.8}$$

$$\Phi_i = \frac{AFR_{stoich}}{AFR_i} \tag{3.9}$$

Similarly to $n_{air,carbon}$, each of the exhaust species can be expressed in terms of moles per mole of C1 fuel, as n_{HC}, n_{CO}, etc. These allow for the calculation of the emissions index (EI) in g/kg-fuel and the indicated specific emissions (IS) in g/kW-hr.

$$EI_i = 1000 \cdot n_i\frac{MW_i}{MW_{fuel}} \tag{3.10}$$

$$EI_{PM} = \left(\frac{AFR + 1}{1000}\right) \cdot \left(\frac{\rho_{PM}}{\rho_{exh}}\right) \tag{3.11}$$

$$IS_i = \frac{EI_i \cdot ISFC_g}{1000} \tag{3.12}$$

3.5.2.3 Intake Air and Trapped Mass

The mass flow rates of air and fuel were measured directly, and can be used to determine total trapped mass. When EGR is used, it increases the total intake flow rate and also dilutes the charge, as represented by the charge-mass equivalence ratio Φ':

$$\dot{m}_{int} = \frac{\dot{m}_{air}}{1 - EGR} \tag{3.13}$$

$$\Phi' = \Phi(1 - EGR) \tag{3.14}$$

The mass of fuel and air per thermodynamic cycle were calculated in identical fashion as:

$$m_{fuel} \left[\frac{\text{g}}{\text{cycle}}\right] = \dot{m}_{fuel} \left[\frac{\text{g}}{\text{s}}\right] \times \frac{60 \left[\frac{\text{s}}{\text{min}}\right]}{RPM} \times 2 \left[\frac{\text{rev}}{\text{cycle}}\right] \tag{3.15}$$

The residual mass fraction ω_{res} was calculated with the Yun & Mirsky correlation, in which V_{EVC} and V_{EVO} are the cylinder volume at EVC and EVO, P_{EVC} and P_{EVO} are the cylinder pressure at EVC and EVO, and k_{exh} was the polytropic coefficient during expansion.

$$\omega_{res} = \left(\frac{V_{EVC}}{V_{EVO}}\right)\left(\frac{P_{EVC}}{V_{EVO}}\right)^{\frac{1}{k_{exh}}} \tag{3.16}$$

This allowed for estimation of the residual mass, and therefore the total trapped mass:

$$m_{res} = \frac{\omega_{res}}{1 - \omega_{res}}(m_{air} + m_{EGR} + m_{fuel}) \tag{3.17}$$

$$m_{trap} = m_{air} + m_{EGR} + m_{fuel} + m_{res} \tag{3.18}$$

3.5.2.4 Efficiency Metrics

The thermal efficiency calculations were based on the indicated work calculated from the in-cylinder pressure data, which will be discussed in Section 3.5.3.3. Gross and net thermal efficiency were determined by the ratio of indicated work to the total energy input from the fuel, E_{fuel}, and the pumping loss fraction η_{pump} was the difference between these two quantities. Exhaust losses result from combustion products leaving the system at elevated temperature, and are expressed by η_{exh} as the ratio of the difference between intake and exhaust enthalpy to E_{fuel}. The combustion loss due to unburned species (HC and CO) in the exhaust is equal to the ratio of their heating value to E_{fuel}, or 1 - η_{comb}. The total heat loss was determined by energy conservation, and therefore encompasses losses such as heat transfer from the coolant, oil, and EGR coolers, as well as radiative and convective losses from the engine.

$$E_{fuel} = m_{fuel} LHV_{fuel} \tag{3.19}$$

$$\eta_{net} = \frac{W_{net}}{E_{fuel}} \tag{3.20}$$

$$\eta_{gross} = \frac{W_{gross}}{E_{fuel}} \tag{3.21}$$

$$\eta_{pump} = \eta_{gross} - \eta_{net} \tag{3.22}$$

$$\eta_{exh} = \frac{m_{exh} h_{exh} - m_{int} h_{int}}{E_{fuel}} \tag{3.23}$$

$$\eta_{comb} = 1 - \frac{m_{exh} \sum \omega_i LHV_i}{E_{fuel}} \tag{3.24}$$

$$\eta_{HT} = 1 - [\eta_{net} + \eta_{pump} + \eta_{exh} + (1 - \eta_{comb})] \tag{3.25}$$

The indicated specific fuel consumption (ISFC) was based on indicated power, as:

$$\mathrm{ISFC}_{net}\left[\frac{\mathrm{g}}{\mathrm{kW-hr}}\right]=\frac{\dot{m}_{fuel}\left[\frac{\mathrm{g}}{\mathrm{s}}\right]\times 3600\left[\frac{\mathrm{s}}{\mathrm{hr}}\right]}{P_{net}\ [\mathrm{kW}]} \tag{3.26}$$

$$\mathrm{ISFC}_{gross}\left[\frac{\mathrm{g}}{\mathrm{kW-hr}}\right]=\frac{\dot{m}_{fuel}\left[\frac{\mathrm{g}}{\mathrm{s}}\right]\times 3600\left[\frac{\mathrm{s}}{\mathrm{hr}}\right]}{P_{gross}\ [\mathrm{kW}]} \tag{3.27}$$

The required combined isentropic turbocharger efficiency η_{turbo} was determined by using an air-standard turbocharger model, in which the mass added by fuel was treated as air in the exhaust stream. The fluid in both the compressor and turbine was assumed to be air, and the ratio of specific heats γ was calculated at the intake and exhaust surge tank temperatures. $\mathrm{P_{comp,in}}$ and $\mathrm{T_{comp,in}}$ were assumed to be the ambient air pressure and temperature, $\mathrm{P_{comp,out}}$ was the intake surge tank pressure P_{in}, $\mathrm{P_{turb,in}}$ and $\mathrm{T_{turb,in}}$ were the exhaust surge tank pressure P_{exh} and temperature T_{exh}, and $\mathrm{P_{turb,out}}$ was the ambient air pressure. As implemented, this model neglects the pressure losses due to filters, piping, and aftertreatment devices, and therefore represents the lowest possible estimate of required turbocharger efficiency.

$$\eta_{turbo}=\frac{\left(\frac{\gamma_{comp}}{\gamma_{comp}-1}\right)}{\left(\frac{\gamma_{turb}}{\gamma_{turb}-1}\right)}\left(\frac{T_{comp,in}}{T_{turb,in}}\right)\frac{\left[\left(\frac{P_{comp,out}}{P_{comp,in}}\right)^{\left(\frac{\gamma_{comp}-1}{\gamma_{comp}}\right)}-1\right]}{\left(1+\frac{1}{AFR}\right)\left[1-\left(\frac{P_{turb,out}}{P_{turb,in}}\right)^{\left(\frac{\gamma_{turb}-1}{\gamma_{turb}}\right)}\right]} \tag{3.28}$$

The volumetric efficiency indicates pumping losses in the intake by the ratio of the actual mass inducted to the mass that would be theoretically held at the displacement volume $\mathrm{V_d}$ at the density of the intake tank ρ_{int}:

$$\eta_{vol}=\frac{m_{int}}{\rho_{int}V_d} \tag{3.29}$$

3.5.3 Individual Cycle Calculations

The array of in-cylinder pressure data P_{array} was pegged to crank angle θ by the crank shaft encoder. With the exception of the volume and area calculations, each of the following procedures was performed using individual cycles P (column vectors) of P_{array}.

3.5.3.1 Volume and Area

With the given dimensions of bore B, stroke L, connecting rod length ℓ, and compression ratio r_c, along with the encoder-measured value of θ, the volume V and surface area A of the combustion chamber were calculated as function of θ with the following relations:

$$a = L/2 \tag{3.30}$$

$$R = \ell/a \tag{3.31}$$

$$A_c = \frac{\pi B^2}{4} \tag{3.32}$$

$$V_d = A_c L \tag{3.33}$$

$$V_{TDC} = \frac{V_d}{r_c - 1} \tag{3.34}$$

$$V(\theta) = V_{TDC}\left[1 + \frac{1}{2}(r_c - 1)\left(R + 1 - \cos\theta - \sqrt{R^2 - \sin^2\theta}\right)\right] \tag{3.35}$$

$$\frac{dV(\theta)}{d\theta} = \left(\frac{\pi}{180}\right)\left(\frac{V_{TDC}}{2}\right)(r_c - 1)\sin\theta\left[1 + \frac{\cos\theta}{\sqrt{R^2 - \sin^2\theta}}\right] \tag{3.36}$$

$$A(\theta) = 2A_c + \frac{\pi B V(\theta)}{A_c} \tag{3.37}$$

Here a is the crank radius, R is the connection rod to crank radius ratio, A_c is the cross-sectional area of the combustion chamber, and V_d is the displacement volume. Note that this model of surface area treats the piston crown and fire deck as flat planes, and therefore represents a lower bound on the total surface area possible in an engine with the specified geometry B, L, ℓ, and r_c.

3.5.3.2 Pressure

The in-cylinder pressure P was filtered with a zero-phase, low-pass, 5th-order Butterworth filter with a cutoff frequency at 2200 Hz. As P is supposed to represent a steady-state cycle, the vector was padded with circular repetition of the elements before being passed to the filter in order to minimize end effects. After filtering, the vector was clipped back to the original size. Because the in-cylinder pressure transducer offers a dynamic measurement that is prone to drift, each cycle must be "pegged" to a reference value. The pegging was accomplished by averaging the P data between -185° and -175°, subtracting that value from the intake pressure P_{in}, and adding the resulting offset $\Delta \mathrm{P}_{peg}$ to P. The numerical derivative of P was calculated by the central difference method with a three-point stencil

$$f'_k = \frac{f_{k+1} - f_{k-1}}{2h} \tag{3.38}$$

where k is the current element and h is the step size, which in this case is 0.1 CAD. This equation was applied in a circular manner, such that for $k = 0$, the values for f_{k-1} were taken from the end of the vector, and for $k = N$, the values for f_{k+1} were taken from the beginning of the vector. This avoided end effects, and allowed for $dP/d\theta$ to be the same length as the original vector P. With the vectors for P and $dP/d\theta$, scalar quantities such as peak pressure (PP), location of peak pressure (LPP), peak pressure rise rate (PPRR) and location of peak pressure rise rate (LPPRR) were also calculated.

3.5.3.3 Indicated Work

The net indicated work W_{net} is calculated for the full thermodynamic cycle, while W_{gross} includes only the range from BDC before firing TDC (-180° aTDC) to BDC after firing TDC (+180° aTDC). The net and gross indicated power per cycle (P_{net} and P_{gross}) and the net and gross indicated mean effective pressure (IMEP_n and IMEP_g, a.k.a. net and gross load) are calculated from W_{net} and W_{gross} as follows:

$$W_{net}\ [J] = \int_{-360ATDC}^{+360ATDC} PdV\ \left[Pa \cdot m^3\right] \tag{3.39}$$

$$W_{gross}\ [J] = \int_{-180ATDC}^{+180ATDC} PdV\ \left[Pa \cdot m^3\right] \tag{3.40}$$

$$P\ [W] = W\ [J] \cdot \frac{RPM}{60\ \left[\frac{s}{min}\right]} \cdot \frac{1}{2} \left[\frac{cyc}{rev}\right] \tag{3.41}$$

$$IMEP\ [Pa] = \frac{W}{V_d} \left[\frac{Pa \cdot m^3}{m^3}\right] \tag{3.42}$$

3.5.3.4 Noise Metrics

Two of the most common methods of assessing noise level in the literature are PPRR and ringing intensity (RI). PPRR is straightforward to calculate but only describes changes in noise on a relative basis. PPRR increases in boosted conditions and does not account for the frequency spectrum of the pressure waves, and therefore is not a good predictor of audible noise. The RI metric, developed by Eng et al. [32], finds the intensity of the pressure waves based on amplitude and the speed of sound, and is applicable over a wider range than PPRR due to normalization by peak pressure. However, RI estimates the amplitude of the pressure waves from pressure rise rate in the time domain. The scaling factor β is typically assumed to be a constant (0.05), although in reality it can change significantly depending on operating conditions and combustion strategy. Also, as with PPRR, RI does not account for the frequency spectrum of the pressure waves.

$$PPRR = \frac{dP}{d\theta}_{max} \tag{3.43}$$

$$RI = \frac{1}{2\gamma} \frac{(\Delta P)^2}{P_{max}} \sqrt{\gamma R T_{max}} \tag{3.44}$$

$$\Delta P = \beta \frac{dP}{dt}_{max} \tag{3.45}$$

A more universal method of describing combustion noise is the sound pressure level (SPL), which is found by performing Fourier analysis of the raw pressure data to obtain power spectral density (PSD). Attenuation curves for the engine block and human hearing are then applied to the PSD, and the resulting signal is integrated to find the root mean square pressure, which allows for calculation of SPL in units of dB(A). This method is similar to that used in commercial products such as the AVL Combustion Noise Meter, and is described in detail by Shahlari, et al. [95], who show that SPL is not generally proportional to PPRR or RI when operating in different combustion modes.

3.5.3.5 Heat Release

The adiabatic apparent heat release rate (HRR) was calculated with a single-zone first law analysis and the cumulative adiabatic heat release (HR) was determined by trapezoidal integration. Because this model is based on a constant mass assumption, HRR and HR were calculated only for the closed part of the cycle between IVC and EVO. With the vectors for HRR and HR, scalar quantities such as peak heat release rate (PHRR), location of peak heat release rate (LPHRR), and the locations of 10%, 20%, 50%, etc., of HR (CA10, CA20, CA50, etc.) could be calculated.

$$\frac{dQ_{ad}}{d\theta} = \frac{\gamma}{\gamma - 1} P \frac{dV}{d\theta} + \frac{1}{\gamma - 1} V \frac{dP}{d\theta} \tag{3.46}$$

The polytropic constants for the compression and expansion strokes, n_{comp} and n_{exp}, were calculated by a linear regression fit to $\log P$ vs. $\log V$ in the ranges IVC + 50 CAD to TDC - 10 CAD and TDC + 40 CAD to EVO - 10 CAD, respectively. These polytropic constants were used to estimate of the ratio of specific heats γ used in the HRR calculation. The value of n_{comp} was used during compression and n_{exp} during expansion, with the transition centered at LPHRR and the duration of the transitional region being proportional to the duration of heat release as estimated by the number of crank angles between 10% and 90% cumulative heat release (CA10-90), as shown in Equation 3.47. An illustration of

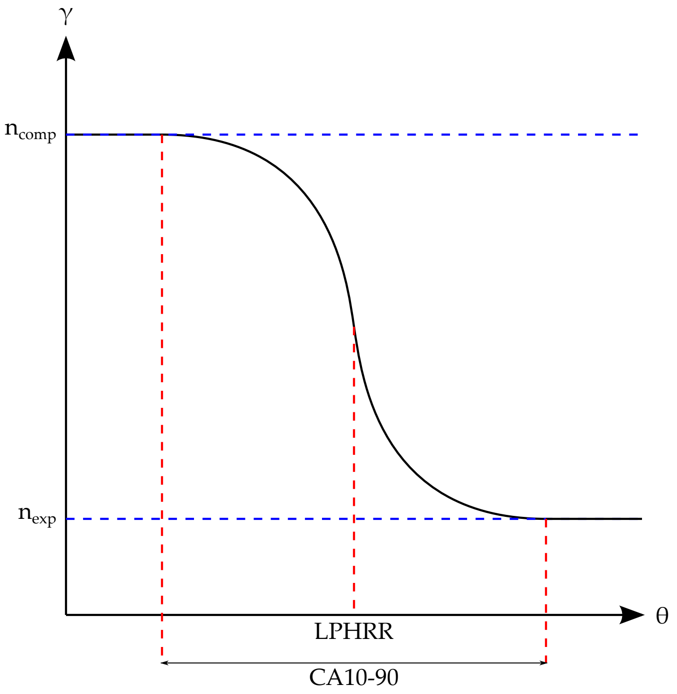

Figure 3.8: Process for estimating γ as a function of θ.

this γ estimation procedure is shown in Figure 3.8. As the γ estimate relies on information derived from HRR, this procedure was performed iteratively, with the initial transition centered at TDC with a step change from n_{comp} to n_{exp}.

$$\gamma = n_{comp} + \frac{n_{exh} - n_{comp}}{1 + 0.1 \exp\left(\frac{\theta - LPHRR}{CA90 - CA10}\right)} \tag{3.47}$$

3.5.3.6 Statistics and Ensembles

Ensemble statistics were created for each variable $f(\theta)$ resolved in the crank angle domain (P, HRR, etc.). At each index k of θ, the data $f(\theta_k)$ were fit to a normal distribution, resulting in the mean $\overline{f(\theta_k)}$, standard deviation $\sigma_f(\theta_k)$, and 95% confidence interval $\epsilon_f(\theta_k)$. By performing this process at each θ_k, the vectors $\overline{f(\theta)}$, $\sigma_f(\theta)$, and $\epsilon_f(\theta)$ can be created, as shown in Figure 3.9.

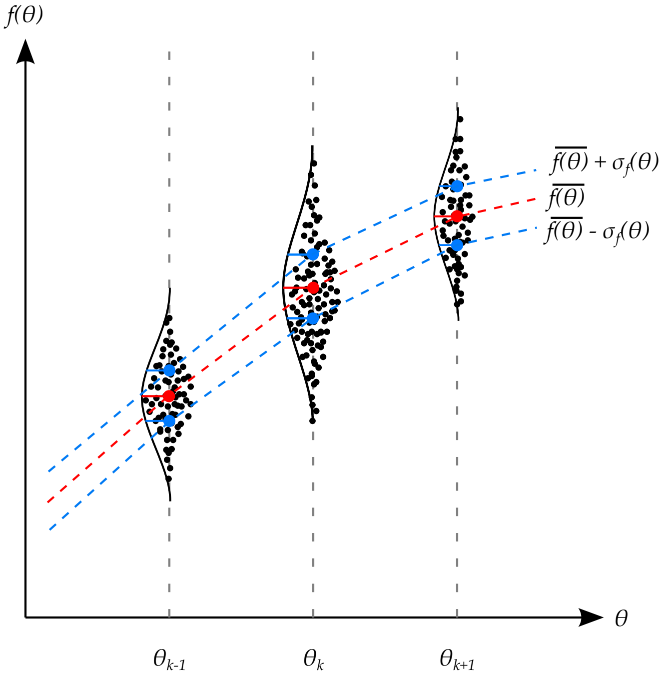

Figure 3.9: Fitting array data to normal distributions to create ensemble statistics.

Each of the scalar variables f calculated on a per-cycle basis (PPRR, CA50, etc.) were fit to normal distributions, resulting in the mean $\bar{f}$, standard deviation σ_f, and 95% confidence interval ϵ_f. This allows for the cyclic variations of each of these variables to be quantified, and for uncertainty propagation to be calculated when these variables are used as independent variables in other equations.

4 COMPUTATIONAL INVESTIGATION OF REACTIVITY CONTROLLED COMPRESSION IGNITION COMBUSTION USING METHANE IN A LIGHT-DUTY ENGINE

This chapter reports on multidimensional modeling work to examine the operating range for methane/diesel RCCI combustion in a light-duty diesel engine. In Section 4.1, details on the multidimensional engine computational fluid dynamics (CFD) model are presented. In Sections 4.2 and 4.3, an overview of the light-duty engine configuration and operating conditions is given. Then, in Section 4.4, results are presented from a study on the effect of premixed fuel reactivity on operating range for a light-duty engine.

4.1 Multi-Dimensional Engine CFD

In this work the KIVA-CHEMKIN code, which is based on the KIVA3V Release 2 code, was used [2–4]. The KIVA3V code uses the Lagrangian-Drop Eulerian-Fluid approach for modeling engine sprays, in which liquid fuel is treated as a Lagrangian parcel and the ambient gas is discretized into cells. The physical properties of gasoline and diesel fuel (for spray break-up, evaporation, and mixing) are taken to be those of iso-octane (iC_8H_{18}) and tetradecane ($C_{14}H_{30}$), respectively. Figure 4.1 shows an illustration of the modeling aspects of dual-fuel RCCI combustion using gasoline/diesel in an engine with a conventional diesel piston geometry.

Several submodel improvements have been made to the KIVA3V code, including fuel droplet breakup, droplet evaporation, droplet collision modeling, turbulence modeling, grid independent spray models, and the development of primary reference fuel chemical mechanisms, as summarized next. Beale and Reitz [7] implemented a hybrid spray breakup model, namely the KH-RT model. The droplet collision model is from the original KIVA3V code and is based on O’Rourke’s model. However, a radius-of-influence method was

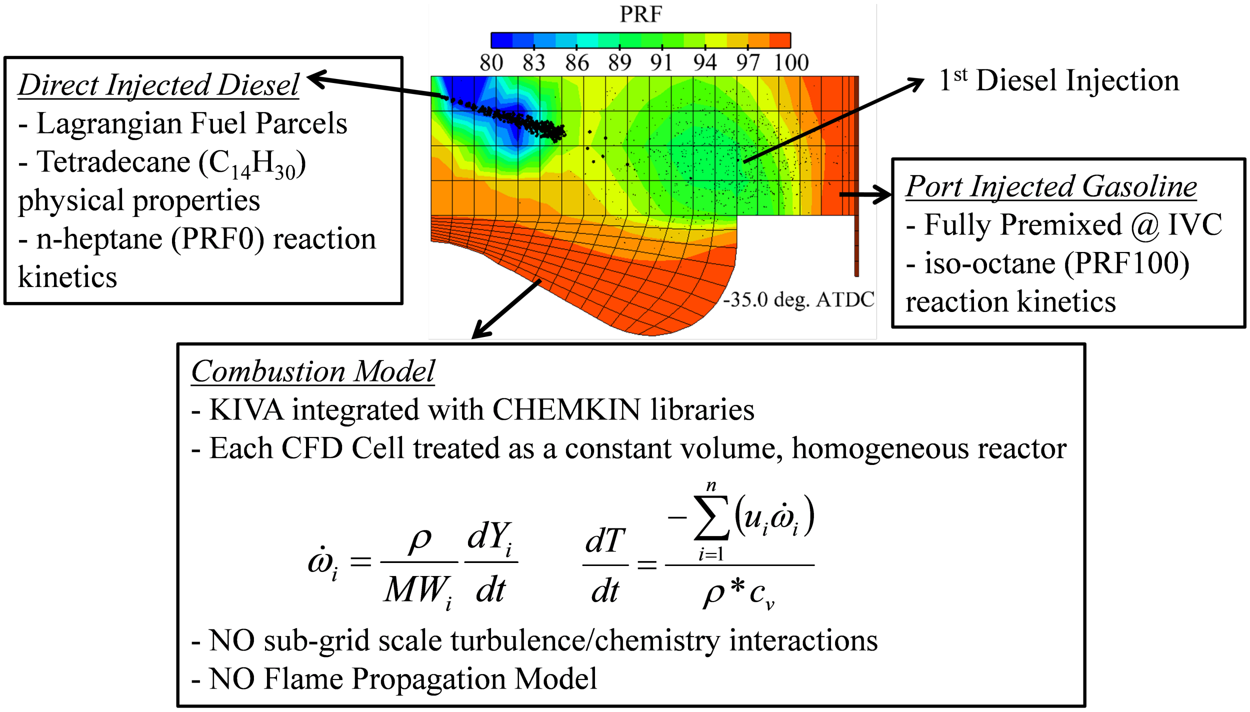

Direct Injected Diesel
- Lagrangian Fuel Parcels
- Tetradecane ($C_{14}H_{30}$) physical properties
- n-heptane (PRF0) reaction kinetics

1^{st} Diesel Injection

Port Injected Gasoline
- Fully Premixed @ IVC
- iso-octane (PRF100) reaction kinetics

Combustion Model
- KIVA integrated with CHEMKIN libraries
- Each CFD Cell treated as a constant volume, homogeneous reactor

$$\dot{\omega}_i = \frac{\rho}{MW_i}\frac{dY_i}{dt} \qquad \frac{dT}{dt} = \frac{-\sum_{i=1}^{n}(u_i\dot{\omega}_i)}{\rho * c_v}$$

- NO sub-grid scale turbulence/chemistry interactions
- NO Flame Propagation Model

Figure 4.1: Illustration of multi-dimensional engine CFD modeling of gasoline/diesel RCCI combustion using KIVA [21].

implemented to reduce the mesh dependency of the collision process [1]. The interaction of the liquid fuel parcels with the wall was modeled with the standard KIVA3V wall film model developed by O'Rourke and Amsden [81]. Ra and Reitz [85] made improvements to the droplet vaporization sub model. The RNG k-ϵ turbulence model was modified and implemented into the KIVA3V code by Han and Reitz [36]. In order to reduce the grid size dependence of the Lagrangian spray model, the GASJET model of Abani *et al.* [1] was used to model the relative velocity between the fuel droplets and the gas phase in the very near nozzle region of the injector. Finally, to further reduce the simulation time, a dynamic maximum timestep strategy was implemented [22].

The KIVA-CHEMKIN code has been coupled to the CHEMKIN II libraries for detailed combustion chemistry calculations [54]. Conventional gasoline and diesel fuels are multicomponent fuels and consist of a wide range of hydrocarbon species, and it is thus not practical in engineering applications to kinetically model each species in the real fuel.

Therefore, the ignition and combustion characteristics of automotive fuels are typically represented by blends of the primary reference fuels (PRF), namely iso-octane (iC_8H_{18}) and n-heptane (nC_7H_{16}). In this work, the ignition and combustion characteristics of iso-octane and n-heptane are used to model the kinetics of gasoline and diesel fuel, respectively; CH_4 oxidation is built in to the mechanism. A reduced PRF mechanism consisting of 45 species and 142 reactions, which includes NO_x chemistry, was utilized in the present study to represent the autoignition and subsequent combustion of gasoline and diesel fuel [86]. Soot emissions were predicted using a phenomenological soot model. Two competing processes are considered in the model, namely soot formation and soot oxidation. Acetylene (C_2H_2) is used as the soot inception species in the formation rate equation [65]. The NO_x formation chemistry is represented by 4 species and 12 reactions, which is a reduced version of the GRI NO_x mechanism [104].

4.2 Light-Duty Single-Cylinder Engine

The light-duty diesel engine is based on the General Motors/Fiat JTD 1.9L platform, the specifications of which are shown in Table 4.1, and the sector mesh shown in Figure 4.2.

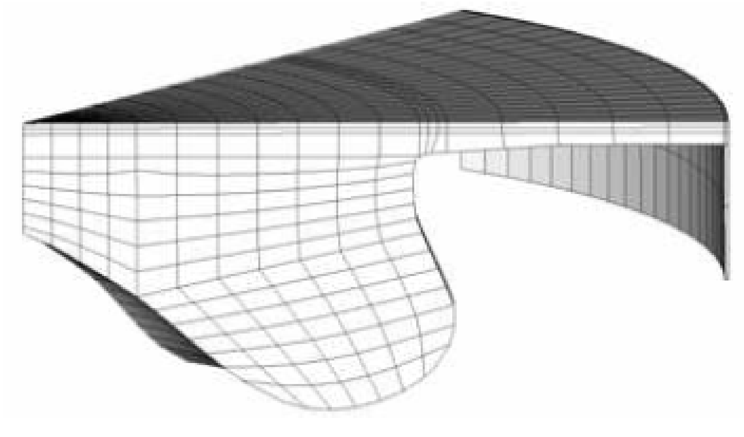

Figure 4.2: KIVA computational sector mesh of the GM 1.9L engine geometry with the stock CDC piston.

Table 4.1: Light-duty engine specifications.

Base Engine	GM/Fiat JTD 1.9L 4-cylinder DI Diesel
Bore x Stroke	82.0 mm x 90.4 mm
Connecting Rod Length	145.54 mm
Displacement	0.477 L
Compression Ratio	16.7:1
Intake Valve Opening/Closing	344°/-132° aTDC
Exhaust Valve Opening/Closing	112°/388° aTDC
Piston Bowl Type	Stock CDC

4.3 Engine Simulation Conditions

In this study detailed CFD modeling is used to examine the use of natural gas as the premixed low-reactivity fuel for RCCI engine operation. The direct-injected (high-reactivity) fuel is PRF0, and the premixed (low-reactivity) fuels include PRF75 (25% n-heptane and 75% iso-octane), PRF100 (pure iso-octane), and CH_4 (methane). To examine the operating space for each fuel combination, the premixed fuel amount is varied from 50% to 95% and the EGR amount is varied from 0% to 50%. Three constraints have been imposed to define the acceptable operating range: a NO_x limit of 0.27 g/kW-hr, a combustion efficiency limit of 90%, and a peak pressure rise rate (PPRR) of 10 bar/degree. The engine operating conditions are listed in Table 4.3.

Table 4.2: Engine operating conditions for the CFD study.

Engine Speed	2000 rev/min
IMEP	6 bar nominal
Total Fuel Energy	650 J/cycle
CRI Injection Pressure	500 bar
CRI Hole Number	7
CRI Hole Size	140 µm
CRI Spray Angle	144°
DI Injection Timings	-57°/-37° aTDC
Intake Pressure	1.3 bar
Intake Temperature	60 °C
Swirl Ratio	2.2
PFI Mass Fraction	0.5 to 0.95
EGR Rate	0% to 50%
DI (High-Reactivity) Fuel	PRF0
PFI (Low-Reactivity) Fuel	PRF75, PRF100, CH_4

4.4 Results and Discussion

4.4.1 Effect of Fuel Reactivity on Operating Range

Figure 4.3 shows the RCCI operating map for a DI/PFI fuel combination of PRF0/PRF75 for the medium load condition of Table 4.3. This fuel combination gives the shortest global ignition delay of all the combinations simulated. It is seen that the PPRR limit is surpassed at lower EGR rates and, in tandem with the combustion efficiency limit, the acceptable operating range is confined to relatively high EGR rates across a wide range of premixed fuel amount conditions. The NO_x constraint is violated a low EGR rates and low premixed amounts; however, this does not have an effect on the viable operating range.

Figure 4.4 shows the operating map for a DI/PFI fuel combination of PRF0/PRF100. This fuel combination gives a broader operating range relative to PRF0/PRF75. A wide range of EGR rate and a premixed fuel amount up to approximately 85% is allowable for acceptable combustion performance. PPRR and NO_x levels are of concern at low EGR rates and low premixed amounts, with both violating the imposed constraints. Also, relative to

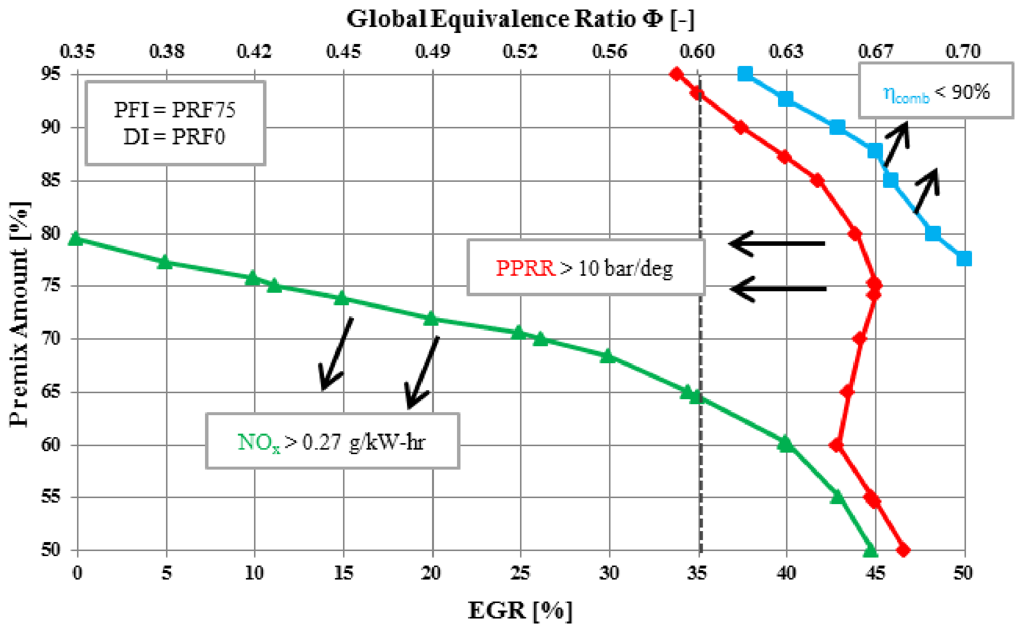

Figure 4.3: Operating map for DI/PFI fuel combination of PRF0/PRF75 with the NO_x (green), PPRR (red), and η_{comb} (blue) limits imposed.

PRF0/PRF75, a fuel combination of PRF0/PRF100 is more dependent on the DI amount to satisfy the combustion efficiency constraint.

Figure 4.5 shows the operating map for a DI/PFI fuel combination of PRF0/CH4. This fuel combination gives the longest global ignition delay of all the combinations presented here. As seen, the PPRR constraint is met everywhere in the map; however, there is an extremely narrow acceptable operating range. This is attributed to the load condition for this map. At 6 bar IMEP, the rate of energy release is insufficient to sustain high-performance combustion across a wide range of operating conditions. Coupled with the relatively long ignition delay, the acceptable operating range becomes very limited.

In summary, as the premixed fuel becomes less reactive (i.e., PRF75 → PRF100 → CH_4) the dependence on EGR to mitigate the formation of NO_x is reduced; in addition, more DI fuel is required to stay within the acceptable operating window; and finally, the PPRR constraint becomes less of a factor in defining the acceptable operating range.

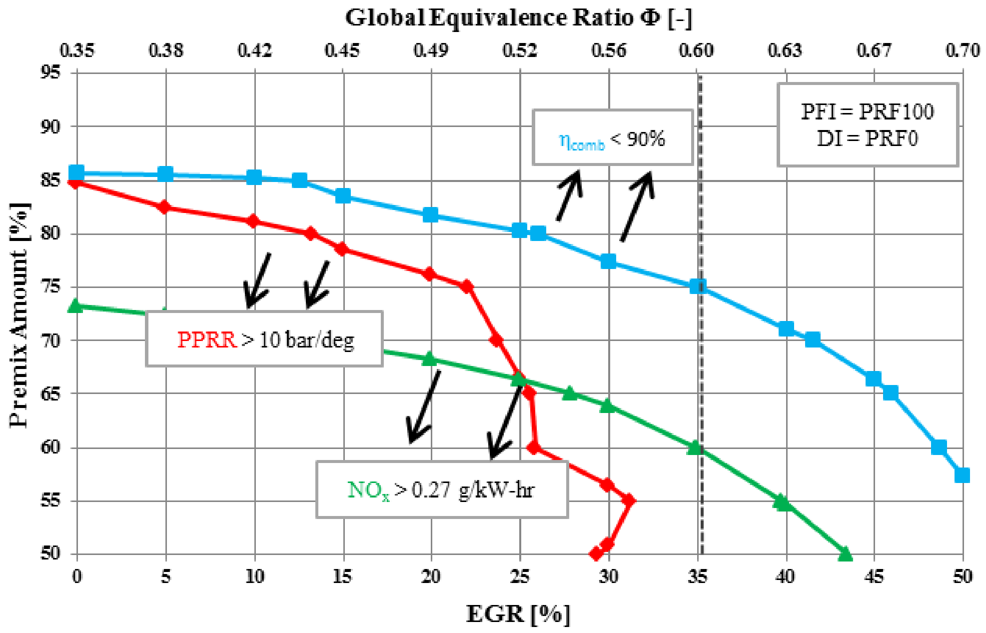

Figure 4.4: Operating map for DI/PFI fuel combination of PRF0/PRF100 with the NO_x (green), PPRR (red), and η_{comb} (blue) limits imposed.

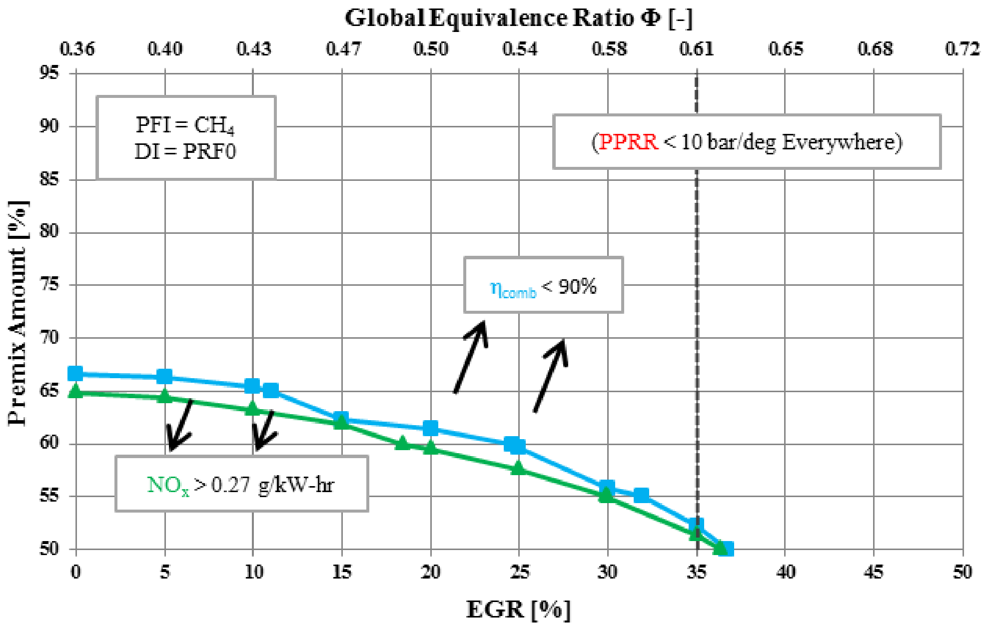

Figure 4.5: Operating map for DI/PFI fuel combination of PRF0/CH_4 with the NO_x (green), PPRR (red), and η_{comb} (blue) limits imposed.

4.4.2 Comparison of Operation at Fixed EGR Rate

Figure 4.6 shows the pressure and heat release data for the simulated cases which use 35% EGR (see also Figures 4.3, 4.4 and 4.5). The EGR rate was selected for comparison of performance results which approximately meet the boundaries of PPRR < 10 bar/deg, NO_x < 0.27 g/kW-hr, and $\eta_{comb} > 90\%$. The PRF0/PRF75 case is shown in red, the PRF0/PRF100 case is shown in green, and the PRF0/CH_4 case is shown in blue.

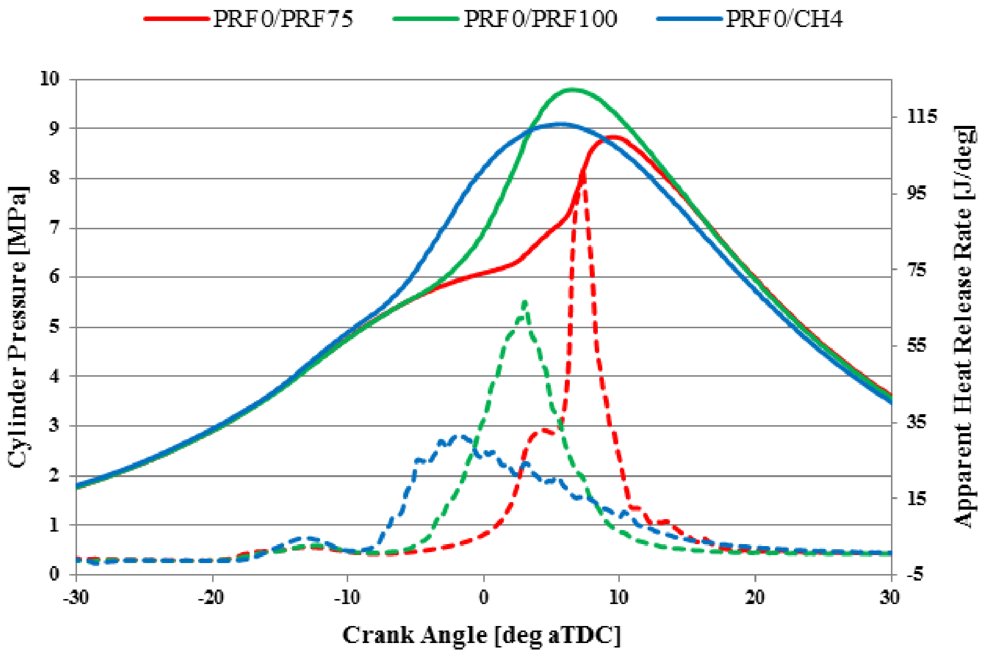

Figure 4.6: Pressure and heat release rates for 35% EGR conditions.

It is shown that the fuel combination strongly affects the achievable combustion performance at a fixed EGR rate. The PRF0/PRF75 case uses 95% premixed fuel, the PRF0/PRF100 case uses 70% premixed fuel, and the PRF/CH_4 case uses 50% premixed fuel. It is seen that as the premixed fuel becomes less-reactive (i.e., longer ignition delay) the peak heat release rate is reduced, and an earlier combustion phasing is required to meet the performance metrics. As a result, the combustion durations become considerably lengthened.

Table 4.3: Performance and emissions results for the 35% EGR cases.

	PRF0/PRF75	**PRF0/PRF100**	**PRF0/CH$_4$**
Premix Fuel [%]	95	70	50
CA50 [° aTDC]	7.0	2.8	1.0
PPRR [bar/deg]	8.8	6.8	4.5
$\eta_{\mathbf{therm}}$ [%]	43.3	43.8	40.4
ISFC [g/kW-hr]	189.7	187.6	192.6
Soot [g/kW-hr]	0.016	0.014	0.073
NO$_x$ [g/kW-hr]	0.01	0.05	0.32
CO [g/kW-hr]	4.7	4.3	12.2
HC [g/kW-hr]	9.0	6.1	11.8

Table 4.3 shows the performance and emissions results for the selected 35% EGR simulations. (It should be noted that for the PRF0/CH$_4$ case, the NO$_x$ emission exceed 0.27 g/kW-hr. The case selected is the closest condition in the simulation domain along the NO$_x$ threshold. Refining the simulation domain would provide a case close to, but below, 0.27 g/kW-hr.) It is seen that as the premixed fuel becomes less-reactive (i.e., longer ignition delay), the NO$_x$ emissions increase significantly. This is predominantly due to the increase in DI fuel mass required to achieve acceptable combustion performance. In fact, the DI fuel amount required for the PRF0/CH$_4$ case is nearly twice as much as is required for the PRF0/PRF75 case, which leads to an order-of-magnitude increase in NO$_x$. It is also seen that for premixed fuels with longer ignition delays, the peak pressure rise rate is significantly reduced due to the lower rate of heat release during combustion. As a result of these observations it can be suggested that by moving to premixed fuels with longer ignition delays, EGR requirements for meeting combustion noise limits may be reduced, thus leading to the potential for an extension of the upper load limit for a given operating condition.

4.5 Conclusions

In Section 4.4.1, it was predicted that as the premixed fuel becomes less reactive (i.e., PRF75 → PRF100 → CH_4) the dependence on EGR to mitigate the formation of NO_x is reduced; in addition, more DI fuel is required to stay within the acceptable operating window; and finally, the PPRR constraint becomes less of a factor in defining the acceptable operating range. Figure 4.7 summarizes of the predicted acceptable combustion range (NO_x < 0.27 g/kW-hr, a combustion efficiency > 90%, and a peak pressure rise rate < 10 bar/deg) for the light-duty mid-load operating conditions listed in Table 3-2.

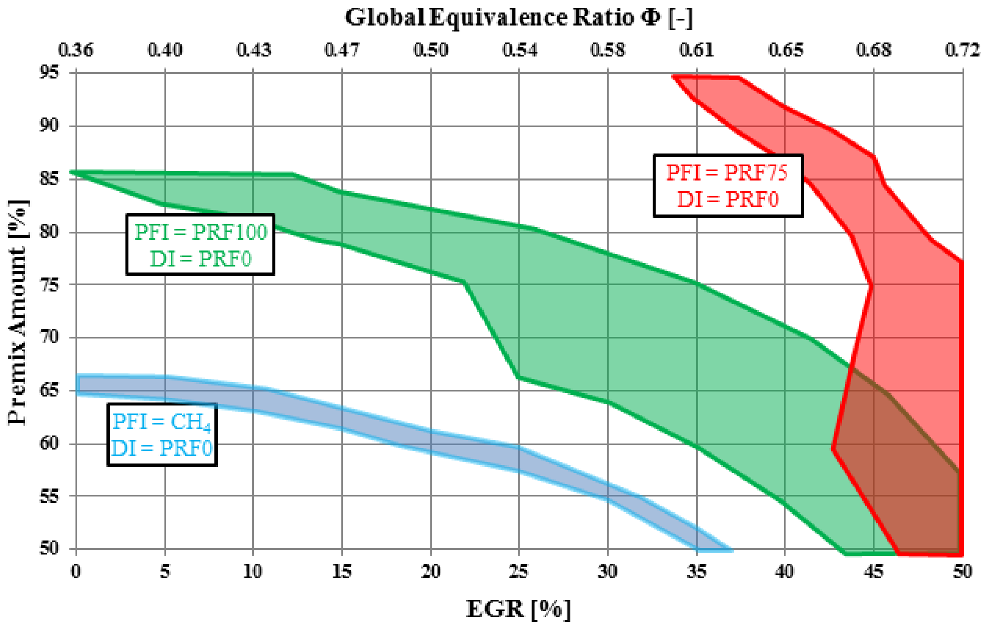

Figure 4.7: Overview of acceptable operating ranges for PRF0/PRF75, PRF0/PRF100, and PRF0/CH_4 fuel combinations.

In Section 4.4.2, when comparing engine operation at a fixed EGR rate, it was observed that by moving to premixed fuels with longer ignition delays, EGR requirements for meeting combustion noise limits may be reduced, thus leading to the potential for an extension of the upper load limit for a given operating condition. This is explored further in the next chapters.

5 NATURAL GAS FOR HIGH LOAD DUAL-FUEL REACTIVITY CONTROLLED COMPRESSION IGNITION IN HEAVY-DUTY ENGINES

This chapter[5] reports on the comparison of the engine load capabilities of gasoline and methane as the low-reactivity fuels for reactivity controlled compression ignition in a heavy-duty engine. The objective of the study was to investigate the use of methane (as a natural gas surrogate fuel) as the less-reactive fuel for RCCI operation and to develop an understanding of the impact on load range and characteristics of the combustion process.

5.1 Experimental Setup

The following engine experiments were performed in the Caterpillar SCOTE Laboratory as outlined in Chapter 3, with the injector specifications given in Table 5.2.

Table 5.1: 3401 Caterpillar SCOTE heavy-duty engine specifications.

Displacement	2.44 L
Bore x Stroke	137.2 mm x 165.1 mm
Connecting Rod Length	261.6 mm
Number of Valves	4
Intake Valve Opening/Closing	335/-143° aTDC
Exhaust Valve Opening/Closing	130/-355° aTDC
Swirl Ratio	0.7
Piston Type	Articulated
Piston Profile	Bathtub
Compression Ratio	14.9:1

Table 5.2: Common rail injector specifications.

Injector Series	Bosch CRI2.2
Number of Holes	6
Hole Diameter	250 μm
Included Spray Angle	145°

---

[5] Chapter 5 was formally published at the following Reference [114]: Walker, N. R. *et al.*, 2015, http://dx.doi.org/10.1115/1.4030110.

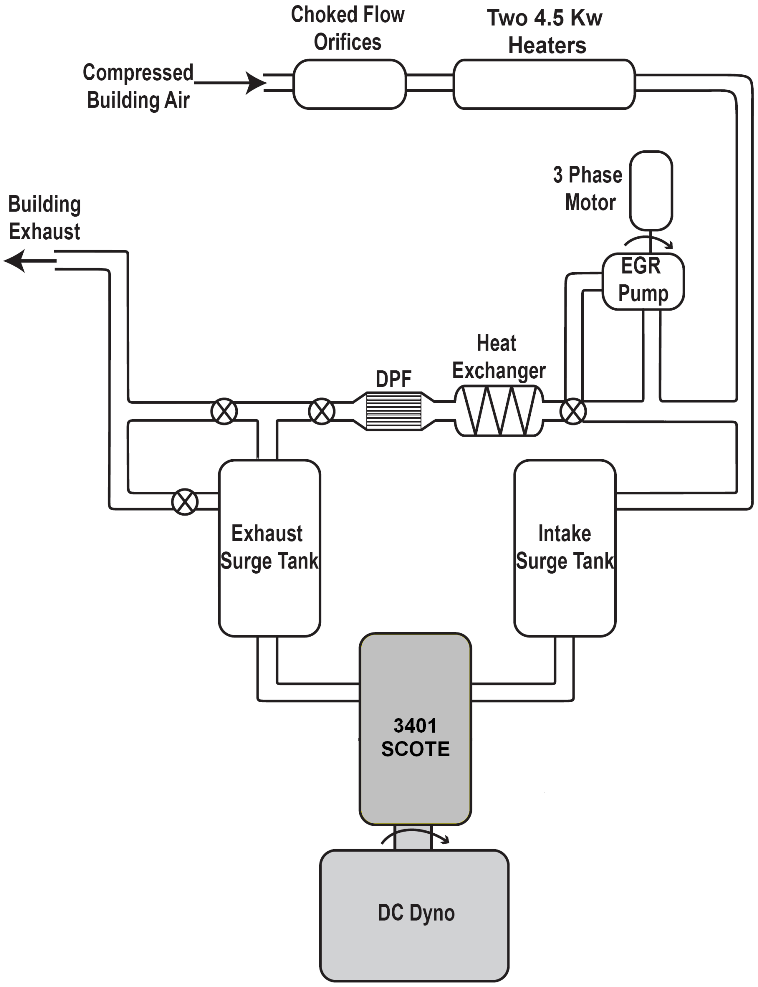

Figure 5.1: SCOTE Laboratory configuration for the Chapter 5 experiments.

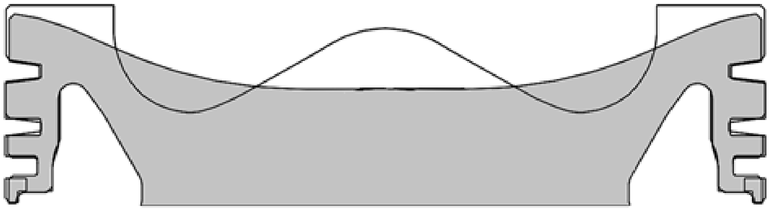

Figure 5.2: The modified RCCI piston (gray, CR = 14.9) profile used in the Chapter 5 experiments.

5.2 Operating Conditions

To study the effect of using methane as the less-reactive fuel for RCCI combustion, methane / diesel RCCI experiments were performed and compared against gasoline / diesel RCCI operation. 2007 CERT diesel was direct-injected at a pressure of 500 bar as the more reactive fuel, which has a lower heating value (LHV) of 42.7 MJ/kg. Gasoline with a pump octane number of 91 was port-injected as one of the less reactive fuels, and it has a LHV of 43.0 MJ/kg. Methane was port-injected as the other less reactive fuel, and it has a LHV of 50.0 MJ/kg. A single DI injection strategy was employed and, as the load was increased, the DI SOI timing was advanced to control the combustion phasing. The DI diesel fuel amount was fixed for all cases at 13 mg/cycle. The DI SOI timings used in the present study are shown in Fig. 5.3.

Boosted RCCI combustion was established at a low load condition at an engine speed of 1300 rev/min, and the load was increased by increasing the amount of port-injected low-reactivity fuel. In order to fix the global equivalence ratio at $\phi = 0.3$ the intake air flow rate was increased by increasing the intake boost pressure until the desired equivalence ratio at each experimental point. The intake pressures used in this study are shown in Figure 5.4. With the strong controllability over combustion phasing provided by the RCCI combustion strategy, it is of interest to examine the ability to modify the combustion phasing to study the effect on the engine load regime. As such, two combustion phasings were studied: CA50 = 0° aTDC and CA50 = 4° aTDC, with the DI SOI timing being adjusted to reach the desired combustion phasing. EGR was not used for all cases and the intake temperature was fixed at 40 °C. Table 5.3 lists the engine operating conditions for this study.

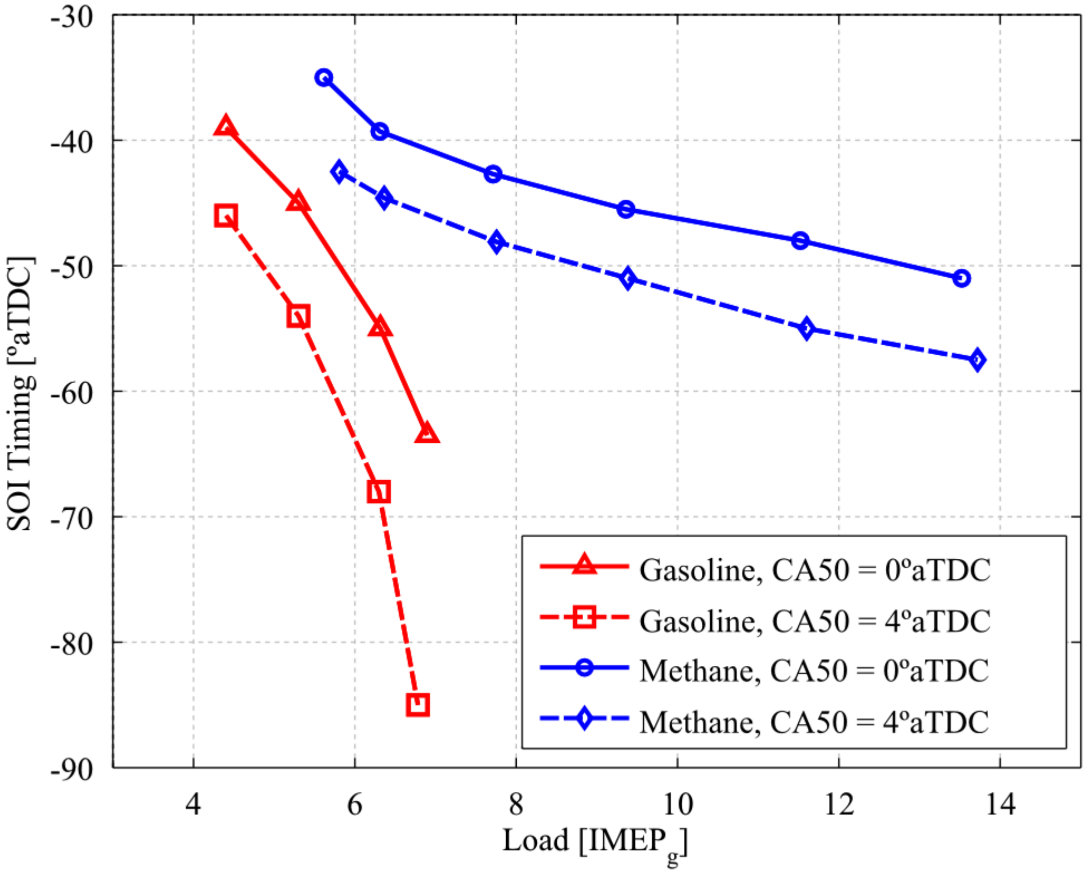

Figure 5.3: DI SOI timings as a function of engine load. Earlier injection timings are required for gasoline/diesel operation relative to methane/diesel operation.

Table 5.3: Engine operating conditions.

Engine Speed	1300 rev/min
Global ϕ	0.3
EGR Rate	0%
Intake Temperature	40 °C
SOI Timing	-35° to -85° aTDC
Diesel Fuel Mass	13 mg/cycle
DI Injection Pressure	500 bar
DI Fuel	Diesel
PFI Fuels	Gasoline / Methane

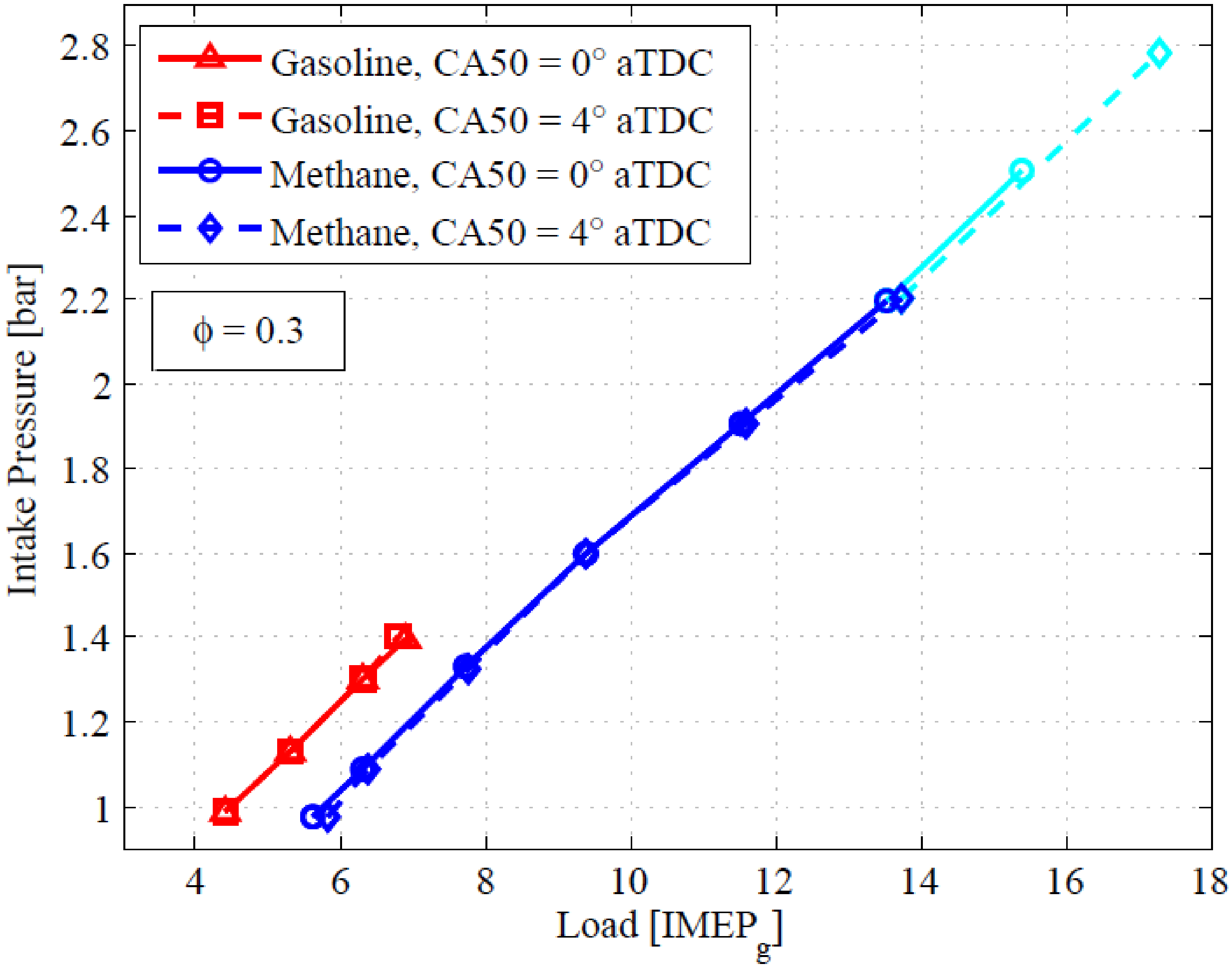

Figure 5.4: Intake pressures for the experimental conditions presented in Chapter 5.

5.3 Results and Discussion

Four sets of operating points were taken. For both gasoline/diesel and methane/diesel fuel combinations, and two combustion phasings (CA50 = 0° aTDC and CA50 = 4° aTDC), a viable load operating space was studied. For heavy-duty engines, a combustion noise limit of 15 bar/deg is considered acceptable, however for this study a conservative upper bound on the satisfactory load range was imposed by setting a 10 bar/deg peak pressure rise rate (PPRR) noise limit. Once establishing stable low-load RCCI engine operation, the load was increased until the combustion noise constraint was reached.

5.3.1 Heat Release Analysis

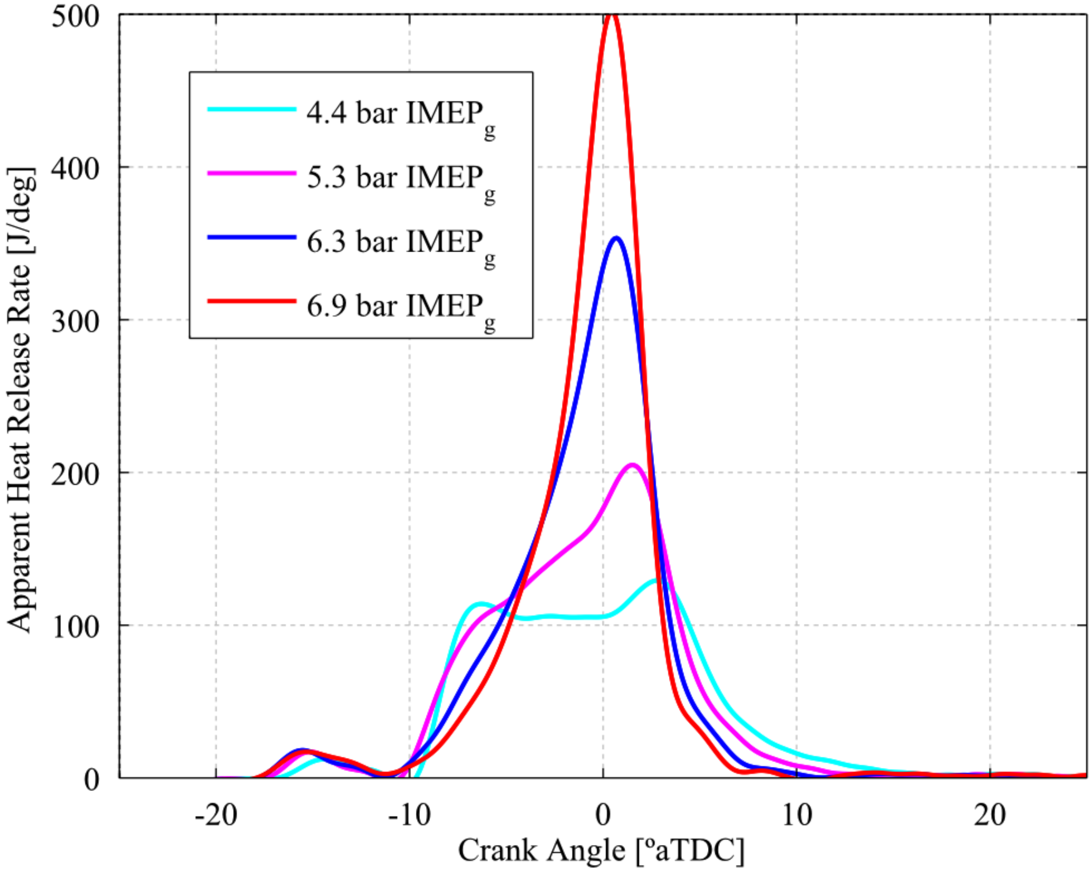

Figure 5.5: Apparent heat release rates for gasoline/diesel RCCI operation with CA50 = 0° aTDC combustion phasing.

In Fig. 5.5, apparent heat release rates are shown for the four conditions under gasoline/diesel RCCI operation at a combustion phasing of CA50 = 0° aTDC. The maximum load obtained before the imposed peak pressure rise rate limit was 6.9 bar IMEP$_g$. It was observed that as the load was increased, the combustion duration decreased while the peak apparent heat release rate increased. It was also seen that the low temperature heat release advanced and increased in magnitude as the load was increased.

The 4.4 bar IMEP$_g$ case displayed a two-stage high temperature heat release, which is indicative of a strong in-cylinder fuel reactivity stratification prior to ignition, leading to a very broad heat release profile. The late DI SOI timing of -39° aTDC allowed for a relatively short window for mixing of the DI fuel spray. This leads to locally-rich regions of diesel fuel which autoignites. After the diesel autoignition the heat release rate slows down, however combustion was sustained due to energy release from combustion of surrounding gasoline/diesel mixtures.

The diesel/gasoline mixtures have an intermediate reactivity between that of neat gasoline and neat diesel. It is this mechanism that sustains sequential autoignition through the in-cylinder fuel reactivity range. Finally, in-cylinder conditions are reached where the remaining gasoline in the cylinder ignites leading to the completion of the combustion process. Further discussion on this two-stage dual-fuel combustion phenomena is found in Reference [112].

Figure 5.6 shows the apparent heat release rates for the four conditions under gasoline/diesel RCCI operation at a combustion phasing of CA50 = 4° aTDC. The maximum load obtained before meeting the peak pressure rise rate limit was 6.8 bar IMEP_g. Again, it is seen that as the load is increased, the combustion duration decreases while the peak apparent heat release rate increases, giving a more Gaussian-like heat release curve. It is also the situation that the low temperature heat release advances and increases in magnitude as the load is increased. It is interesting to note that the 4.4 bar IMEP_g case does not display an obvious two-stage high temperature heat release, as in the condition with a combustion phasing of CA50 = 0° aTDC. Instead, a single-stage high temperature heat release is present, which is favorable for optimum RCCI combustion, as detailed by Reference [58]. This is due to the increase in mixing time allowed for the DI spray prior to ignition. For a combustion phasing of CA50 = 4° aTDC, the DI SOI timing is -46° aTDC, giving a DI mixing time 7 crank angle degrees (CAD) longer than the combustion phasing of CA50 = 0° aTDC, which is sufficient to generate a smooth sequential autoignition process throughout the cylinder.

Figure 5.7 shows the apparent heat release rates for the six conditions under methane / diesel RCCI operation at a combustion phasing of CA50 = 0° aTDC. The maximum load

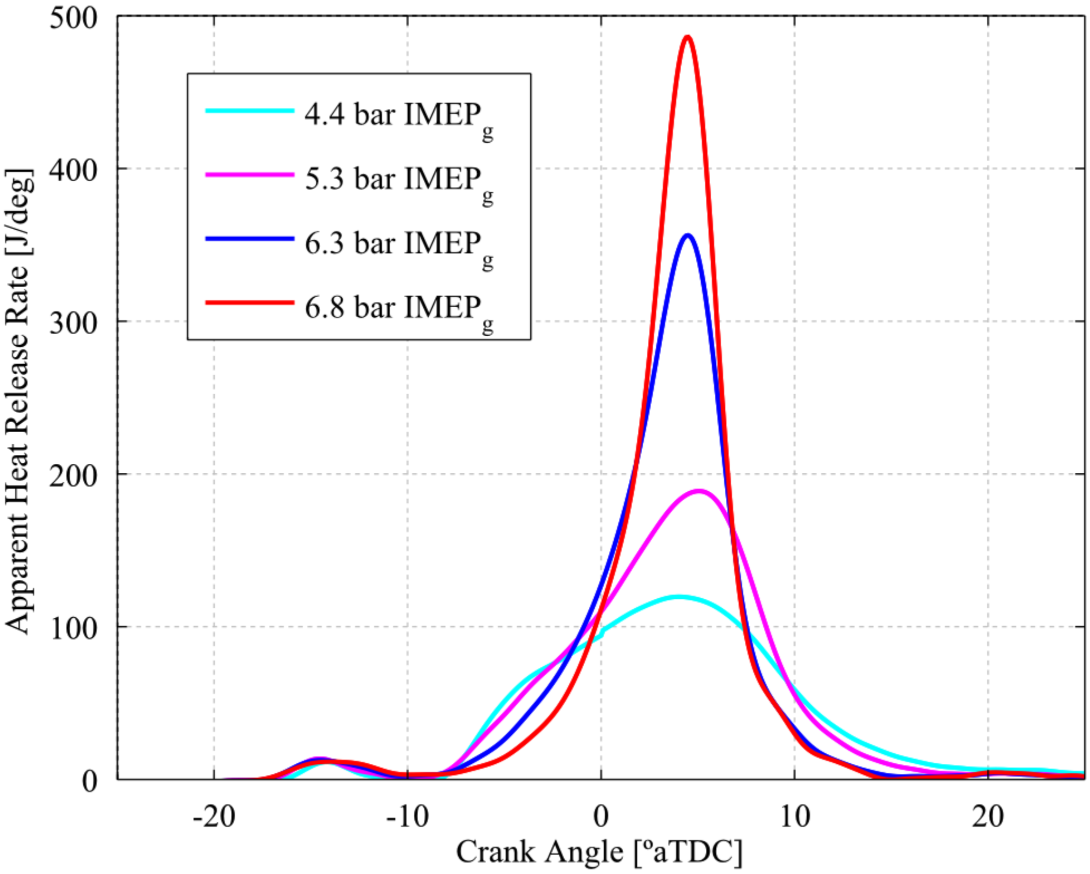

Figure 5.6: Apparent heat release rates for gasoline/diesel RCCI operation with CA50 = 4° aTDC combustion phasing.

obtained was 13.5 bar IMEP$_g$, which results in a peak pressure rise rate of 7.8 bar/deg. The 10 bar/deg load limit constraint was not reached due to limitations of the gaseous port fuel injector flow rate with the current experimental setup. In contrast to gasoline/diesel operation, it is seen that, as the load is increased, the combustion duration increases. However, the peak apparent heat release rate also generally increases with load. It is seen that the low temperature heat release advances as the load is increased. Both the 5.6 bar IMEP$_g$ and 6.3 bar IMEP$_g$ cases display two-stage high temperature heat release, and have DI SOI timings of -35° aTDC and -39.3° aTDC, respectively, providing insufficient time for mixing before diesel autoignition occurs. The rest of the conditions display single-stage high temperature heat release. Based on this observation and that of Figure 5.5, there is

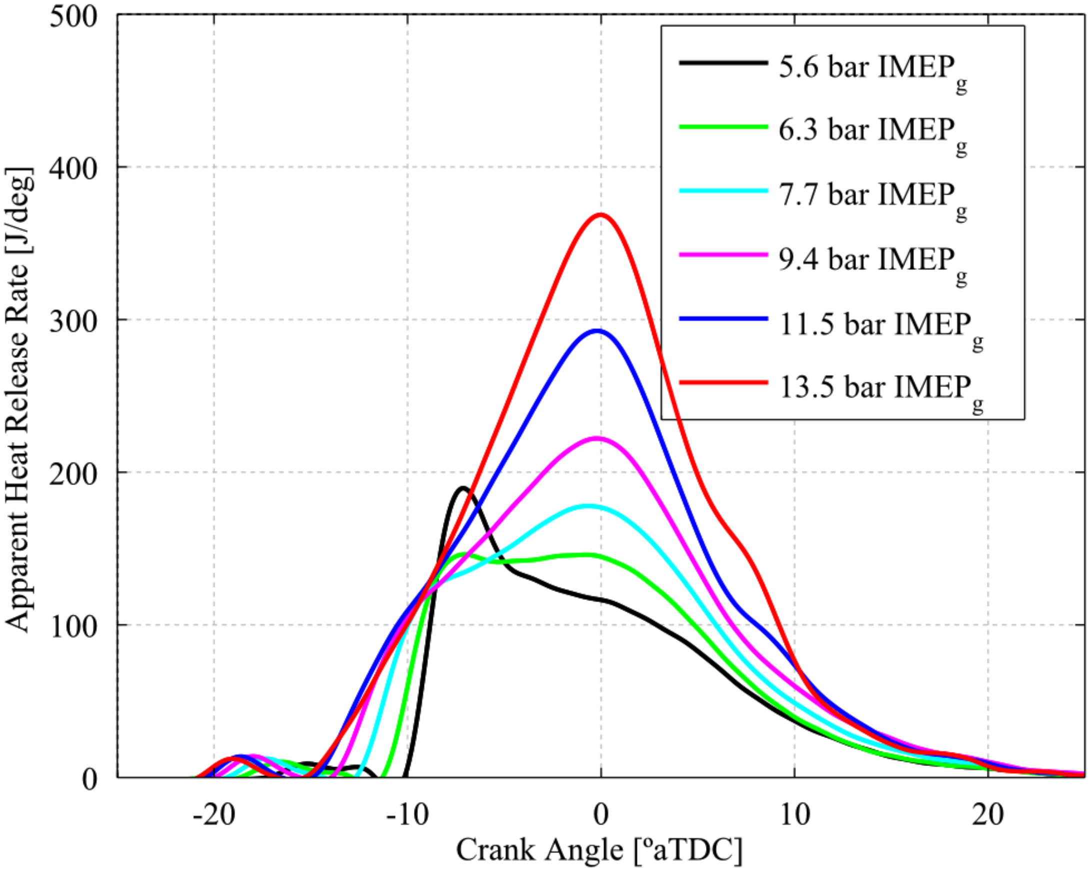

Figure 5.7: Apparent heat release rates for methane/diesel RCCI operation with CA50 = 0° aTDC combustion phasing.

evidence of a characteristic DI SOI timing at approximately -40° aTDC, which allows for sufficient mixing time to allow for single-stage high temperature heat release.

Figure 5.8 shows the apparent heat release rates for the six obtained conditions under methane/diesel RCCI operation at a combustion phasing of CA50 = 4° aTDC. The maximum load obtained was 13.7 bar IMEP$_g$, which results in a peak pressure rise rate of 6.6 bar/deg. All six load conditions possess a single-stage high temperature heat release. It is again observed that, unlike gasoline/diesel RCCI operation, as the load is increased the burn duration also increases. It is similarly seen that the low temperature heat release advances as the load is increased.

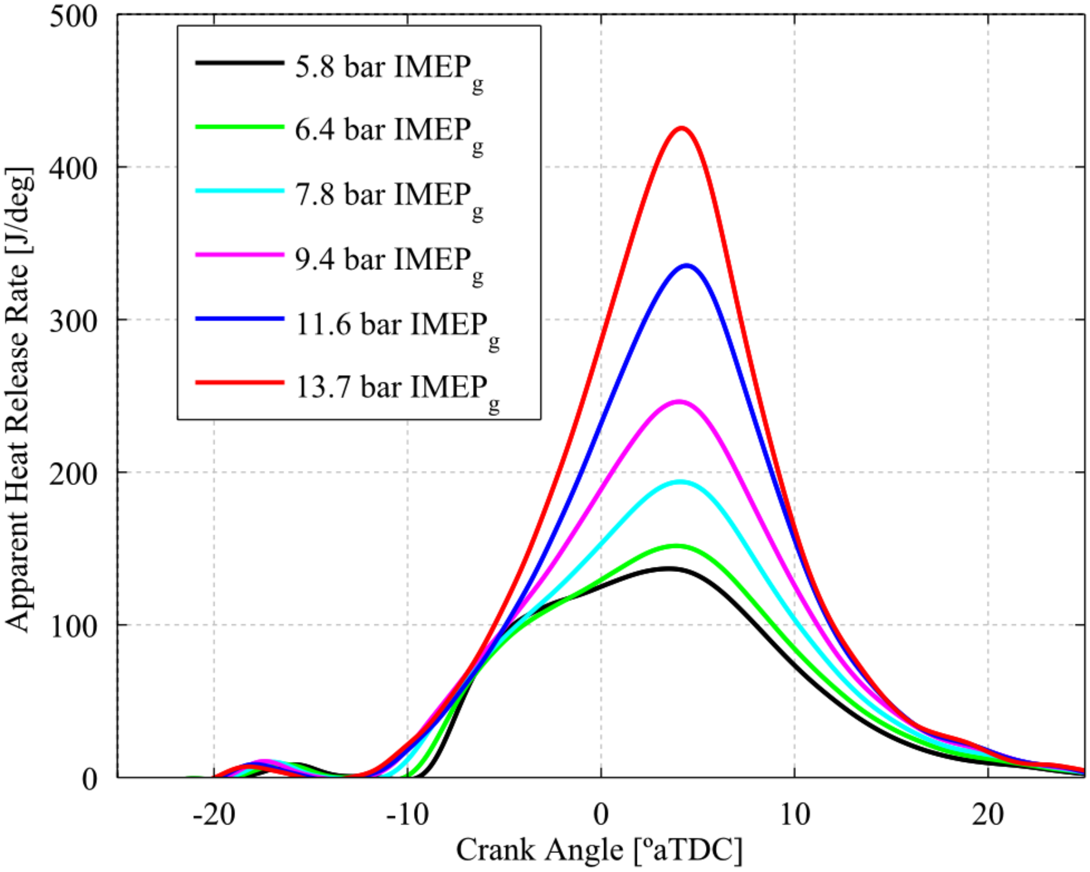

Figure 5.8: Apparent heat release rates for methane/diesel RCCI operation with CA50 = 4° aTDC combustion phasing.

It is worth noting that one significant difference in combustion characteristics between gasoline/diesel RCCI operation and methane/diesel RCCI operation is the combustion duration. The combustion duration is defined as the crank angle duration between crank angle at 10% of total heat release (CA10) and the crank angle at 90% of total heat release (CA90), also referred to as CA10-90. Based on the data shown in Figures 5.5-5.8, an estimation of the CA10-90 duration can be made. For gasoline/diesel RCCI operation the CA10-90 duration is approximately 15 CAD; for methane/diesel RCCI operation the CA10-90 duration is approximately 25 CAD. This extension of the burn duration, presumably due to slower chemical kinetics processes, as supported in Figure 2.5, allows for lower peak heat release rates and thus an extension of the upper load limit for methane/diesel RCCI operation.

Another unique trait of methane/diesel RCCI operation, as evidenced in Figure 5.8, is the trend of advancing start of high temperature combustion. Even though the DI SOI timing is advanced (thus reducing the fuel reactivity gradient prior to ignition), to control the overall combustion phasing, methane/diesel RCCI operation retains a sensitive link between the DI SOI timing and the start of high temperature heat release. It is seen in Figure 5.3 that for methane/diesel operation, in order to maintain a fixed combustion phasing, as the load increases the required changes in DI SOI timings are reduced (with the opposite being the case for gasoline/diesel operation). The underlying processes governing this relationship are not yet fully understood, but are certainly due to differences in chemical kinetic rates of the various fuel combinations.

5.3.2 Fuel Effects on Engine Performance

As a kinetically-controlled combustion process, it is important to examine the combustion stability for RCCI engine operation. Two metrics are examined: COV of IMEP and COV of PPRR, where COV is the coefficient of variance. The COV is calculated as the ratio of the standard deviation to the mean of the total number of recorded cycles for the given metric (e.g., IMEP or PPRR).

Figure 5.9 shows the COV of IMEP for the experimental conditions presented in this study. It is observed that for all cases, diesel/methane RCCI operation provides a significantly lower COV of IMEP across the entire load range. It is also interesting to note the trend, that for both fuel combinations, as the engine load is increased, the COV of IMEP decreases, leading to increased combustion stability at higher engine load. It is also seen that for both fueling combinations utilizing an earlier combustion phasing of CA50 = 0° aTDC leads to improved load stability relative to the later combustion phasing of CA50 =

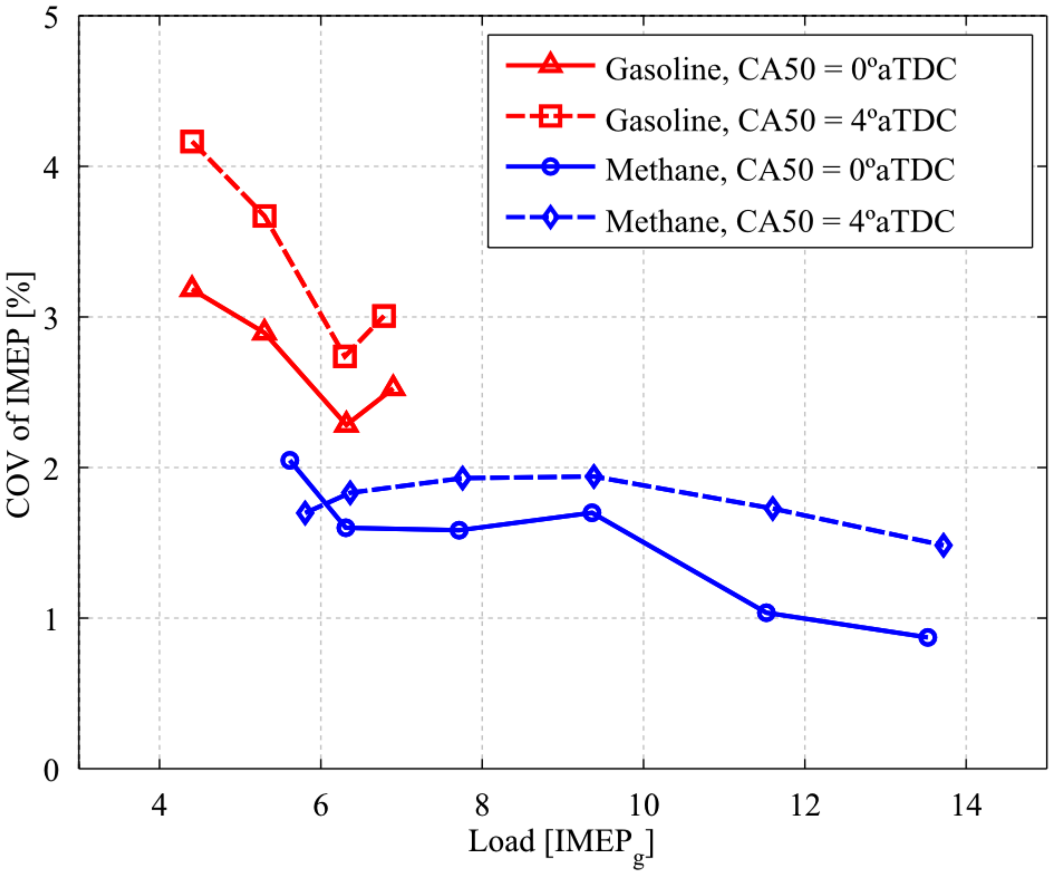

Figure 5.9: COV of IMEP. Methane/diesel operation has lower COV of IMEP relative to gasoline/diesel operation.

4° aTDC. Overall, all of the experimental cases are relatively stable in terms of IMEP, with a COV of less than 5%.

In Figure 5.10, COV of PPRR is presented. In general, methane/diesel RCCI operation has a lower COV of PPRR compared to gasoline/diesel RCCI operation. However, as distinctly highlighted by gasoline/diesel RCCI operation, the characteristics of the apparent heat release rate are strongly related to the COV of PPRR. The two-stage heat release, shown by the 4.4 bar IMEP$_g$ case in Figure 5.5, results in a significantly lower COV of PPRR than the other single-stage heat releases. Similarly to COV of IMEP, it is also seen that for both fueling combinations utilizing an earlier combustion phasing of CA50 = 0° aTDC leads to reduced COV if PPRR relative to the later combustion phasing of CA50 = 4° aTDC.

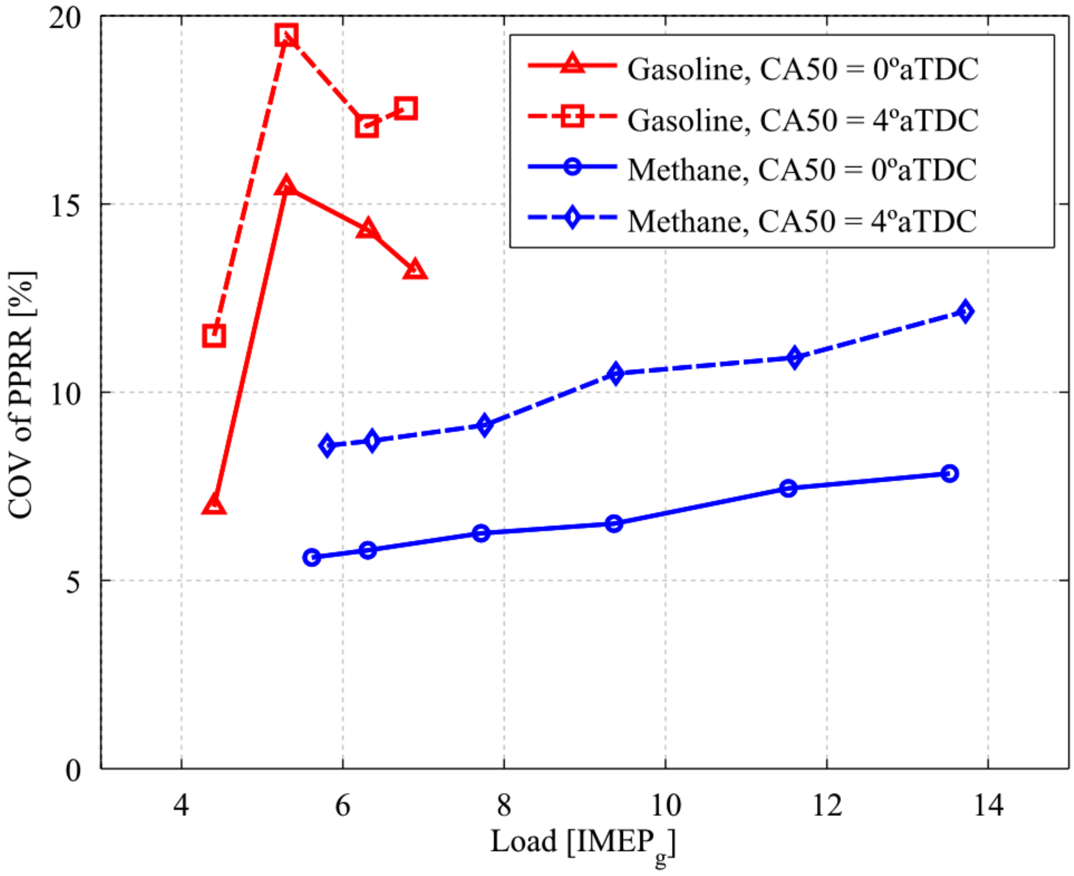

Figure 5.10: COV of PPRR. Methane/diesel operation has lower COV of PPRR relative to gasoline/diesel operation.

Figure 5.11 displays the peak cylinder pressure as a function of engine load, where it is shown that the peak cylinder pressure increases linearly with engine load. It is seen that gasoline/diesel RCCI operation has higher peak cylinder pressures at a fixed load relative to methane/diesel RCCI operation. It is also observed that at CA50 = 4° aTDC, the peak cylinder pressures are lower than at a combustion phasing of CA50 = 0° aTDC. This is due to the fact that at a combustion phasing of CA50 = 0° aTDC, the combustion process occurs in a more constant-volume system than at the later combustion phasing of CA50 = 4° aTDC, where combustion is still occurring when sensible expansion begins to occur, thus leading to lower peak cylinder pressures.

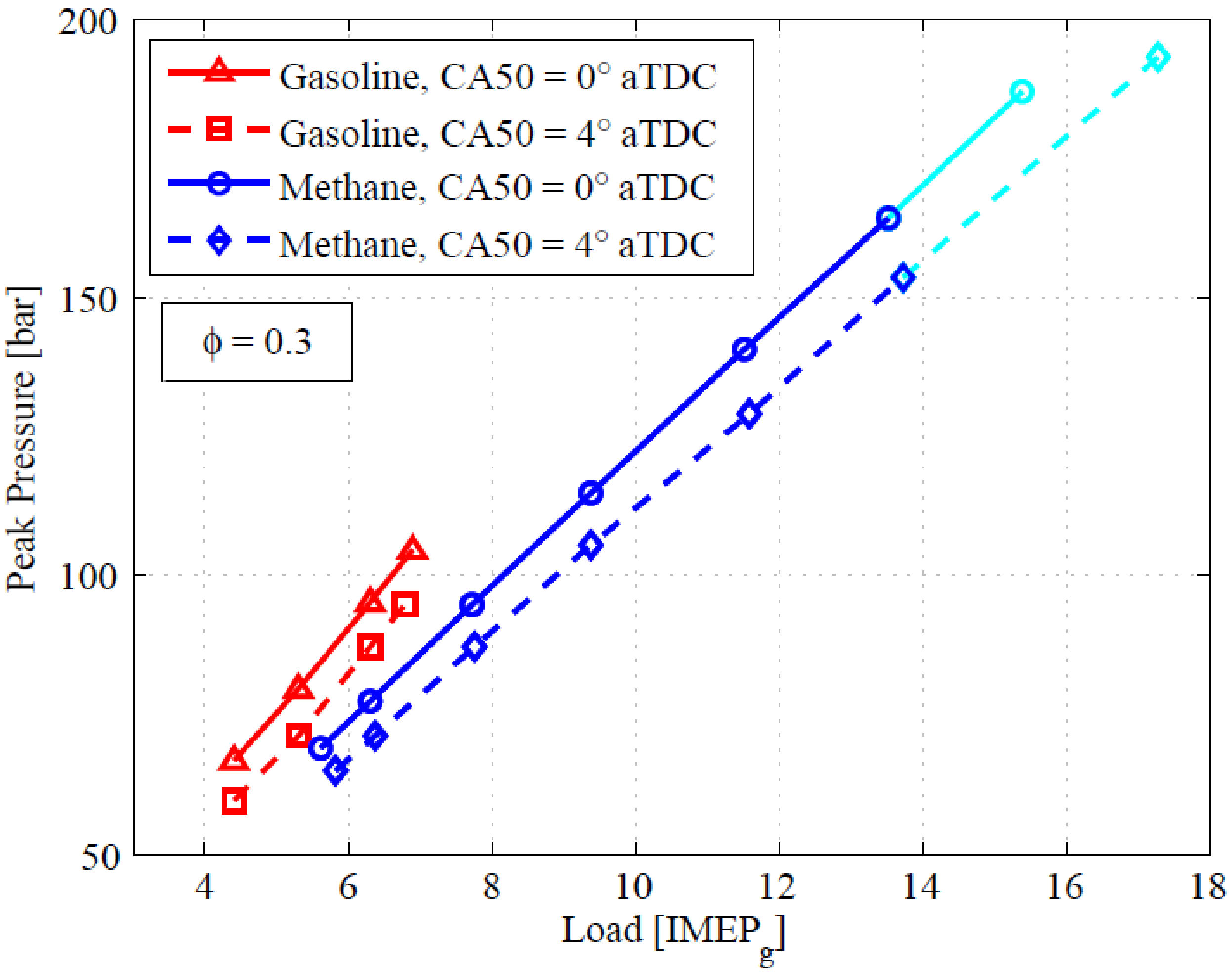

Figure 5.11: Peak cylinder pressure as a function of engine load. Both methane/diesel operation and delayed CA50 have lower peak cylinder pressure relative to gasoline/diesel operation and advanced CA50.

5.3.3 Analysis of Engine Load Capability

Figure 5.12 highlights the main focus of the present study: the load operating range while maintaining a peak pressure rise rate below 10 bar/deg. For gasoline/diesel RCCI operation, the highest load achievable without EGR was approximately 7 bar IMEP$_g$. For methane/diesel RCCI operation, the engine load limit was expanded to over 13 bar IMEP$_g$, limited in this case only by the maximum methane delivery of the gaseous port fuel injector used in these experiments. It is evident that methane/diesel RCCI operation allows for a significant load extension over gasoline/diesel RCCI operation. Also, by retarding the CA50

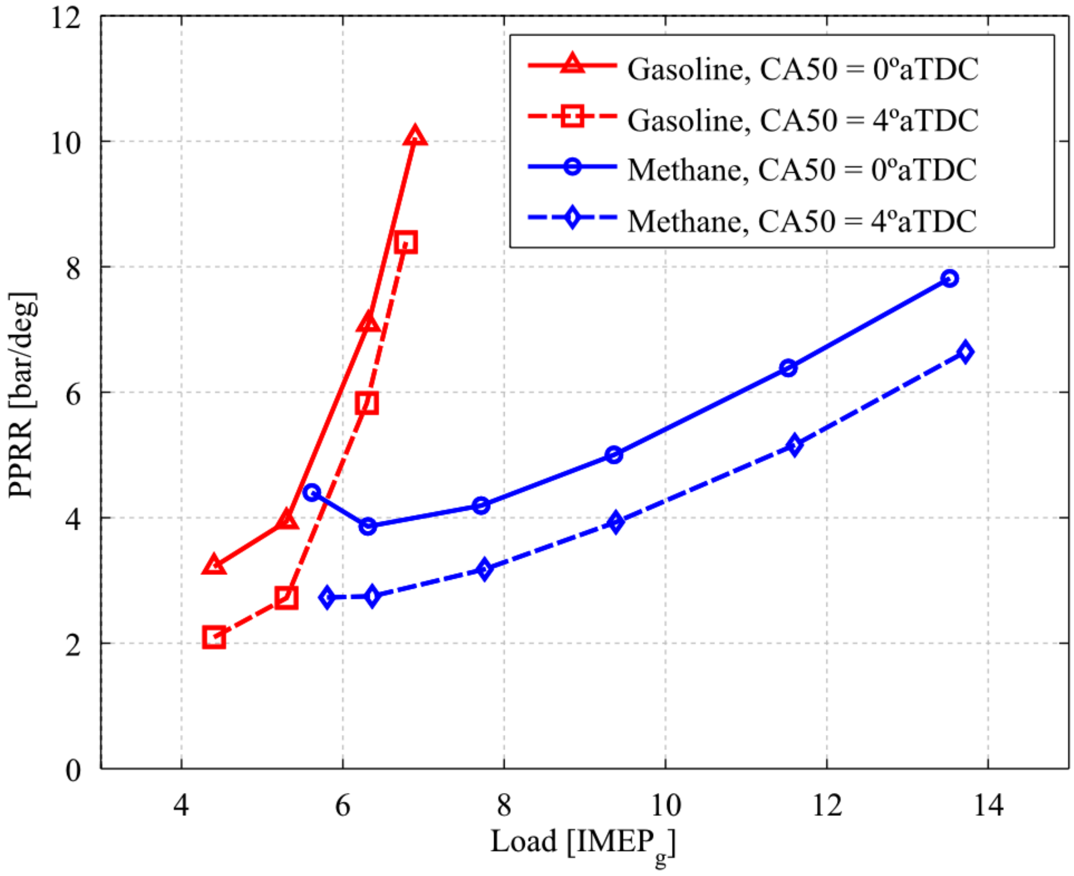

Figure 5.12: Peak pressure rise rate as a function of engine load. both methane/diesel operation and delayed CA50 have lower peak pressure rise rate relative to gasoline/diesel operation and advanced CA50.

combustion phasing from 0° aTDC to 4° aTDC, the combustion noise was reduced, thus expanding the upper load limit for a given less-reactive/more-reactive fuel combination.

Even though the present methane/diesel RCCI conditions did not reach the upper load limit, it is worth estimating the maximum achievable engine load, based on the experimental data, before reaching the 10 bar/deg peak pressure rise rate constraint. A second-order regression fit of the experimental data shown in Fig. 5.12 was used to establish a relationship between peak pressure rise rate and engine load. The coefficients (α_1,α_2,α_3) along with the coefficient of determination (R^2) determined from the regression analysis are given in Tab. 5.4 for each operating condition.

Table 5.4: Maximum load at PPRR = 10 bar/deg using the equation [PPRR = α_1*(LOAD)^2 + α_2*(LOAD) + α_3]

Engine Condition	α_1	α_2	α_3	R^2	**Load**
Gasoline, CA50 = 0°	1.22	-11.1	28.3	1.0	**6.9 bar**
Gasoline, CA50 = 4°	1.34	-12.3	30.5	0.99	**7.0 bar**
Methane, CA50 = 0°	.064	-0.74	6.26	0.98	**15.4 bar**
Methane, CA50 = 4°	.037	-0.22	2.70	0.99	**17.3 bar**

Table 5.4 shows the estimated maximum load achievable at a peak pressure rise rate of 10 bar/deg from the regression analysis. It is seen that gasoline/diesel RCCI operation reaches an engine load limit of approximately 7 bar $IMEP_g$. Retarding the CA50 combustion phasing to 4° aTDC allows for a slight increase in maximum engine load. However, for methane/diesel RCCI operation the upper load limits far surpass what could be reached experimentally. Also, retarding the combustion phasing allows for a significant increase in upper load limit. At a combustion phasing of CA50 = 0° aTDC, the upper load limit is 15.4 bar $IMEP_g$, while by retarding the combustion phasing to CA50 = 4° aTDC, the load can be extended considerably to 17.3 bar $IMEP_g$. However, as can be seen in the extrapolation of Figures 5.4 and 5.11, peak pressures approaching 200 bar and intake pressures of about 2.8 bar would be needed to reach this load. Thus, methane/diesel RCCI operation allows for demonstrable increases in the upper load limit compared to gasoline/diesel RCCI operation.

5.4 Conclusions

The focus of this study was to investigate the use of methane (as a natural gas surrogate fuel) as the less-reactive fuel for RCCI operation and to develop an understanding of the impact on load range and characteristics of the combustion process. Gasoline/diesel RCCI and methane/diesel RCCI experiments were performed to establish load operating ranges without the use of EGR at two different combustion phasings: CA50 = 0° aTDC and CA50 = 4° aTDC.

It was observed (see Figures 5.5-5.8) that there are distinct differences in the combustion characteristics between gasoline/diesel RCCI combustion and methane/diesel RCCI combustion. For gasoline/diesel operation, the CA10-90 combustion duration *shortened* as the engine load was increased. Conversely, for methane/diesel operation the CA10-90 combustion duration *lengthened* as the engine load was increased. On average, for gasoline/diesel RCCI combustion the CA10-90 combustion duration was 15 CAD, while for methane/diesel RCCI the CA10-90 combustion phasing was 25 CAD. In addition, (as shown in Figure 5.3) when the load was increased for gasoline/diesel operation, the start of high temperature heat release became *less* sensitive to DI SOI timing to control combustion phasing, while for methane/diesel operation the opposite was observed with respect to combustion phasing control: as the engine load was increased the start of high temperature heat release became *more* sensitive to DI SOI timing.

Upon examining two metrics of combustion stability, COV of IMEP and COV of PPRR, it was shown that methane/diesel RCCI combustion is significantly more stable than gasoline/diesel RCCI combustion. In addition, by moving to an earlier combustion phasing, both the COV of IMEP and COV of PPRR could be reduced. Furthermore, the characteristics of the heat release rates (i.e., two-stage heat release vs. single-stage heat-release) were seen to be related to combustion stability. Overall, load stability as determined by COV of IMEP was found to be very consistent, at less than 5%, for both fueling combinations.

By imposing a combustion noise constraint of 10 bar/deg peak pressure rise rate, an upper load limit could be estimated based on the experimental data. For gasoline/diesel RCCI operation, the upper load limit was found to be approximately 7 bar IMEP_g. For methane/diesel RCCI operation, the engine load was extended to 15.4 bar IMEP_g at a combustion phasing of CA50 = 0° aTDC. By retarding the combustion phasing to CA50 = 4° aTDC, the maximum load was estimated to be extended considerably to 17.3 bar IMEP_g. Thus, methane/diesel RCCI operation allows for significant engine load extension over gasoline/diesel RCCI combustion.

6 COMPARISON OF DIESEL PILOT IGNITION (DPI) AND REACTIVITY CONTROLLED COMPRESSION IGNITION (RCCI) IN A HEAVY-DUTY ENGINE

This chapter[6] reports on the comparison of two dual-fuel combustion strategies, reactivity controlled compression ignition (RCCI) and diesel pilot ignition (DPI), which are capable of utilizing natural gas in heavy-duty engines. The objective of the study was to examine the use of methane (as a natural gas surrogate fuel) as the less-reactive fuel for RCCI and DPI and to develop an improved understanding of the impact of each dual-fuel combustion regime on engine noise, emissions, and efficiency.

6.1 Experimental Setup

The following engine experiments were performed in the Caterpillar SCOTE Laboratory as outlined in Chapter 3, with the injector specifications given in Table 6.2.

Table 6.1: 3401 Caterpillar SCOTE heavy-duty engine specifications.

Displacement	2.44 L
Bore x Stroke	137.2 mm x 165.1 mm
Connecting Rod Length	261.6 mm
Number of Valves	4
Intake Valve Opening/Closing	335/-143° aTDC
Exhaust Valve Opening/Closing	130/-355° aTDC
Swirl Ratio	0.7
Piston Type	Articulated
Piston Profile	Bathtub
Compression Ratio	14.9:1

---

[6] Chapter 6 was formally published at the following Reference [113]: Walker, N. R. *et al.*, 2015, http://dx.doi.org/10.1115/ICEF2015-1128.

Table 6.2: Common rail injector specifications.

Injector Series	Bosch CRI2.2
Number of Holes	7
Hole Diameter	141 μm
Included Spray Angle	148°

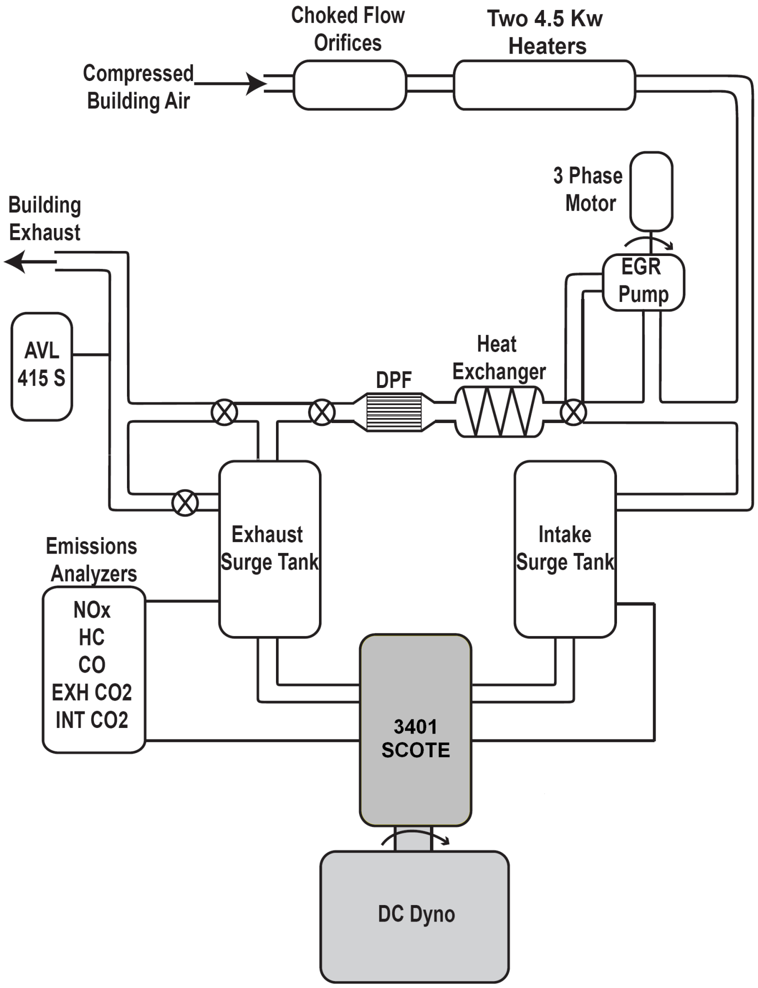

Figure 6.1: SCOTE Laboratory configuration for the Chapter 6 experiments.

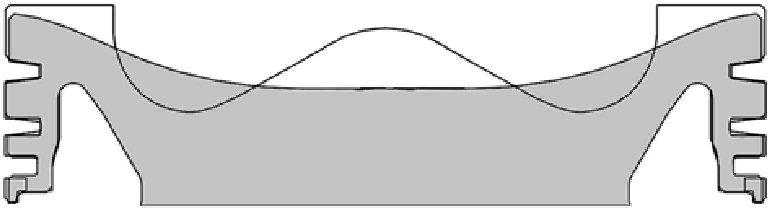

Figure 6.2: The modified RCCI piston (gray, CR = 14.9) profile used in the Chapter 6 experiments.

6.2 Results and Discussion

6.2.1 Combustion Regime Change from DPI to RCCI with Injection Timing

In order to examine the effects of fuel mixing and mixture preparation on the dual-fuel combustion process, a start of injection (SOI) timing sweep was performed. This allowed for the transition between the DPI (late-injection) and RCCI (early-injection) combustion regimes at a fixed engine operating condition. At an equivalence ratio of $\phi = 0.72$ and a fuel mass split of 85% methane and 15% F76, a nominal 6 bar IMEP engine load was established at a fixed fuel energy rate of 3500 J/cycle at all points without use of EGR. A single injection strategy was used, and the SOI timing was varied from -14.1° aTDC (DPI combustion) to -38.1° aTDC (RCCI combustion) in increments of 6° CA. The DPI and RCCI SOI timings were selected to fix the combustion phasing at 6° aTDC. Table 6.3 shows the experimental engine operating conditions for the work in Section 6.2.1.

Table 6.3: Section 6.2.1 engine operating conditions.

Engine Speed	1300 rev/min
IMEP$_g$	6 bar nominal
Fuel Energy	3500 J/cycle
Methane Energy %	85%
F76 Energy %	15%
Equivalence Ratio ϕ	0.72
Intake Temperature	40 °C
Intake Pressure	0.75 bar
SOI Timing	-14.1° to -38.1° aTDC
DI Injection Pressure	1000 bar
DI Fuel	F76
PFI Fuel	Methane
EGR Rate	0%

Figure 6.3 shows the combustion performance metrics (CA50, PPRR, SPL, IMEP$_g$, and COV$_{IMEP}$) as a function of SOI timing. The vertical lines in each data marker represent the range of one standard deviation of each metric derived from the experimental data.

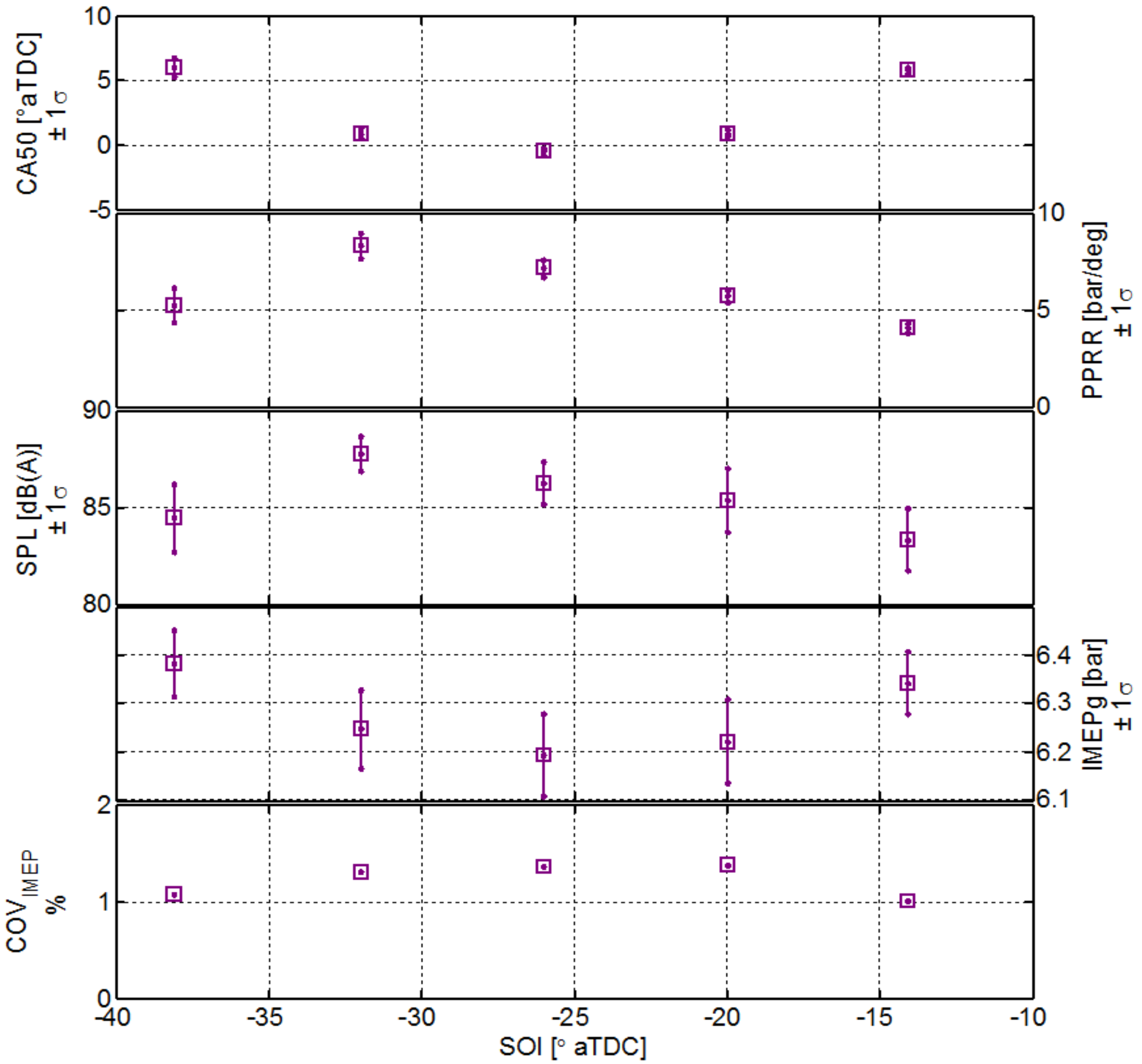

Figure 6.3: Pressure performance measurements for the SOI sweep. The vertical lines in each marker represent the range of one standard deviation.

The transition between the DPI and RCCI combustion regimes is most easily identified by the combustion phasing metric. With an SOI of -14.1° aTDC, DPI combustion has an initial CA50 of 6° aTDC. As the SOI timing is advanced the combustion phasing advances significantly, as shown in Figure 6.3. The intermediate combustion regime, at a SOI timing of -26.1° aTDC, has a CA50 of -0.5° aTDC. As the SOI is advanced further, the combustion process transitions into the RCCI combustion regime, at a SOI timing of -38.1° aTDC and the CA50 again retards. The transition between the DPI and RCCI combustion regimes is directly linked to the in-cylinder mixture preparation controlled by the direct-injection event. As the SOI timing advances, more time for mixing is allowed, which leans out the direct-injection of the F76 and mixing control becomes less influential. In addition, earlier SOI timings inject into in-cylinder conditions at lower temperatures and pressures, and coupled with lower local equivalence ratios from the direct-injection spray, allow for the extension of the ignition delay, eventually transitioning into the kinetically controlled RCCI combustion regime.

Two engine noise metrics, peak pressure rise rate (PPRR) and sound pressure level (SPL), also highlight the transition between the DPI and RCCI combustion regimes. Both PPRR and SPL are metrics commonly used throughout the engine industry. PPRR is used for structural integrity considerations of an engine, whereas SPL is used with regard to audible engine noise. (Further discussion on engine combustion noise metrics can be found in References [95, 116].) It is seen that both the PPRR and SPL increase with advancing SOI timing (corresponding with advancing combustion phasing), and are reduced during the transition into the RCCI combustion regime. Both RCCI and DPI offer comparable engine noise levels at this operating condition.

Figure 6.3 shows that the engine load is slightly diminished during the transition from DPI combustion into the intermediate regime, with the load being recovered fully for RCCI combustion. This observation is attributed to the significantly advanced combustion phasing depicted in Figure 6.5 where the bulk gas spends a longer time at high temperature, leading to increased heat transfer losses through the cylinder surfaces.

For all the experimental points in Section 6.2.1, during the transition from DPI to RCCI, the combustion is very stable, with the combustion stability, as measured by $\mathrm{COV}_{\mathrm{IMEP}}$, at less than 2%.

Figure 6.4 provides the emissions ($\mathrm{NO_x}$, HC, CO, PM) and efficiency (η_{gross}) measurements as a function of SOI timing. For both DPI and RCCI the gross indicated thermal

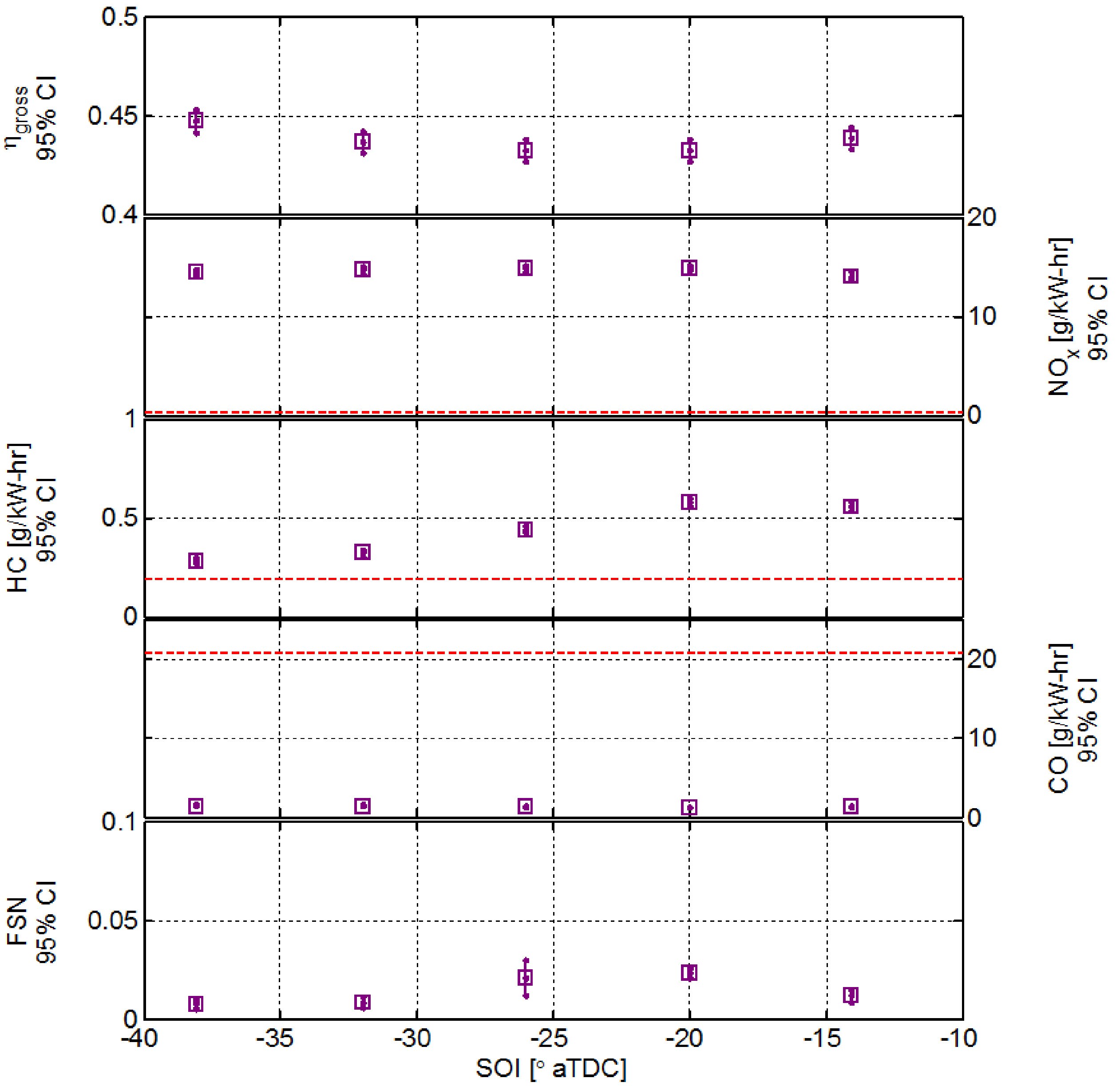

Figure 6.4: Emission and efficiency performance measurements for the SOI sweep. The vertical lines in each marker represent the range of the 95% confidence interval.

efficiency is in the range from 44-45%. The red dashed lines in Fig. 6.4 indicate the U.S. EPA 2010 Heavy-Duty emissions standards for reference. Across the range of SOI timings, the NO_x remains constant at approximately 14 g/kW-hr. The elevated NO_x emissions is related to the lack of EGR and the elevated in-cylinder temperatures resulting from the absence of port-injection spray vaporization cooling of the intake air-fuel mixture. Both CO and PM are below the EPA 2010 H.D. limit, and do not vary significantly with SOI. However, HC emissions are shown to be strongly influenced by the combustion regime: DPI combustion generates approximately 0.6 g/kW-hr of HC emissions while RCCI produces roughly half at 0.3 g/kW-hr. The driving factor behind the difference in HC emissions is not yet understood fully, however differences in the heat release mechanism in addition to the longer combustion duration for DPI combustion may contribute to the increase in HC emissions.

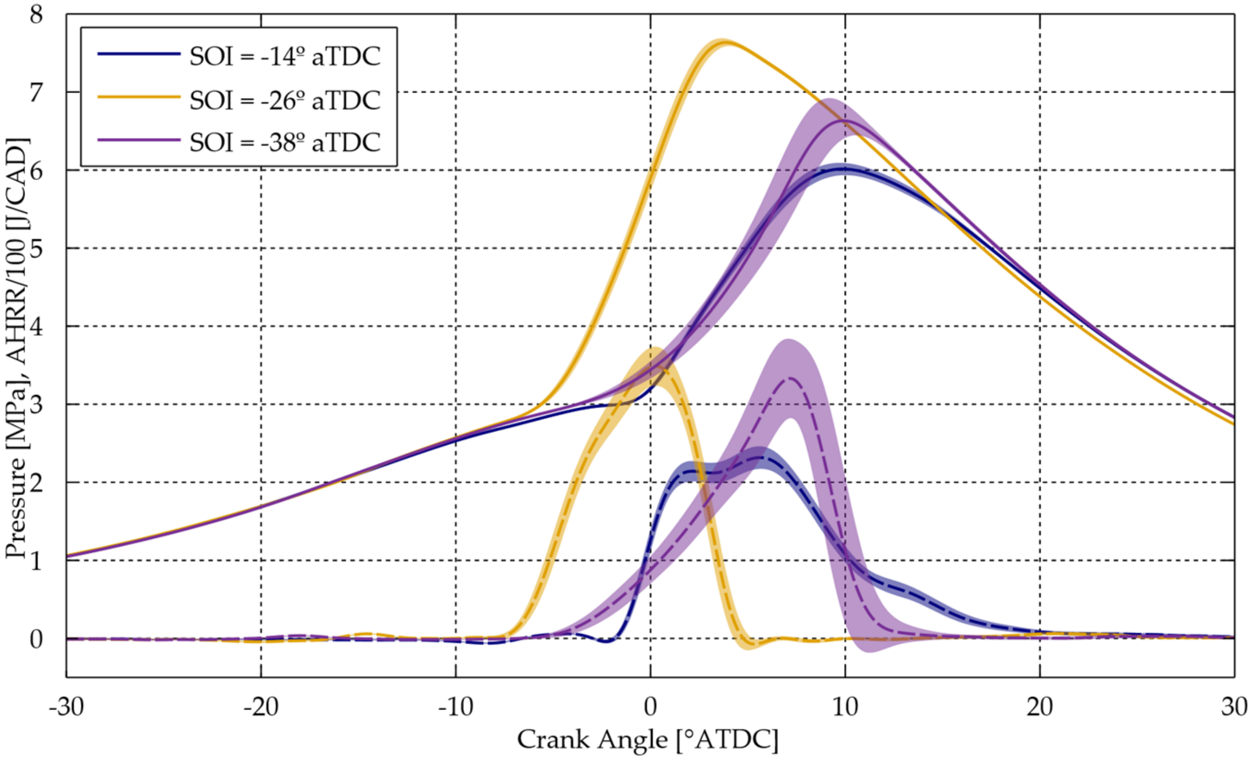

Figure 6.5: Cylinder pressure (solid lines) and heat release rate (dashed lines) for the SOI sweep. Lines represent the ensemble average value, while shaded regions represent one standard deviation.

As observed in Figure 6.3, it is seen in Figure 6.5 that the combustion phasing advances significantly as the combustion regimes moves from DPI into the intermediate regime. However, the heat release characteristics vary in nature between DPI and RCCI combustion. DPI combustion commonly exhibits two-stage heat release: the locally-rich direct-injection of F76 readily auto ignites (diffusion combustion), and then the premixed methane subsequently burns through what is generally thought to be a flame propagation mechanism, as detailed in Reference [96]. On the other hand, RCCI combustion commonly exhibits a single-stage heat release with a Gaussian-like heat release profile: the direct-injection of F76 mixes out lean enough to provide a reactivity (i.e., ignition delay) stratification throughout the cylinder resulting in a sequential autoignition process, as detailed in Reference [62]. (Further discussion on heat release characteristics of RCCI combustion can be found in Reference [112].) These contrasting heat release characteristics indicate a potential difference in the heat release mechanism(s) between DPI and RCCI combustion, that is being studied in further detail in the next chapters.

6.2.2 Effect of Equivalence Ratio on DPI and RCCI Combustion

In Section 6.2.1 it was observed that there are distinct differences between DPI and RCCI combustion, and that the transition between the two combustion regimes can be directly controlled via the SOI timing of the direct-injection. In addition, given the relatively rich engine operating condition used in Section 6.2.1, it was seen that both combustion strategies offered comparable noise, emissions, and efficiency characteristics. In Section 6.2.2, the effect of equivalence ratio on both DPI and RCCI combustion is examined. By modifying the intake air pressure (i.e., intake mass air flow rate), the equivalence ratio was varied between 0.72 and 0.5. For both combustion strategies, the SOI timing was adjusted to fix the combustion phasing at CA50 = 6° aTDC. Table 6.4 shows the experimental engine operating conditions for the work in this section.

Figure 6.6 shows the combustion performance metrics (CA50, PPRR, SPL, IMEP_g, and COV_{IMEP}) as a function of equivalence ratio. The vertical lines in each data marker represent the range of one standard deviation of each metric derived from the experimental data; the horizontal lines in each data marker represent the range of the 95% confidence interval for the calculated equivalence ratio.

Table 6.4: Section 6.2.2 engine operating conditions.

Engine Speed	1300 rev/min
IMEP$_g$	6 bar nominal
Fuel Energy	3500 J/cycle
Methane Energy %	85%
F76 Energy %	15%
Equivalence Ratio ϕ	0.5 to 0.72
Intake Temperature	40 °C
Intake Pressure	1.0 bar to 0.75 bar
SOI Timing	Vary to fix CA50 @ 6° aTDC
DI Injection Pressure	1000 bar
DI Fuel	F76
PFI Fuel	Methane
EGR Rate	0%

As observed in Section 6.2.1 that at the richest condition, $\phi = 0.72$, both DPI and RCCI offer comparable performance in terms of the pressure performance metrics, as shown in Figure 6.6. However, performance is seen to vary strongly with equivalence ratio for both combustion regimes. As the equivalence ratio moves leaner, for RCCI combustion both noise metrics (PPRR and SPL) monotonically decrease; however for DPI combustion, both noise metrics increase monotonically as the air-fuel charge becomes leaner. Similar behavior is observed in terms of engine load (IMEP$_g$) for both combustion strategies: for RCCI the load increases to above 7 bar IMEP$_g$ as the equivalence ratio decreases, and for DPI the load decreases to below 6 bar IMEP$_g$ as the equivalence ratio decreases. The primary factor governing this observation, as displayed in Figure 6.7, is a marked increase in HC emissions for DPI combustion at leaner equivalence ratios, resulting in valuable unconverted fuel energy in the exhaust stream. Across the range of equivalence ratios, combustion is stable (below 3% COV$_{IMEP}$) but for both combustion regimes the COV$_{IMEP}$ monotonically increases as the equivalence ratio decreases.

Figure 6.7 provides the emissions (NO$_x$, HC, CO, PM) and efficiency (η_{gross}) measurements as a function of equivalence ratio. Again, the red dashed lines in Figure 6.7 indicate the U.S. EPA 2010 Heavy-Duty emissions standards for reference. As observed in

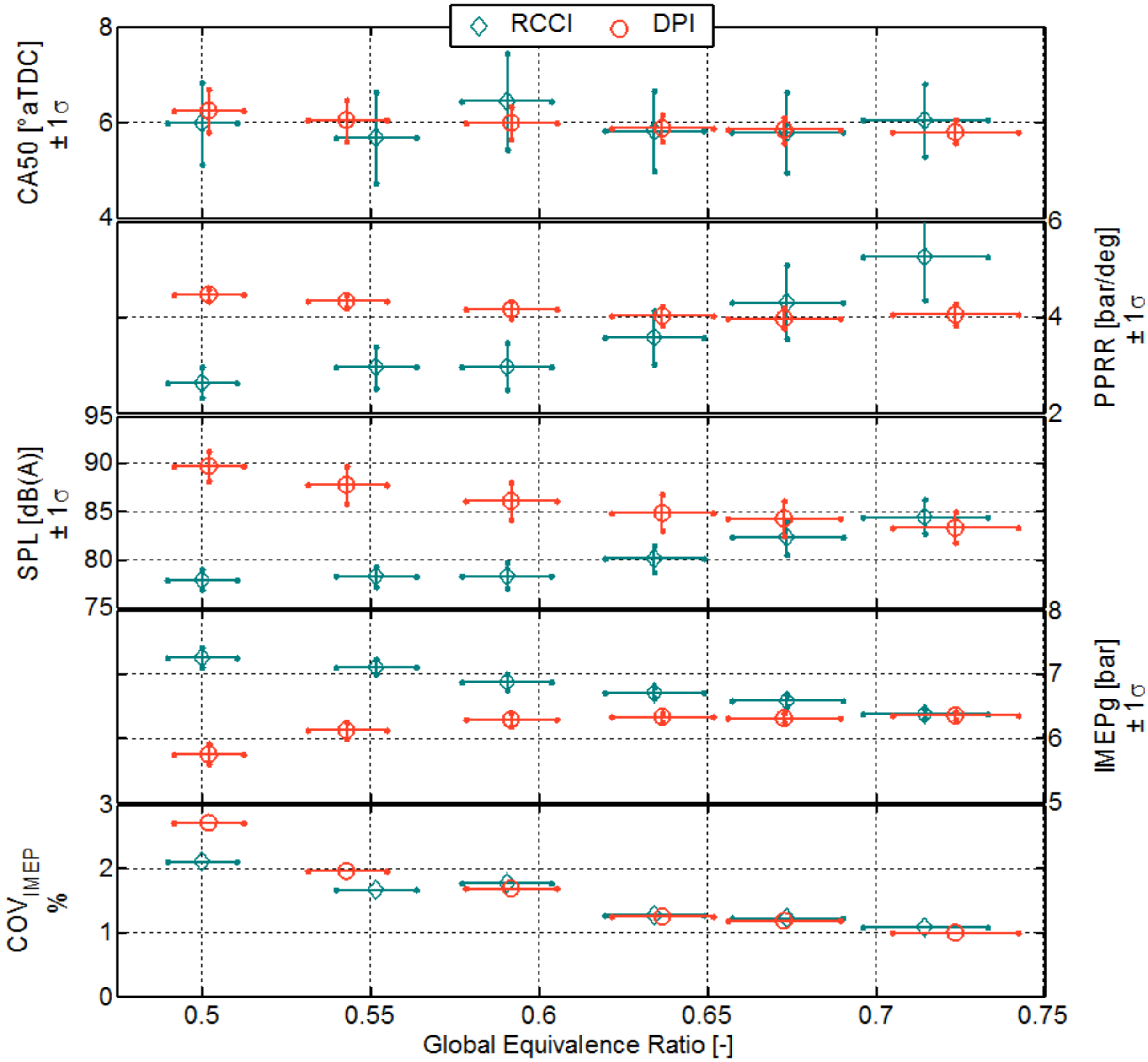

Figure 6.6: Pressure performance measurements for the equivalence ratio sweep. The vertical lines in each marker represent the range of one standard deviation.

Figure 6.6, both DPI and RCCI perform similarly in terms of emissions and efficiency at the highest equivalence ratio. Again, performance is observed to be strongly affected by the equivalence ratio for both combustion regimes. For both DPI and RCCI combustion, NO_x emissions decrease as the equivalence ratio decreases. With respect to HC emissions, RCCI produces low HC emissions across the range of equivalence ratios. However for DPI combustion, HC emissions significantly increase as the equivalence ratio decreases.

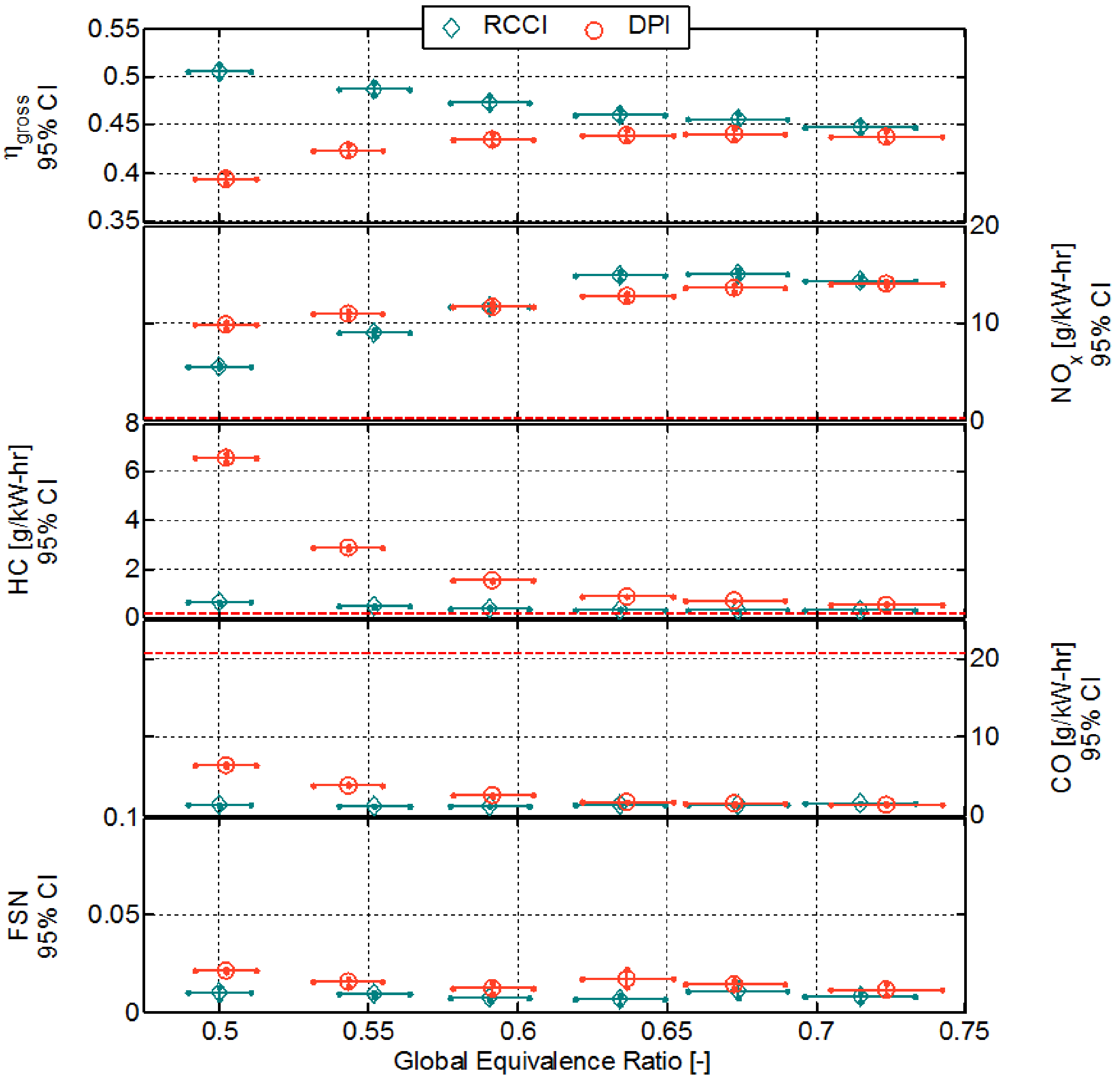

Figure 6.7: Emission and efficiency performance measurements for the equivalence ratio sweep. The vertical lines in each marker represent the range of the 95% confidence interval.

This observation regarding HC emissions leads to the suggestion that the heat release mechanism(s) for DPI combustion are more strongly influenced by equivalence ratio than for RCCI combustion (suggesting different heat release mechanism(s) for each combustion regime), and this aspect is studied further in the next chapters. CO emissions remain low for both combustion strategies, but it is observed that for DPI combustion the CO emissions roughly double from the richest condition to the leanest condition. Finally, PM emissions remain near-zero for both combustion regimes across the range of equivalence ratios.

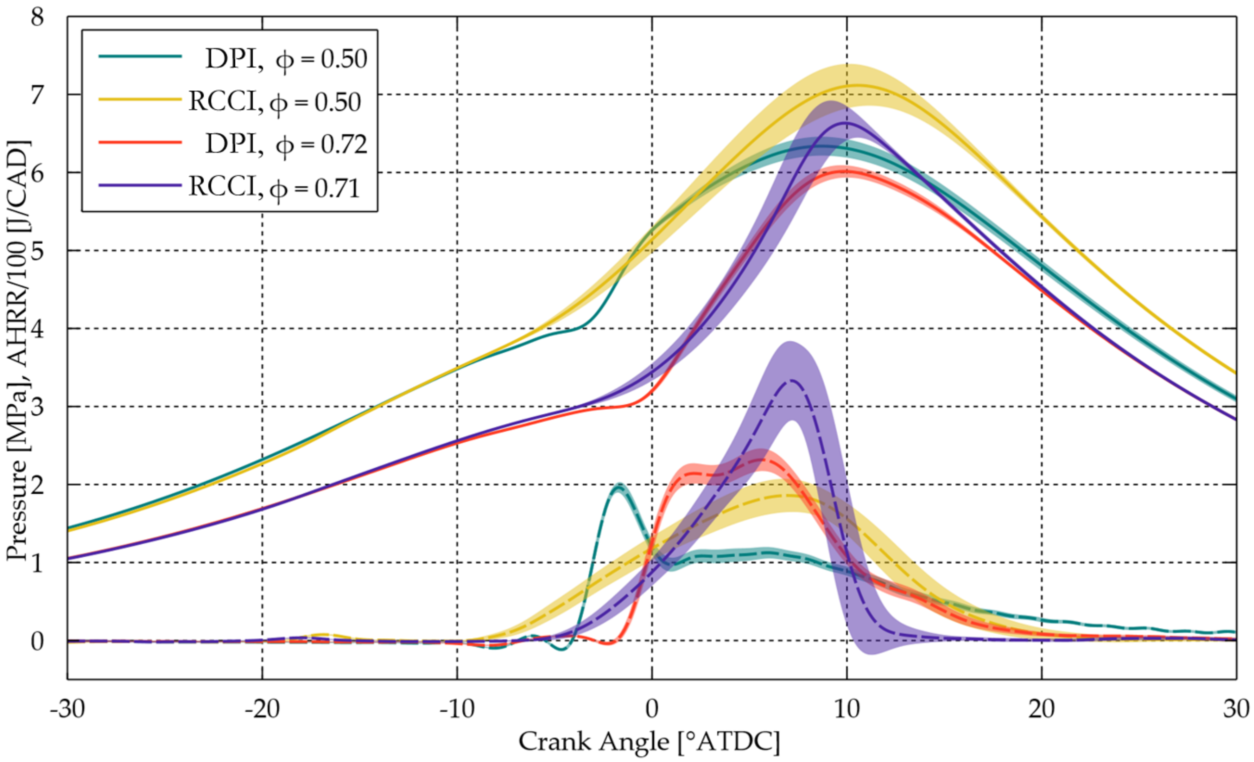

Figure 6.8: Cylinder pressure (solid lines) and heat release rate (dashed lines) for the equivalence ratio sweep. Lines represent the ensemble average value, while shaded regions represent one standard deviation.

In Figure 6.8, pressure and heat release data are shown for both the DPI and RCCI combustion regimes at the richest and leanest conditions presented in Section 6.2.2. For both combustion strategies, it is seen that the equivalence ratio has a strong effect on the heat release characteristics during the combustion process. For RCCI combustion, as the air-fuel charge moves leaner, the Gaussian-like heat release profile lengthens in duration while the peak heat release rate is reduced. However, the increased cylinder charge mass still results in a higher peak cylinder pressure at the lowest equivalence ratio. For DPI combustion, the two-stage heat release becomes more apparent at the leanest air-fuel mixture. Similar to RCCI combustion, at the lowest equivalence ratio, the heat release mechanism(s) slows considerably, resulting in an extended combustion duration coupled with a reduced peak heat release rate. Again, the increased cylinder charge mass still results in a higher peak cylinder pressure at the lowest equivalence ratio.

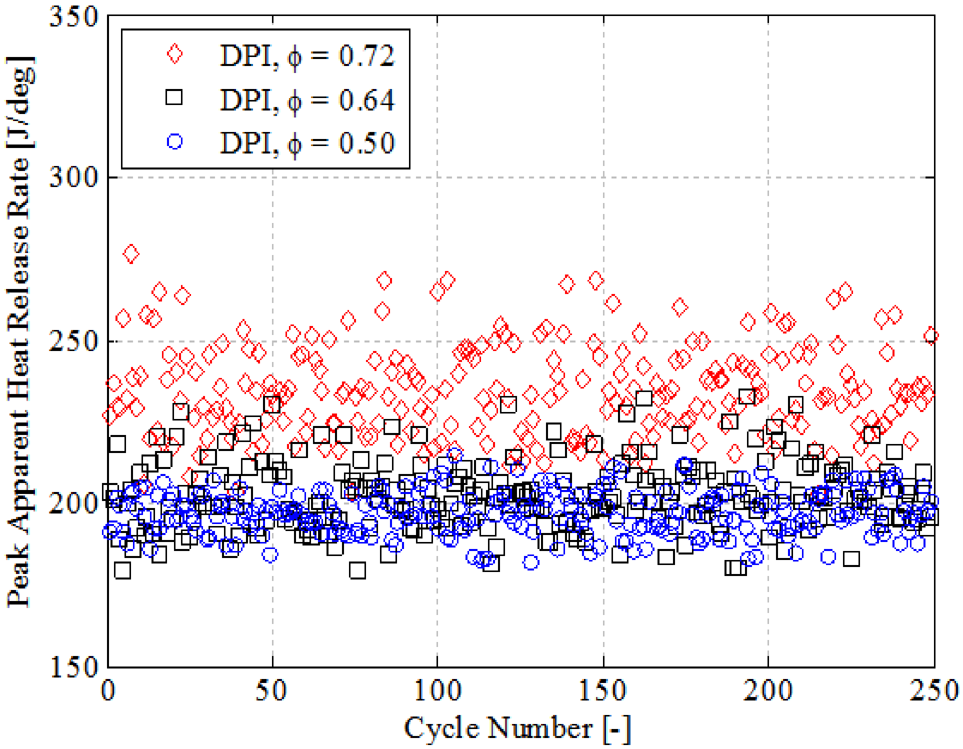

Figure 6.9: Measured cyclic dispersion of peak apparrent heat release rate for DPI combustion. Red diamonds denote ϕ=0.72, black squares denote ϕ=0.64, and blue circles denote ϕ=0.50.

While it is shown in Figure 6.6 that the combustion stability, in terms of COV_{IMEP}, is very stable for both combustion strategies across the range of equivalence ratios, it is of interest to examine the measured cyclic dispersion of two combustion characteristics: peak apparent heat release rate (PAHRR) and engine load ($IMEP_g$). Figures 6.9-6.12 plot the cyclic dispersion for both the DPI and RCCI combustion regimes in terms of both PAHRR and $IMEP_g$ at the highest and lowest equivalence ratios studied in Section 6.2.2. (It should be noted that due to data acquisition limitations, the measured cycle data is not consecutive in nature, and thus no cycle-to-cycle inter-relationship inferences can be drawn from the data presented in Figures 6.9-6.12. Please refer to Reference [34] for further analysis of cycle-to-cycle inter-relationships.) In Figures 6.9-6.12, the red diamond markers represent the richest condition at an equivalence ratio of approximately ϕ=0.7, the black square markers represent the intermediate condition at an equivalence ratio of approximately ϕ=0.6, and the blue circle markers represent the leanest condition at an equivalence ratio of approximately ϕ=0.5.

In Figure 6.9 it is observed that the average PAHRR for the DPI combustion regime is centered around 200-250 J/deg across the range of equivalence ratios. Relative to RCCI (Figure 6.10), the cyclic dispersion of PAHRR only increases in a relatively negligible manner as the equivalence ratio is increased.

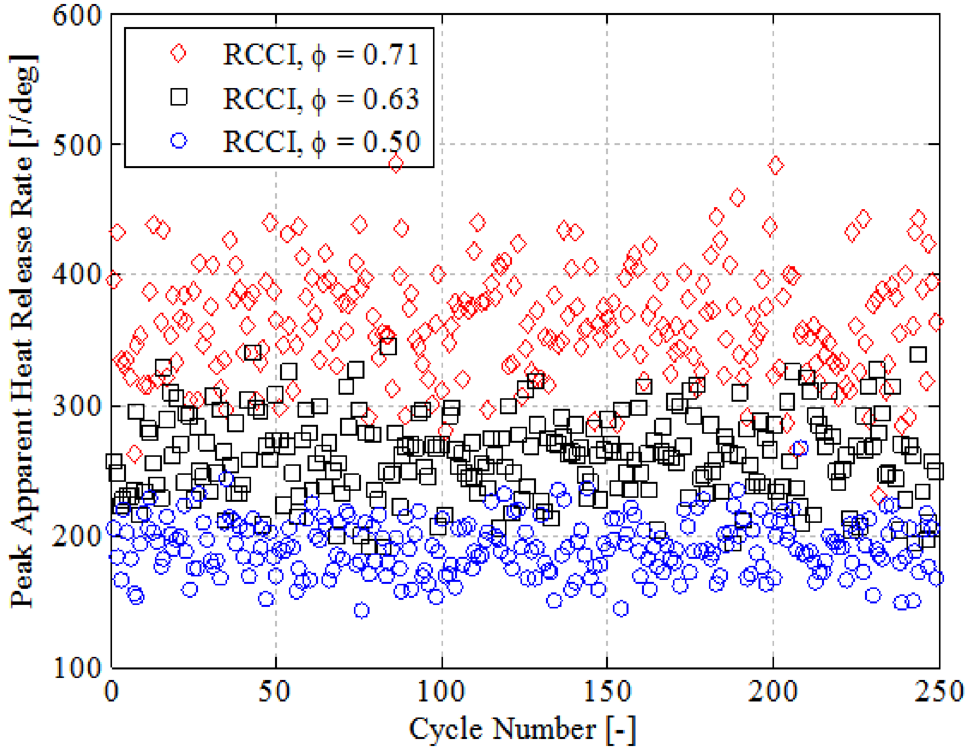

Figure 6.10: Measured cyclic dispersion of peak apparrent heat release rate for RCCI combustion. Red diamonds denote ϕ=0.71, black squares denote ϕ=0.64, and blue circles denote ϕ=0.50.

For RCCI combustion, in Figure 6.10 it is seen that the average PAHRR is centered around 200 J/deg at ϕ=0.50, 250 J/deg at ϕ=0.63, and 350 J/deg at ϕ=0.71. Unlike DPI combustion, the cyclic dispersion of PAHRR significantly increases with increasing equivalence ratio.

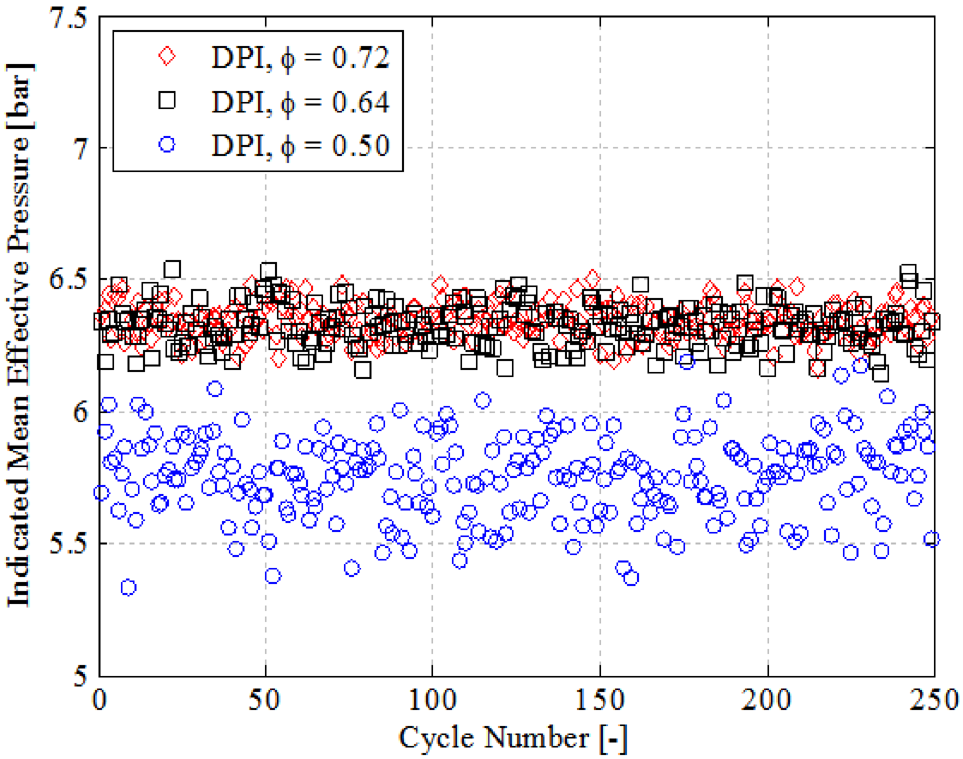

Figure 6.11: Measured cyclic dispersion of indicated mean effective pressure for DPI combustion. Red diamonds denote ϕ=0.72, black squares denote ϕ=0.64, and blue circles denote ϕ=0.50.

In Figure 6.11 it is observed that the average IMEP_g for the rich and intermediate DPI conditions are centered around 6.4 bar. At the leanest condition, the average IMEP_g is centered around 5.8 bar. Relative to RCCI (Figure 6.12), the cyclic dispersion of IMEP_g is similar in magnitude as the equivalence ratio is increased.

For RCCI combustion, in Figure 6.12, as with the average PAHRR, the average IMEP_g is sensitive to equivalence ratio. It is observed that the average IMEP_g is centered around 7.3 bar at ϕ=0.50, 6.7 bar at ϕ=0.63, and 6.4 bar at ϕ=0.71. Unlike the PAHRR trend in Figure 6.10, the cyclic dispersion of IMEP_g increases as the equivalence ratio decreases, however in a negligible manner as the COV_{IMEP} is still below 3%.

Overall, for RCCI combustion there is a marked increase in cyclic dispersion of PAHRR as the equivalence ratio is increased. The inverse trend is observed in terms of engine load as the cyclic dispersion of IMEP_g slightly decreases as the equivalence ratio is increased.

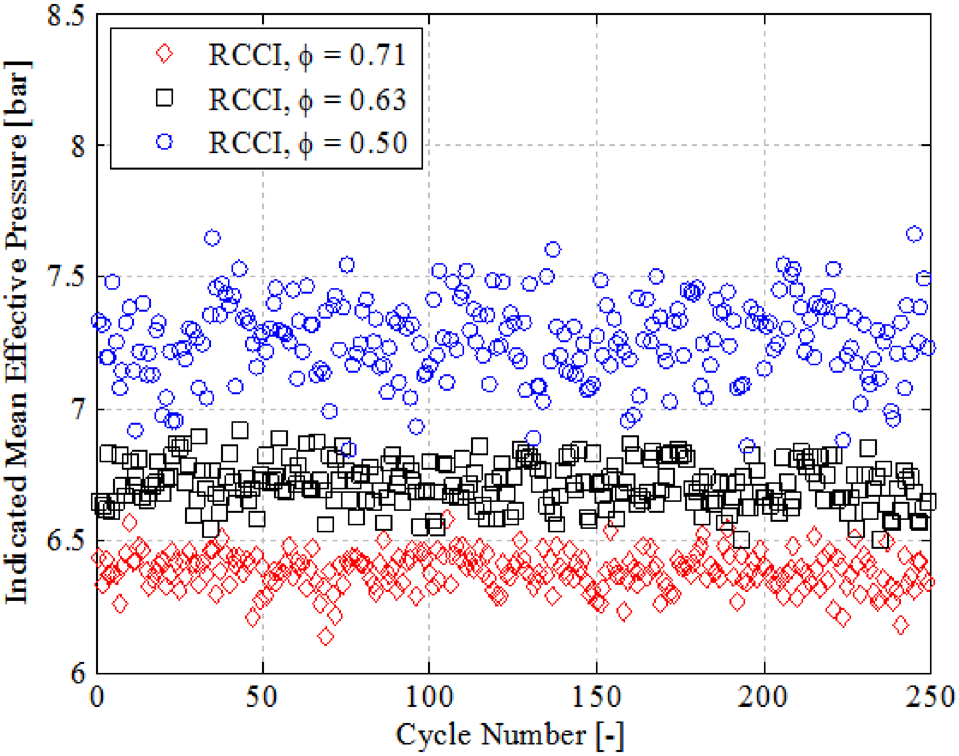

Figure 6.12: Measured cyclic dispersion of indicated mean effective pressure for RCCI combustion. Red diamonds denote ϕ=0.71, black squares denote ϕ=0.64, and blue circles denote ϕ=0.50.

For the DPI combustion regime, the opposite behavior is seen with respect to the PAHRR: a slight increase in the cyclic dispersion of PAHRR as the equivalence ratio is increased is observed. However for the DPI combustion regime, in terms of the engine load, the cyclic dispersion of IMEP_g slightly decreases as the equivalence ratio is increased, similar to the RCCI combustion regime. Additional information regarding cyclic variability in partially-premixed dual-fuel natural gas combustion is detailed by Srinivasan *et al.* [103].

6.2.3 DPI and RCCI Response to Fueling Rate Increase

In this section, the effect of increased fueling rate (i.e., engine load) is studied for the DPI and RCCI combustion regimes. Three fueling rates are selected: 4000 J/cycle, 5000 J/cycle, and 6000 J/cycle, at a methane energy fraction of 90%, 94%, and 95%, respectively. The equivalence ratio is fixed at ϕ=0.52, and the nominal engine load ranges from 6 bar to 11 bar IMEP_g, and as before, no EGR is employed. Table 6.5 shows the experimental engine operating conditions for the work in Section 6.2.3.

Table 6.5: Section 6.2.3 engine operating conditions.

Engine Speed	1300 rev/min
IMEP_g	6 bar to 11 bar
Fuel Energy	4000, 5000, 6000 J/cycle
Methane Energy %	90%, 94%, 95%
F76 Energy %	10%, 6%, 5%
Equivalence Ratio ϕ	0.52
Intake Temperature	40 °C
Intake Pressure	1.0 bar, 1.4 bar, 1.7 bar
SOI Timing	DPI/RCCI: -14°/-38° aTDC
DI Injection Pressure	DPI/RCCI: 1000/500 bar
DI Fuel	F76
PFI Fuel	Methane
EGR Rate	0%

Figure 6.13 shows the combustion performance metrics (CA50, PPRR, SPL, IMEP_g, and COV_{IMEP}) as a function of equivalence ratio. The vertical lines in each data marker represent the range of one standard deviation of each metric derived from the experimental data; the horizontal lines in each data marker represent the range of the 95% confidence interval for the calculated equivalence ratio.

Unlike the strong influence of equivalence ratio on combustion performance observed in Section 6.2.2, an increased fueling rate has relatively little effect for both DPI and RCCI combustion. In Figure 6.13 is it seen CA50 retards slightly, due to the increase in combustion duration for both combustion strategies. Both PPRR and SPL remain steady across the range of fueling rates; however the combustion noise is significantly reduced for RCCI combustion relative to DPI combustion. For both combustion regimes, the COV_{IMEP} increases slightly with fueling rate, and RCCI combustion is more stable at approximately 2% lower COV_{IMEP} (in absolute terms) than DPI combustion.

Figure 6.14 provides the emissions (NO_x, HC, CO, PM) and efficiency (η_{gross}) measurements as a function of equivalence ratio. The red dashed lines in Figure 6.14 indicate the U.S.

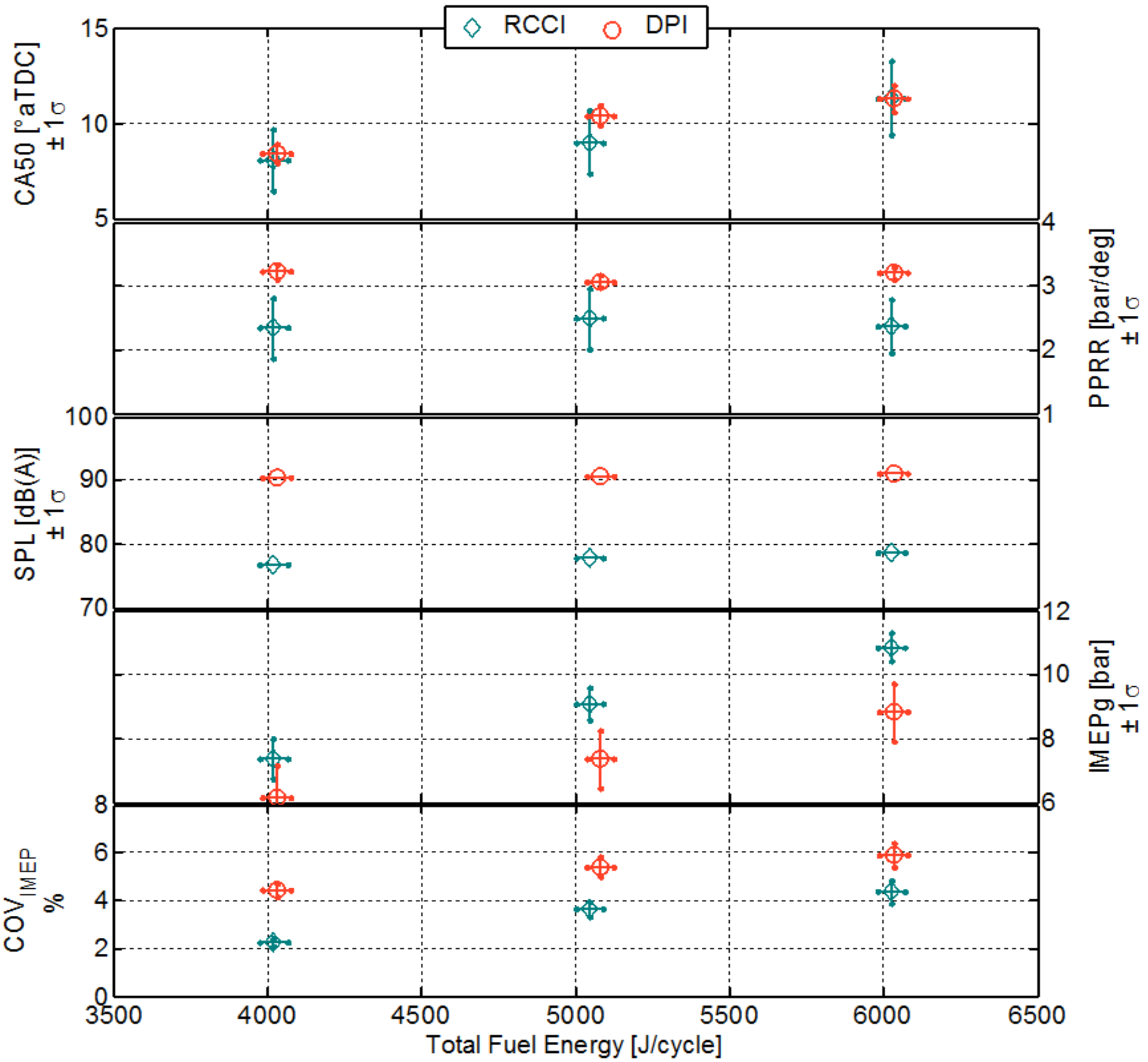

Figure 6.13: Pressure performance measurements for the fueling rate sweep. The vertical lines in each marker represent the range of one standard deviation.

EPA 2010 Heavy-Duty emissions standards for reference. Unlike in Section 6.2.1 (ϕ=0.72), at the leaner equivalence ratio of ϕ=0.52 the emissions and efficiency of the RCCI combustion regime outperforms the DPI combustion regime at all fueling rates. On the other hand, it is seen in Figure 6.14 that the emission and efficiency performance of both combustion strategies are largely uninfluenced by the fueling rate. NO_x emissions are slightly reduced for both combustion regimes, with RCCI combustion producing significantly less NO_x

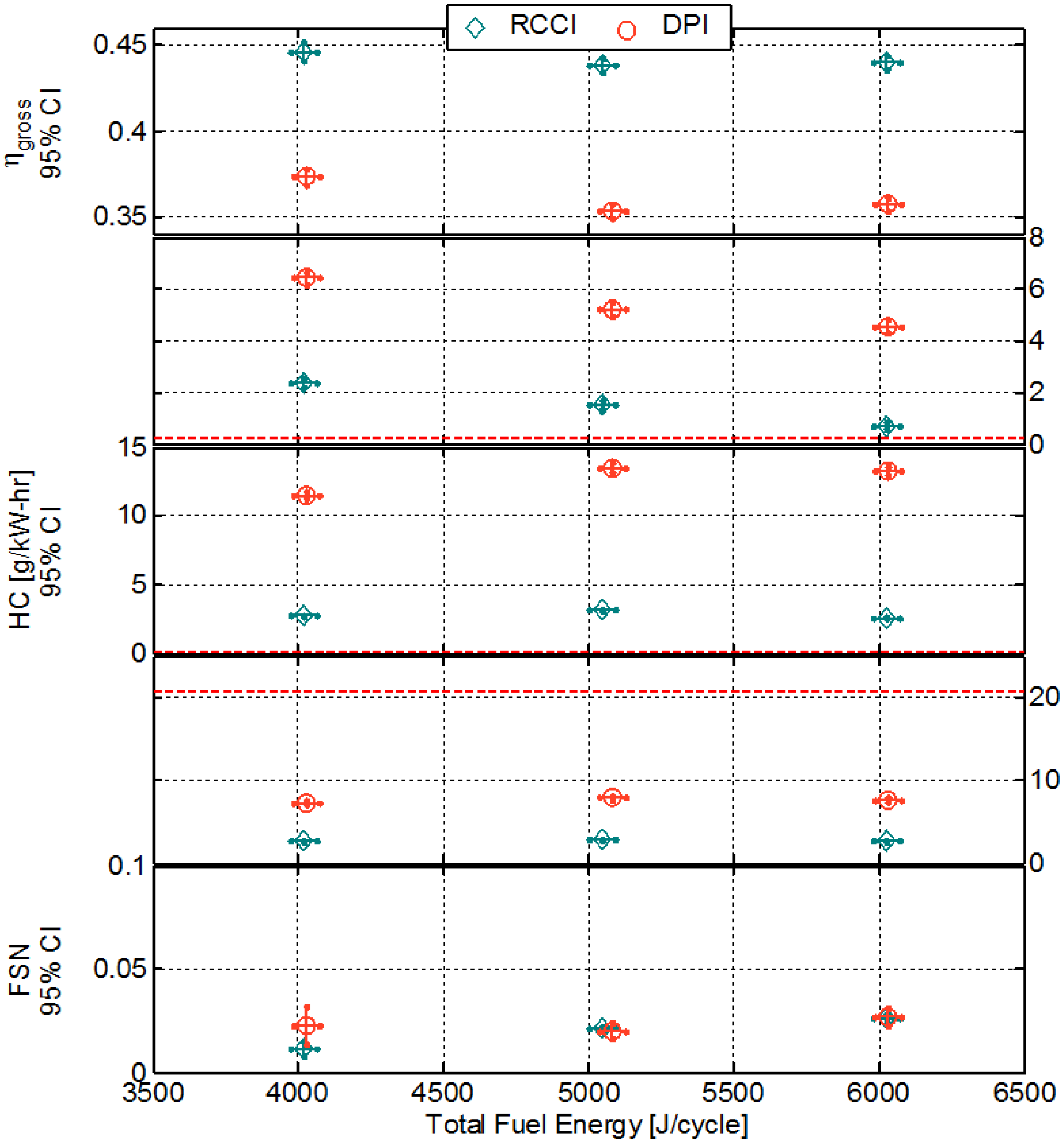

Figure 6.14: Emission and efficiency performance measurements for the fueling rate sweep. The vertical lines in each marker represent the range of the 95% confidence interval.

than DPI combustion. Both HC and CO levels are reduced for RCCI combustion relative to DPI combustion, and both species remain steady across the range of fueling rates for both combustion regimes. PM is near-zero for both RCCI and DPI combustion.

As observed in Figure 6.14, the gross indicated thermal efficiency is in the range of 44-45% for RCCI combustion and 35-37% for DPI combustion. Figure 6.15 shows the energy

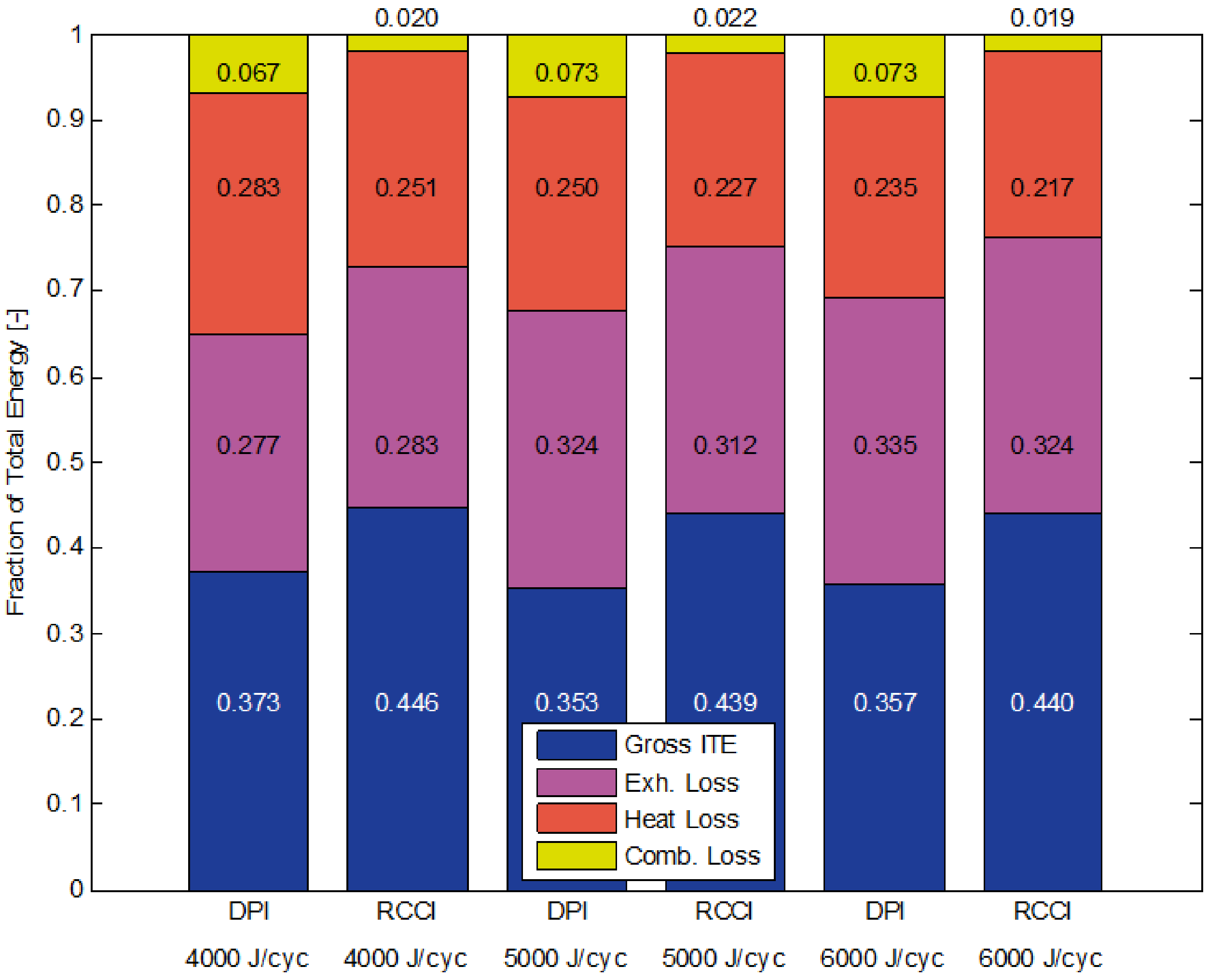

Figure 6.15: Energy balances for the fueling rate sweep.

fractionalization for both combustion regimes at each fueling rate. It is seen that RCCI combustion has approximately an 8% absolute increase in thermal efficiency over DPI combustion. The rest of the energy distribution indicates that, on average across the range of fueling rates, the DPI combustion regime has a 5% absolute greater combustion loss, 3% absolute heat loss, and 1% absolute greater exhaust loss relative to the RCCI combustion regime. The observed differences in the energy fractionalization further suggest that each dual-fuel combustion regime may be controlled by different heat release mechanisms during the combustion process, and this the focus of the next chapters.

6.3 Conclusions

The objective of the current study is to examine the use of methane (as a natural gas surrogate fuel) as the less-reactive fuel for two advanced dual-fuel combustion strategies - diesel pilot ignition (DPI) and reactivity controlled compression ignition (RCCI) - and to develop an understanding of the impact of each dual-fuel combustion regime on engine noise, emissions, and efficiency.

In Section 6.2.1, the transition between the DPI and RCCI combustion regimes was studied via control of the SOI timing. At the relatively rich condition of ϕ=0.72 the performance (noise, emissions, and efficiency) characteristics of both combustion strategies was comparable. However, RCCI combustion generated approximately half of the HC emissions compared to DPI combustion. Furthermore, an examination of the heat release rates for the two combustion strategies indicated that there may be differences in the heat release mechanism(s) of each combustion strategy.

In Section 6.2.2, the effect of the equivalence ratio on each combustion regime was examined in detail. It was observed that at relatively rich conditions (ϕ=0.72) the combustion performance of each combustion regime was similar. However, as the conditions became leaner, the combustion performance improved for RCCI combustion and was degraded for DPI combustion. At the leanest condition (ϕ=0.50), RCCI has significantly higher thermal efficiency, markedly reduced combustion noise, and lower emissions. An analysis of the measured cyclic dispersion in terms of peak apparent heat release rate (PAHRR) and engine load (IMEP_g) revealed that for RCCI combustion there is a marked increase in cyclic dispersion of PAHRR as the equivalence ratio is increased. The inverse trend is observed in terms of engine load as the cyclic dispersion of IMEP_g slightly decreases as the equivalence ratio is increased. For the DPI combustion regime, the opposite behavior is seen with respect to the PAHRR: a slight increase in the cyclic dispersion of PAHRR as the equivalence ratio is increased is observed. However for the DPI combustion regime, in terms of the engine load, the cyclic dispersion of IMEP_g slightly decreases as the equivalence ratio is increased, similar to the RCCI combustion regime.

In Section 6.2.3, the effect of fueling rate was explored at a relatively lean operating condition (ϕ=0.52). It was seen that the fueling rate has little effect on the combustion performance as the engine load was increased. However, combustion noise, emissions, and efficiency was markedly improved with RCCI combustion relative to DPI combustion. RCCI combustion offered, on average, an 8% absolute increase in thermal efficiency over DPI combustion. Further analyis showed that, on average across the range of fueling rates, the DPI combustion regime has a 5% absolute greater combustion loss, 3% absolute heat loss, and 1% absolute greater exhaust loss relative to the RCCI combustion regime.

In all, the strong influence of the equivalence ratio on the combustion performance of the RCCI and DPI combustion strategies indicates that each regime relies upon different mechanisms of heat release during the combustion process. For RCCI combustion it has been determined that sequential autoignition is responsible for the bulk heat release; for DPI combustion it is accepted that flame propagation from the pilot ignition sites is the main mechanism for the bulk heat release. As a result, implications arise which suggest that both the DPI and RCCI combustion regimes can be utilized in engine applications where the air handling systems allow for relatively rich in-cylinder conditions; alternatively, the results suggest that the RCCI combustion regime be utilized in engine applications where the air handling systems allow for relatively lean in-cylinder conditions. However, it is of interest to study the observed phenomena in greater detail in order to develop an improved understanding of the governing heat release mechanisms through which each combustion regime relies in its ideal operating condition (leaner for the RCCI combustion regime, richer for the DPI combustion regime.). The next chapters explore the effects of equivalence ratio, premixed methane ratio, and other factors on engine noise, emissions, and efficiency with respect to engine sub-systems such as air handling and exhaust aftertreatment systems.

7 EFFECT OF PREMIXED METHANE RATIO ON DPI AND RCCI COMBUSTION IN A HEAVY-DUTY ENGINE

In Chapter 6 it was observed that equivalence ratio had a significant impact on the emissions and efficiency characteristics of both RCCI and DPI combustion. In more focused examination, Chapter 7 studies both RCCI and DPI combustion over a range of premixed methane ratios from 86% to 95% and a range of equivalence ratios from $\phi = 0.3$ to $\phi = 0.6$ and takes into consideration the global emission/efficiency tradeoffs.

7.1 Experimental Setup

The following engine experiments were performed in the Caterpillar SCOTE Laboratory as outlined in Chapter 3, with the injector specifications given in Table 7.2. Note the higher compression ratio and different piston geometry for Chapter 7 relative to Chapters 5 and 6.

Table 7.1: 3401 Caterpillar SCOTE heavy-duty engine specifications.

Displacement	2.44 L
Bore x Stroke	137.2 mm x 165.1 mm
Connecting Rod Length	261.6 mm
Number of Valves	4
Intake Valve Opening/Closing	335/-143° aTDC
Exhaust Valve Opening/Closing	130/-355° aTDC
Swirl Ratio	0.7
Piston Type	Articulated
Piston Profile	Re-entrant
Compression Ratio	16.1:1

Table 7.2: Common rail injector specifications.

Injector Series	Bosch CRI2.2
Number of Holes	7
Hole Diameter	141 µm
Included Spray Angle	148°

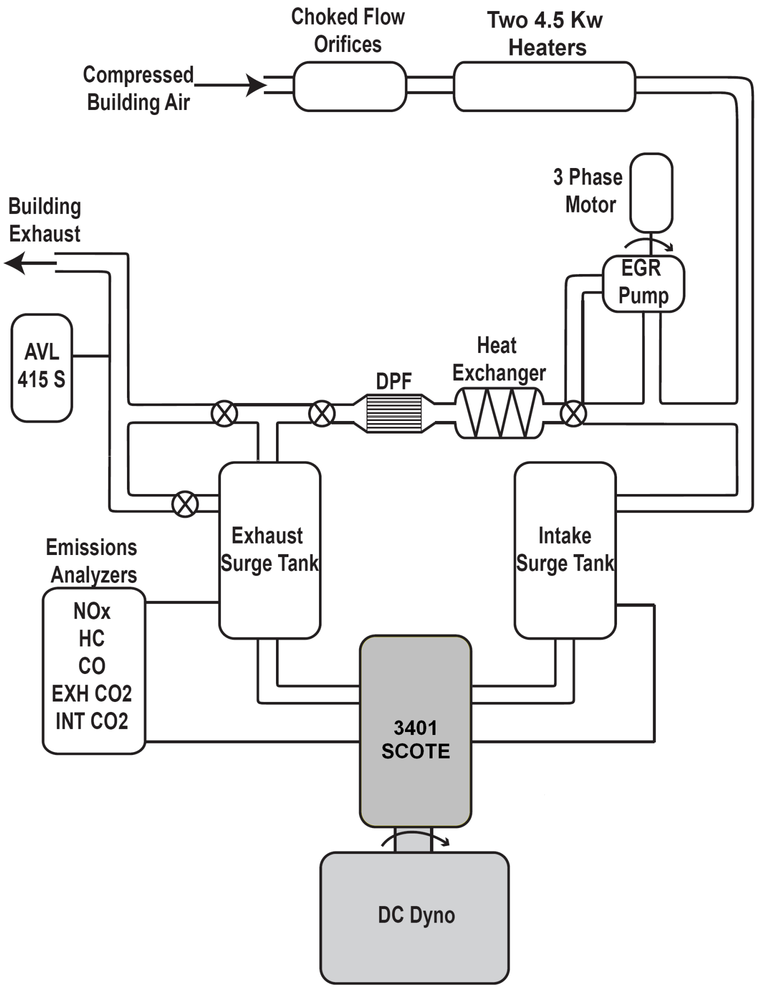

Figure 7.1: SCOTE Laboratory configuration for the Chapter 7 experiments.

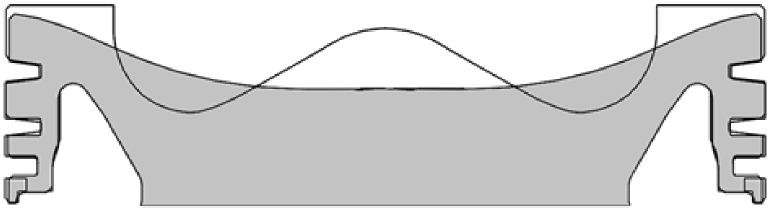

Figure 7.2: The stock CDC re-entrant piston (white, CR = 16.1) profile used in the Chapter 7 experiments.

7.2 Results and Discussion

In order to compare the two dual-fuel combustion strategies, for this study the following engine parameters are fixed: engine speed, intake temperature, injection pressure, and fuel energy per cycle. For DPI and RCCI, three premixed methane energy ratios are studied: 86%, 90%, and 95%. The start of high temperature heat release (HTHR) is fixed at -5° aTDC via the DISOI timing. In order to bound the experimental study, two emissions thresholds are assigned: at the highest equivalence ratios, a NO_x production limit of 2000 ppm is established; at the lowest equivalence ratios, a HC production limit of 9000 ppm is established. F76 and methane have lower heating values of 42.6 MJ/kg and 50.0 MJ/kg, respectively. 0% EGR is used. Table 8.5 shows the experimental engine operating conditions for the work in Chapter 7.

Table 7.3: Chapter 7 engine operating conditions.

	DPI	**RCCI**
Global Equivalence Ratio ϕ	0.64 to 0.43	0.63 to 0.34
Premixed Equivalence Ratio ϕ	0.59 to 0.35	0.56 to 0.29
SOI Timing	-17° aTDC	-54° to -33° aTDC
Engine Speed	1300 rev/min	
IMEP$_g$	7 bar nominal	
Fuel Energy	3500 J/cycle	
Intake Temperature	40 °C	
Intake Pressure	Vary to fix ϕ	
DI Injection Pressure	500 bar	
DI Fuel	F76	
PFI Fuel	Methane	
Methane Energy %	86%, 90%, 95%	
F76 Energy %	14%, 10%, 5%	
EGR Rate	0%	

7.2.1 Effect of Equivalence Ratio and Premix Methane Ratio on Dual-Fuel Performance and Emissions

In Section 7.2.1, the viable engine operating range with the imposed NO_x and HC exhaust concentration limits of 2,000 ppm and 9,000 ppm, respectively, is determined. Furthermore, the effect of equivalence ratio and premix methane ratio on engine noise, emissions, and efficiency is examined.

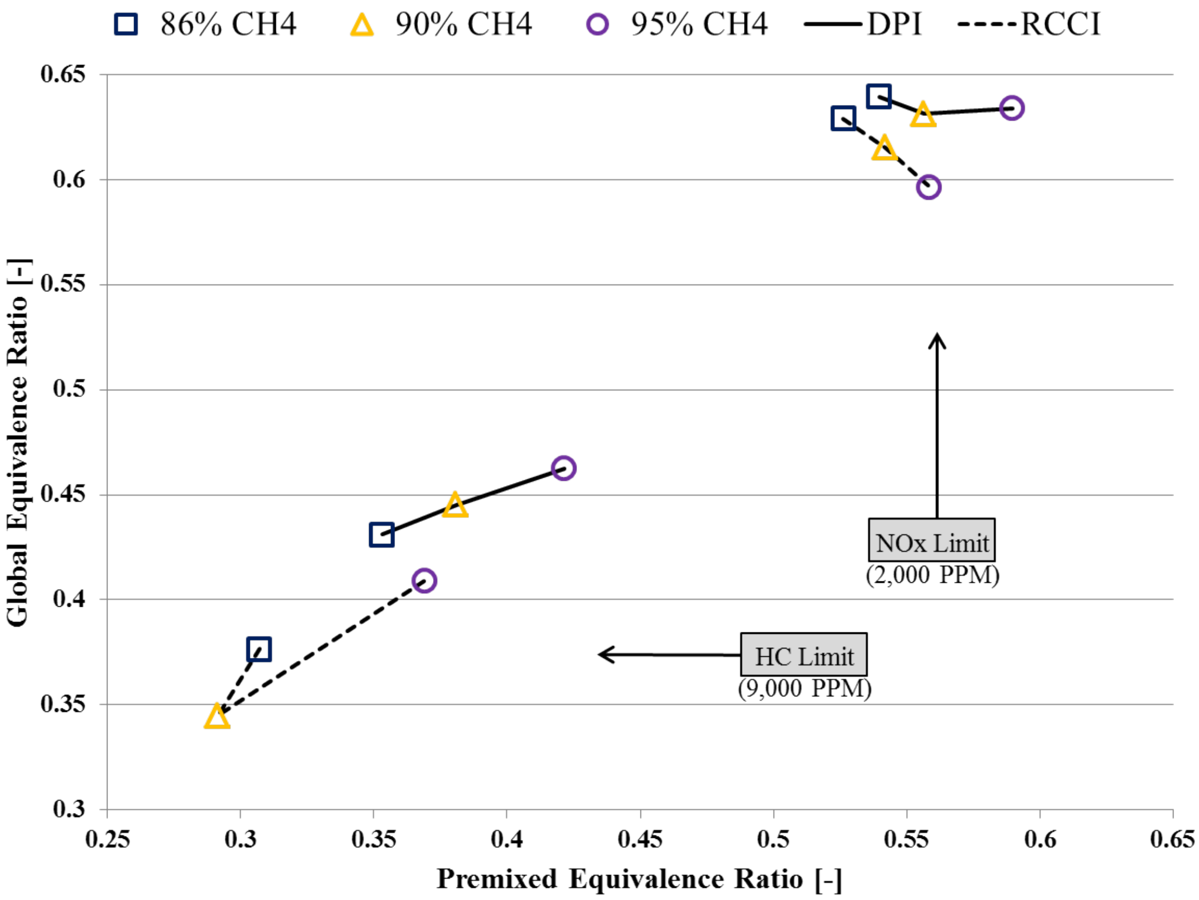

Figure 7.3: Maximum NO_x (2,000 ppm) and HC (9,000 ppm) exhaust concentration limits for the DPI (solid lines) and RCCI (dashed lines) cases.

Figure 7.3 shows the limiting operating points for the DPI and RCCI combustion strategies. The results are shown with respect to both the global equivalence ratio and the premixed equivalence ratio. (In Figure 7.3 the blue squares, yellow triangles, and purple circles denote 86%, 90%, and 95% premixed methane, respectively. DPI is denoted by solid lines and RCCI is denoted by dashed lines.) It is observed that the premixed equivalence ratio has a stronger influence on the combustion performance than the global equivalence ratio in relation to the three different premixed methane ratios studied. In addition, it is shown that at high equivalence ratios, DPI is able to operate richer than RCCI before meeting the NO_x concentration threshold of 2,000 PPM. It is also seen that at low equivalence ratios, RCCI is able to operate leaner than DPI before meeting the HC concentration threshold of 9,000 PPM.

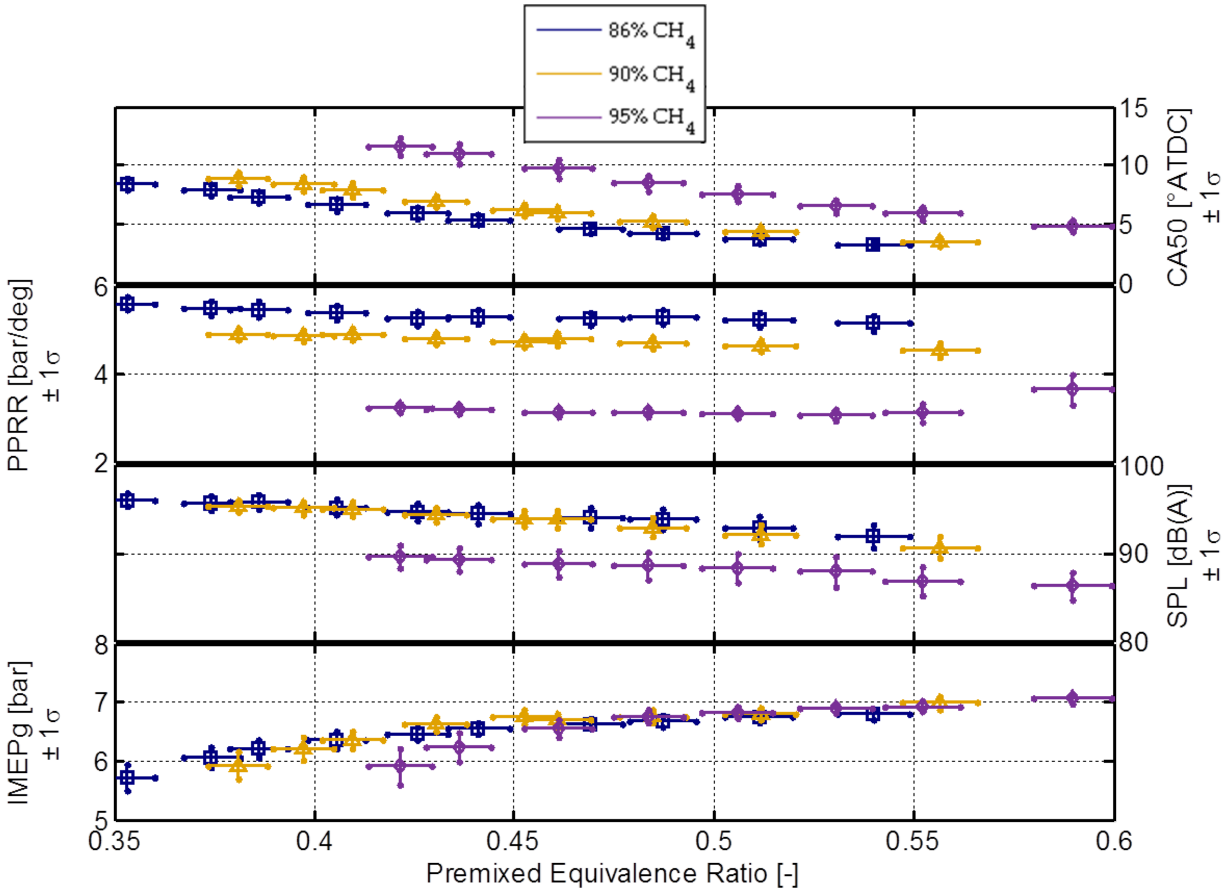

Figure 7.4: Pressure performance metrics for the DPI cases. Blue squares, yellow triangles, and purple circles denote 86%, 90%, and 95% premixed methane, respectively. The vertical lines in each marker represent the range of one standard deviation.

Figure 7.4 shows the pressure performance metrics of CA50, PPRR, SPL, and $IMEP_g$ for the DPI cases, where the blue squares, yellow triangles, and purple circles denote 86%, 90%, and 95% premixed methane, respectively. It is observed that increased amounts of premixed methane result in longer combustion durations, given the fixed start of HTHR at -5° aTDC. In addition, combustion noise, in terms of PPRR and SPL, is significantly reduced with increased premixed methane ratio. It is seen that the achievable engine load is largely unaffected by the premixed methane ratio for DPI combustion.

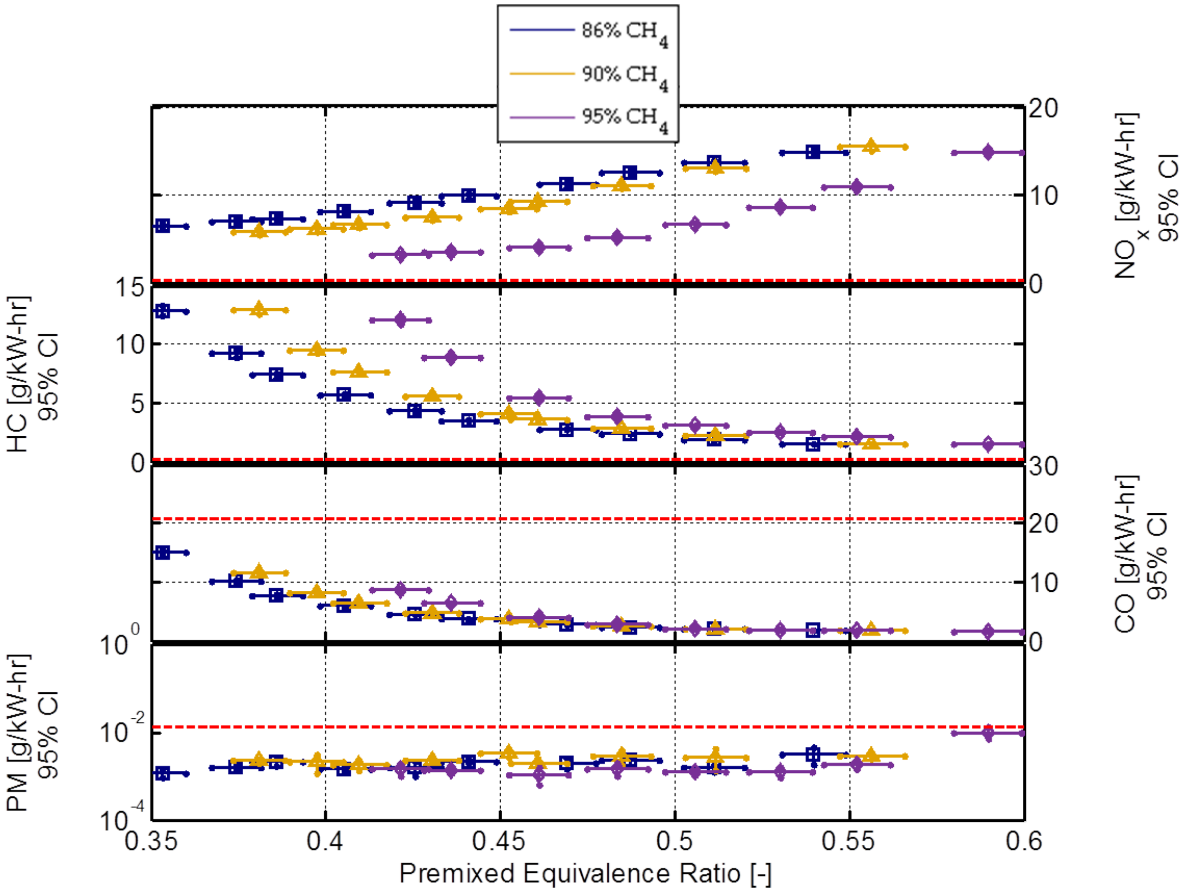

Figure 7.5: Emissions metrics for the DPI cases. Blue squares, yellow triangles, and purple circles denote 86%, 90%, and 95% premixed methane, respectively. The vertical lines in each marker represent the range of the 95% confidence interval.

Figure 7.5 shows the emissions measurements for NO_x, HC, CO and PM for the DPI cases, where the blue squares, yellow triangles, and purple circles denote 86%, 90%, and 95% premixed methane, respectively. The red dashed lines indicate the U.S. EPA 2010 Heavy-Duty emissions standards for reference. It is shown that NO_x emission are reduced, at a given equivalence ratio, with higher amounts of premixed methane. However, with respect to HC and CO emissions, increased amounts of premixed methane result in increased levels of both species, though CO to a lesser extent. For all cases, PM is below the EPA 2010 HD limit.

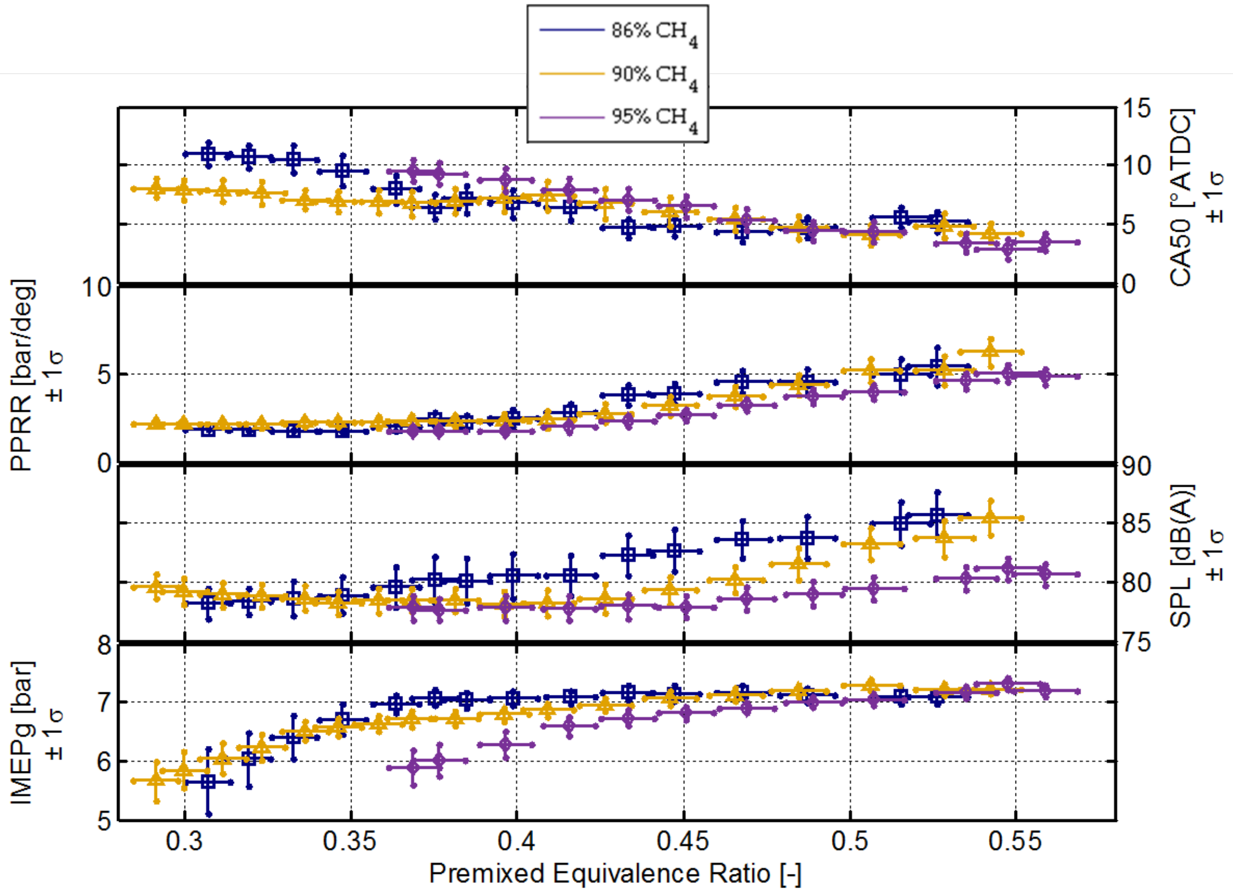

Figure 7.6: Pressure performance metrics for the RCCI cases. Blue squares, yellow triangles, and purple circles denote 86%, 90%, and 95% premixed methane, respectively. The vertical lines in each marker represent the range of one standard deviation.

Figure 7.6 shows the pressure performance metrics of CA50, PPRR, SPL, and IMEP$_g$ for the RCCI cases, where the blue squares, yellow triangles, and purple circles denote 86%, 90%, and 95% premixed methane, respectively. It is observed that increased amounts of premixed methane do not significantly affect combustion durations, as with DPI combustion. Again combustion noise, in terms of PPRR and SPL, is reduced with increased premixed methane ratio, though this effect is not a strong as with DPI combustion. Also unlike DPI combustion, the premixed methane ratio has a much stronger influence on the achievable engine load, where this observation is more pronounced at leaner conditions.

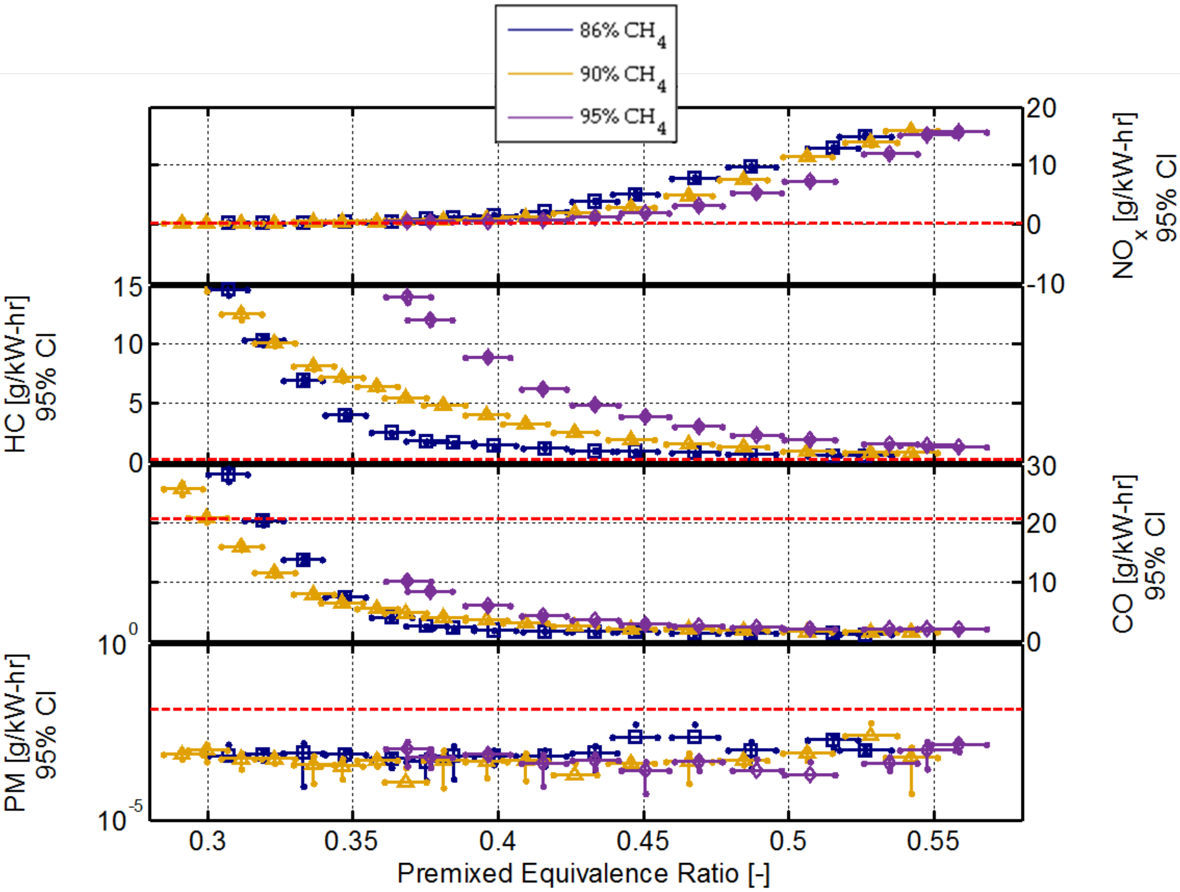

Figure 7.7: Emissions metrics for the RCCI cases. Blue squares, yellow triangles, and purple circles denote 86%, 90%, and 95% premixed methane, respectively. The vertical lines in each marker represent the range of the 95% confidence interval.

Figure 7.7 shows the emissions measurements for NO$_x$, HC, CO and PM for the DPI cases, where the blue squares, yellow triangles, and purple circles denote 86%, 90%, and 95% premixed methane, respectively. The red dashed lines indicate the U.S. EPA 2010 Heavy-Duty emissions standards for reference. It is shown that NO$_x$ emission are slightly reduced, at a given equivalence ratio, with higher amounts of premixed methane (again, this trend is stonger with DPI combustion). However, with respect to HC and CO emissions, increased amounts of premixed methane result in increased levels of both species, though

CO to a lesser extent as with DPI combustion.. For all cases, PM is below the EPA 2010 HD limit.

7.2.2 Analyis of Global Emission and Efficiency Tradeoffs

In Section 7.2.2, the performance and emissions tradeoffs with respect to NO_x are studied. In Figures 7.8 to 7.11, the blue squares, yellow triangles, and purple circles denote 86%, 90%, and 95% premixed methane, respectively; DPI is denoted by open symbols, RCCI is denoted by filled symbols. (It should be noted, that for Figures 7.8 through 7.11, the general relationship is that the richest cases (i.e., the cases with the highest global/premixed equivalence ratios) produce the highest NO_x, and vice-versa with HC for the leanest cases.)

Figure 7.8 shows the HC-NO_x relationship for both DPI and RCCI at each premixed methane ratio. It is seen that there is a stronger HC-NO_x tradeoff with DPI relative to RCCI (i.e., lower combined HC/NO_x with RCCI). Interestingly, the HC-NO_x tradeoff trends are opposite between DPI and RCCI with respect to the premixed methane ratio. With DPI, more premixed methane (less DI fuel) provides lower combined HC/NO_x. However for RCCI, less premixed methane (more DI fuel) provides lower combined HC/NO_x.

Figure 7.9 shows the CO-NO_x relationship for both DPI and RCCI at each premixed methane ratio. As in Figure 4-3, similar behavior is observed with respect to the CO-NO_x tradeoff. DPI has a stronger CO-NO_x tradeoff with DPI relative to RCCI (i.e., lower combined CO/NO_x with RCCI). However, RCCI is not as sensitive to the premixed methane ratio for combined CO/NO_x emissions, while DPI retains sensitivity to the premixed methane ratio. It is thought that combustion chamber geometry combined with spray effects due to the DI SOI timings for DPI and RCCI may be contributing to this observation.

Figure 7.10 shows the noise-NO_x relationship for both DPI and RCCI at each premixed methane ratio. The noise metric is the sound pressure level (SPL) in units of decibels (dB(A)). It is observed that DPI has higher combined SPL/NO_x levels relative to RCCI. It is also worth noting that for DPI combustion, the SPL decreases with increasing NO_x (i.e.,

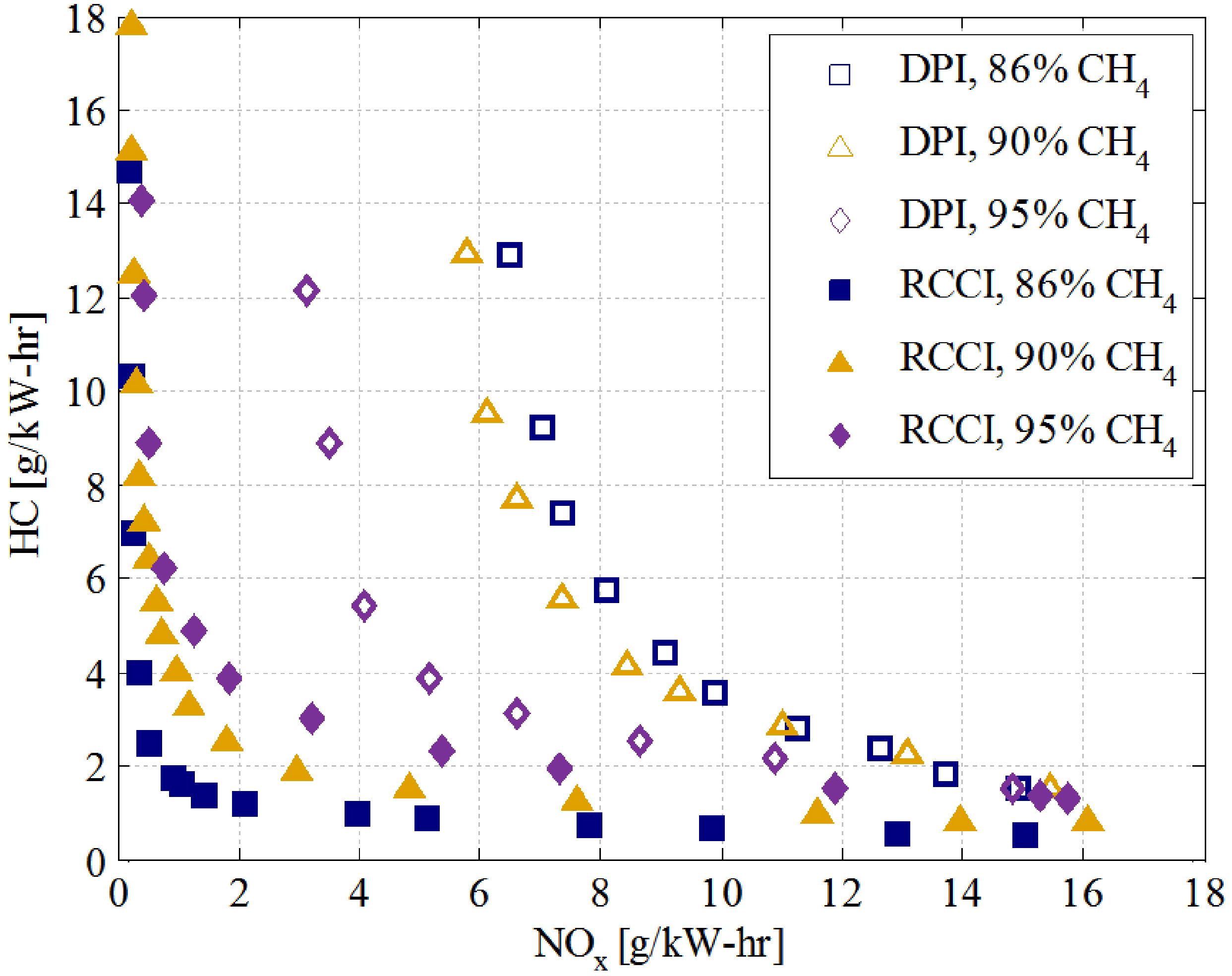

Figure 7.8: HC-NO$_x$ relationship. Filled symbols are RCCI, open symbols are DPI; Square/blue symbols are 86% premixed CH4, triangle/gold symbols are 90% CH4, and diamond/purple symbols are 95% CH4.

the SPL decreases with increasing global/premixed equivalence ratio). However, for RCCI combustion, the SPL increases with increasing NO$_x$ (i.e., the SPL increases with increasing global/premixed equivalence ratio). This opposing behavior between DPI and RCCI is not yet fully understood and will be discussed in the next chapter.

Figure 7.11 shows the efficiency-NO$_x$ relationship. At low NO$_x$ values, for both combustion strategies, the thermal efficiency efficiency drops considerably, and this is directly tied to the increasing HC/CO levels carrying unconverted chemical energy in the engine exhaust stream. Again, the efficiency-NO$_x$ tradeoff trends are opposite between DPI and

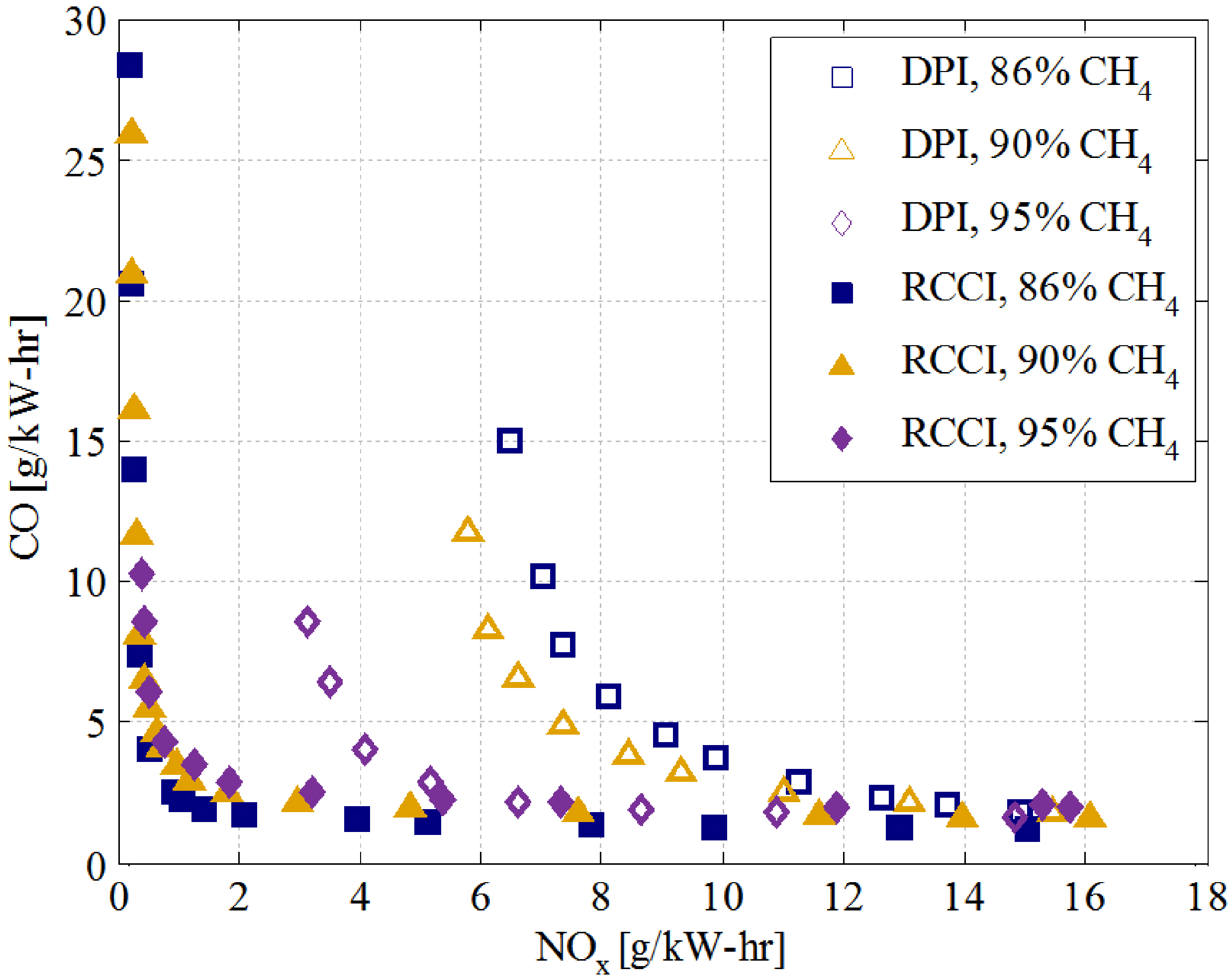

Figure 7.9: CO-NO$_x$ relationship. Filled symbols are RCCI, open symbols are DPI; Square/blue symbols are 86% premixed CH4, triangle/gold symbols are 90% CH4, and diamond/purple symbols are 95% CH4.

RCCI with respect to the premixed methane ratio. With DPI, more premixed methane (less DI fuel) provides reduced NO$_x$ emissions and improved thermal efficiency. However for RCCI, less premixed methane (more DI fuel) provides reduced NO$_x$ emissions and improved thermal efficiency.

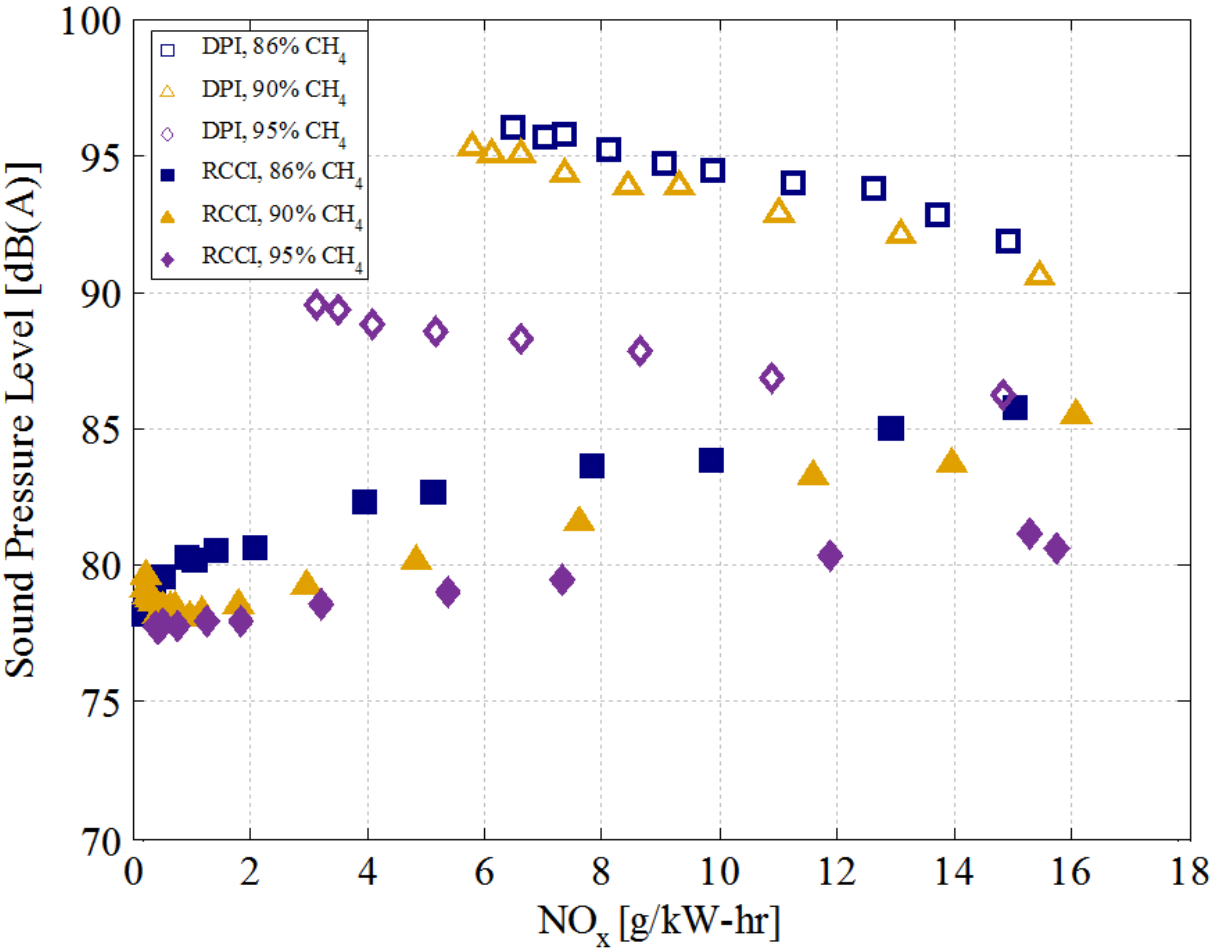

Figure 7.10: Noise-NO$_x$ relationship. Filled symbols are RCCI, open symbols are DPI; Square/blue symbols are 86% premixed CH4, triangle/gold symbols are 90% CH4, and diamond/purple symbols are 95% CH4.

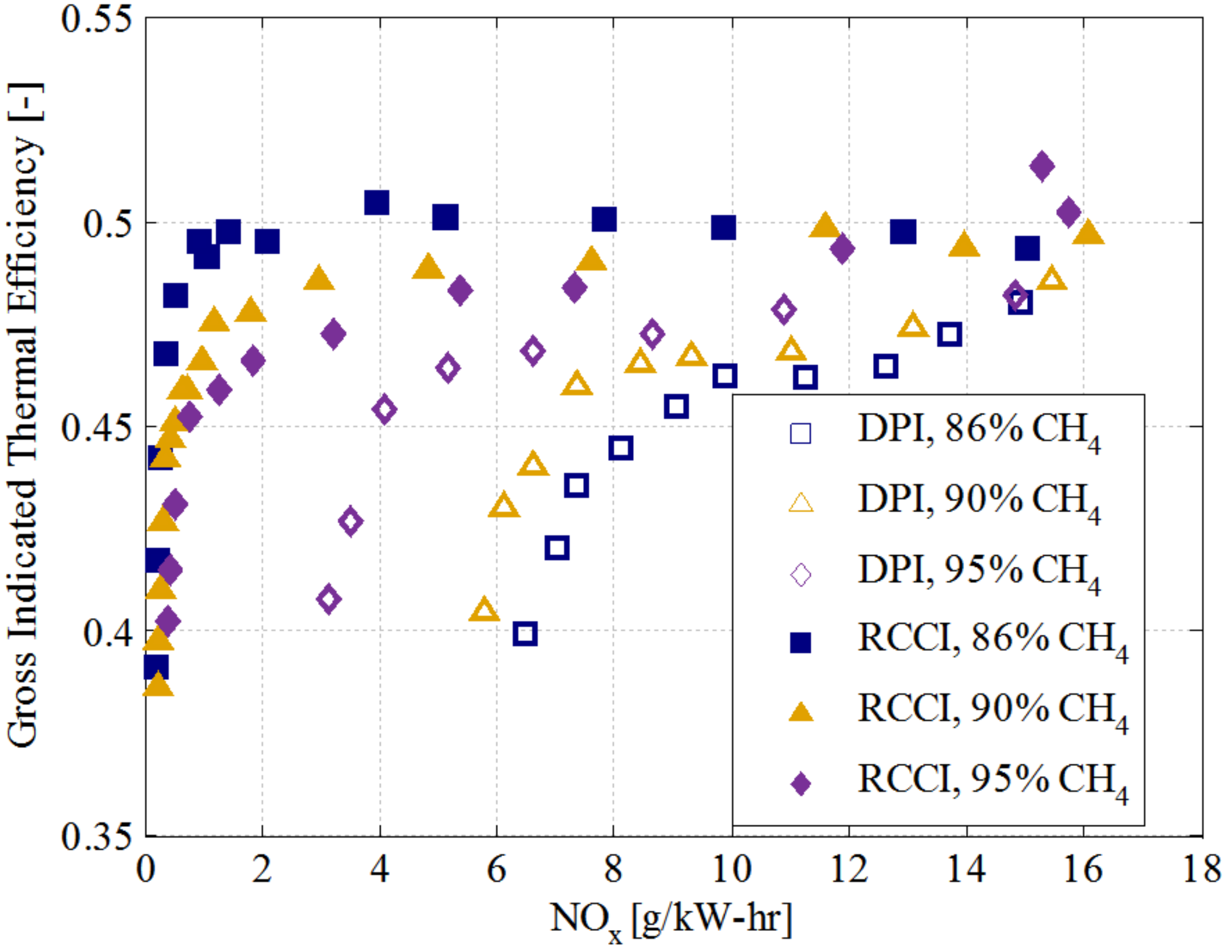

Figure 7.11: Efficiency-NO$_x$ relationship. Filled symbols are RCCI, open symbols are DPI; Square/blue symbols are 86% premixed CH4, triangle/gold symbols are 90% CH4, and diamond/purple symbols are 95% CH4.

7.3 Conclusions

Overall, the combustion performance of both the DPI and RCCI combustion strategies is significantly influenced by both the global/premixed equivalence ratio and the premixed methane ratio. It is possible that RCCI is more dependent on the DI amount (i.e., ignition energy/location) due to the mode(s) of heat release. On the other hand, DPI appears less dependent on the DI amount due to the main heat release mechanism, which is thought to be predominantly flame propagation. (Further research into this phenomenon is presented in the following chapter.)

With respect to the global/premixed equivalence ratio, it was observed that at high equivalence ratios, DPI is able to operate richer than RCCI before meeting the NO_x production threshold of 2,000 ppm. It was also seen that at low equivalence ratios, RCCI is able to operate leaner than DPI before meeting the HC production threshold of 9,000 ppm. Furthermore, for both DPI and RCCI combustion, higher premixed methane ratios provided NO_x reductions, albeit with consequential increases in HC and CO emissions.

Upon examination of the global NO_x tradeoffs, a range of interesting conclusions are drawn. With diesel pilot ignition, a much stronger HC-NO_x tradeoff is shown relative to reactivity controlled compression ignition combustion; that is, RCCI offers lower combined HC+NO_x emissions compared to DPI. Additionally, the HC-NO_x tradeoff trends are opposite between the two dual-fuel combustion strategies: DPI achieves lower emissions with more premixed methane; RCCI achieves lower emissions with less premixed methane. Overall, the CO-NO_x trend is similar for both combustion strategies, however the tradeoff is not as sensitive for CO as it is for HC. In term of combustion noise, both strategies offer reduced noise at higher premixed methane ratios. Interestingly, DPI combustion is quieter with increasing equivalence ratio whereas RCCI combustion is louder. Finally, a stronger efficiency-NO_x compromise is made with DPI combustion compared to RCCI combustion, again with similar trends with respect to the premixed methane ratio.

8 DETERMINATION OF HEAT RELEASE MECHANISM IN A LEAN-BURN DUAL-FUEL HEAVY-DUTY ENGINE

In Chapters 6 and 7 it was observed that equivalence ratio had a significant impact on the emissions and efficiency characteristics of both RCCI and DPI combustion. At moderate equivalence ratios, the results indicated that RCCI and DPI exhibit different mechanisms of heat release during high temperature combustion. In order to verify this observation, Chapter 8 studies four combustion strategies on a heavy-duty engine platform: dual-fuel homogeneous charge compression ignition (DF-HCCI), reactivity controlled compression ignition (RCCI), diesel pilot ignition (DPI), and spark ignition (SI). Then, the RCCI and DPI dual-fuel combustion strategies are compared to baseline SI data over a range of engine speeds in order to determine the characteristic mode of heat release for the RCCI and DPI dual-fuel combustion strategies.

8.1 Experimental Setup

The following engine experiments were performed in the Caterpillar SCOTE Laboratory as outlined in Chapter 3, with the injector specifications given in Table 8.2. Note the higher compression ratio and stock piston geometry for Chapter 8 relative to Chapters 5 and 6. Each combustion mode is operated over an equivalence ratio range from $\phi = 0.3$ to $\phi = 1.0$, subject to a peak pressure rise rate constraint of 25 bar per degree and a combustion efficiency constraint of 90%.

As an integral portion of the study presented in this chapter, the engine was converted to operate in spark-ignition (SI) mode in order to operate the engine under a single-fuel combustion regime where the rate of heat release is well-known to be governed by the flame propagation heat release mechanism. In place of the common-rail direct-injector, a modified spark plug assembly was designed and implemented in the engine. This allowed

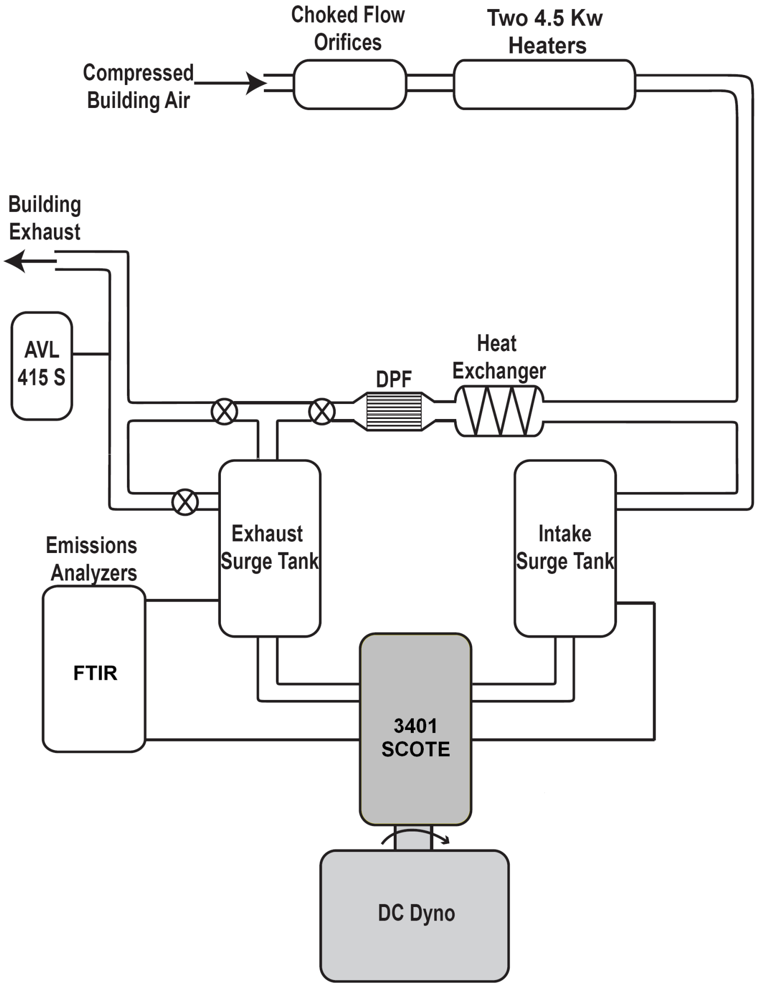

Figure 8.1: SCOTE Laboratory configuration for the Chapter 8 experiments.

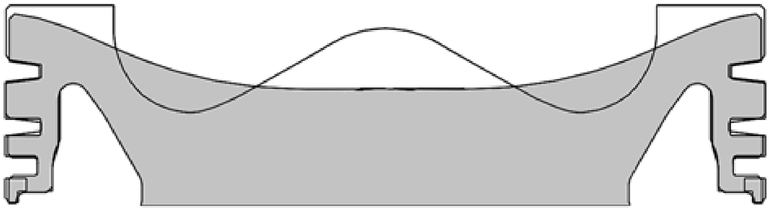

Figure 8.2: The stock CDC re-entrant piston (white, CR = 16.1) profile used in the Chapter 8 experiments.

Table 8.1: 3401 Caterpillar SCOTE heavy-duty engine specifications.

Displacement	2.44 L
Bore x Stroke	137.2 mm x 165.1 mm
Connecting Rod Length	261.6 mm
Number of Valves	4
Intake Valve Opening/Closing	335/-143° aTDC
Exhaust Valve Opening/Closing	130/-355° aTDC
Swirl Ratio	0.7
Piston Type	Articulated
Piston Profile	Re-entrant
Compression Ratio	16.1:1

Table 8.2: Common rail injector specifications.

Injector Series	Bosch CRI2.2
Number of Holes	7
Hole Diameter	141 μm
Included Spray Angle	148°

reference SI engine cases to be produced over a range of conditions from stoichiometric to fuel-lean. The SI modification is illustrate in Figure 8.3 and Table 8.3 lists the spark-ignition hardware configuration used in Chapter 8.

Table 8.3: SI hardware setup for the Chapter 8 SI experiments.

Spark Plug	NGK ER9EH
Spark Gap	0.65 mm
Spark Duration	3.0 ms
Spark Energy	103 mJ
Spark Driver/Coil	AEM IGBT Smart Coil 30-2853
Spark Control Module	NI 9754 Engine-Synchronous TTL

For all strategies, methane was used as the low reactivity fuel, and was port injected in the gaseous state. For DF-HCCI, n-heptane was port injected in the liquid state; for RCCI and DPI, n-heptane was direct-injected in the liquid state. SI operation utilized methane only. Table 8.4 shows the fueling combinations for the Chapter 8 experiments.

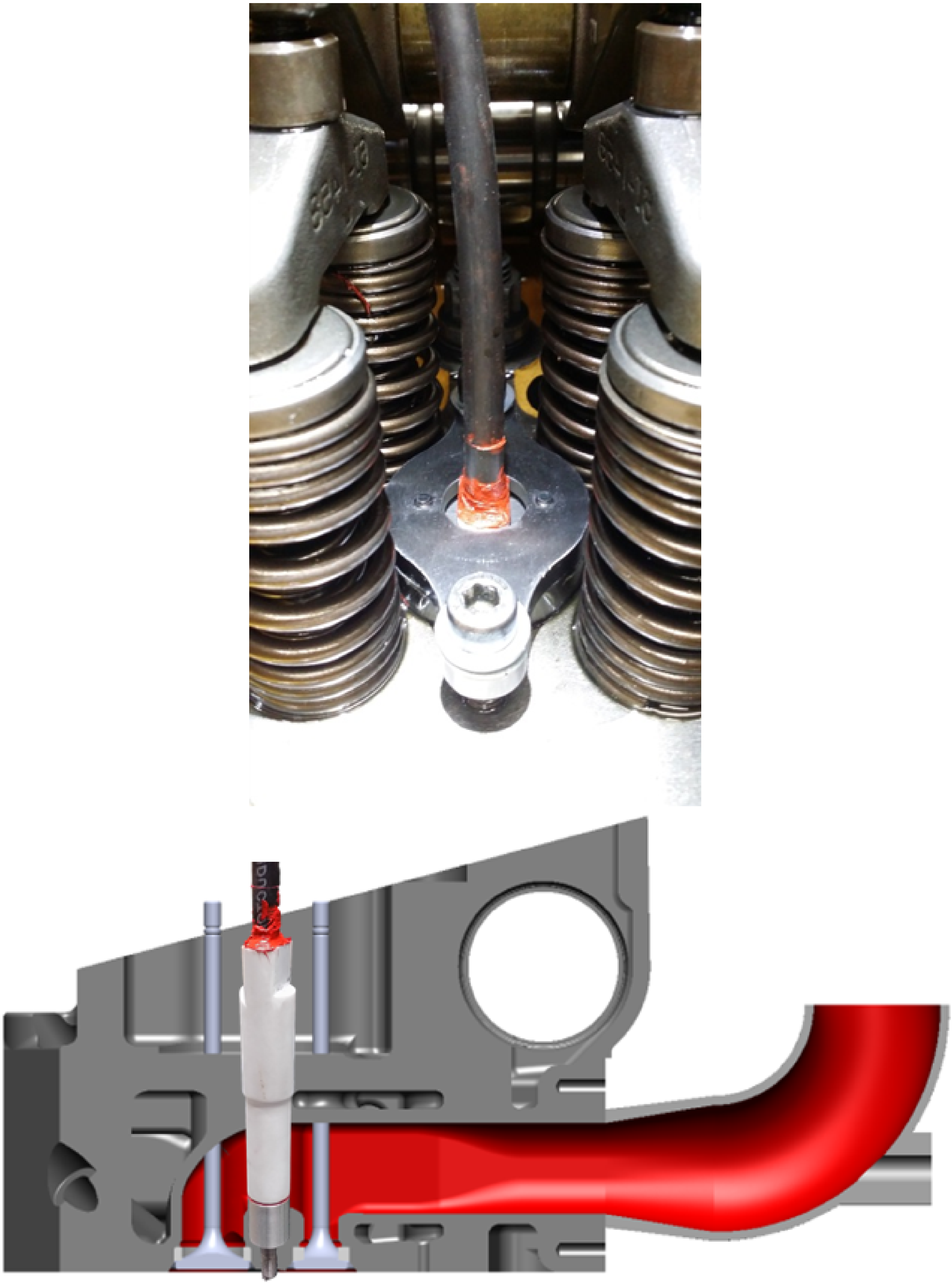

Figure 8.3: Modified NGK ER9EH spark plug in Caterpillar SCOTE engine head.

Table 8.4: Fueling strategies for the multi-mode combustion experiments.

	HRF	**LRF**
DF-HCCI	n-heptane (PFI)	methane (PFI)
RCCI	n-heptane (DI)	methane (PFI)
DPI	n-heptane (DI)	methane (PFI)
SI	-	methane (PFI)

8.2 Results and Discussion

8.2.1 Performance and Emissions Characteristics of DF-HCCI, RCCI, DPI and SI Combustion Regimes in a Heavy-Duty Engine

In order to compare the four combustion strategies, for this study the following engine parameters are fixed: engine speed, intake pressure, and intake temperature. In order to bound the experimental study, two performance thresholds are assigned: a peak pressure rise rate of less than 25 bar per degree, and a combustion efficiency greater than 90%. Methane and n-heptane have lower heating values of 50.0 MJ/kg and 44.6 MJ/kg, respectively. 0% EGR is used for all cases. Table 8.5 shows the experimental engine operating conditions and Figure 8.4 details the ignition timings required to obtain a combustion phasing of CA50 = 10° aTDC for the SI, DPI, and RCCI strategies. Figure 8.5 shows the methane energy fraction for all combustion regimes as a function of equivalence ratio.

Table 8.5: Section 8.2.1 engine operating conditions.

	DF-HCCI	**RCCI**	**DPI**	**SI**
Global Equivalence Ratio ϕ	0.5 to 0.3	1.0 to 0.45	1.0 to 0.45	1.0 to 0.5
Engine Speed	1300 rev/min			
IMEP$_g$	4 bar to 10 bar			
Intake Temperature	40 °C			
Intake Pressure	Naturally Aspirated (1 bar)			
DI Injection Pressure	-	500 bar	500 bar	-
HRF Fuel	n-Heptane	n-Heptane	n-Heptane	-
LRF Fuel	Methane			
EGR Rate	0%			

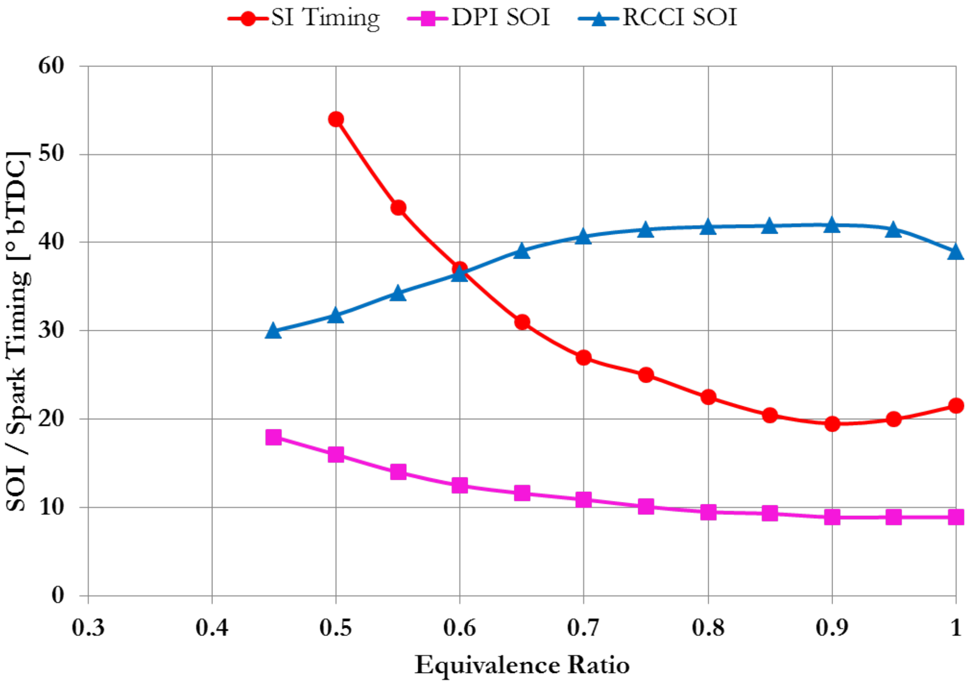

Figure 8.4: Ignition timings for the SI, DPI, and RCCI combustion regimes.

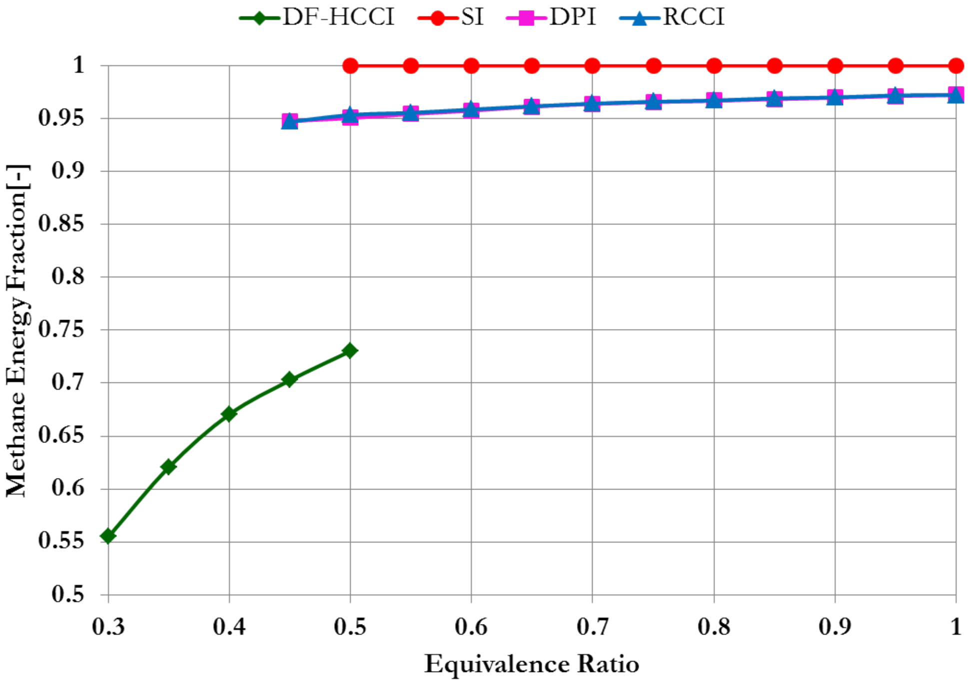

Figure 8.5: Methane energy fraction as a function of equivalence ratio for DF-HCCI, SI, DPI, and RCCI combustion regimes.

Figure 8.6 shows the combustion performance metrics (CA50, PPRR, SLP, IMEP$_g$, and COV$_{IMEP}$), for the DF-HCCI (green diamonds), SI (red circles), DPI (pink squares), and RCCI (blue triangles) combustion regimes. The vertical lines in each data marker represent the range of one standard deviation of each metric derived from the experimental data; the horizontal lines in each data marker represent the range of the 95% confidence interval for the calculated equivalence ratio.

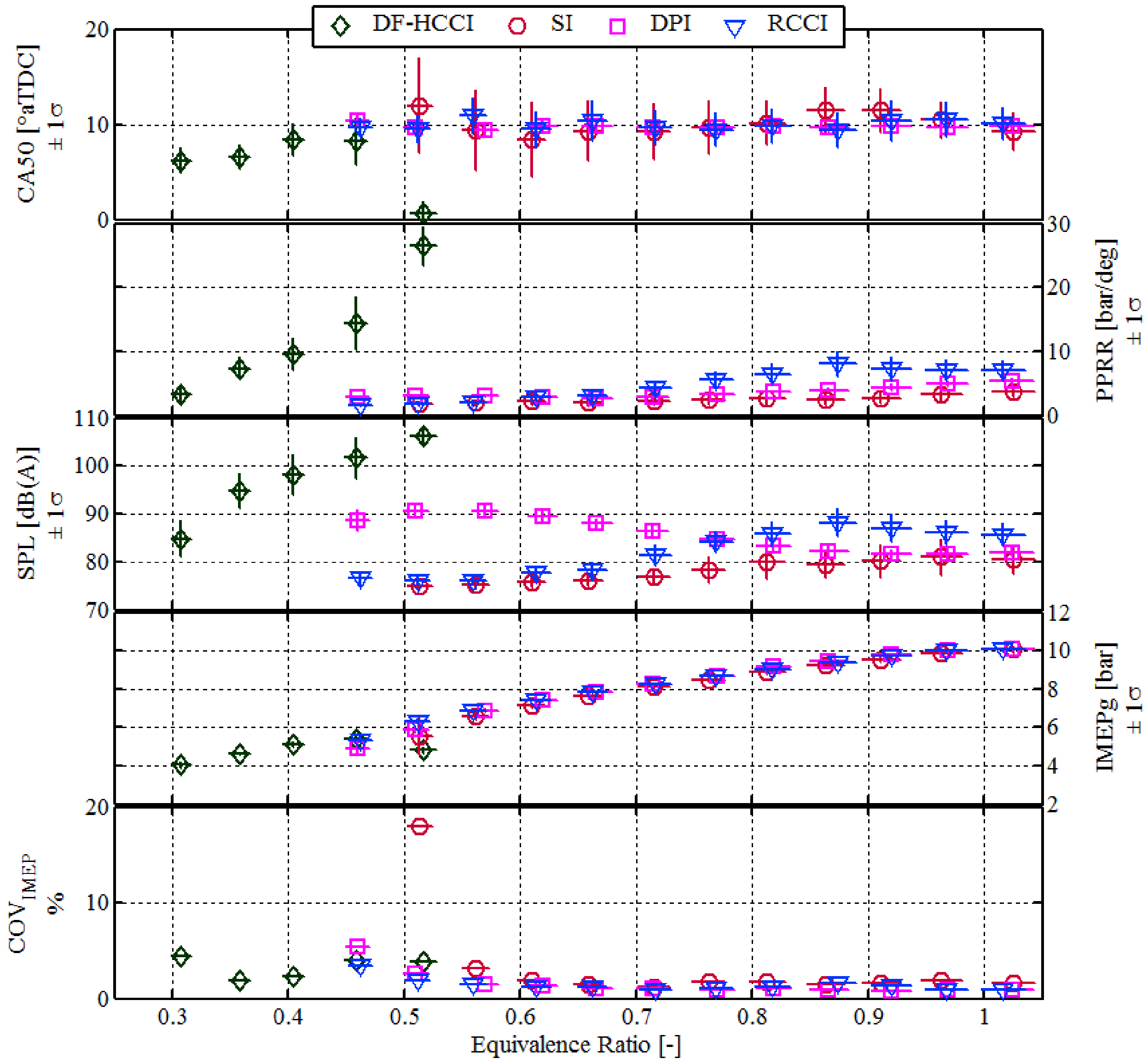

Figure 8.6: Pressure performance metrics for the DF-HCCI (green diamonds), SI (red circles), DPI (pink squares), and RCCI (blue triangles) cases. The vertical lines in each marker represent the range of one standard deviation.

Importantly, the viable operating range achieved for each combustion strategy, with respect to equivalence ratio, shows that fully-premixed DF-HCCI combustion is severely limited to a naturally-aspirated operating range of $\phi = 0.3$ to $\phi = 0.5$. At the $\phi = 0.5$ limit, the DF-HCCI strategy meets the peak pressure rise constraint with a PPRR in excess of 25 bar per degree. As the equivalence ratio (i.e., engine load) is increased, combustion noise in terms of both PPRR and SPL increase, and due to the fully-premixed compression ignition nature of DF-HCCI the most severe combustion noise levels are displayed compared to all combustion strategies. $\mathrm{COV}_{\mathrm{IMEP}}$ is below 5% for all DF-HCCI cases.

Conversely, the viable operating range for fully-premixed SI combustion covers an equivalence ratio range from $\phi = 0.5$ to $\phi = 1.0$. Over this range it is seen that SI combustion provides the lowest combustion noise in term of both PPRR and SPL. Clearly, holding combustion phasing constant at CA50 = 10° aTDC via the spark timings used in Figure 8.4 does not approach the knock advance limit for each condition, thus providing quiet combustion. At the SI lean limit, $\phi = 0.5$, combustion stability deteriorates where $\mathrm{COV}_{\mathrm{IMEP}}$ approached 20%, and the combustion efficiency constraint is exceeded.

For DPI and RCCI combustion, similar performance is obtained across the equivalence ratio range from $\phi = 0.45$ to $\phi = 1.0$. For both strategies the direct-injected n-heptane energy fraction is 5% at the lean limit and approximately 3% at the rich limit, as shown in Figure 8.5. At the lean limit, even at lower premixed equivalence ratio relative to SI, both DPI and RCCI allow the direct-injected dual-fuel lean limit to be extended by 0.05 points. Similar to the results presented in Figure 6.6, RCCI is louder in both PPRR and SPL compared to DPI at richer conditions; however RCCI is also quieter in both PPRR and SPL at leaner conditions relative to DPI.

Figure 8.7 shows the emissions (NO_x, HC, CO, PM) and efficiency (η_{gross}) measurements as a function of equivalence ratio for the DF-HCCI (green diamonds), SI (red circles), DPI (pink squares), and RCCI (blue triangles) combustion regimes. The vertical lines in each data marker represent the range of one standard deviation of each metric derived from the

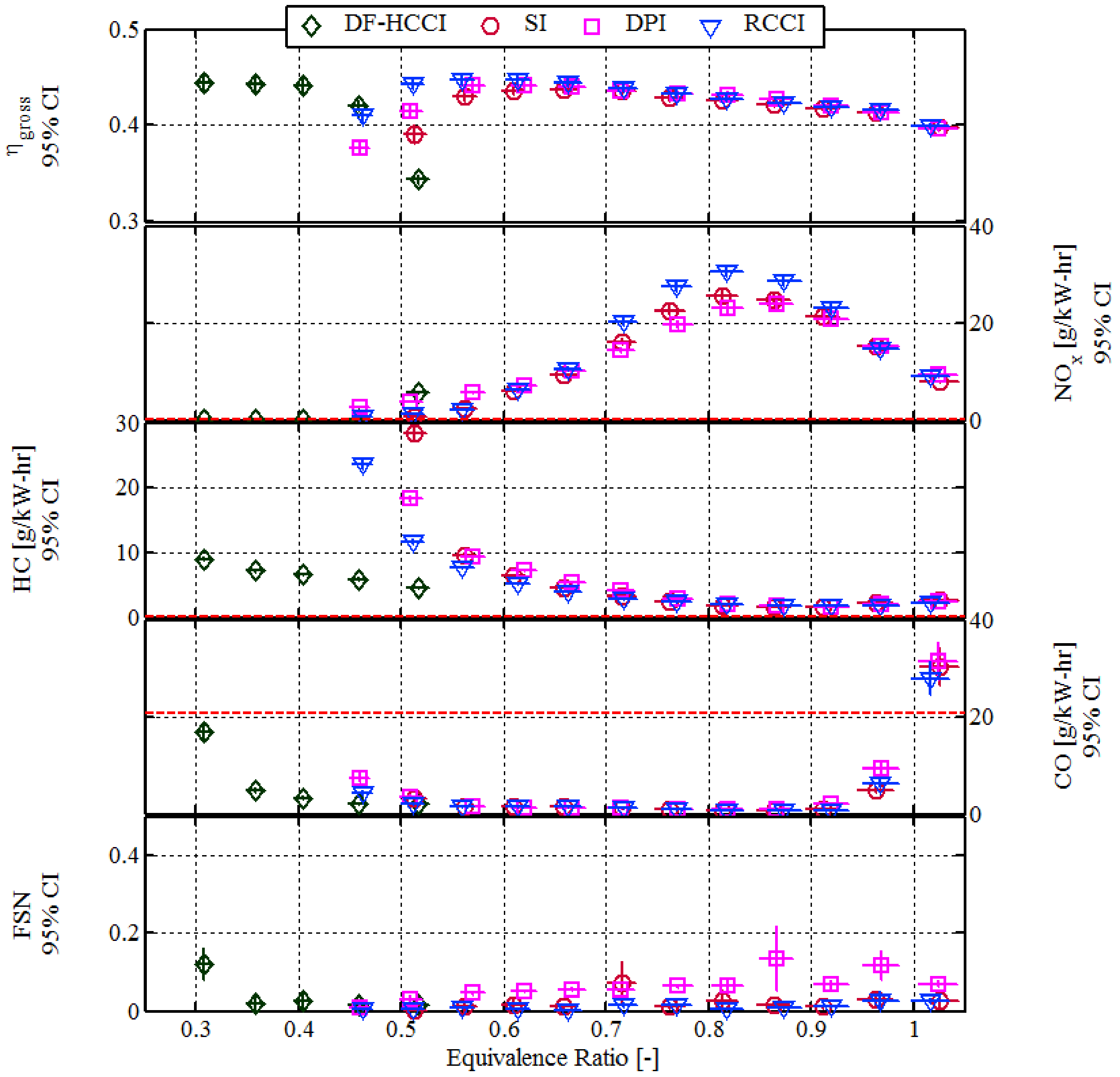

Figure 8.7: Efficiency and emissions metrics for the DF-HCCI (green diamonds), SI (red circles), DPI (pink squares), and RCCI (blue triangles) cases. The vertical lines in each marker represent the range of the 95% confidence interval.

experimental data; the horizontal lines in each data marker represent the range of the 95% confidence interval for the calculated equivalence ratio.

In the top panel of Figure 8.7 it is seen that over the equivalence ratio range from ϕ = 0.6 to ϕ = 1.0, the gross indicated thermal efficiency for SI, DPI, and RCCI is comparable and begins to drop quickly at conditions leaner than ϕ = 0.6. For SI and DPI the thermal efficiency peaks at approximately 44% (45% for RCCI) in the range of $\phi = 0.55$ - $\phi = 0.6$; Whereas for DF-HCCI, the thermal efficiency peaks at 44% in the range of $\phi = 0.3$ - $\phi = 0.4$. For DF-HCCI, conditions richer than $\phi = 0.4$ lead due to significant reductions in thermal efficiency due to the rapid rates of combustion increasing heat losses through the combustion chamber boundaries. It is interesting to note that direct-injected dual-fuel operation allows leaner operation relative to SI combustion, and RCCI allows for higher efficiencies at leaner conditions than those of DPI.

NO_x emissions for SI, DPI, and RCCI are characteristically similar, with NO_x levels peaking around $\phi = 0.8$, due to the combination of sufficient oxygen availability and combustion temperatures in excess of 2000 K; in this region, RCCI produces more NO_x (approximately 30 g/kW-hr peak) than SI or DPI, which can be attributed to the more rapid RCCI combustion process completing faster than SI or DPI, leading to longer in-cylinder residence times for the high temperature combustion gases prior to expansion. For DF-HCCI, NO_x levels remain relatively low across the viable operating range, however due to the advanced combustion phasing at $\phi = 0.5$, increased levels of NO_x approaching 4 g/kW-hr are measured.

For all DF-HCCI points, HC emissions below 10 g/kW-hr and CO emissions below 20 g/kW-hr are delivered; for a given equivalence ratio, DF-HCCI provides the lowest HC + CO emissions. For SI, DPI, and RCCI it is seen that HC levels are similar, with the exception of lower HC concentrations at the lean limit for RCCI, relative to SI and DPI. For all strategies, PM is near-zero due to the elimination of mixing-limited fuel-rich zones associated with conventional diesel combustion.

Figure 8.8 highlights the breakdown of NO_x and THC emissions for the DF-HCCI (green diamonds), SI (red circles), DPI (pink squares), and RCCI (blue triangles) cases. The vertical lines in each data marker represent the range of one standard deviation of each metric derived from the experimental data; the horizontal lines in each data marker represent the range of the 95% confidence interval for the calculated equivalence ratio.

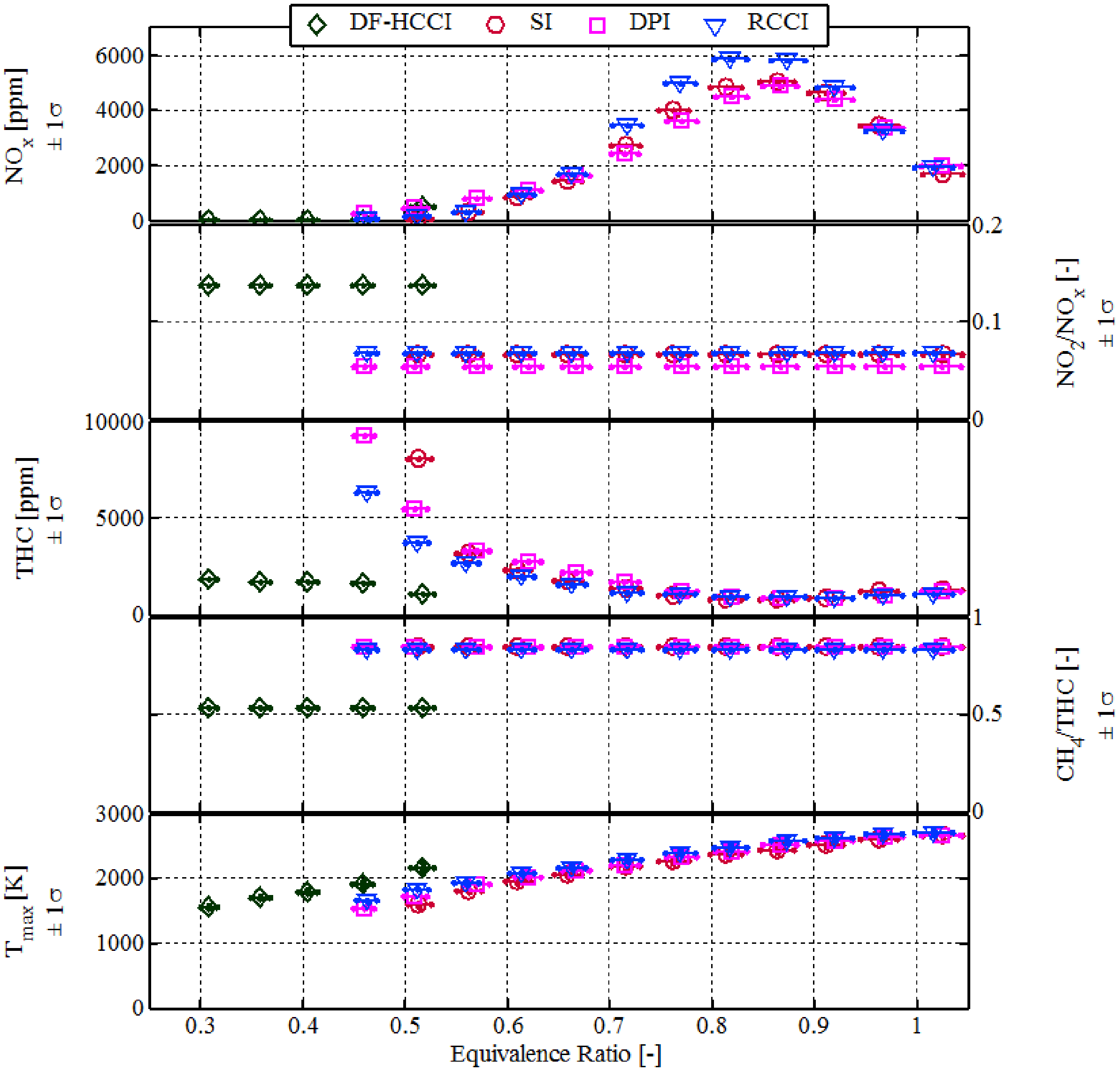

Figure 8.8: Breakdown of NO$_x$ and THC emissions concentrations for the DF-HCCI (green diamonds), SI (red circles), DPI (pink squares), and RCCI (blue triangles) cases. The vertical lines in each marker represent the range of one standard deviation.

It is measured that the NO_2/NO_x ratio is similar for SI, DPI, and RCCI. However for DF-HCCI the NO_2/NO_x ratio is effectively doubled. Taking into consideration that for each combustion strategy the NO_2/NO_x ratio does not respond to the change in equivalence ratio, it is taken that the elevated NO_2/NO_x ratio for DF-HCCI is the result of the significantly higher n-heptane concentrations required relative to DPI and RCCI combustion.

With respect to the relative amount of unburned methane in the exhaust, it again appears that the CH_4/THC ratio is uncorrelated with equivalence ratio for all combustion strategies. Again the SI, DPI, and RCCI combustion strategies all produce the same CH_4/THC ratio. For DF-HCCI, the CH_4/THC ratio is reduced significantly, yet remains unchanged with the changing methane/n-heptane ratios shown in Figure 8.5. This suggests that the methane emissions are resulting from trapped volumes in the near-liner/crevice regions of the combustion chamber; it is possible that the n-heptane is oxidizing in the low-temperature regime, but in the high-surface area volumes the exothermic reactions are thermally isolated and subsequently quenched, inhibiting methane oxidation. Using n-pentene (nC_5H_{10}) as an indicator of n-heptane oxidation, the third panel in Figure 8.9 shows that n-pentene exhaust concentrations are well correlated with the n-heptane concentrations. From this, it can be suggested in DF-HCCI combustion that lower n-heptane concentrations (i.e., higher equivalence ratios) reduce the near-liner/crevice n-heptane oxidation rates, leaving the exhaust CH_4/THC ratio unchanged over the range of equivalence ratios.

Figure 8.9 shows the measured ethylene (C_2H_4), formaldehyde (CH_2O), and n-pentene (nC_5H_{10}) emissions concentrations for the DF-HCCI (green diamonds), SI (red circles), DPI (pink squares), and RCCI (blue triangles) cases. The vertical lines in each marker represent the range of one standard deviation. Ethylene, an alkene hydrocarbon, is a species that acts both as a precursor for soot formation and also as an agent for carbonaceous deposits on engine surfaces. Both behaviors are generally taken as detrimental to clean and efficient combustion. The first panel in Figure 8.9 shows that the ethylene exhaust concentrations are strongly influenced by equivalence ratio. However, in the richer regions, RCCI and SI

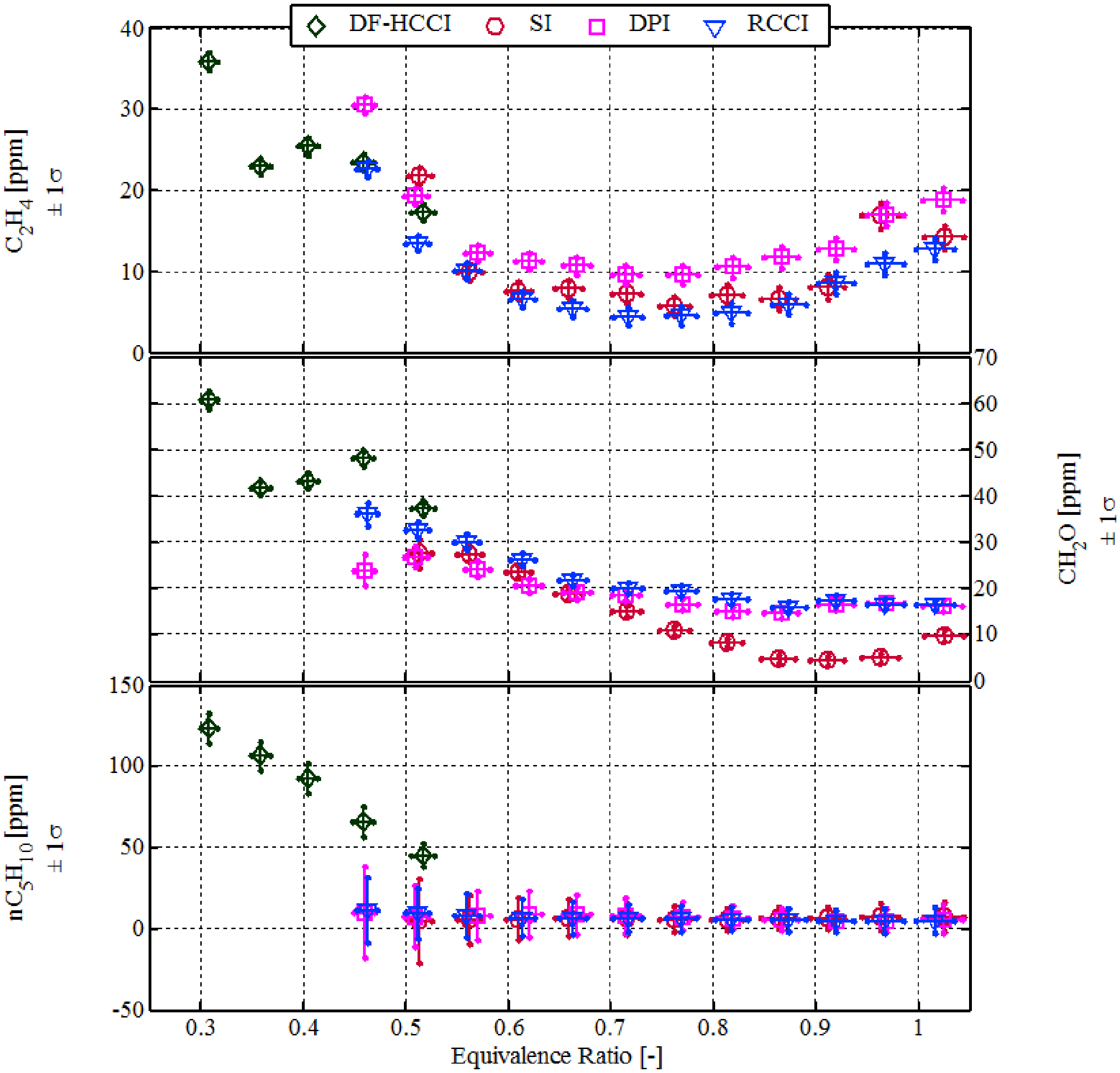

Figure 8.9: Ethylene (C_2H_4), formaldehyde (CH_2O), and n-pentene (nC_5H_{10}) emissions concentrations for the DF-HCCI (green diamonds), SI (red circles), DPI (pink squares), and RCCI (blue triangles) cases. The vertical lines in each marker represent the range of one standard deviation.

combustion (both which lack over-rich fuel regions) generate the lowest levels of ethylene relative to DPI combustion, which produces fuel-rich regions resulting from the close-coupled injection and combustion timings. Not enough data is available to make a sufficient comparison to DF-HCCI combustion, yet it is observed that DF-HCCI ethylene emissions reflect the equivalence ratio influence well.

The second panel in Figure 8.2.1 shows the measured exhaust concentrations of formaldehyde (CH_2O), an oxygenated aldehyde hydrocarbon that is adversely reactive in the human respiratory system. In the range of $\phi = 0.7$ - $\phi = 1.0$, SI combustion produces the lowest levels of formaldehyde, relative to RCCI and DPI combustion. This observation is attributed to the absence of in-cylinder pockets of n-heptane present during the SI combustion process. At leaner conditions, the formaldehyde emissions for all strategies are similar and increase with decreasing equivalence ratio (i.e., increasing oxygen concentrations).

8.2.2 Comparison of SI, DPI, RCCI, and DF-HCCI in a Heavy-Duty Engine at $\phi = 0.5$

In Section 8.2.1 a single equivalence ratio was seen where SI, DPI, RCCI, and DF-HCCI could be operated while meeting the performance constraints at $\phi = 0.5$. This section highlights the pressure and heat release characteristics and examines the energy balances with respect to each combustion strategy at $\phi = 0.5$.

Figure 8.10 shows the pressure and heat release data for the SI, DPI, RCCI, and DF-HCCI combustion strategies. The pressure traces are represented by solid lines and the calculated heat release rates are represented by dashed lines; SI data are colored red, DPI data are colored pink, RCCI data are colored blue, and DF-HCCI data are colored green.

As shown in Figure 8.6, the richest condition the DF-HCCI strategy could be operated was at $\phi = 0.5$, and was subject to the 25 bar per degree PPRR constraint. An advanced combustion phasing of 1° aTDC was required for stable combustion, and this resulted in a peak pressure of approximately 90 bar and a peak heat release rate of 550 J/degree.

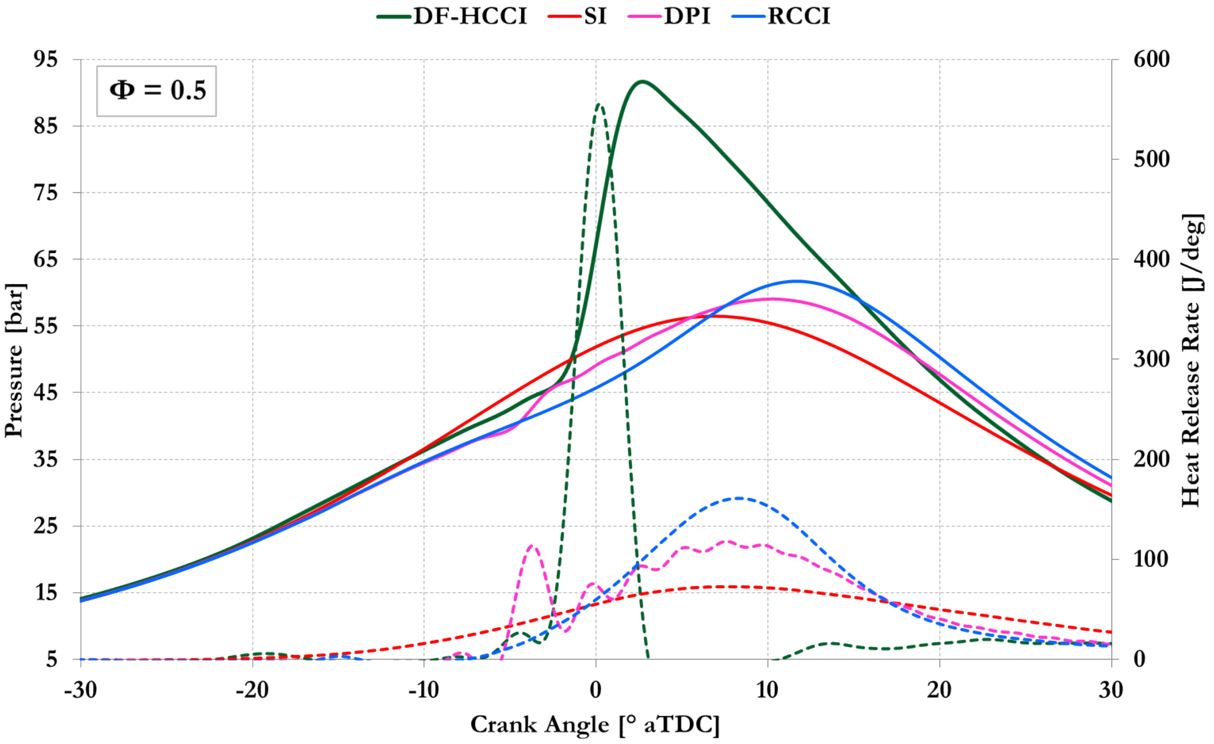

Figure 8.10: Cylinder pressure (solid lines) and heat release rate (dashed lines) for the equivalence ratio sweep. SI is denoted by red data, DPI is denoted by pink data, RCCI is denoted by blue data, and DF-HCCI is denoted by green data.

This rapid rate of heat release is characteristic of fully-premixed kinetically-controlled combustion. From the flame-rate-controlled SI combustion regime, a peak pressure of 56 bar and a peak heat release rate below 100 J/degree was measured. This docile combustion process is representative of the lean flame-extinction limit for methane where flame speeds rapidly approach zero in the range of $\phi = 0.6$ to $\phi = 0.5$ [91].

The direct-injected DPI and RCCI combustion strategies offer peak cylinder pressures below 65 bar and heat release rates between 100 and 200 J/degree. However, as highlighted in Chapter 6, the naturally-aspirated $\phi = 0.5$ DPI and RCCI heat release rates differ. DPI characteristically displays a two-stage high temperature heat release, whereas RCCI displays a single-stage high temperature heat release. The close-coupled injection and combustion event for DPI combustion generates a rapid autoignition event (which produces increased ringing as evidenced in Figure 8.6) during ignition; conversely RCCI combustion utilizes the reactivity stratification gradient to produce a smooth transition into high temperature heat release during ignition, generating a more sedate combustion event. For DPI combustion, the utilization of pilot ignition is capable of enhancing the rate of high temperature heat release relative to SI combustion. For RCCI combustion, the utilization of the early direct injection for controlling the reactivity stratification allows for significant reduction of the peak heat release rate (and thus, peak cylinder pressure) relative to fully-premixed DF-HCCI combustion.

Figure 8.11 shows the energy fractionalization for the dual-fuel homogeneous charge compression ignition, spark ignition, diesel pilot ignition, and reactivity controlled compression ignition combustion regimes at $\phi = 0.5$. It is shown that DF-HCCI achieves the lowest gross indicated thermal efficiency, below 35%. Even though the combustion efficiency is greater than 97%, the rapid heat release generates heat losses in excess of 40%. SI combustion achieves a thermal efficiency of approximately 39%, yet while heat losses are relatively low, it is the high amounts of unconverted fuel in the exhaust that provides the greatest inefficiency. DPI combustion obtains a thermal efficiency approaching 42% yet, like SI combustion, poor combustion efficiency impacts performance significantly. RCCI combustion is able to obtain a thermal efficiency in excess of 44%, with better fuel conversion than DPI combustion; in addition the heat losses are reduced with RCCI relative to DPI, providing an improved thermal efficiency.

Overall, in terms of lean-burn engine operation under naturally-aspirated conditions, the experimental results indicate that RCCI is the preferred lean-burn dual-fuel combustion strategy compared to DPI due to the improved fuel conversion efficiency and reduced heat loss, which results in a significant thermal efficiency gain of 2.8% absolute (6.7% relative).

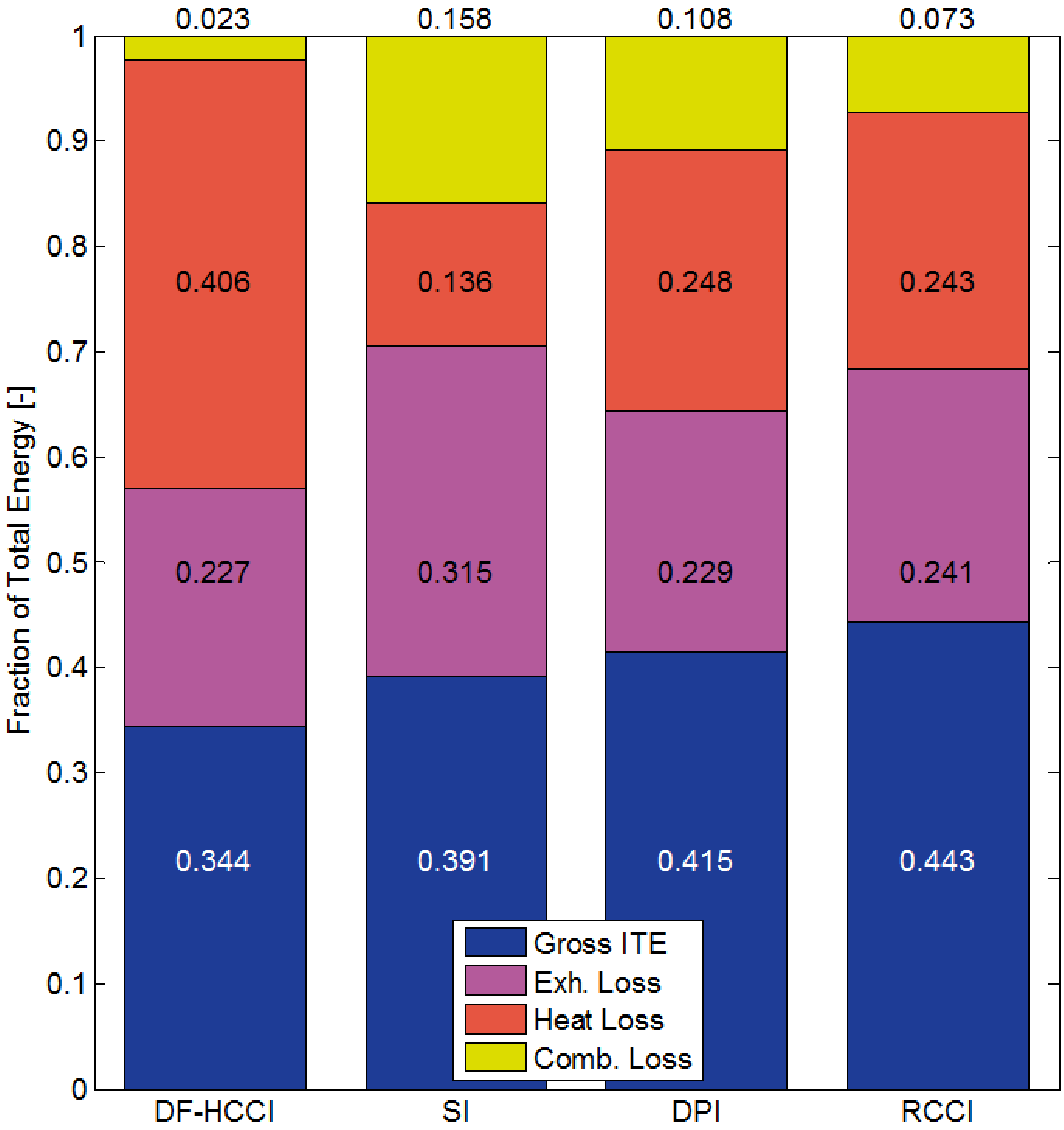

Figure 8.11: Energy balances for the DF-HCCI, SI, DPI, and RCCI combustion regimes at $\phi = 0.5$.

8.2.3 Effect of Engine Speed on the Rate of Heat Release in a Lean-Burn Dual-Fuel Heavy-Duty Engine

In the previous chapters it was demonstrated that two direct-injected dual-fuel combustion strategies, diesel pilot ignition and reactivity controlled compression ignition, provide superior engine performance over the fully-premixed combustion strategies, dual-fuel homogeneous charge compression ignition and single-fuel spark ignition, under matched engine conditions. The emissions profiles and heat release characteristics suggest that the DPI and RCCI combustion regimes may be dominated by different modes of heat release during high temperature combustion: flame propagation and autoignition, respectively.

For autoignition, volumetric energy release (demonstrated by DF-HCCI in Figure 8.10) is controlled by the kinetic rates of the in-cylinder species during the combustion process. The global kinetic rate is predominantly controlled by fuel composition, pressure, temperature, and availability of oxidizer. For flame propagation, an initial flame kernel in SI combustion is generated (or multiple kernels for DPI combustion), from which a flame front grows. The flame speed is then controlled by varying parameters such as oxidizer availability, pressure, temperature, chemical transport/diffusion, and localized turbulence levels.

While autoignition occurs simultaneously at multiple sites (DF-HCCI and RCCI) in the combustion chamber, a propagating flame is established at one (SI) or multiple (DPI) induced ignition locations from which the flame front grows. For RCCI engine operation, it is generally accepted that the combustion process depends upon sequential autoignition. The work of Kokjohn [58] demonstrated that the inception and growth of a flame kernel is inhibited under lean RCCI conditions; however, under richer RCCI operation, the inception and growth of a flame kernel can be established in a stable manner. For DPI engine operation, it is understood that the combustion process depends upon flame propagation [31]. Further work by Dronniou *et al.* [29] indicated the presence of a threshold for achieving flame propagation under RCCI-like engine conditions. However, high-fidelity direct numerical simulations (DNS) by Bhagatwala *et al.* [9] at $\phi = 0.52$ and $\phi = 0.69$ show that the heat release is dominated by flame propagation; It was also shown that the ignition location is generated where n-heptane concentration gradients are present.

In this section, experiments are undertaken to determine the dominant heat release mechanism for the RCCI and DPI combustion regimes. Using SI combustion as a baseline combustion regime where flame propagation is known to be the dominant mode of heat release, the characteristics of the heat release during RCCI and DPI combustion regimes are analyzed and compared. The engine operating conditions are presented in Table 8.6.

Table 8.6: Section 8.2.3 engine operating conditions.

Engine Speed	900, 1300, 1700 rev/min
IMEP$_g$	6 bar nominal
Fuel Energy	3,500 J/cycle
SI Methane Energy %	100%
DPI/RCCI Methane Energy %	96%
DPI/RCCI n-Heptane Energy %	4%
Equivalence Ratio ϕ	0.51 - 0.52
Intake Temperature	40 °C
Intake Pressure	1.0 bar
DI Injection Pressure	500 bar
DI Fuel	n-Heptane
PFI Fuel	Methane
EGR Rate	0%

The basis for the experiments in Section 8.2.3 is to examine the effect of engine speed on SI, DPI, and RCCI combustion. For SI combustion pure methane is fully premixed; for DPI and RCCI combustion 4% n-heptane is direct injected. The ignition timings (injection and spark) are held constant in time-space; the crank-angle-space timings are presented in Table 8.7.

Table 8.7: Section 8.2.3 ignition timings for the SI, DPI, and RCCI regimes.

	900 RPM	**1300 RPM**	**1700 RPM**
SI Spark Timing	-37.4° aTDC	-54.0° aTDC	-
DPI Injection Timing	-12.3° aTDC	-17.8° aTDC	-23.4° aTDC
RCCI Injection Timing	-20.8° aTDC	-30.0° aTDC	-39.2° aTDC

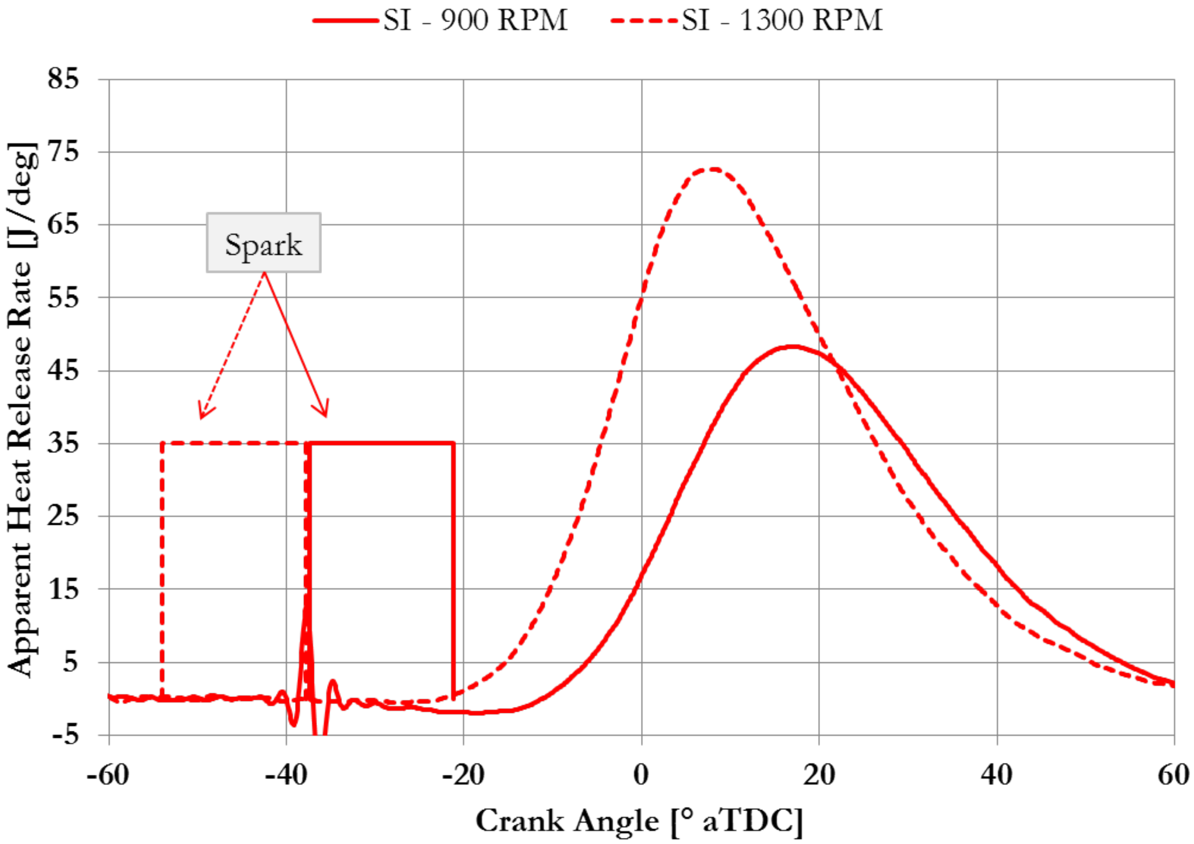

Figure 8.12: Crank angle-based heat release rates for SI combustion. 900 RPM data are denoted by solid lines; 1300 RPM data are denoted by dashed lines. Spark timing and duration is illustrated.

Figure 8.12 shows the *crank angle-based* heat release rates for SI combustion at 900 RPM and 1300 RPM. It is observed that the advanced spark timing results in advancing start of combustion. However, it is seen that the combustion duration is lengthened with increased engine speed: 60.3 CAD at 900 RPM compared to 66.0 CAD at 1300 RPM. In addition, the peak heat release rate is increased with increasing engine speed, showing that for SI combustion increasing engine speed is able to increase the rate of combustion during high temperature heat release, as expected.

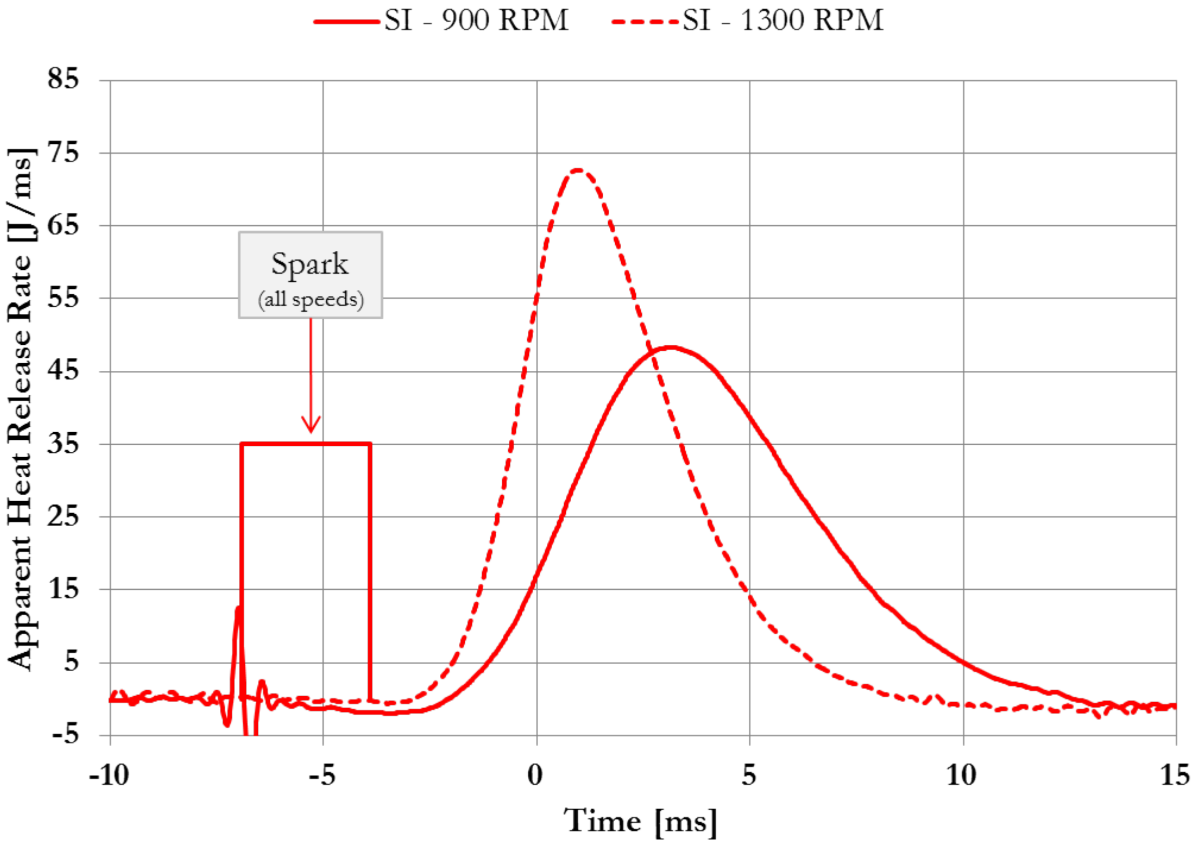

Figure 8.13: Time-based heat release rates for SI combustion. 900 RPM data are denoted by solid lines; 1300 RPM data are denoted by dashed lines. Spark timing and duration is illustrated.

Figure 8.13 shows the *time-based* heat release rates for SI combustion at 900 RPM and 1300 RPM. It is observed that the matched spark timing results in advancing start of combustion. Yet, it is seen that the combustion duration is decreased with increased engine speed: 11.2 ms at 900 RPM compared to 8.5 ms at 1300 RPM. As with the crank angle-based results, the peak heat release rate is increased with increasing engine speed, showing that for SI combustion increasing engine speed is able to increase the rate of combustion during high temperature heat release.

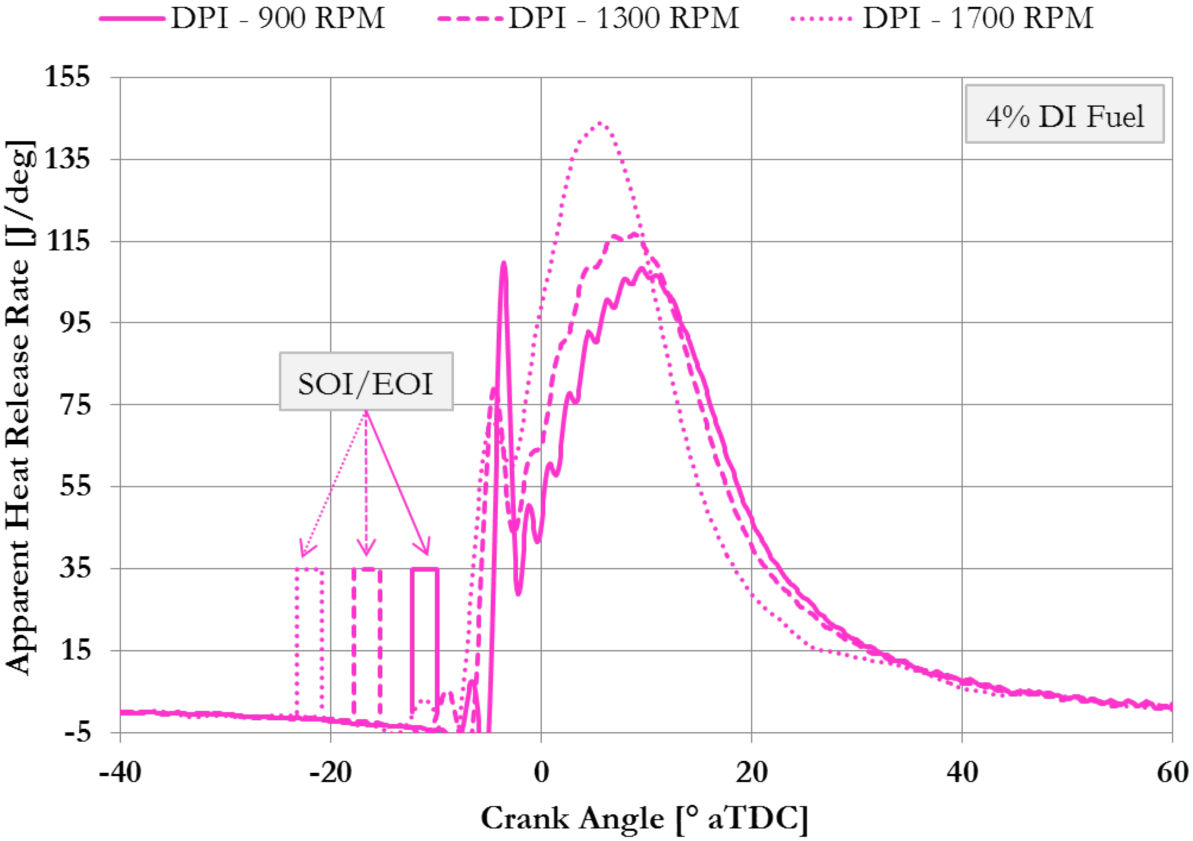

Figure 8.14: Crank angle-based heat release rates for DPI combustion. 900 RPM data are denoted by solid lines; 1300 RPM data are denoted by dashed lines; 1700 RPM data are denoted by dotted lines. Injection timing and duration is illustrated.

Figure 8.14 shows the *crank angle-based* heat release rates for DPI combustion at 900 RPM, 1300 RPM, and 1700 RPM. It is observed that the advanced ignition (i.e., injection) timing acutely advances the start of combustion, characteristic of the coupled injection-combustion event associated with DPI combustion. Again, like SI combustion, it is seen that the combustion duration is lengthened with increased engine speed, yet relatively weakly: 51.3 CAD at 900 RPM, 52.8 CAD at 1300 RPM, and 53.0 CAD at 1700 RPM. Furthermore, the peak heat release rate is also increased with increasing engine speed, showing that for DPI combustion increasing engine speed is able to increase the rate of combustion during the high temperature heat release phase.

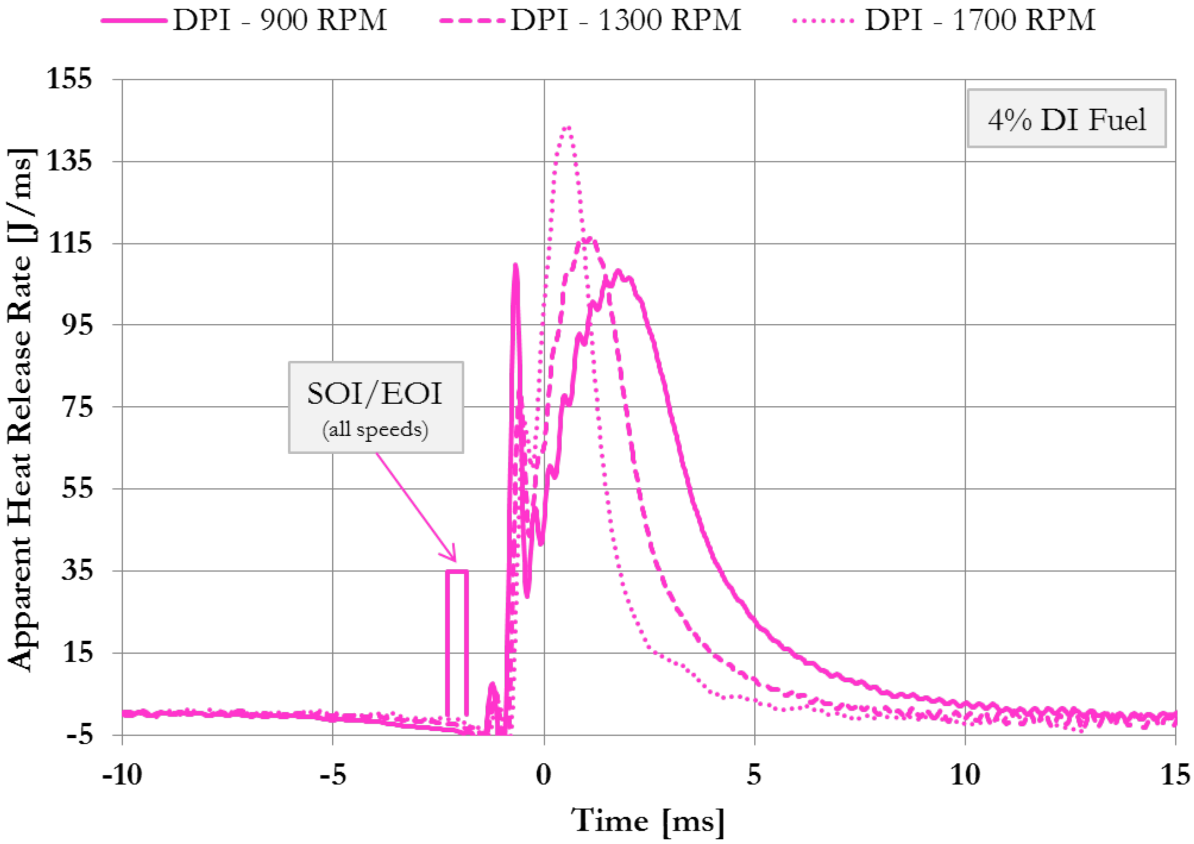

Figure 8.15: Time-based heat release rates for DPI combustion. 900 RPM data are denoted by solid lines; 1300 RPM data are denoted by dashed lines; 1700 RPM data are denoted by dotted lines. Injection timing and duration is illustrated.

Figure 8.15 shows the *time-based* heat release rates for DPI combustion at 900 RPM, 1300 RPM, and 1700 RPM. It is observed that the matched injection timing results in negligible delay of the start of combustion with increasing engine speed. Similar to SI combustion, for DPI combustion it is seen that the combustion duration is decreased with increased engine speed: 9.5 ms at 900 RPM, 6.8 ms at 1300 RPM, and 4.8 ms at 1700 RPM. As with the crank angle-based results, the peak heat release rate is increased with increasing engine speed, showing that for DPI combustion increasing engine speed is able to increase the rate of combustion during high temperature heat release.

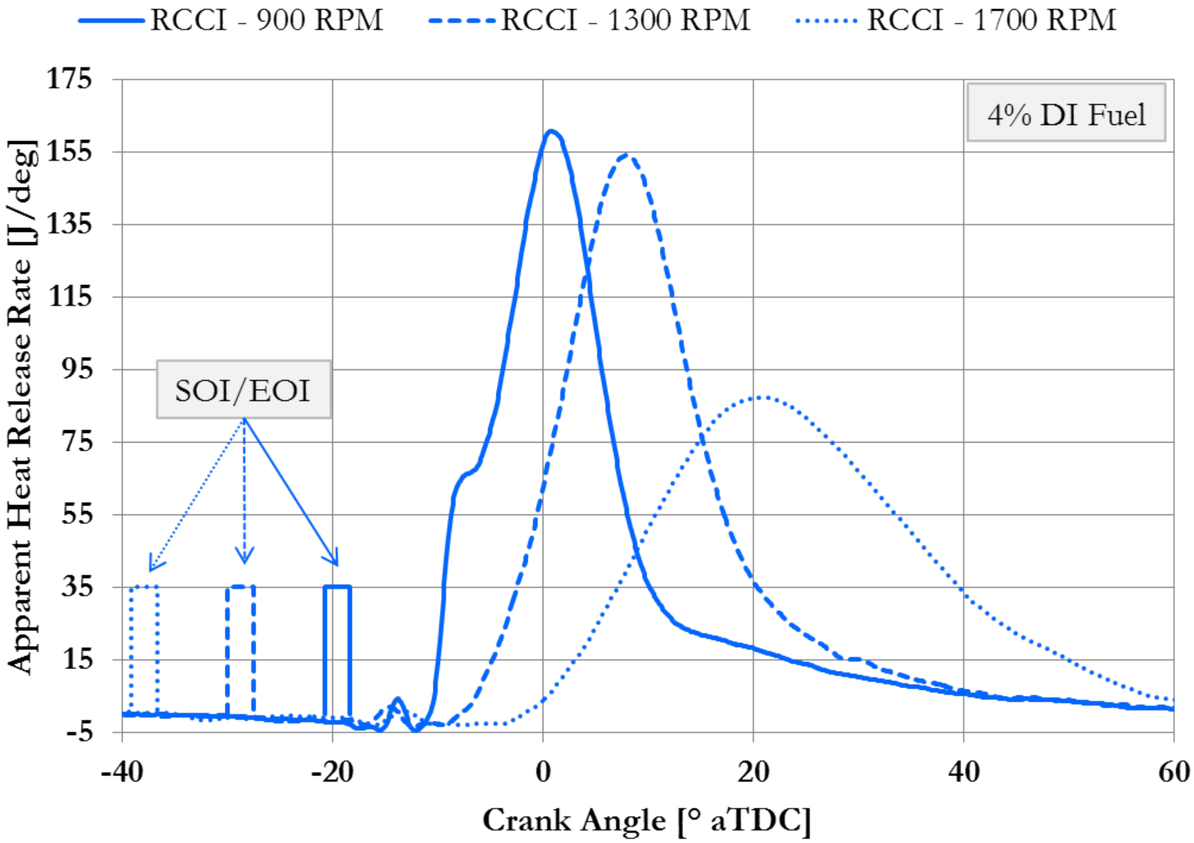

Figure 8.16: Crank angle-based heat release rates for RCCI combustion. 900 RPM data are denoted by solid lines; 1300 RPM data are denoted by dashed lines; 1700 RPM data are denoted by dotted lines. Injection timing and duration is illustrated.

Figure 8.16 shows the *crank angle-based* heat release rates for RCCI combustion at 900 RPM, 1300 RPM, and 1700 RPM. It is observed that the advanced injection timings retard the start of combustion, characteristic of the decoupled injection event associated with RCCI combustion. Similar to SI combustion, it is seen that the combustion duration is lengthened with increased engine speed: 47.7 CAD at 900 RPM, 49.1 CAD at 1300 RPM, and 57.2 CAD at 1700 RPM. However, unlike SI and DPI combustion, the peak heat release rate is decreased with increasing engine speed. This is attributed to the over-leaning of the direct injection.

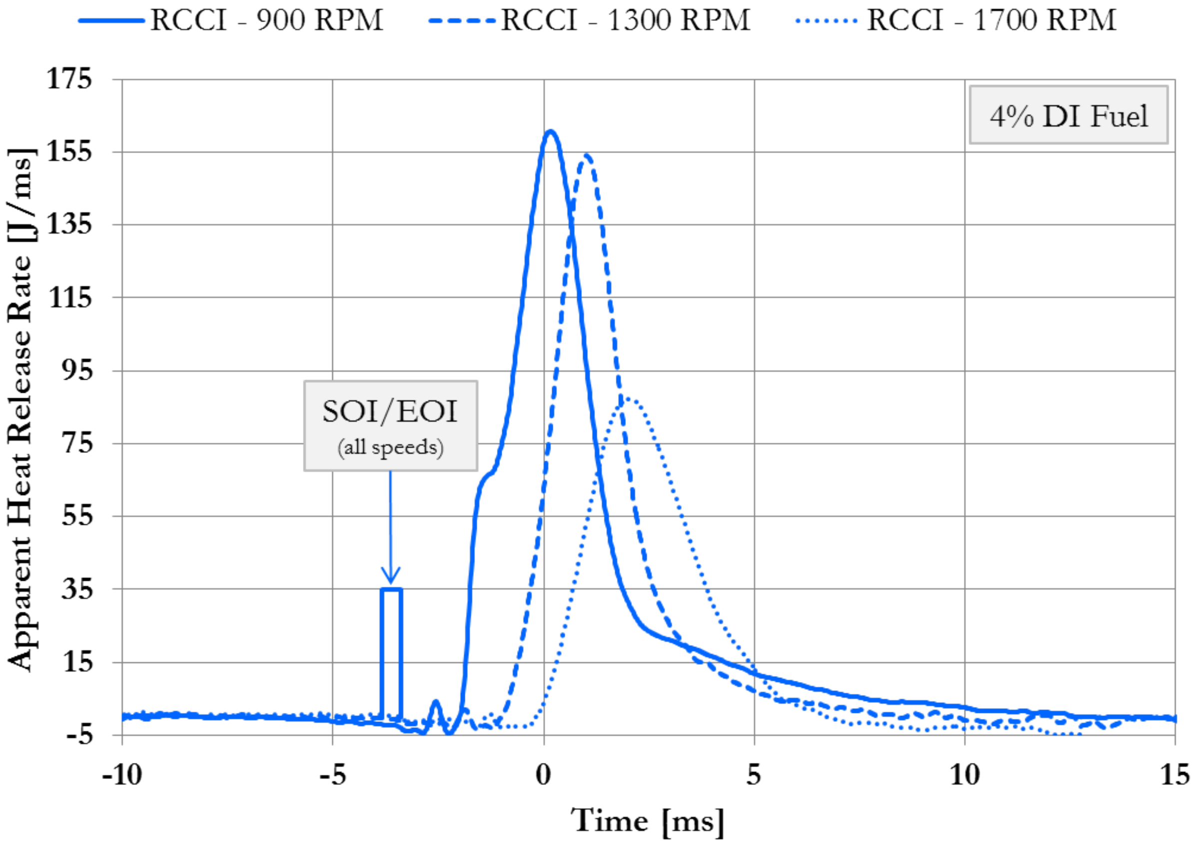

Figure 8.17: Time-based heat release rates for RCCI combustion. 900 RPM data are denoted by solid lines; 1300 RPM data are denoted by dashed lines; 1700 RPM data are denoted by dotted lines. Injection timing and duration is illustrated.

Figure 8.17 shows the *time-based* heat release rates for RCCI combustion at 900 RPM, 1300 RPM, and 1700 RPM. It is observed that the matched injection timing results in measurable delay of the start of combustion with increasing engine speed. Similar to SI and DPI combustion, for RCCI combustion it is seen that the combustion duration is decreased with increased engine speed: 9.6 ms at 900 RPM, 6.3 ms at 1300 RPM, and 5.6 ms at 1700 RPM. As with the crank angle-based results, the peak heat release rate is decreased with increasing engine speed, showing that for RCCI combustion increasing engine speed is able to extend the ignition delay and shorten the combustion duration.

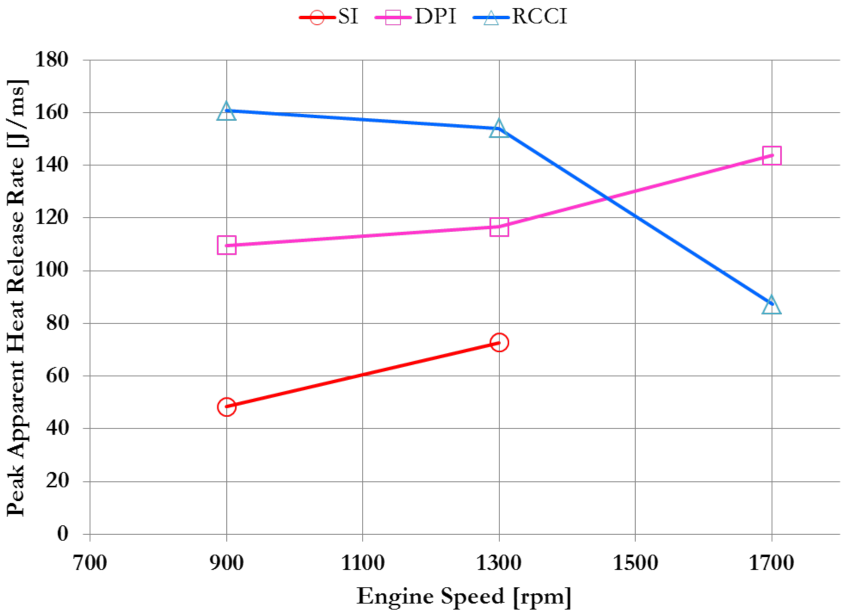

Figure 8.18: Peak apparent heat release rate as a function of engine speed. SI data are denoted by red circles; DPI data are denoted by pink squares; RCCI data are denoted by blue triangles.

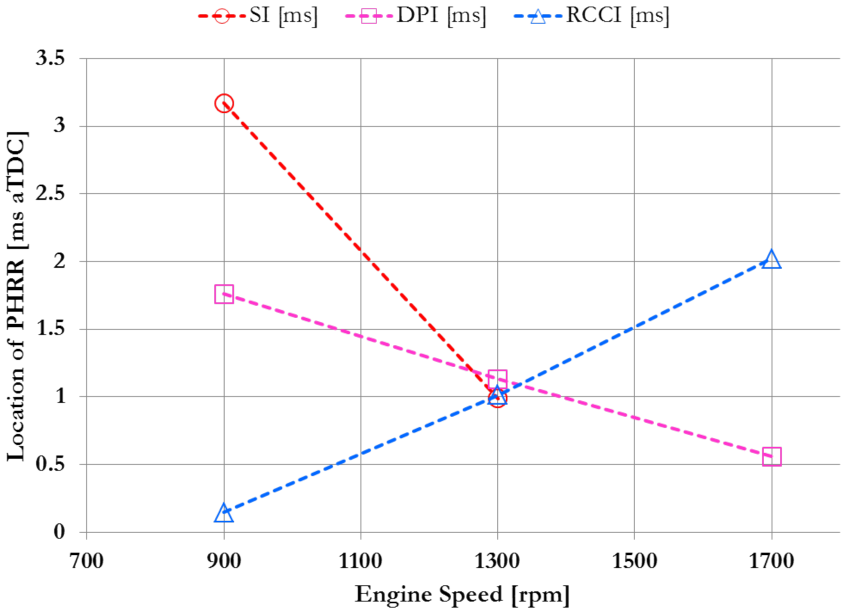

Figure 8.19: Time-based location of peak apparent heat release rate as a function of engine speed. SI data are denoted by red circles; DPI data are denoted by pink squares; RCCI data are denoted by blue triangles.

Finally, it should be noted that insufficient DF-HCCI results were obtained for valid comparison and analysis. At 1300 RPM, HCCI operation was established at $\phi = 0.5$, albeit with a limiting peak pressure rise rate of 25 bar per degree. With HCCI combustion widely understood to depend upon autoignition as the dominant mode of heat release, the ignition delay of the air-fuel mixture directly controls the combustion phasing. Keeping the same fuel ratio as the representative 1300 RPM DF-HCCI condition, at 900 RPM the combustion noise limits were exceeded, with peak pressure rise rates much greater than 25 bar per degree, conditions too severe for sustained engine operation long enough to obtain steady-state performance and subsequent data measurement. Conversely, at 1700 RPM, the engine simply misfired due to insufficient time for autoignition to occur for the air-fuel mixture, again insufficient for data measurement. However, relative to the RCCI results, with advancing phasing at lower engine speeds and retarding phasing at higher engine speeds further indicates the involvement of autoignition in both the DF-HCCI and RCCI combustion regimes.

8.3 Conclusions

Upon examination of the results presented in Section 8.2.3, namely Figures 8.13, 8.15, and 8.17, it is evident that the characteristics of the DPI combustion strategy behave similar in fashion to those of flame-controlled SI combustion. Figure 8.18 shows for SI and DPI, the peak apparent heat release rate increases with increasing engine speed. In Figure 8.19 is is shown that the location of the peak apparent heat release rate advances in time with increasing engine speed. These two factors, coupled with the observation that for both SI and DPI the combustion duration decreases with increasing engine speed, lead to the conclusion that flame propagation is involved and that the flame speed increases with engine speed.

In consideration of the turbulent processes influencing the combustion progression of the internal combustion engine, applying the Equations 8.1 and 8.2 from Pope [83]:

$$L = k^{(3/2)}/\epsilon \tag{8.1}$$

$$\tau = k/\epsilon \tag{8.2}$$

And using the relation of the engine speed, *RPM*, as the characteristic timescale and the bore, *b*, as the characteristic lengthscale:

$$RPM = 1/\tau \tag{8.3}$$

$$b = L \tag{8.4}$$

The following relation, stating that the turbulent kinetic energy is proportional to engine speed, is determined:

$$k = (b * RPM)^2 \tag{8.5}$$

With the following proportionalities [10, 68, 109]:

$$k \propto (u')^2 \tag{8.6}$$

$$S_T \propto u' \tag{8.7}$$

Leads to:

$$S_T \propto RPM \tag{8.8}$$

With this relationship, and based on the response of the heat release rate to engine speed, *the DPI combustion regime is concluded to be dominated by the flame propagation mode of heat release*, even in the lean flammability limit at an equivalence ratio of $\phi = 0.5$. It is also evidenced that the coupled injection-combustion event under DPI operation (i.e., advanced injection timing advances combustion phasing) is relatively uninfluenced by the effect of engine speed, as only negligible delays in the start of high temperature heat release are observed in Figure 8.15.

However, with respect to RCCI combustion, the influence of engine speed both reduces the peak apparent heat release rate and delays the start of high temperature combustion (i.e., extends the ignition delay). With the decoupled injection event under RCCI operation (i.e., advanced injection timing retards combustion phasing), the mixing timescale of the direct injection is significantly lengthened, allowing for the intensifying turbulence at higher engine speeds to have an effect on the DI mixing process. The turbulent viscosity, ν_T:

$$\nu_T \propto k^2/\epsilon \tag{8.9}$$

Which the turbulent diffusivity, *D*, is proportional to, and applying the above relations gives:

$$D \propto b^2 * RPM \tag{8.10}$$

This results states that the mixing rate of the direct injection spray will be directly influenced by the engine speed. With relation to the results in Figure 8.17, Equation 8.10 supports the experimental measurements that show the increasing ignition delay with increasing engine speed. Thus, based on the response of the ignition delay to engine speed at an equivalence ratio of $\phi = 0.5$, *the RCCI combustion regime is concluded to be governed by the autoignition mode of heat release*.

Furthermore, it is interesting to note that there is a measurable response of the combustion duration to engine speed, as shown in Figure 8.17. This indicates the possibility of a mixed mode combustion event for RCCI combustion where ignition and early-stage high temperature heat release depend upon the autoignition of the air-fuel mixture in the localized regions of the direct injected spray, and late-stage high temperature heat release is dominated by turbulent flamelets throughout the rest of the premixed air-fuel mixture in the combustion chamber. However, insufficient evidence exists to fully determine the extent of the roles of either mode of heat release.

9 SUMMARY & FUTURE WORK

9.1 CFD Investigation of Reactivity Controlled Compression Ignition Using Methane

In Chapter 4 a computational study was performed to explore the effects of using methane as the premixed fuel for RCCI combustion in a light-duty engine geometry. PRF75, PRF100, and CH_4 were selected as low reactivity fuels. The results are summarized as follows.

9.1.1 Effect of Fuel Reactivity on Operating Range

It was shown that as the premixed fuel becomes less reactive, the dependence on EGR to mitigate the formation of NO_x is reduced; in addition, more DI fuel is required to stay within the acceptable operating window; and finally, the PPRR constraint becomes less of a factor in defining the acceptable operating range.

9.1.2 Comparison of Operation at Fixed EGR Rate

When comparing engine operation at a fixed EGR rate, it was observed that by moving to premixed fuels with longer ignition delays, EGR requirements for meeting combustion noise limits may be reduced, thus leading to the potential for an extension of the upper load limit for a given operating condition.

9.2 Natural Gas for High Load Reactivity Controlled Compression Ignition

Based upon the results of the computational study of Chapter 4, heavy-duty single-cylinder experiments were performed next to examine the load extension capability of methane for RCCI combustion. Methane was compared against gasoline as the low reactivity fuel.

9.2.1 Heat Release Analysis

For gasoline/diesel operation, as seen in Chapter 5 the CA10-90 combustion duration *shortened* as the engine load was increased. Conversely, for methane/diesel operation the CA10-90 combustion duration *lengthened* as the engine load was increased. In addition, (as shown in Figure 5.3) when the load was increased for gasoline/diesel operation, the start of high temperature heat release became *less* sensitive to DI SOI timing to control combustion phasing, while for methane/diesel operation the opposite was observed with respect to combustion phasing control: as the engine load was increased the start of high temperature heat release became *more* sensitive to DI SOI timing.

9.2.2 Fuel Effects on Engine Performance

Upon examining two metrics of combustion stability, COV of IMEP and COV of PPRR, it was shown that methane/diesel RCCI combustion is significantly more stable than gasoline/diesel RCCI combustion. In addition, by moving to an earlier combustion phasing, both the COV of IMEP and COV of PPRR could be reduced.

9.2.3 Analysis of Engine Load Capability

For gasoline/diesel RCCI operation, the upper load limit was found to be approximately 7 bar IMEP_g. For methane/diesel RCCI operation, the engine load was extended to 15.4 bar IMEP_g at a combustion phasing of CA50 = 0° aTDC. By retarding the combustion phasing to CA50 = 4° aTDC, the maximum load was estimated to be extended considerably to 17.3 bar IMEP_g. Thus, methane/diesel RCCI operation allows for significant engine load extension over gasoline/diesel RCCI combustion.

9.3 Comparison of Diesel Pilot Ignition and Reactivity Controlled Compression Ignition

The objective of the study described in Chapter 6 was to examine the use of methane (as a natural gas surrogate fuel) as the less-reactive fuel for RCCI and DPI and to develop an improved understanding of the impact of each dual-fuel combustion regime on engine noise, emissions, and efficiency.

9.3.1 Combustion Regime Change from DPI to RCCI with Injection Timing

Figure 6.3 highlights the transition between the DPI and RCCI combustion regimes. At the relatively rich condition of ϕ=0.72 the performance (noise, emissions, and efficiency) characteristics of both combustion strategies was comparable. However, RCCI combustion generated approximately half of the HC emissions compared to DPI combustion. Furthermore, an examination of the heat release rates for the two combustion strategies indicated that there may be differences in the heat release mechanism(s) of each combustion strategy.

9.3.2 Effect of Equivalence Ratio on DPI and RCCI Combustion

It was observed that at relatively rich conditions (ϕ=0.72) the combustion performance of each combustion regime was similar. However, as the conditions became leaner, the combustion performance improved for RCCI combustion, but was degraded for DPI combustion. At the leanest condition (ϕ=0.50), RCCI has significantly higher thermal efficiency, markedly reduced combustion noise, and lower emissions.

9.3.3 DPI and RCCI Response to Fueling Rate Increase

It was seen that the fueling rate has little effect on the combustion performance as the engine load was increased. However, combustion noise, emissions, and efficiency was markedly improved with RCCI combustion relative to DPI combustion. RCCI combustion offered, on average, an 8% absolute increase in thermal efficiency over DPI combustion. Further analyis showed that, on average across the range of fueling rates, the DPI combustion regime has a 5% absolute greater combustion loss, 3% absolute heat loss, and 1% absolute greater exhaust loss relative to the RCCI combustion regime.

9.4 Effect of Premixed Methane Ratio on DPI and RCCI Combustion

In a more focused examination, Chapter 7 studied both RCCI and DPI combustion over a range of premixed methane ratios from 86% to 95% and a range of equivalence ratios from $\phi = 0.3$ to $\phi = 0.6$ and considered the global emission/efficiency tradeoffs.

9.4.1 Effect of Equivalence Ratio and Premix Methane Ratio on Performance and Emissions

With respect to the global/premixed equivalence ratio, it was observed that at high equivalence ratios, DPI is able to operate richer than RCCI before meeting the NO_x threshold. It was also seen that at low equivalence ratios, RCCI was able to operate leaner than DPI before meeting the HC threshold. Furthermore, for both DPI and RCCI combustion, higher premixed methane ratios provided NO_x reductions.

9.4.2 Analysis of Global Emission and Efficiency Tradeoffs

With diesel pilot ignition, a much stronger HC-NO$_x$ tradeoff was shown relative to reactivity controlled compression ignition combustion. Additionally, the HC-NO$_x$ tradeoff trends are opposite between the two dual-fuel combustion strategies: DPI achieved lower emissions with more premixed methane; RCCI achieved lower emissions with less premixed methane. Interestingly, DPI combustion was quieter with increasing equivalence ratio whereas RCCI combustion was louder.

9.5 Determination of Heat Release Mechanism for Diesel Pilot Ignition and Reactivity Controlled Compression Ignition

In Chapter 8 four combustion strategies were compared on a heavy-duty engine platform: dual-fuel homogeneous charge compression ignition (DF-HCCI), reactivity controlled compression ignition (RCCI), diesel pilot ignition (DPI), and spark ignition (SI). Then, the RCCI and DPI dual-fuel combustion strategies were compared to baseline SI data over a range of engine speeds in order to determine the characteristic mode of heat release for the RCCI and DPI dual-fuel combustion strategies.

9.5.1 Performance and Emissions Characteristics of DF-HCCI, RCCI, DPI and SI Combustion Regimes

Importantly, the viable operating range achieved for each combustion strategy, with respect to equivalence ratio, showed that fully-premixed DF-HCCI combustion was severely limited to a naturally-aspirated operating range of $\phi = 0.3$ to $\phi = 0.5$. Conversely, the viable operating range for fully-premixed SI combustion covered an equivalence ratio range from

$\phi = 0.5$ to $\phi = 1.0$. For DPI and RCCI combustion, similar performance was obtained across the equivalence ratio range from $\phi = 0.45$ to $\phi = 1.0$.

9.5.2 Comparison of SI, DPI, RCCI, and DF-HCCI in a Heavy-Duty Engine at $\phi = 0.5$

Overall, in terms of lean-burn engine operation under naturally-aspirated conditions, the experimental results indicated that RCCI is the preferred lean-burn dual-fuel combustion strategy compared to DPI due to the improved fuel conversion efficiency and reduced heat loss, which resulted in a significant thermal efficiency gain of 2.8% absolute (6.7% relative).

9.5.3 Effect of Engine Speed on the Rate of Heat Release

Based on the response of the heat release rate to engine speed changes, *the DPI combustion regime is concluded to be dominated by the flame propagation mode of heat release*, even in the considered lean flammability range at an equivalence ratio of $\phi = 0.5$. It was also evidenced that the coupled injection-combustion event under DPI operation (i.e., advanced injection timing advances combustion phasing) was relatively uninfluenced by the effect of engine speed. The RCCI results suggested that the mixing rate of the direct injection spray was directly influenced by the engine speed. Based on the response of the ignition delay to engine speed at an equivalence ratio of $\phi = 0.5$, *the RCCI combustion regime is concluded to be governed by the autoignition mode of heat release*.

9.6 Future Work

9.6.1 CFD Optimization of High Power Density Natural Gas Dual-Fuel Engine

In the present research it was shown that, by moving to a premixed fuel that is more resistant to autoignition (i.e., higher octane number), the dependence on EGR to mitigate NO_x and combustion noise can be reduced. A corollary to that finding indicates the capability to moving to higher compression ratios for utilization of premixed fuels that are more resistant to autoignition. Powerful CFD optimization techniques can be applied, coupling multi-dimensional combustion modeling and multi-objective genetic algorithms, to predict a specified combustion chamber (and even broader engine system) model for experimental study in the laboratory. Considering the low-mass direct injections for RCCI and DPI, injection pressures above 500 bar are deemed unnecessary, which may play an influencing role in determining the best-performing piston geometry.

9.6.2 Kinetic Analysis of Dual-Fuel Combustion using Natural Gas

Experimental results in this work revealed different significantly different combustion characteristics for gasoline/diesel RCCI combustion relative to methane/diesel RCCI combustion. Applying kinetic modeling and analysis techniques will provide further insight into the chemical processes governing heat release during combustion. In addition, the results from this work can provide important experimental validation data for mechanism and model development for computational research.

9.6.3 Multi-Mode Control Strategy for Natural Gas Dual-Fuel Engine

Modern and legacy natural gas dual-fuel engine systems rely broadly upon the diesel pilot ignition combustion strategy. However, vast improvements in engine air handling systems have allowed for leaner engine operation providing reduced emissions and increased efficiency. As this research has noted, DPI combustion is dependent upon the flame speed of the air-fuel mixture, whereas RCCI combustion is not. In order to harness the benefits of lean-burn natural gas dual-fuel engines, the development of a multi-mode combustion control system is proposed, where RCCI combustion operates below the lean flammability limit of the premixed fuel, and DPI combustion operates above the lean flammability limit up to stoichiometric operation, resulting in an improved operating map.

9.6.4 Study of Combustion Noise Effects in Natural Gas Dual-Fuel Combustion

Results throughout this work showed that DPI combustion generated less combustion noise compared to RCCI combustion at richer conditions. However, at leaner conditions RCCI generated less combustion noise compared to DPI combustion. Further investigation into the physical processes and influence of engine parameters on the generated combustion noise for natural gas dual-fuel combustion strategies is warranted.

9.6.5 Detailed Study of Heat Release Mechanisms in Natural Gas Dual-Fuel Combustion

Overall, this body of work concluded that DPI was dominated by the flame propagation mode of heat release and RCCI was dominated by the autoignition mode of heat release for the experiments performed at $\phi = 0.5$. The equivalence ratio of $\phi = 0.5$ appears to be a transition point where autoignition dominates under leaner conditions and flame propagation dominates under richer conditions, as $\phi = 0.5$ was the maximum equivalence ratio obtained for DF-HCCI and the minimum equivalence ratio obtained for SI. It is encouraged that similar experimental studies investigate the role of autoignition and flame propagation at leaner and richer equivalence ratio to further understand the governing heat release processes controlling RCCI and DPI combustion for natural gas dual-fuel engines.

9.6.6 Investigation of Natural Gas Fuel for Advanced Dual-Fuel Combustion

Methane, as the major constituent of natural gas, is a low-carbon fuel amenable to high-efficiency engine operation. Yet, a variety of other natural gas fuels exist in the marketplace which warrant further investigation on their use in engines. For example, propane and dimethyl ether are two natural gas fuels that are liquid under moderate pressure (unlike high pressure CNG/LNG) that behave like improved gasoline and diesel fuels, respectively. The ability to efficiently and safely handle propane and dimethyl ether as liquid fuels suggests opportunities for use in mobile natural gas engine systems, which warrants further study.

BIBLIOGRAPHY

---

[1] N. Abani, A. Munnannur, and R. D. Reitz. Reduction of Numerical Parameter Dependencies in Diesel Spray Models. *Journal of Engineering for Gas Turbines and Power*, 130, 2008.

[2] A. A. Amsden. KIVA-3V: A Block-Structured KIVA Program for Engines with Vertical or Canted Valves. In *Los Alamos National Laboratory Report LA-13313-MS*, 1997.

[3] A. A. Amsden. KIVA-3V, Release 2, Improvements to KIVA-3V. In *Los Alamos National Laboratory Report LA-UR-99-915*, 1999.

[4] A. A. Amsden, P. J. O'Rourke, and T. D. Butler. KIVA-II - A Computer Program for Chemically Reactive Flows with Sprays. In *Los Alamos National Laboratory Report LA-11560-MS*, 1989.

[5] M. L. Aucott and J. M. Melillo. A Preliminary Energy Return on Investment Analysis of Natural Gas from the Marcellus Shale. *Journal of Industrial Ecology*, 2013.

[6] R. Basshuysen and F. Schäfer. *Internal Combustion Engine Handbook*, pages 1–7. Society of Automotive Engineers International, Germany, 2002.

[7] J. C. Beale and R. D. Reitz. Modeling Spray Atomization with the Kelvin-Helmholtz/Rayleigh-Taylor Hybrid Model. *Atomization and Sprays*, 9:623 – 650, 1999.

[8] P. W. Bessonette, C. H. Schleyer, K. P. Duffy, W. L. Hardy, and M. P. Liechty. Effects of Fuel Property Changes on Heavy-Duty HCCI Combustion. *SAE Technical Paper 2007-01-0191*, 2007.

[9] A. Bhagatwala, R. Sankaran, S. L. Kokjohn, and J. H. Chen. Numerical Investigation of Spontaneous Flame Propagation Under RCCI Conditions. *Combustion and Flame*, 162:3412 – 3426, 2015.

[10] S. Bopp, C. Vafidis, and J. H. Whitelaw. The Effect of Engine Speed on the TDC Flowfield in a Motored Reciprocating Engine. *SAE Technical Paper 860023*, 1986.

[11] R. L. Boyer. Status of Dual Fuel Engine Development. *Society of Automotive Engineers*, 1949.

[12] J. Buglass, T. Morgan, and J. Graupner. Interactions Between Exhaust Gas Composition and Oxygen Sensor Performance. *SAE Technical Paper 982646*, 1998.

[13] H. M. Cho and B. Q. He. Spark Ignition Natural Gas Engines - A Review. *Energy Conversion & Management*, 48:610–618, 2007.

[14] S. Curran, V. Prikhodko, K. Cho, C. S. Sluder, J. Parks, R. Wagner, S. Kokjohn, and R. D. Reitz. In-Cylinder Fuel Blending of Gasoline/Diesel for Improved Efficiency and Lowest Possible Emissions on a Multi-Cylinder Light-Duty Diesel Engine. *SAE Technical Paper 2010-01-2206*, 2010.

[15] S. Curran, R. Hanson, and R. Wagner. Effect of E85 on RCCI Performance and Emissions on a Multi-Cylinder Light-Duty Diesel Engine. *SAE Technical Paper 2012-01-0376*, 2012.

[16] S. Curran, R. Hanson, R. Wagner, and R. Reitz. Efficiency and Emissions Mapping of RCCI in a Light-Duty Diesel Engine. *SAE Technical Paper 2013-01-0289*, 2013.

[17] M. Dahodwala, S. Joshi, E. Koehler, and M. Franke. Investigation of Diesel and CNG Combustion in a Dual Fuel Regime and as an Enabler to Achieve RCCI Combustion. *SAE Technical Paper 2014-01-1308*, 2014.

[18] J. E. Dec and Y. Yang. Boosted HCCI for High Power without Engine Knock and with Ultra-Low NOx Emissions - Using Conventional Gasoline. *SAE Technical Paper 2010-01-1086*, 2010.

[19] J. E. Dec, Y. Yang, and N. Dronniou. Boosted HCCI - Controlling Pressure-Rise Rates for Performance Improvements using Partial Fuel Stratification with Conventional Gasoline. *SAE Technical Paper 2011-01-0897*, 2011.

[20] A. Dempsey, S. Curran, J. Storey, M. Eibl, J. Pihl, V. Prikhodko, R. Wagner, and J. Parks. Particulate Matter Characterization of Reactivity Controlled Compression Ignition (RCCI) on a Light Duty Engine. *SAE Technical Paper 2014-01-1596*, 2014.

[21] A. B. Dempsey. *Dual-Fuel Reactivity Controlled Compression Ignition (RCCI) with Alternative Fuels*. Doctoral dissertation, University of Wisconsin - Madison, 2013.

[22] A. B. Dempsey and R. D. Reitz. Computational Optimization of a Heavy-Duty Compression Ignition Engine Fueled with Conventional Gasoline. *SAE Technical Paper 2011-01-0356*, 2011.

[23] A. B. Dempsey, B. Das Adhikary, S. Viswanathan, and R. D. Reitz. Reactivity Controlled Compression Ignition Using Premixed Hydrated Ethanol and Direct Injection Diesel. In *ASME 2011 Internal Combustion Engine Division Fall Technical Conference*, pages 963–975, 2001.

[24] A. B. Dempsey, B. Das Adhikary, S. Viswanathan, and R. D. Reitz. Characterization of Reactivity Controlled Compression Ignition (RCCI) Using Premixed Hydrated Ethanol and Direct Injection Diesel in Heavy-Duty and Light-Duty Engines. In *THIESEL 2012 Conference on Thermo- and Fluid Dynamic Processes in Direct Injection Engines*, Valencia, Spain, Sept. 2012.

[25] A. B. Dempsey, N. R. Walker, E. Gingrich, and R. D. Reitz. Comparison of Low Temperature Combustion Strategies for Advanced Compression Ignition Engines with a Focus on Controllability. *Combustion Science and Technology*, 186(2):210–241, 2013.

[26] A. B. Dempsey, N. R. Walker, and R. D. Reitz. Effect of Cetane Improvers on Gasoline, Ethanol, and Methanol Reactivity and the Implications for RCCI Combustion. *SAE Int. J. Fuels Lubr.*, 6(1):170–187, 2013.

[27] R. Diesel. Internal Combustion Engine. *Patent No. US608845 A*, 1898.

[28] E. Doosje, F. Willems, and R. Baert. Experimental Demonstration of RCCI in Heavy-Duty Engines using Diesel and Natural Gas. *SAE Technical Paper 2014-01-1318*, 2014.

[29] N. Dronniou, J. Kashdan, B. Lecointe, K. Sauve, and D. Soleri. Optical Investigation of Dual-fuel CNG/Diesel Combustion Strategies to Reduce CO2 Emissions. *SAE Technical Paper 2014-01-1313*, 2014.

[30] J. Eichmeier, F. Bach, C. Sauer, and U. Wagner. Gasoline Auto Ignition with Diesel Pilot Injection. *MTZ - Motortechnische Zeitschrift*, 2013.

[31] M. A. Elliott and R. F. Davis. Dual-Fuel Combustion in Diesel Engines. *American Chemical Society*, 1951.

[32] J. Eng. Characterization of Pressure Waves in HCCI Combustion. *SAE Technical Paper 2002-01-2859*, 2002.

[33] C. R. Ferguson and A. T. Kirkpatrick. *Internal Combustion Engines: Applied Thermosciences*, pages 1–29. Wiley, United Kingdom, 2015.

[34] C. E. A. Finney, B. C. Kaul, C. S. Daw, R. M. Wagner, K. D. Edwards, and J. B. Green. A Review of Deterministic Effects in Cyclic Variability of Internal Combustion Engines. *International Journal of Engine Research*, 16(3):366 – 378, 2015.

[35] M. Gallagher. The Future of Natural Gas as a Transportation Fuel. In *DOE EIA 2013 Energy Conference*, June 2013.

[36] Z. Han and R. D. Reitz. Turbulence Modeling of Internal Combustion Engines Using RNG k-e Models. *Combustion Science and Technology*, 106:267 – 295, 1995.

[37] R. Hanson, D. Splitter, and R. D. Reitz. Operating a Heavy-Duty Direct-Injection Compression Ignition Engine with Gasoline for Low Emissions. *SAE Technical Paper 2009-01-1442*, 2009.

[38] R. Hanson, S. Kokjohn, D. Splitter, and R. D. Reitz. Fuel Effects on Reactivity Controlled Compression Ignition (RCCI) Combustion at Low Load. *SAE Int. J. Engines*, 4 (1):394–411, 2011.

[39] R. Hanson, A. Ickes, and T. Wallner. Use of Adaptive Injection Strategies to Increase the Full Load Limit of RCCI Operation. In *ASME 2015 Internal Combustion Engine Division Fall Technical Conference*, 2015.

[40] R. Hanson, A. Ickes, and T. Wallner. Comparison of RCCI Operation with and without EGR over the Full Operating Map of a Heavy-Duty Diesel Engine. *SAE Technical Paper 2016-01-0794*, 2016.

[41] R. M. Hanson. *RCCI Combustion in a Light-Duty Multi-Cylinder Engine*. Doctoral dissertation, University of Wisconsin - Madison, 2013.

[42] R. M. Hanson, S. L. Kokjohn, D. A. Splitter, and R. D. Reitz. An Experimental Investigation of Fuel Reactivity Controlled PCCI Combustion in a Heavy-Duty Engine. *SAE Technical Paper 2010-01-0864*, 2010.

[43] R. Hasegawa and H. Yanagihara. HCCI Combustion in DI Diesel Engine. *SAE Technical Paper 2003-01-0745*, 2003.

[44] J. B. Heywood. *Internal Combustion Engine Fundamentals*, pages 1–40. McGraw-Hill, New York, 1988.

[45] J. Hiltner. Private Communication, 2015.

[46] J. Hiltner, S. Fiveland, R. Agama, and M. Willi. System Efficiency Issues for Natural Gas Fueled HCCI Engines in Heavy-Duty Stationary Applications. *SAE Technical Paper 2002-01-0417*, 2002.

[47] J. Hiltner, R. Agama, F. Mauss, B. Johansson, and M. Christensen. Homogeneous Charge Compression Ignition Operation with Natural Gas: Fuel Composition Implications. *Journal of Engineering for Gas Turbines and Power*, 125:837–844, 2003.

[48] V. Hosseini and M. D. Checkel. Reformer Gas Composition Effect on HCCI Combustion of n-Heptane, iso-Octane, and Natural Gas. *SAE Technical Paper 2008-01-0049*, 2008.

[49] K. Inagaki, T. Fuyuto, K. Nishikawa, K. Nakakita, and I. Sakata. Dual-Fuel PCI Combustion Controlled by In-Cylinder Stratification of Ignitability. *SAE Technical Paper 2006-01-0028*, 2006.

[50] Y. Ishibashi. Basic Understanding of Activated Radical Combustion and Its Two-Stroke Engine Application and Benefits. *SAE Technical Paper 2000-01-1836*, 2000.

[51] T. Ishiyama, M. Shioji, S.-i. Mitani, and H. Shibata. Improvement of Performance and Exhaust Emissions in a Converted Dual-Fuel Natural Gas Engine. *SAE Technical Paper 2000-01-1866*, 2000.

[52] S. Jung, M. Ishida, H. Ueki, and D. Sakaguchi. Ignition Characteristics of Methanol and Natural-Gas in a HCCI Engine Assisted by DME. *SAE Technical Paper 2007-01-1863*, 2007.

[53] G. T. Kalghatgi, P. Risberg, and H.-E. Angstrom. Advantages of Fuel with High Resistance to Auto-Ignition in Late-Injection, Low-Temperature, Compression Ignition Combustion. *SAE Technical Paper 2006-01-3385*, 2006.

[54] R. J. Kee, F. M. Rupley, and J. A. Miller. CHEMKIN-II: A FORTRAN Chemical Kinetics Package for the Analysis of Gas Phase Chemical Kinetics. In *Sandia National Laboratory Report SAND-89-8009*, 1989.

[55] S. Kimura, O. Aoki, Y. Kitahara, and E. Aiyoshizawa. Ultra-Clean Combustion Technology Combining a Low-Temperature and Premixed Combustion Concept for Meeting Future Emissions Standards. *SAE Technical Paper 2001-01-0200*, 2001.

[56] Y. Kobashi, D. Tanaka, T. Maruko, S. Kato, M. Kishiura, and J. Senda. Effects of Mixedness and Ignition Timings on PCCI Combustion with a Dual Fuel Operation. *SAE Technical Paper 2011-01-1768*, 2011.

[57] S. Kokjohn, R. D. Reitz, D. Splitter, and M. Musculus. Investigation of Fuel Reactivity Stratification for Controlling PCI Heat-Release Rates Using High-Speed Chemiluminescence Imaging and Fuel Tracer Fluorescence. *SAE Int. J. Engines*, 5(2):248–269, 2012.

[58] S. L. Kokjohn. *Reactivity Controlled Compression Ignition (RCCI) Combustion*. Doctoral dissertation, University of Wisconsin - Madison, 2012.

[59] S. L. Kokjohn and R. D. Reitz. A Modeling Study of Charge Preparation and Combustion in an HCCI Engine Using a Variable Pressure Pulse (VPP) Injection System and Optimized PRF Blends. In *11th International Conference on Liquid Atomization and Spray Systems*, July 2009.

[60] S. L. Kokjohn, R. M. Hanson, D. A. Splitter, and R. D. Reitz. Experiments and Modeling of Dual-Fuel HCCI and PCCI Combustion Using In-Cylinder Fuel Blending. *SAE Technical Paper 2009-01-2647*, 2009.

[61] S. L. Kokjohn, R. Hanson, D. Splitter, J. Kaddatz, and R. D. Reitz. Fuel Reactivity Controlled Compression Ignition (RCCI) Combustion in Light- and Heavy-Duty Engines. *SAE Int. J. Engines*, 4(1):360–374, 2011.

[62] S. L. Kokjohn, R. M. Hanson, D. A. Splitter, and R. D. Reitz. Fuel Reactivity Controlled Compression Ignition (RCCI): A Pathway to Controlled High-Efficiency Clean Combustion. *International Journal of Engine Research*, 12(3):209–226, 2011.

[63] S. L. Kokjohn, D. A. Splitter, R. M. Hanson, R. D. Reitz, V. Manente, and B. Johansson. Modeling Charge Preparation and Combustion in Diesel Fuel, Ethanol, and Dual-Fuel PCCI Engines. *Atomization and Sprays*, 21(2):107–119, 2011.

[64] C. Kolodziej, M. Wissink, D. Splitter, H. R., R. D. Reitz, and J. Benajes. Particle Size and Number Emissions from RCCI with Direct Injections of Two Fuels. *SAE Technical Paper 2013-01-1661*, 2013.

[65] S. C. Kong and R. D. Reitz. Modeling Diesel Spray Flame Liftoff, Sooting Tendency, and NOx Emissions Using Detailed Chemistry with Phenomenological Soot Model. *Journal of Engineering for Gas Turbines and Power*, 129:245 – 251, 2007.

[66] T. Korakianitis, A. M. Namasivayam, and R. J. Crookes. Natural-Gas Fueled Spark-Ignition (SI) and Compression-Ignition (CI) Engine Performance and Emissions. *Progress in Energy and combustion Science*, 37:89–112, 2011.

[67] H. Ku. Notes on the Use of Propagation of Error Formulas. *Journal of Research of the National Bureau of Standards, Section C: Engineering and Instrumentation*, 70C(4):263 – 273, 1966.

[68] T. M. Liou, M. Hall, D. A. Santavicca, and B. F. V. Laser Doppler Velocimetry Measurements in Valved and Ported Engines. *SAE Technical Paper 840375*, 1984.

[69] J. Liu, F. Yang, H. Wang, M. Ouyang, and S. Hao. Effects of Pilot Fuel Quantity on the Emissions Characteristics of a CNG/Diesel Dual Fuel Engine with Optimized Pilot Injection Timing. *Applied Energy*, 110:201–206, 2013.

[70] M. Malenshek and D. B. Olsen. Methane Number Testing of Alternative Gaseous Fuels. *Fuel*, 88:650 – 656, 2009.

[71] V. Manente, B. Johansson, P. Tunestal, and W. J. Cannella. Influence of Inlet Pressure, EGR, Combustion Phasing, Speed and Pilot Ratio on High Load Gasoline Partially Premixed Combustion. *SAE Technical Paper 2010-01-1471*, 2010.

[72] V. Manente, B. Johansson, P. Tunestal, and W. J. Cannella. Effects of Ethanol and Different Type of Gasoline Fuels on Partially Premixed Combustion from Low to High Load. *SAE Technical Paper 2010-01-0871*, 2010.

[73] D. J. Murphy and C. A. S. Hall. Year in Review - EROI or Energy Return on (Energy) Invested. *Ecological Economics Reviews*, 2010.

[74] P. M. Najt and D. E. Foster. Compression-Ignited Homogeneous Charge Combustion. *SAE Technical Paper 830264*, 1983.

[75] D. E. Nieman. *Computational Study and Optimization of Heavy-Duty Natural Gas/Diesel RCCI Operation*. PhD thesis, University of Wisconsin - Madison, 2012.

[76] D. E. Nieman, A. B. Dempsey, and R. D. Reitz. Heavy-Duty RCCI Operation Using Natural Gas and Diesel. *SAE Technical Paper 2012-01-0379*, 2012.

[77] C. Noehre, M. Andersson, B. Johansson, and A. Hultqvist. Characterization of Partially Premixed Combustion. *SAE Technical Paper 2006-01-3412*, 2006.

[78] H. Ogawa, N. Miyamoto, C. Li, S. Nakazawa, and K. Akao. Low Emission and Knock-Free Combustion with Rich and Lean Biform Mixture in a Dual-Fuel CI Engine with Induced LPG as the Main Fuel. *SAE Technical Paper 2001-01-3502*, 2001.

[79] I. C. on Combustion Engines. Impact of Gas Quality on Gas Engine Performance. In *CIMAC Working Group 17 Position Paper*, July 2015.

[80] S. Onishi, S. H. Jo, K. Shoda, P. D. Jo, and S. Kato. Active Thermo-Atmosphere Combustion (ATAC) - A New Combustion Process for Internal Combustion Engines. *SAE Technical Paper 790501*, 1979.

[81] P. J. O'Rourke and A. A. Amsden. A Spray/Wall Interaction Submodel for the KIVA-3 Wall Film Model. *SAE Technical Paper 2000-01-0271*, 2000.

[82] A. Paykani, A. H. Kakaee, P. Rahnama, and R. D. Reitz. Progress and Recent Trends in Reactivity-Controlled Compression Ignition Engines. *International Journal of Engine Research*, 17:481 – 524, 2016.

[83] S. B. Pope. *Turbulent Flows*, pages 358 – 386. Cambridge University Press, New York, 2000.

[84] W. W. Pulkrabek. *Engineering Fundamentals of the Internal Combustion Engine*, pages 1–36. Pearson Prentice-Hall, New Jersey, 2003.

[85] Y. Ra and R. D. Reitz. The Application of a Multicomponent Droplet Vaporization Model to Gasoline Direct Injection Engines. *International Journal of Engine Research*, 4:193 – 218, 2003.

[86] Y. Ra and R. D. Reitz. A Reduced Chemical Kinetic Model for IC Engine Combustion Simulations with Primary Reference Fuels. *Combustion and Flame*, 155:719 – 738, 2008.

[87] Y. Ra, P. Loeper, R. D. Reitz, M. Andrie, R. Krieger, D. E. Foster, R. Durrett, V. Gopalakrishnan, A. Plazas, R. Peterson, and P. Szymkowicz. Study of High Speed Gasoline Direct Injection Compression Ignition (GDICI) Engine Operation in the LTC Regime. *SAE Technical Paper 2011-01-1182*, 2011.

[88] R. J. Reed. *North American Combustion Handbook*. North American Manufacturing Company, Cleveland, 1986.

[89] S. Regitz and N. Collings. Study of Cycle-By-Cycle Air-to-Fuel Ratio Determined from the Exhaust Gas Composition and a Novel Fast Response Device Based on a Wide Band Lambda Sensor. *SAE Technical Paper 2008-01-2439*, 2008.

[90] R. D. Reitz and G. Duraisamy. Review of High Efficiency and Clean Reactivity Controlled Compression Ignition (RCCI) Combustion in Internal Combustion Engines. *Progress in Energy and Combustion Science*, 46:12–71, 2015.

[91] G. Rozenchan, D. L. Zhu, C. K. Law, and S. D. Tse. Outward Propagation, Burning Velocities, and Chemical Effects of Methane Flames up to 60 ATM. *Proceedings of the Combustion Institute*, 29:1461 – 1469, 2002.

[92] M. Sellnau, J. Sinnamon, K. Hoyer, and H. Husted. Full-Time Gasoline Direct-Injection Compression Ignition (GDCI) for High Efficiency and Low NOx and PM. *SAE Technical Paper 2012-01-0384*, 2012.

[93] M. Sellnau, M. Foster, K. Hoyer, W. Moore, J. Sinnamon, and H. Husted. Development of a Gasoline Direct Injection Compression Ignition (GDCI) Engine. *SAE Technical Paper 2014-01-1300*, 2014.

[94] M. Sellnau, M. Foster, W. Moore, J. Sinnamon, K. Hoyer, and W. Klemm. Second Generation GDCI Multi-Cylinder Engine for High Fuel Efficiency and US Tier 3 Emissions. *SAE Technical Paper 2016-01-0760*, 2016.

[95] A. J. Shahlari, C. Hocking, E. Kurtz, and J. Ghandhi. Comparison of Compression Ignition Engine Noise Metrics in Low-Temperature Combustion Regimes. *SAE Technical Paper 2013-01-1659*, 2013.

[96] S. Singh, L. Liang, S. C. Kong, and R. D. Reitz. Development of a Flame Propagation Modesl for Dual-Fuel Partially Premixed Compression Ignition Engines. *International Journal of Engine Research*, 7(1):65 – 75, 2006.

[97] D. Splitter, R. D. Reitz, and R. Hanson. High Efficiency, Low Emissions RCCI Combustion by Use of a Fuel Additive. *SAE Int. J. Fuels Lubr.*, 3(2):742–756, 2010.

[98] D. Splitter, R. Hanson, S. Kokjohn, and R. D. Reitz. Reactivity Controlled Compression Ignition (RCCI) Heavy-Duty Engine Operation at Mid-and High-Loads with Conventional and Alternative Fuels. *SAE Technical Paper 2011-01-0363*, 2011.

[99] D. Splitter, M. Wissink, D. DelVescovo, and R. Reitz. RCCI Engine Operation Towards 60% Thermal Efficiency. *SAE Technical Paper 2013-01-0279*, 2013.

[100] D. A. Splitter, R. N. Hanson, S. L. Kokjohn, and R. D. Reitz. Improving Engine Performance by Optimizing Fuel Reactivity with a Dual Fuel PCCI Strategy. In *THIESEL Conference on Thermo and Fluid Dynamic Processes in Diesel Engines*, 2010.

[101] D. A. Splitter, S. L. Kokjohn, K. Rein, R. M. Hanson, S. Sanders, and R. D. Reitz. An Optical Investigation of Ignition Processes in Fuel Reactivity Controlled PCCI Combustion. *SAE Technical Paper 2010-01-0345*, 2010.

[102] D. A. Splitter, M. L. Wissink, T. L. Hendricks, J. B. Ghandhi, and R. D. Reitz. Comparison of RCCI, HCCI, and CDC Operation from Low to Full Load D.A. In *THIESEL Conference on Thermo and Fluid Dynamic Processes in Direct Injection Engines*, 2012.

[103] K. K. Srinivasan, S. R. Krishnan, and Y. Qi. Cyclic Combustion Variations in Dual Fuel Partially Premixed Pilot-Ignited Natural Gas Engines. *Journal of Energy Resources Technology*, 2013.

[104] Y. Sun. *Diesel Combustion Optimization and Emissions Reduction Using Adaptive Injection Strategies (AIS) with Improved Numerical Models*. Doctoral dissertation, University of Wisconsin - Madison, 2007.

[105] K. Sung. Private Communication, 2011.

[106] Y. Takeda, N. Keiichi, and N. Keiichi. Emissions Characteristics of Premixed Lean Diesel Combustion with Extremely Early Staged Fuel Injection. *SAE Technical Paper 961163*, 1996.

[107] E. Tomita, N. Kawahara, Z. Piao, and S. Fujita. Hydrogen Combustion and Exhaust Emissions Ignited with Diesel Oil in a Dual Fuel Engine. *SAE Technical Paper 2001-01-3503*, 2001.

[108] E. Tomita, N. Kawahara, Z. Piao, and R. Yamaguchi. Effects of EGR and Early Injection of Diesel Fuel on Combustion Characteristics and Exhaust Emissions in a Methane Dual Fuel Engine. *SAE Technical Paper 2002-01-2723*, 2002.

[109] S. E. Trautwein, A. Grudno, and G. Adomeit. The Influence of Turbulence Intensity and Laminar Flame Speed on Turbulent Flame Propagation Under Engine Like Conditions. *Symposium (International) on Combustion*, 23(1):723 – 728, 1991.

[110] R. Wagner, S. Curran, A. Dempsey, S. Sluder, D. Splitter, J. Szybist, and B. West. ORNL Advanced Combustion Research and Future Fuel Opportunities. In *Saudi Aramco Workshop "Future of Transport Fuels"*, Mar. 2014.

[111] N. R. Walker, A. B. Dempsey, M. J. Andrie, and R. D. Reitz. Experimental Study of Low-Pressure Fueling Under RCCI Engine Operation. In *Americas 24th Annual Conference on Liquid Atomization and Spray Systems*, May 2012.

[112] N. R. Walker, A. B. Dempsey, M. J. Andrie, and R. D. Reitz. Use of Low-Pressure Direct-Injection for Reactivity Controlled Compression Ignition (RCCI) Light-Duty Engine Operation. *SAE Int. J. Engines*, 6(2):1222–1237, 2013.

[113] N. R. Walker, F. D. F. Chuahy, and R. D. Reitz. Comparison of Diesel Pilot Ignition (DPI) and Reactivity Controlled Compression Ignition (RCCI) in a Heavy-Duty Engine. *ASME Technical Paper ICEF2015-1128*, 2015.

[114] N. R. Walker, M. L. Wissink, D. A. DelVescovo, and R. D. Reitz. Natural Gas for High Load Dual-Fuel Reactivity Controlled Compression Ignition in Heavy-Duty Engines. *Journal of Energy Resources Technology*, 2015.

[115] C. S. Weaver and S. H. Turner. Dual Fuel Natural Gas/Diesel Engines: Technology, Performance, and Emissions. *SAE Technical Paper 940548*, 1994.

[116] M. Wissink, Z. Wang, D. Splitter, A. Shahlari, and R. D. Reitz. Investigation of Pressure Oscillation Modes and Audible Noise in RCCI, HCCI and CDC. *SAE Technical Paper 2013-01-1652*, 2013.

[117] M. L. Wissink. *Direct Injection for Dual Fuel Stratification (DDFS): Improving the Control of Heat Release in Advanced IC Engine Combustion Strategies*. Doctoral dissertation, University of Wisconsin - Madison, 2015.

[118] M. L. Wissink and R. D. Reitz. Direct Dual Fuel Stratification, a Path to Combine the Benefits of RCCI and PPC. *SAE Technical Paper 2015-01-0856*, 2015.

[119] J. Yamaguchi. Honda Readies Activated Radical Combustion Two-Stroke Engine for Production Motorcycle. *Automotive Engineering*, 1997.

[120] P. Zoldak, A. Sobiesiak, M. Bergin, and D. D. Wickman. Computational Study of Reactivity Controlled Compression Ignition (RCCI) Combustion in a Heavy-Duty Diesel Engine Using Natural Gas. *SAE Technical Paper 2014-01-1321*, 2014.